

# DEVELOPMENT OF LABORATORY AND SYNCHROTRON BASED 2D/3D XRF TECHNIQUES FOR MULTIDISCIPLINARY RESEARCH

Word count: 52,548

Brecht Laforce

Student number: 00802323

Supervisor(s): Prof. Dr. Laszlo Vincze,  
Prof. Dr. Luc Van Hoorebeke, Dr. Bart Vekemans

A dissertation submitted to Ghent University in partial fulfilment of the requirements for the degree of Doctor of Science: Chemistry

Academic year: 2017 – 2018



# Dankwoord

Aan het eind gekomen van mijn doctoraatsopleiding is het tijd eens stil te staan en achterom te kijken naar de lange weg die ik afgelegd heb sinds mijn begindagen aan de XMI-onderzoeksgroep. Het indienen van deze thesis is ook het afsluiten van een hoofdstuk in mijn leven dat vol zat met mooie en leerrijke momenten van verwondering en diepgaande wetenschappelijke discussies maar evenzeer goed gespijsd was met humor en vriendschap. Daarom wil ik graag deze kans grijpen om iedereen die mij langsheen deze weg geholpen en gesteund heeft te bedanken.

The very first person I would like to thank is prof. Laszlo Vincze, my supervisor. Thank you Laszlo, for giving me the opportunity to join your research group. Throughout the years, I have knocked on your door innumerable times and always you were ready to discuss yet another aspect of my research, guiding me along the track of my PhD with an always present smile and lots of encouragements. Without your support and advice, completing all projects and sides projects I embarked upon these last four years would have been very hard indeed.

Wanneer ik prof. Vincze bedank, moet ik in één adem Dr. Bart Vekemans vermelden, het tweede lid van de XMI-tandem, op wiens bureau ik eveneens vele uren doorgebracht heb. Onze samenwerking startte bij het prille begin van mijn doctoraat in de vorm van je doorgedreven training voor mijn IWT verdediging en is daarna nooit stilgevallen. Wanneer je aanwezig was wist ik dat ik steeds welkom was voor een bespreking en wat bijsturing, een feit waar ik dan ook gretig gebruik (of misbruik?) van gemaakt heb. Mijn hartelijk dank hiervoor!

Verder wil ik mijn co-promotor prof. Luc Van Hoorebeke van harte bedanken. Naast wetenschappelijke input en interessante gesprekken over de HERAKLES scanner, zorgde je er ook voor dat ik mijn eigen stekje

kreeg in jullie gebouw op het INW, waardoor ik me er meteen welkom voelde.

Ik heb volop genoten van deze afgelopen vier jaar en dat was in grote mate te danken aan mijn fijne collega's, te beginnen bij de leden van de XMI-groep. Wanneer ik toekwam als groentje, net afgestudeerd, werd ik met open armen ontvangen door Lien, Jan, Eva en Pieter. Altijd stonden jullie klaar voor een gesprek (wetenschappelijk of juist niet) en hulp wanneer dat nodig was. De middagpauzes zouden niet dezelfde geweest zijn zonder jullie en het bureau een stuk leger. Door de jaren heen heb ik velen van jullie een nieuwe weg zien inslaan, wat steeds gepaard ging met een beetje spijt. Naast vrienden die vertrokken, zag ik tijdens mijn doctoraat ook heel wat nieuwe gezichten toekomen in de groep. Björn, met wie ik de eer heb nu al enkele jaren een bureau te delen en die steeds te vinden is voor een aangename wetenschappelijke discussie en natuurlijk onze youngsters Ella en Niels die voor een frisse wind binnen XMI zorgen. Een speciale vermelding ook voor Stephen, we zijn op hetzelfde moment begonnen bij XMI en zullen ook op hetzelfde moment ons doctoraat afgerond hebben. Daar in het verre Frankrijk sprong je stevast eens binnen tijdens onze beamtimes, wat steeds voor een leuke afleiding zorgde en vaak ook voor waardevolle hulp.

Ook enkele wetenschappers en (ex-)leden van het UGCT groep verdienen met absoluut hun stekje in dit dankwoord. In de eerste plaats wil ik daarom Dr. Bert Masschaele bedanken, zonder wiens rijke ervaring en ontembaar enthousiasme de ontwikkeling van HERAKLES ongetwijfeld veel moeizamer zou verlopen zijn. Verder wens ik ook Dr. Manuel Dierick te bedanken. Je herhaalde hulp bij het begrijpen van de LabVIEW code heeft me vaak verder geholpen wanneer ik geen kant meer uit kon. Tot slot was Matthieu Boone er ook steeds om me verder te helpen bij heel wat praktische problemen en experimentele uitdagingen. Voor onze volgende conferentie zal ik op mijn fiets blijven zitten! Met het risico te veralgemenend over te komen wil ik ook alle andere mensen van het UGCT bedanken voor de hulp.

During my beamtimes at the European Synchrotron Radiation Facility, I really appreciated the good, professional help I received from the beamline staff. Whenever you called them they were ready to give assistance or guide you through a difficult moment (yes, even during weekends!). For that I would like to thank Remi, Julie and JP from ID16B and Manfred, Andreas and Tilman from ID13.

Doorheen dit doctoraat ben ik heel wat samenwerkingen aangegaan. Het is onmogelijk iedereen individueel te vermelden, maar ik wens toch in het bijzonder Steven, Charlotte en Lisa te bedanken voor de aangename beamtimes die we samen mochten beleven.

Het Instituut voor Wetenschap en Technologie (IWT) wens ik te bedanken voor hun financiële steun, zonder dewelke dit project nooit tot stand had kunnen komen. Daarnaast dien ik ook de Hercules foundation te bedanken voor de financiering van ontwikkeling van de Herakles 3D X-ray scanner

Het leven is meer dan werken alleen, hoe interessant het werk ook mag zijn. Van tijd tot tijd moet een mens wat kunnen ontspannen. Op die momenten kon ik steeds rekenen op vrienden en familie. Mama en papa, ik kan steeds bij jullie terecht met problemen groot en klein en weet dat ik steeds een luisterend oor of helpende hand zal vinden. Ook bij Elien en Dries ben ik altijd welkom. De wekelijkse zwemdate zorgt steeds voor een aangename afwisseling van de werkweek. Wat bijpraten, ook al is het maar 5 minuutjes, doet altijd deugd.

Het laatste stukje tekst heb ik gespaard voor de belangrijkste persoon in dit lijstje. Dankjewel Jolien om er altijd voor me te zijn, me op te beuren als het wat moeilijker ging en met veel liefde mijn klaaguurtje te doorstaan als ik er nood aan had frustraties te ventileren. Je was er bij van aan het begin en deelde alle lief en leed van de afgelopen jaren. Ik ben blij en fier dat ik me jouw man mag noemen.

*Brecht Laforce,*

*Februari 2018, Hertsberge*

# List of symbols

## Abbreviations and acronyms

2D	Two dimensional
3D	Three dimensional
BM	Bending magnet
CCD	Charged coupled device
CMOS	Complementary Metal Oxide Semiconductor
cXRF	Confocal XRF
DCC	Doubly curved crystal (optics)
ED	Energy dispersive
EDXRF	Energy Dispersive XRF
ECM	Extracellular matrix
ESRF	European Synchrotron radiation facility
FET	Field effect transistor
FPM	Fundamental parameter method
FWHM	Full width at half maximum
HPGe	High purity germanium (detector)
ID	Insertion device
IP	Intraperitoneal (chemotherapy)
KB	Kirkpatrick-Baez (mirrors)
LINAC	Linear accelerator
LOD	Limit of detection
LT	Live time
MC	Monte Carlo (simulation)
$\mu$ CT	Microscopic X-ray computed tomography
NIST	National Institute of Standards and Technology
RGB	Red/green/blue (image)
RT	Real time
ROI	Region of interest
SDD	Silicon drift detector

Si(Li)	Silicon lithium drifted (detector)
SORS	Spatially offset Raman spectroscopy
SR	Synchrotron radiation
SRM	Standard reference material
VI	(LabVIEW) virtual instrument
XANES	X-ray absorption near-edge structure
XAS	X-ray absorption spectroscopy
XMIMSIM	Monte Carlo aided quantification software
XRD	X-ray diffraction
XRF	X-ray fluorescence
XRF-CT	X-ray fluorescence computed tomography

## Symbols

$A_{i,cor}$	Absorption correction factor for element i
$c$	Speed of light
$d$	Lattice spacing of diffracting crystal
$e^-$	Electron
$E_{res}$	Energy resolution
$F$	Fano factor
$G$	Geometry factor (fundamental parameter method)
$I$	Intensity of the X-ray beam
$I_0$	Incident intensity of the X-ray beam
$K$	Deflection parameter of an insertion device
$m_e$	Rest mass of an electron
$p$	Degree of linear polarization
$Q_{iK\alpha}$	X-ray fluorescence production cross-section
$w_i$	Weight fraction of element i
$x$	Momentum transfer
$Z$	Atomic number
$\mu$	Total mass attenuation coefficient
$\gamma$	Lorentz factor
$\theta_c$	Critical angle for total reflection
$\lambda$	Wavelength

$\nu$	Frequency
$\rho$	Density
$\sigma$	Total linear attenuation coefficient
$\sigma_C$	Compton scattering cross-section
$\sigma_R$	Rayleigh scattering cross-section
$\sigma_T$	Thompson scattering cross-section
$\tau$	Photoelectric cross-section
$\omega$	Fluorescence yield
$\Omega$	Solid angle



# Contents

Chapter 1	Introduction.....	1
Chapter 2	X-rays, their generation and interactions with matter.....	4
2.1.	Discovery and early history .....	4
2.2.	Generating X-rays .....	5
2.2.1.	X-ray tubes.....	5
2.2.2.	Synchrotron radiation.....	8
2.2.3.	Radioactive isotopes .....	13
2.3.	Interactions of X-rays with matter .....	13
2.3.1.	Photoelectric effect .....	13
2.3.2.	Scattering .....	15
2.3.3.	Attenuation of X-rays .....	18
2.4.	Optics for X-rays.....	19
2.4.1.	Capillary optics .....	19
2.4.2.	Kirkpatrick-Baez Mirrors.....	21
2.4.3.	Monochromators and Doubly Curved Crystal optics .....	22
2.5.	Detecting X-rays .....	23
2.5.1.	Non-energy dispersive X-ray detection .....	23
2.5.2.	Energy dispersive X-ray detection.....	26
2.6.	References .....	30
Chapter 3	3D X-ray based analysis techniques .....	32
3.1.	Tomography .....	32
3.1.1.	Principle .....	33
3.1.2.	Reconstruction algorithms .....	34

3.2. Quantification of XRF data.....	36
3.2.1. Semi-quantitative analysis using elemental yields .....	36
3.2.2. Fundamental parameter method.....	37
3.2.3. Monte Carlo simulation aided quantification .....	40
3.3. Recent trends in XRF techniques.....	42
3.3.1. Latest trends in laboratory XRF imaging.....	42
3.3.2. Developments at synchrotron radiation facilities .....	45
3.4. References .....	47
Chapter 4 HERAKLES: a combined 3D-XRF and X-ray computed tomography scanner .....	50
4.1. Concept of the scanner.....	51
4.2. Components of the HERAKLES scanner .....	53
4.2.1. High-resolution X-ray computed tomography module.....	53
4.2.2. Confocal XRF module .....	54
4.2.3. XRF tomography module .....	59
4.2.4. Complementarity of the XRF techniques .....	63
4.2.5. Overview of the HERAKLES X-ray equipment .....	64
4.3. Instrument stability and safety measures .....	65
4.4. Integration of the end-stations .....	67
4.4.1. Motor system .....	67
4.4.2. Control software.....	70
4.4.3. $\mu$ CT – XRF linking software .....	72
4.5. Alignment and calibration of the instrument .....	73
4.5.1. $\mu$ CT alignment .....	74
4.5.2. Calibration of the coordinate system .....	75
4.5.3. Alignment of the confocal setup .....	77
4.6. Instrument characterization and test cases .....	78

4.6.1. Beamsize determination.....	78
4.6.2. Limits of detection (LOD) determination .....	82
4.6.3. Test-case: $\mu$ CT – confocal XRF linking .....	85
4.7. References .....	87
Chapter 5     Applications of HERAKLES .....	89
5.1. Ecotoxicology: <i>Daphnia magna</i> model organism .....	90
5.2. Catalysis: Expanded perlite support material .....	94
5.3. Layered samples in cultural heritage .....	102
5.3.1. Methods.....	103
5.3.2. Materials .....	104
5.3.3. Results.....	105
5.4. References .....	111
Chapter 6     Towards nanometer resolution at ESRF ID16B-NA .....	112
6.1. Experimental Setup: ID16B-NA beamline .....	113
6.2. Analytical characteristics during the experiments .....	114
6.3. First Earth and planetary science applications at ID16B - April 2014.....	118
6.3.1. Sample preparation and mounting .....	120
6.3.2. Results and Discussion .....	122
6.3.3. Conclusions.....	128
6.4. Biomedical application: assessing the effect of cisplatin on ovarian cancer tumors .....	129
6.5. Nano-XANES experiments on cisplatin treated ovarian cancer tumors .....	134
6.6. References.....	138
Chapter 7     The symbiosis between laboratory and synchrotron.....	140
7.1. How a synchrotron experiment benefits from lab-based analysis .....	141

7.1.1. Lab-based microscopy to locate the ROI.....	141
7.1.2. Lab-based micro-XRF as a tool for sample selection.....	144
7.1.3. $\mu$ CT revealing the internal morphology of the samples .....	145
7.2. Methodologies developed in the lab .....	145
7.3. Synchrotron know-how transferred to the lab .....	147
7.3.1. Basic principles and layout of the scanner.....	147
7.3.2. Sample visualization .....	148
7.3.3. User interface for ROI selection .....	149
7.4. Experimental case: microkrystites and –meteorites.....	150
7.4.1. Microkrystite samples .....	151
7.4.2. Preliminary scans at the HERAKLES scanner .....	152
7.4.3. Synchrotron nano-XRF experiment: experimental setup ESRF ID16B.....	154
7.5. References.....	162
Chapter 8 Summary, conclusions and outlook .....	163
8.1. Summary and conclusions .....	163
8.1.1. The HERAKLES 3D X-ray scanner.....	163
8.1.2. Nanoscopic XRF imaging at SR facilities .....	165
8.1.3. Symbiosis of the laboratory and synchrotron .....	167
8.2. Future outlook.....	167
8.3. Summary of the authors input to HERAKLES.....	168
A1: English summary .....	170
Methods.....	171
HERAKLES 3D X-ray scanner .....	171
Results.....	173
Conclusions.....	176
References.....	177

A2: Nederlandse samenvatting .....	178
Methodes.....	179
HERAKLES 3D X-straal scanner.....	179
Resultaten.....	181
Conclusies .....	184
References .....	185
A3: Software Manual .....	186
HERAKLES.....	186
Imaging the sample in transmission mode.....	188
Movement and alignment of the sample.....	189
Camera settings .....	191
Starting a $\mu$ CT scan.....	192
Performing an XRF experiment.....	194
$\mu$ CT – XRF linking software .....	199
A4: Start-up procedures for HERAKLES.....	208
Normal procedure .....	208
Procedure after complete shutdown of the instrument .....	209
A5: List of beamtimes.....	211
A6: List of publications .....	213

# Chapter 1

## Introduction

This dissertation focusses on three-dimensional (3D) X-ray based analysis techniques being microscopic computed tomography ( $\mu$ CT), confocal X-ray fluorescence (confocal XRF) and X-ray fluorescence tomography (XRF-CT). Each of these techniques has versatile applications in scientific research including archaeology, (bio)medical imaging, cosmology, ecology, geology, material sciences and many more. Three-dimensional XRF analysis yields the 3D distribution of the detectable composing elements of a sample through the detection of the characteristic fluorescent X-rays. With the exception of H, He and Li, all elements in the periodic table have a specific and unique set of fluorescent X-ray energies, characteristic X-ray emission lines, which yield qualitative element information on the sample, while the intensity of the emitted fluorescent radiation carries quantitative information. Using  $\mu$ CT, it is possible to image the 3D morphology of an object by means of differences in X-ray attenuation depending on the internal structures.

It was the combination/integration of these complementary non-destructive 3D analytical techniques which was the goal of this project. These developments resulted in the HERAKLES 3D X-ray scanner, a novel instrument for integrated 3D element/structural micro-analysis. A second focus of this work was the development and application of nano-XRF imaging methodologies at state-of-the-art synchrotron radiation facilities such as the ID16 NINA beamline at the European Synchrotron Radiation Facility (ESRF) in Grenoble (France). Finally, the

complementarity of laboratory and synchrotron based experiments was used to optimize the output of synchrotron beamtimes.

This thesis aims at introducing the two main topics (laboratory instrument development and synchrotron radiation based experiments) separately before moving on to the chapters detailing the integration of these two scientific settings.

Chapter 2 contains the theoretical background concerning X-rays which the reader may find useful in understanding the rest of this thesis. It elaborates on the history of X-rays, their physical properties and details the interactions of X-rays with material. To conclude this chapter, the hardware necessary for X-ray generation, beam conditioning (i.e. by X-ray optics) and detection is discussed. These components will of course play a major role in the instrument development discussed in this work.

In Chapter 3, the applied X-ray methodologies are discussed. More specifically, the principle of tomography is introduced together with a short section on reconstruction algorithms. Furthermore, this chapter deals with quantification of XRF experiments through semi-quantitative analysis, the fundamental parameter method and Monte Carlo aided XRF quantification.

The development of the HERAKLES 3D X-ray scanner is described in Chapter 4. This chapter elucidates the concept of this instrument and lists its advantages compared to similar instruments. The different techniques incorporated in the HERAKLES scanner are given with their specifications and a short characterization. Finally, the integration of the separate techniques is discussed, together with a test case experiment.

After introducing HERAKLES, Chapter 5 focusses on the applications of this novel scientific instrument in two showcase examples in the field of environmental science, with representative samples being the ecotoxicological model organism *Daphnia magna* and perlite support material pellets for biocatalysis in the context of waste gas treatment.

Next, Chapter 6 deals with synchrotron radiation based nano-XRF imaging experiments, focussing on the experiments performed during my PhD at the state-of-the-art ID16B beamline of the ESRF. This chapter describes experiments on cosmological, geological and biomedical samples at the nanoscopic scale.

Chapter 7 highlights the complementarity of the laboratory and a synchrotron radiation based X-ray imaging experiments. It demonstrates how preparatory laboratory experiments can contribute to maximizing the output of a synchrotron beamtime, and also how the analysis procedures established for laboratory instruments can be used to optimize synchrotron radiation experiments and vice versa.

The results obtained in this project are summarized in the last chapter, Chapter 8, coupled with some conclusions and an outlook for future work.



# Chapter 2

## X-rays, their generation and interactions with matter

### 2.1. Discovery and early history

X-ray radiation is electromagnetic radiation emitted by charged particles during transitions in atomic energy levels or by accelerated charged particles, conventionally with wavelengths between 0.01 and 10 nm, which approximately corresponds to photon energies in the range of 0.1 to 100 keV (Figure 2-1). The photons with these characteristics are invisible to the human eye, it is therefore no surprise that X-rays were only discovered at the end of the 19<sup>th</sup> century, after the discovery of electromagnetic radiation.

In 1895 Wilhelm Conrad Röntgen<sup>1</sup> was performing experiments using a Crookes tube when he noticed a visible fluorescence glow from a screen painted with BaPt(CN)<sub>4</sub> located close to the tube.<sup>2,3</sup> The name “X-rays” was given by W.C. Röntgen himself to indicate that this was a new and unknown type of radiation, propagating along straight lines. For this discovery, he received the first Nobel prize in Physics (1901).<sup>4</sup>

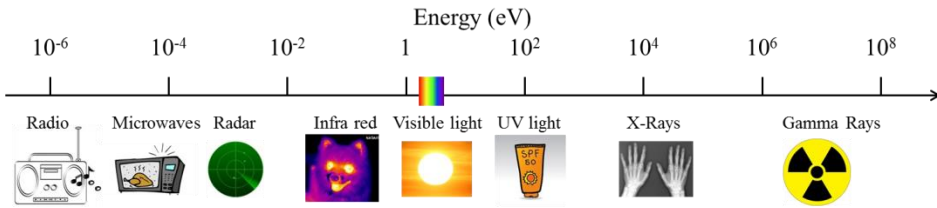


Figure 2-1 Electromagnetic spectrum in terms of photon energy (expressed in electronvolt), with the types of radiation and a pictorial representation. (Artwork by the author)

Soon after their discovery, the penetrating character of X-rays was quickly recognized and applied for imaging purposes. Among others, by visualizing bones in human hands, Röntgen established the most well-known form of X-ray imaging: i.e. medical diagnosis via radiography which is still widely used today.<sup>2,5</sup>

## 2.2. Generating X-rays

### 2.2.1. X-ray tubes

Initially only cathode-ray tubes have been used to generate X-rays, since the discovery of this type of electromagnetic radiation happened when Röntgen was performing experiments with a Crookes tube. The latter is an evacuated glass bulb with a cathode and anode encapsulated within the tube which was mainly used to study electrons. The first type of X-ray tubes carried the same name as this experimental device and was based on essentially the same design. The high voltage electric field in these cold cathode tubes ionized the residual air in the low-pressure environment, producing ions which upon impact with the cathode produce the so-called cathode-rays, or electrons. These electrons are in turn accelerated towards the anode, generating X-rays upon their impact.<sup>3</sup>

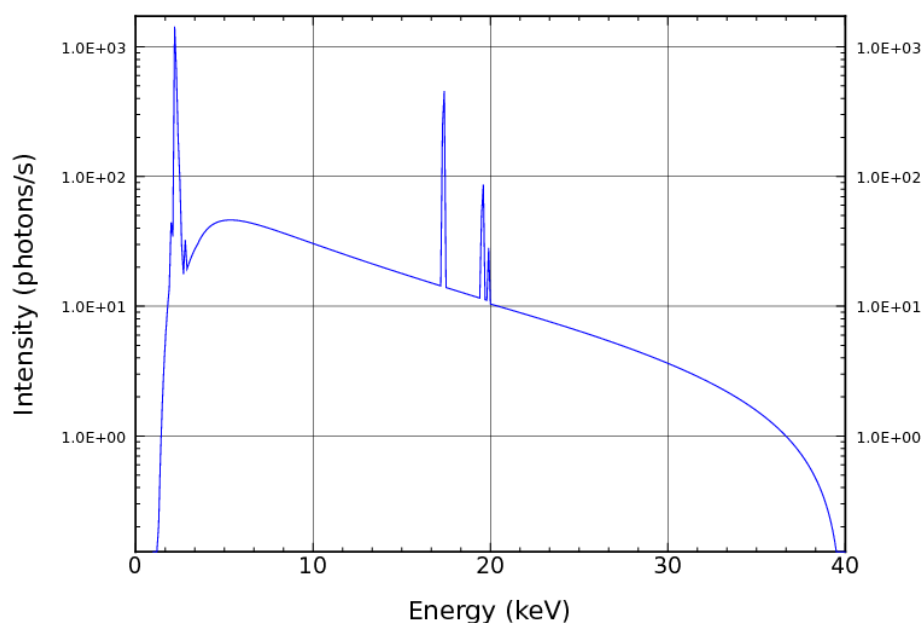


*Figure 2-2 Spectrum of an X-ray tube: the represented spectrum is the simulated spectrum of a Mo tube (at 40 kV and 0.6 mA) with moncapillary optics, as installed at the HERAKLES scanner (chapter 4) using the XMIMSIM software (see section 3.2.3. ).*

The design of the Crookes tubes rapidly evolved towards that of the modern X-ray tube: starting from the 1920s, they were gradually replaced by the hot cathode tubes, developed by Coolidge and hence also dubbed the Coolidge tube.<sup>3,6,7</sup> The basic principle of the Coolidge tube, as shown schematically in Figure 2-3, is still used in most X-ray tubes today.<sup>8</sup> Figure 2-2 shows the simulated spectrum of such tube (with Mo target). In the hot cathode tube, the electrons are no longer generated through ionization of the residual air, but through the thermionic effect taking place in the tungsten filament cathode. The electrons emitted from the filament are accelerated by the high voltage applied between the cathode and the anode (i.e. the target material of the tube), generating X-rays upon impact. Several metals are suitable as anode or target material (e.g. Cu, Mo, Rh, Ag, W), the selected material depending on the envisaged applications of the tube.

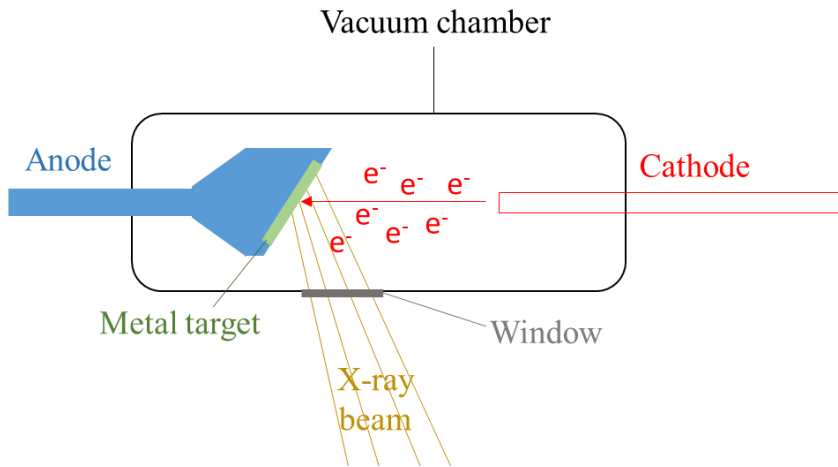


Figure 2-3 Schematic representation showing the working principle of an X-ray tube.

There are two physical processes responsible for generating X-rays in an X-ray tube. The first process is the deceleration of the electrons in the (screened) Coulomb fields of the atomic nuclei constituting the anode material. During this deceleration, part of the lost energy is emitted as X-ray photons, creating a continuous (background) radiation known as Bremsstrahlung (i.e. “braking radiation”). The second process responsible for X-ray generation is impact ionization. When an incoming electron interacts with a bound electron of an atom of the anode material, part of its energy can be transferred to this electron, removing it from the atom, thus creating a vacancy. When the vacancy is present in one of the inner shells of the atom, an electron from a higher shell (with a lower binding energy) fills this vacancy, ultimately resulting in a cascade of electron transitions causing the relaxation of the atom from its excited state. The energy difference between the shells involved in these transitions will then be emitted as characteristic X-ray photons. Due to the discrete energy levels of electrons in a certain element and the quantum mechanics governing this transition process, only a relatively small number of characteristic X-ray photon energies can be produced, giving rise to several relatively sharp and intense peaks present in a typical X-ray tube emission spectrum, superimposed on top of the Bremsstrahlung continuum as shown in Figure 2-2.

## 2.2.2. Synchrotron radiation

### 2.2.2.1. History of synchrotron radiation

A synchrotron is an installation in which due to a strong magnetic field charged particles (most often electrons or positrons) are forced to follow a (quasi)circular path at relativistic speeds. Originally, these particle accelerators were applied for experiments in the field of particle physics (e.g. collision experiments). In 1946, using General Electric's synchrotron accelerator, it was demonstrated that the accelerated electrons emitted electromagnetic radiation due to their centripetal acceleration, which at this early stage in the history of synchrotron radiation (SR) was considered disadvantageous (first generation synchrotron radiation facilities).<sup>9-12</sup> When the excellent characteristics of this radiation were discovered (e.g. high degree of natural collimation and extreme intensity), scientists started to use SR to perform experiments, at first in parasitic mode, but later on in dedicated facilities which have been designed specifically to yield synchrotron radiation with unmatched characteristics. The second generation synchrotrons used the radiation generated by their bending magnets to perform experiments in facilities which were no longer used for particle physics experiments, but were dedicated to the generation of synchrotron radiation.<sup>9,12</sup> The next step forward was the use of insertion devices (ID) which yield photon beams with even better characteristics in the so-called third generation synchrotron radiation facilities. These insertion devices, called wigglers and undulators, are arrays of strong alternating pole magnets which are inserted in the linear sections of the storage ring in between two bending magnets.<sup>9,13</sup> These magnets force the particles to deviate from their straight paths with a high frequency, which causes them to emit radiation. SR generated by a synchrotron radiation facility can cover a broad spectral range. In order to obtain radiation within the (hard) X-ray regime, the electrons (or positrons) must be accelerated to energies of several GeV.<sup>12</sup>

### 2.2.2.2. Generating synchrotron radiation

Since an important part of this thesis will deal with experiments performed at synchrotron radiation sources, the generation of this radiation will be explained in more detail.

Synchrotron radiation is generated by bending the trajectory of a relativistic charged particle in a magnetic field. The force responsible for this bending is the Lorentz force, which can be calculated by following equation:

$$\vec{F}_B = q(\vec{v} \times \vec{B}) \quad (2.1)$$

From the above formula it can be deduced that the magnitude of the Lorentz force depends on the charge of the particle  $q$ , its speed  $\vec{v}$  and the strength of the magnetic field  $\vec{B}$ . The direction of the force can be determined using the rules of vector multiplication to be perpendicular to both the magnetic field and the trajectory of the particle (i.e. an inward force as shown in Figure 2-4).

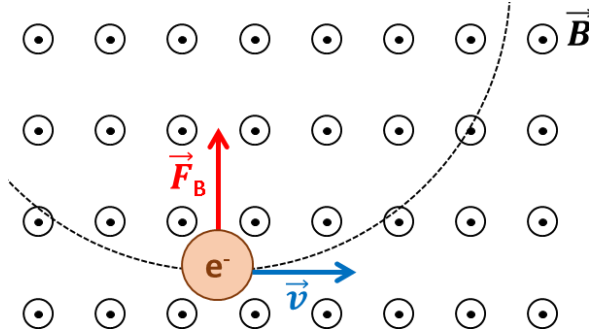


Figure 2-4 The Lorentz force: an electron moving in a homogeneous magnetic field undergoes a force causing it to move in a circular path.

The Lorentz force induces an acceleration which will force the electron to follow a circular trajectory. This acceleration will cause the emission of electromagnetic radiation of which the spectral distribution is mainly governed by the speed of the particle. At relativistic speeds of the particle, the emitted photon beam becomes conical in shape, with an

opening angle which is inversely proportional with the Lorentz factor  $\gamma$ . As can be seen in Equation (2.2), the reciprocal value of the Lorentz factor decreases for increasing particle speeds, indicating the photon beam approaches a nearly parallel beam for particles of which the magnitude of the speed  $v$  approaches the speed of light  $c$ . The Lorentz factor can also be written as the ratio between the total energy of the accelerated electron  $E$  to its rest mass energy which can be calculated from its rest mass  $m_e$  and the speed of light.

$$\gamma = \frac{1}{\sqrt{1-\beta^2}} = \frac{E}{m_e c^2} \quad \text{with } \beta = \frac{v}{c} \quad (2.2)$$

The particles orbiting in the synchrotron storage ring are generated with an electron gun where electron bunches with energies in the MeV range are produced by a linear accelerator (LINAC). Next, the booster ring is used to rise the energy of the electrons to the desired level of a few GeV. Once the needed energy has been achieved, the electrons are transferred into the actual storage ring. It is here where the process of generating usable synchrotron light takes place. The electrons are kept on their quasi-circular (in fact polygonal), closed orbit by the bending magnets, while radio frequency cavities are used to keep the electron beam at the right energy. Synchrotron radiation is either produced by a bending magnet (BM) or an insertion device (ID, i.e. wiggler or undulator) which are all magnetic structures. In terms of brilliance, the undulator sources yield the highest results, while radiation produced by the bending magnets has the lowest brilliance. A schematic overview of a synchrotron radiation facility is given in Figure 2-5. To simplify the figure some components are omitted. E.g. only one bending magnet is shown while in reality much more are obviously needed to keep the electrons in their closed quasi-circular trajectory. The European Synchrotron Radiation Facility (ESRF) in Grenoble uses 32 bending magnets, while the Advanced Photon Source (APS, Lemont, IL, US) uses 40 and the "Super Photon ring-8 GeV" (SPring8, Japan) 48.<sup>13</sup>

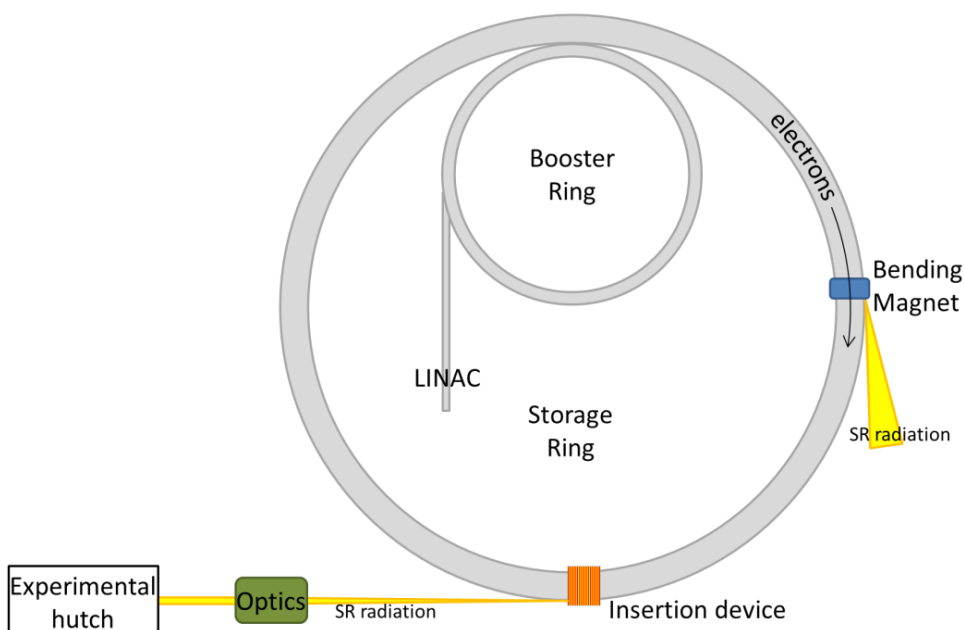


*Figure 2-5 Schematic representation of a synchrotron with some of the major components for the generation of synchrotron radiation (SR) indicated.*

Although the main function of bending magnets in a third generation synchrotron facility is to force the electrons in their closed (quasi)-circular trajectory, they are also a source of SR. They yield a smooth, continuous emission spectrum with characteristics (e.g. critical energy/wavelength) depending on both the parameters of the storage ring and the magnets. The high natural collimation which is typical for synchrotron radiation is lost in the horizontal direction for a bending magnet source due to the relatively large observation path. Slits can be used to provide horizontal collimation and limit the horizontal divergence.<sup>14</sup>

In order to optimize the properties of synchrotron radiation, insertion devices dedicated to the production of very high intensity beams were developed and integrated in the storage ring of third generation synchrotron radiation facilities. These devices consist of an array of



magnets with alternating poles, forcing the electrons to follow an oscillating trajectory around the longitudinal axis of the magnetic array, representing the main propagation path as shown in Figure 2-6.

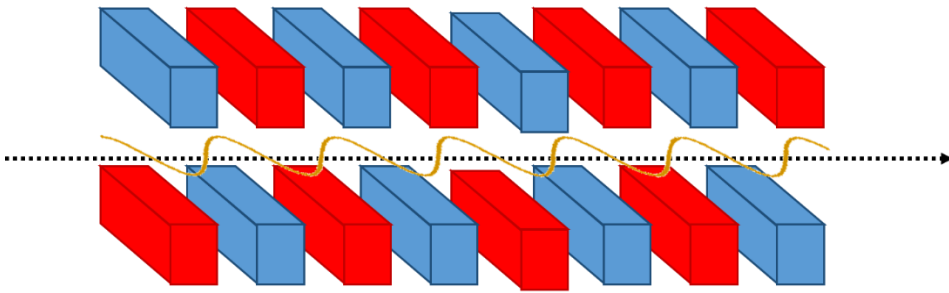


*Figure 2-6 Schematic representation of an ID: the alternating pole magnets (red and blue cuboids) force the electrons on an oscillating path (yellow line) along the main propagation axis (indicated with the dotted line)*

Each time the particles are deflected by these magnets, SR is produced, hence these devices achieve an important increase in photon flux. Furthermore, the spectral distribution of the produced photons can be tuned by changing the magnetic field strength. The main difference between the two types of insertion devices is the deflection they cause to the electron beam, indicated by the deflection parameter  $K$ . Wigglers induce large deflections ( $K \gg 1$ ), while the deflections by undulator sources are much smaller ( $K \leq 1$ ).<sup>14</sup> As a result, the wigglers can be compared to an array of bending magnets, with a large increase in photon flux. For a wiggler with  $N$  periods, the intensity due to the summation of the different sources will increase with a factor of  $2N$ . The resulting radiation will still have a smooth, continuous spectrum. Undulator emission, on the other hand, undergoes coherent addition of the radiation originating from the different positions along the magnetic segments, leading to a few narrow spectral peaks and an intensity increase compared to single magnets that is proportional with  $N^2$ .

### 2.2.3. Radioactive isotopes

A third common source of X-rays is represented by radioisotope sources with X-ray/gamma emission through radioactive decay processes.<sup>15</sup> One example is  $\text{Fe}^{55}$ , which produces the emission of Mn K-lines through electron capture and subsequent X-ray emission. Their use as excitation source in laboratory based X-ray spectroscopic analysis is limited, as such sources are hard to use in a controlled way, the radiation cannot be tuned and most importantly due to the associated safety measures required by the use of radioactive materials. Their main application in the domain of X-ray based analysis techniques is as calibration materials, because of their well-known emission spectra.

## 2.3. Interactions of X-rays with matter

When interacting with matter, X-rays may be scattered, diffracted or absorbed, all leading to attenuation of the incident X-ray beam. This paragraphs will go into some more detail of the main interactions occurring during this process, being the photoelectric effect and subsequent X-ray fluorescence (of prime interest for XRF spectroscopy), X-ray scattering and X-ray attenuation.

### 2.3.1. Photoelectric effect

When the photoelectric effect occurs, the incoming photon transfers all of its energy to one of the inner shell electrons of an atom, thus ejecting an electron from the element with a kinetic energy given by Equation (2.3).

$$E_{kin} = h\nu - E_{binding} \quad (2.3)$$

The photoelectric interaction to take place with an electron having a binding energy of  $E_{binding}$  requires that  $h\nu > E_{binding}$ . The photoelectric process creates an inner shell vacancy and leaves the atom in an excited state.

To relax from this energetically unfavourable state, an electron from a higher shell of the element will fill the vacancy. As a result of this electron transition process, a fluorescent photon with an energy equal to the energy difference between the two shells may be emitted in order to release the excess energy of the excited atom (i.e. the fluorescent X-ray). Since the energy levels of the shells are uniquely characteristic to a specific element, the emitted photon has a characteristic energy (or wavelength) which can be used to identify the element it originated from. The relation between the characteristic photon energy  $E$  and the atomic number  $Z$  of the corresponding element is given by Moseley's law (Equation (2.4)).

$$E = k (Z - \sigma)^2 \quad (2.4)$$

where  $k$  is a proportionality constant and  $\sigma$  is the screening constant.

The transition of an electron from a higher shell to the vacancy in its turn creates a new vacancy which can be filled via an analogue process, thus creating a cascade of electron transitions. One absorbed X-ray photon can hence result in several fluorescent photons. It is important to note that not all transitions of electrons between atomic shells are physically possible, but only those following strict quantum mechanical rules ( $\Delta j = \pm 1$  or 0 and  $\Delta l = \pm 1$ ).

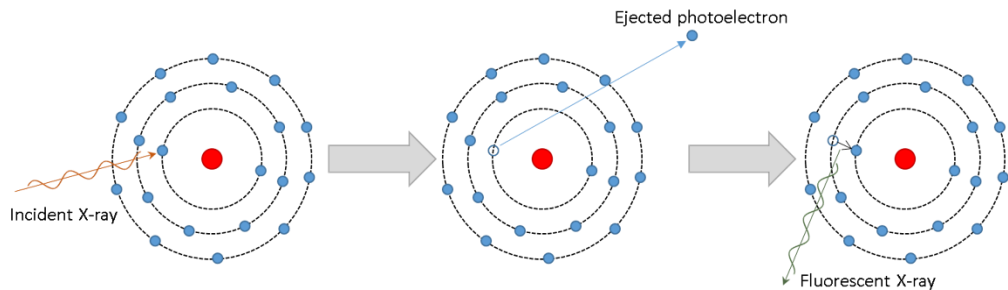


*Figure 2-7 The photoelectric effect: the incident X-ray excites an inner shell electron which is ejected as a photoelectron. The formed vacancy is filled by an electron from a higher shell, while emitting a fluorescent X-ray photon.*

Alternatively, the excited atom can release its excess of energy through radiationless processes such as the production of an Auger electron. In the case of elements with a low atomic number ( $Z$ ), this process will even be the predominant way of relaxation. The probability of the emission of a fluorescent photon (given by the fluorescence yield,  $\omega$ ) compared to Auger electron production will rise with increasing atomic number.<sup>16</sup>

Overall, the atomic number  $Z$  of the irradiated element and the energy of the incoming X-ray photon  $E$  will determine the total photoelectric cross-section  $\tau$  according to Equation (2.5).

$$\tau \sim Z^4 E^{-3} \quad (2.5)$$

There exist several conventions to name the characteristic X-ray lines of an element, but within the field of X-ray fluorescence, the Siegbahn notation is used most often. Here, the X-ray line is given a capital letter corresponding to the shell of the original vacancy (K, L, M) with a Greek letter in subscript to indicate the relative intensity of the different lines ( $\alpha$ ,  $\beta$  and  $\gamma$  from most to least intense). Because the Siegbahn notation groups the lines of several distinct transition under a common name (e.g.  $K_\alpha$ ), IUPAC has proposed a different method, based on the transition responsible for a specific line (e.g.  $K-L_3$ ).

X-ray fluorescence analysis is a widely used elemental analysis technique based on the above described photoelectric effect. Since each element emits a specific set of characteristic X-rays when irradiated with a primary X-ray beam, detecting the fluorescent photon energies originating from a sample enables the researcher to determine its elemental composition.

### 2.3.2. Scattering

One of the possible photon-matter interaction types is the scattering of an incoming X-ray photon in an elastic or inelastic manner.<sup>17</sup> The scattering interaction is called elastic when the photon retains its energy during the

process. In case the photon scatters on a free electron, elastic scattering is referred to as Thomson scattering. When the elastic scattering involves atomic, bound electrons, the process is referred to as Rayleigh scattering, which has a cross-section equal to the Thomson scattering cross-section multiplied with the square of the so-called atomic form factor (see Equation 2.6a).

For X-ray fluorescence (XRF) applications, the observation of Rayleigh scattering is of practical interest. In an X-ray fluorescence spectrum (see e.g. Figure 2-8) obtained from an excitation source also emitting discrete excitation component(s) (e.g. originating from characteristic lines of the X-ray tube target) one can always find the energy (or energies) of the (discrete components of the) incident photon beam, since no energy is lost during the scattering process. The probability of the elastic or coherent X-ray scattering interaction can be determined using the total Rayleigh scattering cross-section  $\sigma_R$ . In addition, the differential Rayleigh scattering cross-section can be employed to calculate the distribution of the scattering direction, which depends on the energy of the photon  $E$  (in keV), the scattering polar angle  $\theta$  and the azimuthal angle  $\varphi$  as can be seen in Equation (2.6b).

$$\frac{d\sigma_R}{d\Omega}(\theta, \varphi, E) = \frac{d\sigma_T}{d\Omega}(\theta, \varphi) F^2(x, Z) \quad (2.6a)$$

$$\frac{d\sigma_R}{d\Omega}(\theta, \varphi, E) = \frac{r_e^2}{2} [2 - \sin^2(\theta)(1 - p + 2p \cos^2(\varphi))] F^2(x, Z) \quad (2.6b)$$

$$x = \sin\left(\frac{\theta}{2}\right) \frac{E}{1.239} \quad (2.6c)$$

In these equations,  $F(x, Z)$  is the atomic form factor dependent on the atomic number  $Z$  and the momentum transfer  $x$  as defined by Equation (2.6c),  $\sigma_T$  is the Thomson scattering cross-section over solid angle  $\Omega$  and  $p$  is the degree of linear polarization.

From these equations it follows that Rayleigh scattering can be minimized when  $\theta$  is  $90^\circ$ ,  $\varphi$  equals  $0^\circ$  and the X-ray beam is 100% linearly polarized ( $p=1$ ). These results will be used later on when optimizing the detector – source positioning. Rayleigh scattering predominates for low energy photons and high atomic number elements.

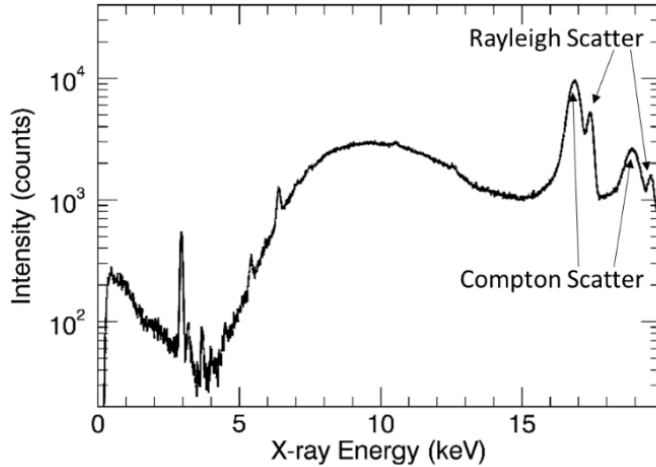


Figure 2-8. XRF spectrum resulting from a scattering experiment using an X-ray tube with Mo target. The Rayleigh and Compton scatter peaks of both the  $K_\alpha$  (left) and  $K_\beta$  (right) lines can be discerned in the spectrum.

Next to the elastic Thomson or Rayleigh scattering, the photon can undergo an inelastic scattering interaction referred to as Compton scattering.<sup>17</sup> During this interaction, part of the energy of the photon is transferred to an atomic (or free) electron, while conserving the total energy and momentum of the particles participating in the scattering process. This means that the energy/wavelength of the photon will change due to the interaction. The energy of the emitted photon after the Compton scattering depends on its initial energy  $E_0$  and the scattering angle  $\theta$  and can be calculated via the following formula:

$$E_C = \frac{E_0}{1 + E_0/m_e c^2 [1 - \cos(\theta)]} \quad (2.7)$$

With  $m_e$  the rest mass of an electron and  $c$  the speed of light.

The probability of an X-ray photon undergoing Compton scattering can be calculated by using its total Compton cross-section  $\sigma_C$ . Compton scattering intensities in the Compton peaks can be used to observe the (electron) density or total irradiated sample in case of samples having intermediate thickness (i.e. in between infinitely thin and infinitely thick). The ratio of Rayleigh and Compton peaks can be used to derive the effective atomic number of the so-called dark matrix of the illuminated sample region.

### 2.3.3. Attenuation of X-rays

When an X-ray beam propagates through matter, both types of scattering and the photoelectric effect will occur simultaneously, causing the beam to be attenuated. The importance of each process in a specific case is given by its cross-section. The total attenuation of the X-ray beam is governed by the sum of these three effects, the total linear attenuation (absorption) coefficient  $\sigma$ , which is a function of the atomic number of the irradiated element  $Z$  and the energy of the X-ray photons  $E$ :

$$\sigma(Z, E) = \sigma_R(Z, E) + \sigma_C(Z, E) + \tau(Z, E) \quad (2.8)$$

A real-life sample will nearly always consists of multiple elements. The mass attenuation coefficient ( $\mu = \sigma / \rho$ ) of such a sample can then be calculated when the elements  $i$  ( $n$  in total) and their respective weight fraction  $w_i$  are known:

$$\mu(E) = \sum_{i=1}^n \frac{w_i \sigma(Z_i, E)}{\rho} \quad (2.9)$$

The mass attenuation coefficient can be used in the Lambert-Beer equation to calculate the transmitted intensity of an X-ray beam with intensity  $I_0$  after passing through an object with known thickness  $T$  and density  $\rho$  (Equation 2.10).

$$I = I_0 \exp(-\mu(E)\rho T) \quad (2.10)$$

This equation can be easily extended to the case of  $k$  stacked layers with different composition, thickness and density:

$$I = I_0 \exp(-\sum_{i=1}^k \mu_i(E)\rho_i T_i) \quad (2.11)$$

In many ways Equation (2.11) forms the basis for quantifying XRF measurements as will be discussed later on.

## 2.4. Optics for X-rays

X-ray beams possibly generated by different X-ray sources need to be further altered in order to achieve properties that are necessary to efficiently perform microscopic/nanoscale XRF analysis. Therefore, specialized X-ray optics are used to improve for example the beam shape and size, or to monochromatize the X-ray beam. Since the refractive index of X-rays is very close to unity, “normal” lenses, as known from applications in the visible light regime, cannot be used directly for X-rays.<sup>18</sup> Although a wide variety of X-ray optics exists, only the ones which were used during this work are discussed in the following sections.

### 2.4.1. Capillary optics

#### 2.4.1.1. Monocapillary optics

A monocapillary is a specially shaped single glass capillary tube used to concentrate/focus the X-rays into a small (typically microscopic) spot. The principle used to focus the photons is based on total reflection and can be considered a milestone in X-ray analysis.<sup>18,19</sup> This effect occurs when a photon enters an interface between two media having different refractive indices under a very shallow angle of incidence and the wave passes from a medium with high refractive index to a medium with a lower index. The angle between the X-ray propagation vector and the



surface should be smaller than the critical angle of total (external) reflection, which is energy dependent. For glass in air, a good approximation for the critical angle of total reflection is given by Equation (2.12).<sup>20</sup>

$$\theta_c \approx \frac{30}{E_{\text{photon}}[\text{keV}]} [\text{mrad}] \quad (2.12)$$

Under these circumstances, the incoming X-rays will not refract at the medium boundary, but will instead be totally reflected (see Figure 2-9).

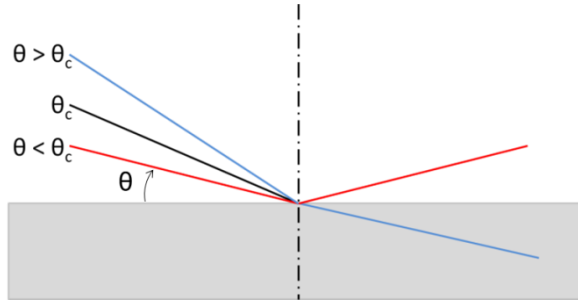


Figure 2-9 Total reflection: when the angle  $\theta$  between the surface and the incoming X-ray is smaller than the critical angle ( $\theta_c$ ), it gets reflected (red) instead of refracted (blue).

Using this phenomenon and by carefully shaping a capillary tube, it is possible to concentrate/focus an X-ray beam down to a few microns in diameter.<sup>18,19</sup> Although monocapillaries are able to generate a well-focused beam, they have a low efficiency due to their relatively small acceptance with respect to the incident beam. This means a lot of the X-rays generated by the X-ray source will not be captured by the monocapillary and are thus lost, causing a serious reduction in intensity.

#### 2.4.1.2. Polycapillary optics

The use of polycapillary optics represented a logical next step as they basically are consisting of large numbers of single capillaries arranged in such a way that the incoming X-rays are focused in a focal spot.<sup>19-21</sup> An important advantage of polycapillary optics compared to a single

capillary is that they are able to capture a larger fraction of the X-rays generated by the primary source and hence they generally deliver a higher photon flux to the sample, increasing their efficiency. The efficiency of capillary optics is highly dependent on the exact design and envisaged application of the optics and furthermore energy dependent. Both types of capillary optics play an important role, mainly due to the differences in the angular and energy distributions of the focused beam each one produces. In the HERAKLES scanner, the monocapillary optics yield a quasi-parallel pencil beam, while the polycapillary variant focuses the X-rays in a well-defined focal spot at a certain working distance from the tip of the optical system. Depending on the envisaged application, each has its merits and challenges, as will be discussed in Chapter 4 when describing the HERAKLES 3D X-ray scanner.

#### 2.4.2. Kirkpatrick-Baez (KB) Mirrors

Kirkpatrick-Baez (KB) mirrors are another type of X-ray optics next to (poly)capillaries, which are based on the principle of total reflection.<sup>19,20</sup> KB mirrors are a set of two elliptical mirrors, one of which focuses the X-rays horizontally, while the other is responsible for the vertical focusing. These mirrors can be made from a wide range of materials and can also be multi-layered. They can be static or dynamic: in the latter case the curvature of the mirrors can be changed to a certain degree in order to further optimize their focusing capabilities. They are very efficient in focussing the incident X-rays, with efficiency up to 75 % attainable. Using KB mirrors, at synchrotron sources, X-ray beam can be downsized to a few tens of nanometers (e.g. 50 nm at beamline ID16B of the ESRF, Grenoble, FR) allowing nanoscopic analysis. Although their working principle is very straightforward, these devices are extremely difficult to manufacture and hence very expensive.<sup>22</sup> In a laboratory setting, KB mirrors are less suitable due to their typically large size (making them quite heavy), very demanding alignment and vibration isolation, long focal length and high cost.

### 2.4.3. Monochromators and Doubly Curved Crystal (DCC) optics

Monochromatic X-ray beams have several advantages for many X-ray based analysis techniques such as X-ray fluorescence and X-ray computed tomography. The most simple and straightforward method to obtain a (partially) monochromatic beam is by using filters to remove certain parts of the source spectrum. However, this methodology yields far from satisfying results, both in terms of monochromaticity and intensity of the obtained beam.

Much better results are obtained with systems using Bragg diffraction on a crystal surface.<sup>23,24</sup> To select only those photons having the desired wavelength, these crystal (or multilayer) optics use Bragg's law of diffraction:

$$n\lambda = 2 d \sin(\theta) \quad (2.13)$$

Where  $d$  is the lattice spacing of the diffracting crystal,  $\theta$  the angle of incidence,  $\lambda$  is the wavelength of the X-ray photon and  $n$  is the diffraction order. Based on the application, a different crystal will be selected, e.g. Si(111) or Si(311). Inserting the crystal in the beam under a well-defined angle enables the user to select a specific wavelength, together with its higher diffraction orders. Further monochromatization (e.g. by high energy cut off mirrors) might be desired to remove the energies corresponding to the higher diffraction orders.

A special type of optics based on the diffraction principle are Doubly Curved Crystal (DCC) optics.<sup>25</sup> Next to creating a monochromatic beam using the above described Bragg diffraction, the curvature of these optics also focuses the X-rays to a relatively small spot. Although this type of optics has a lot of advantages, its use is not widespread due to the high difficulty of producing high quality DCC optics.

## 2.5. Detecting X-rays

Historically, the first X-ray detection was performed with photographic plates, a practice still in use today in medical and industrial imaging applications. However, when performing experiments based on X-ray/matter interactions, it is important to have optimized detectors to monitor the processes taking place in the irradiated sample and these simple photographic plates no longer qualify.

Depending on the application, these X-ray detectors should be able to differentiate between the different energies (e.g. X-ray fluorescence) of the detected photons and/or spatially resolve the position where the X-ray reaches the detector surface (with or without the need for energy resolution).

### 2.5.1. Non-energy dispersive X-ray detection

#### **Ionization chambers**

An ionization chamber consists of a gas-filled chamber containing two electrodes. Often noble gases (helium, argon, krypton) are used although some ionization chambers employ normal air or nitrogen.<sup>26-28</sup> A high potential difference up to several hundreds of kilovolt<sup>26,28</sup> is placed over the electrodes. An X-ray photon entering the chamber can ionize a gas molecule, resulting in the production of a positively charged ion and an electron. These will be attracted to the cathode and anode electrode respectively. By measuring the electrical current generated by the ion chamber (order of magnitude micro- to nanoamperes), the corresponding X-ray flux can be determined. In practice the current is amplified with a transconductance amplifier, going from current to voltage and then read to a computer using an analog-to-digital converter (ADC).

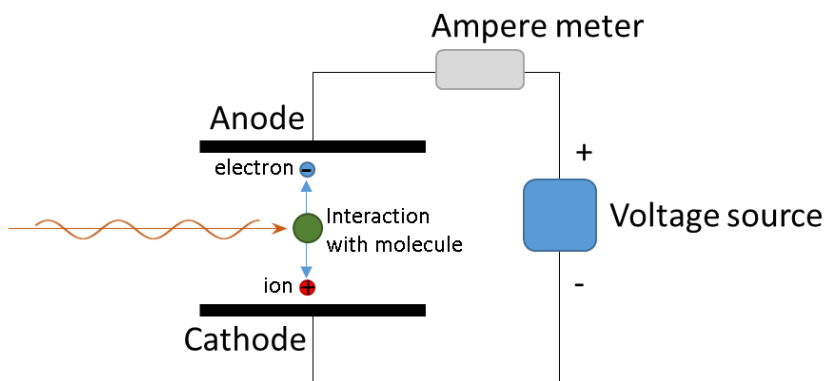


*Figure 2-10 Principle of an ion chamber: the incident radiation ionizes a molecule. The electron moves to the positive anode, while the formed ions migrate in the opposite direction, this creates a current which is measured.*

For optimal functioning of an ion chamber detector, careful selection of the filling gas, pressure and operating conditions is crucial to have a linear relationship between the X-ray intensity and generated current.<sup>26</sup> An ion chamber can resolve the energy of the detected X-rays when operated in pulse-mode, however, semi-conductor technology has largely replaced ion chambers for this application.<sup>29</sup> Ion chambers are still used as X-ray monitoring devices, e.g. to assess the total X-ray flux in applications such as the normalization of an XRF experiment to the ring current at a synchrotron beamline.

### **Spatially (2D) resolved X-ray detection: CCD and CMOS based detectors**

For some applications, it is necessary to know the exact position where the X-ray has interacted with the X-ray detector. Although this can be achieved by using photographic film for X-ray detection, current applications require experimental results in a digital format. The HERAKLES 3D X-ray scanner is equipped with two types of 2D detectors: the Photonic Science detector which is a charged coupled device (CCD) and the Radeye which is a Complementary Metal Oxide Semiconductor (CMOS) detector.

A CCD imaging detector<sup>30</sup> is essentially an integrated circuit etched onto a Si surface. It has a photoactive layer and a transmission layer which consists of a shift register (the actual CCD). The photoactive layer has a 2D array of capacitors. In the capacitors an electric charge is accumulated which is proportional with the incident photon flux. Once the capacitors have been exposed to the photon flux for a predetermined time, the signal is read out. The system works as a shift register where each capacitor moves its charge to the next one, while the last array transfers its contents to the charge amplifier. This device is used to convert the charge of the capacitors into a voltage which is later on translated to a digital signal and sent to the computer. In a stepwise fashion, the complete area of the detector is thus read out, creating the image. In X-ray CCD cameras, a scintillator screen is used to convert the X-rays to visible light before interacting with the photoactive part of the detector. Over the years a vast number of materials have been developed which are suitable for use in a scintillator screen, some examples being  $\text{Gd}_2\text{O}_2\text{S:Tb}$  (Gadox),  $\text{CsI:Tl}$ , YAG ( $\text{Y}_3\text{Al}_5\text{O}_{12}\text{:Ce}$ ) and LAG ( $\text{Lu}_3\text{Al}_5\text{O}_{12}\text{:Eu}$ ).<sup>31</sup> The CCD detector of the HERAKLES scanner is equipped with a Gadox scintillator.

A CMOS detector<sup>32</sup> consists of an array of photoactive pixel sensors, with each individual pixel containing both the detector and a signal amplifier. As with CCD cameras, a scintillator screen is needed to transform the X-rays to visible light.

The main practical difference between a CMOS detector and a CCD imager lies in the conversion of charge to voltage which happens after read-out for CCD detectors and on the chip for CMOS cameras. In this respect CMOS detectors have the advantage of a reduced overhead time and power usage compared to a CCD camera. Furthermore, data leakage from one pixel to the surrounding is typically lower in a CMOS detector and they tend to be cheaper than CCD imagers. However, the quantum efficiency of a CMOS detector is lower compared to a CCD and because the chips of a CMOS detector sit right behind the crystal they are more sensitive to radiation damage. Both types of detector still play a major role in 2D X-ray detection.

## 2.5.2. Energy dispersive (ED) X-ray detection

During this project several types of semi-conductor detectors were used for energy dispersive (ED) X-ray detection. Most often the employed semi-conductor material is silicon or germanium based.<sup>33</sup> These detectors yield information on both the flux and energy of the detected X-rays and are hence well-suited for energy dispersive X-ray fluorescence (EDXRF) experiments.

Upon entering the semiconductor material, the X-ray photon can undergo a number of photon-matter interaction effects, including the typically most important photoelectric effect. The latter interaction generates a photoelectron, which in turn initiates a cascade of interactions in the semiconductor material, dissipating the incident energy and generating multiple electron-hole pairs during the process.

Depending on the used semiconductor, the generation of each electron-hole pairs will require a specific energy of a few eV. As a result, the number of electron-hole pairs generated by a single incident X-ray photon is directly correlated to its photon energy. The detector determines the total charge, i.e. the energy dissipated during the photon absorption (detection) event and adds one count to the corresponding channel of its read-out, ultimately generating the spectrum.

An ideal spectral detector would yield a Dirac-impulse type of distribution for each X-ray photon energy, however, several fundamental physical properties of the semi-conductor detector cause the spectrum to be composed of peaks with a certain width.<sup>29</sup> First of all, there is a statistical component, linked to the impossibility to convert all energy into electron-hole pairs. The Fano factor is introduced as the difference between the true conversion and the conversion as expected from Poisson statistics. Due to dark current (i.e. thermal noise) and recombination of electron-hole pairs the peaks become still a little broader. The width of the peaks defines the energy resolution of the detector. For Si(Li) detectors the energy resolution lies typically around 150 eV at the Mn-K $\alpha$

line (i.e. 5.9 keV)<sup>34</sup>; the more recent SDD technology has comparable or even better energy resolution.

Several parameters are used to express the quality of photon detection of a detector.<sup>34</sup> First of all, the theoretical energy resolution  $E_{res}$  can be calculated to assess how well two X-ray photons having similar energies can be resolved in the XRF spectrum.  $E_{res}$  is dependent on the Fano factor  $F$  and electronic noise  $N$  of the detector. Furthermore, the energy of the considered X-ray photon  $E_{photon}$  and the conversion factor of the energy to the number of charges carried  $\varepsilon$  will influence  $E_{res}$ . The formula to determine  $E_{res}$  is:

$$E_{res} = 2.35 \sqrt{F E_{photon} \varepsilon} + N \quad (2.14)$$

In the case of detectors based on Si the value of  $\varepsilon$  is 3.65 eV.

A second parameter is the quantum efficiency of the detector. It is a measure for the amount of detected photons (i.e. X-rays added to the spectrum) compared to the total amount of X-rays reaching the detector surface. Both the detector material, its thickness and the energy of the specific X-ray photon under consideration will affect the quantum efficiency value. Due to the relatively low atomic number of Si, for the practical detector crystal thickness values employed, it is only efficient for X-ray energies between 1 and 40 keV. Above this upper limit the X-ray photon passes through the Si as it becomes ‘transparent’ for high energies. When a specific application requires detection of high energy X-rays, Ge-based technology will be the better option. Historically, these would be Ge(Li) detector, comparable to the Si(Li) principle, but nowadays this technology has become obsolete because of the possibility to create very pure Ge crystals which are used to construct high purity germanium (HPGe) detectors.

The older Si(Li) detector technology has the disadvantage of requiring liquid nitrogen cooling to avoid drifting of the Li. Furthermore, these detecting systems can only handle a relatively low count rate. Silicon drift detectors can address these drawbacks. The silicon drift detector (SDD) is an improved version of the semi-conductor detector introduced



in the 1980s.<sup>35</sup> It can handle significantly higher photon fluxes and due to the possibility to cool this type of detector using Peltier cooling, the resulting setup will be much smaller as no liquid nitrogen container is required to keep the detector crystals at cryogenic temperatures.

For a conventional pn-diode, the n+ contact covers one side of the semiconductor wafer with the p+ sitting on the other side. However, when positioning p+ electrodes on both sides of the wafer and one comparatively small n+ contact it is also possible to reach full depletion of the bulk, creating a very low capacitance between the two p+ electrodes. Using this configuration, depletion can be achieved with a much lower bias voltage.<sup>35</sup>

An SDD has a circular lay-out with p+ cathodes encircling an n- anode. This structure sits on top of a (n-) Si bulk at the back of which a single p+ electrode is positioned. An additional transversal electric field causes a drift of the generated charge carriers (electron-hole pairs) from the energy potential minimum towards the collector electrode positioned in the midpoint of the circular detector crystal. The collector electrode has a much lower capacitance than conventional pn-diodes and is independent of the active area of the SDD. At short shaping times, electronic noise is proportional to the square of the capacitance, hence minimize capacitance will drastically reduce the noise.<sup>35,36</sup> The connection between the detector and its preamplifier must be kept as short as possible in order to profit to the maximum from the benefits of the low capacitance. In practice, the front-end field effect transistor (FET) of the amplification hardware is mounted on the semiconductor wafer to keep this distance at the absolute minimum, as can be seen in Figure 2-11.<sup>37</sup>

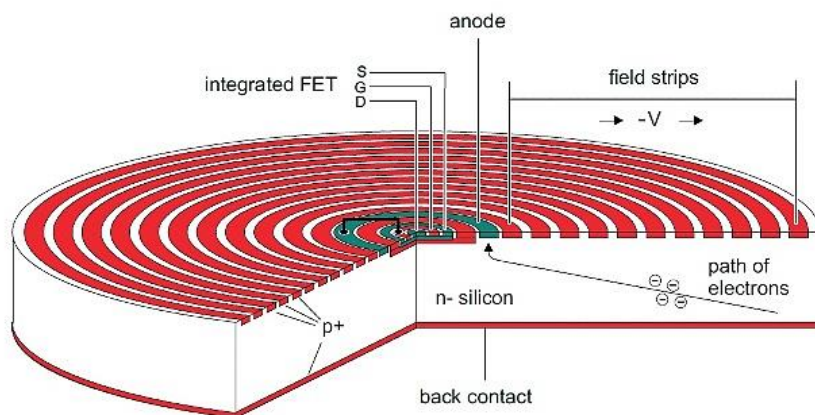


Figure 2-11 Representation of an SDD detector. The white bulk in the middle is the n- silicone, the red rings on top and the full red disk at the back are the p+ electrodes, while the anode is indicate in green. Also indicated is the integrated FET. Figure adapted from ThermoScientific. <sup>36</sup>

## 2.6. References

- (1) Röntgen, W. C. *Annalen der Physik und Chemie* **1896**, 64, 1-37.
- (2) Panchbhai, A. *Journal of Indian Academy of Oral Medicine and Radiology* **2015**, 27, 90-95.
- (3) Glasser, O. *Wilhelm Conrad Röntgen and the Early History of the Roentgen Rays*; Norman Publishing: San Francisco, 1993, p 494.
- (4) Nobelprize.org. 2018.
- (5) Reed, A. B. *Journal of Vascular Surgery* **2011**, 53, 3S-5S.
- (6) Coolidge, W. D.; Google Patents, 1917.
- (7) Coolidge, W. D.; Google Patents, 1934.
- (8) Nascimento, M. L. F. *World Patent Information* **2014**, 37, 48-53.
- (9) Kunz, C. *Journal of Physics: Condensed Matter* **2001**, 13, 7499.
- (10) Mizuki, J. i. *Journal of the Physical Society of Japan* **2012**, 82, 021001.
- (11) Hasnain, S. S.; Helliwell, J. R.; Kamitsubo, H. *J Synchrotron Radiat* **1994**, 1, 1-4.
- (12) Robinson, A. L. In *X-ray Data Booklet*, Thompson, A. C., Ed.; Lawrence Berkeley National Laboratory: Berkeley, California, 2009.
- (13) Bilderback, D. H.; Elleaume, P.; Weckert, E. *Journal of Physics B: Atomic, Molecular and Optical Physics* **2005**, 38, S773.
- (14) Kim, K.-J. In *X-ray Data Booklet*, Thompson, A. C., Ed.; Lawrence Berkeley National Laboratory: Berkeley, California, 2009.
- (15) Cechák, T.; Leonherdt, J. In *Handbook of Practical X-ray Fluorescence Analysis*, Beckhoff, B.; Kanngießer, B.; Langhoff, N.; Wedell, R.; Wolff, H., Eds.; Springer: Berlin, Germany, 2006, pp 54-65.
- (16) Mantler, M. In *Handbook of Practical X-ray Fluorescence Analysis*, Beckhoff, B.; Kanngießer, B.; Langhoff, N.; Wedell, R.; Wolff, H., Eds.; Springer: Berlin, Germany, 2006.
- (17) Kirz, J. In *X-ray Data Booklet*, Thompson, A. C., Ed.; Lawrence Berkeley National Laboratory: Berkeley, California, 2009.
- (18) Kumakhov, M. A. *Nuclear Instruments and Methods in Physics Research Section B: Beam Interactions with Materials and Atoms* **1990**, 48, 283-286.
- (19) Arkadiev, V.; Bjeoumikhov, A. In *Handbook of Practical X-ray Fluorescence Analysis*, Beckhoff, B.; Kanngießer, B.; Langhoff, N.; Wedell, R.; Wolff, H., Eds.; Springer: Berlin, Germany, 2006, pp 54-65.
- (20) MacDonald, C. A. *X-Ray Optics and Instrumentation* **2010**, 2010, 17.
- (21) Vincze, L.; Janssens, K.; Adams, F.; Rindby, A. *X-Ray Spectrometry* **1995**, 24, 27-37.
- (22) Karvinen, P.; Grolimund, D.; Willmann, M.; Meyer, B.; Birri, M.; Borca, C.; Patommel, J.; Wellenreuther, G.; Falkenberg, G.; Guizar-Sicairos, M.; Menzel, A.; David, C. *Optics express* **2014**, 22, 16676-16685.

- (23) Erko, A. In *Handbook of Practical X-ray Fluorescence Analysis*, Beckhoff, B.; Kanngießer, B.; Langhoff, N.; Wedell, R.; Wolff, H., Eds.; Springer: Berlin, Germany, 2006.
- (24) Howells, M. R. In *X-ray Data Booklet*, Thompson, A. C., Ed.; Lawrence Berkeley National Laboratory: Berkeley, California, 2009.
- (25) Wittry, D. B.; Golijanin, D. M. *Applied Physics Letters* **1988**, *52*, 1381-1382.
- (26) Bunker, G. In *Encyclopedia of Spectroscopy and Spectrometry (Second Edition)*; Academic Press: Oxford, 1999, pp 2961-2967.
- (27) Bolozdynya, A. In *Emission Tomography*, Aarsvold, J. N., Ed.; Academic Press: San Diego, 2004, pp 359-381.
- (28) Cherry, S. R.; Sorenson, J. A.; Phelps, M. E. In *Physics in Nuclear Medicine (Fourth Edition)*; W.B. Saunders: Philadelphia, 2012, pp 87-106.
- (29) Knoll, G. F. *Radiation Detectibn and Measurement*; John Wiley & Sons, Inc.: New York, 1999, p 816.
- (30) Gruner, S. M.; Tate, M. W.; Eikenberry, E. F. *Review of Scientific Instruments* **2002**, *73*, 2815-2842.
- (31) Martin, N. *Measurement Science and Technology* **2006**, *17*, R37.
- (32) Rocha, J. G.; Lanceros-Mendez, S. *Recent Patents on Electrical Engineering* **2011**, *4*, 16-41.
- (33) Thompson, A. C. In *X-ray Data Booklet*, Thompson, A. C., Ed.; Lawrence Berkeley National Laboratory: Berkeley, California, 2009.
- (34) Longoni, A.; Fiorini, C. In *Handbook of Practical X-ray Fluorescence Analysis*, Beckhoff, B.; Kanngießer, B.; Langhoff, N.; Wedell, R.; Wolff, H., Eds.; Springer: Berlin, Germany, 2006.
- (35) Gatti, E.; Rehak, P. *Nuclear Instruments and Methods in Physics Research* **1984**, *225*, 608-614.
- (36) ThermoScientific. <https://www.azom.com/article.aspx?ArticleID=11973> **2015**.
- (37) Kemmer, J.; Lutz, G.; Prechtel, U.; Schuster, K.; Sterzik, M.; Strüder, L.; Ziemann, T. *Nuclear Instruments and Methods in Physics Research Section A: Accelerators, Spectrometers, Detectors and Associated Equipment* **1990**, *288*, 92-98.

## Chapter 3

# Three dimensional (3D) X-ray based analysis techniques

During this PhD project, one of the core tasks was the development of the HERAKLES 3D X-ray scanner, a multi-methodological instrument for three-dimensional analysis using several complementary X-ray based techniques. More details on the development of this instrument can be found in Chapter 4. This chapter aims at giving some background information on some of the techniques and the associated data analysis.

### 3.1. Tomography

The concept of tomography played a major role during this project, since two out of three techniques incorporated in the developed HERAKLES 3D X-ray scanner rely on the principle of tomography: microscopic X-ray computed tomography ( $\mu$ CT) and X-ray fluorescence tomography (XRF-CT). Although the focus of this PhD project lies strongly on the XRF methodologies of the developed HERAKLES 3D X-ray scanner, the  $\mu$ CT setup was employed throughout all experiments. Even for straightforward XRF point measurements, the sample positioning is performed based on the transmission images of the tomographic end-station of the scanner or even a fast (and low on statistics)  $\mu$ CT measurement could be used. Hence, tomography, X-ray absorption and fluorescence tomography in particular, will be elaborated on in the first paragraph of this chapter.

### 3.1.1. Principle

Tomography is an experimental procedure to acquire 3D internal information from a sample in the form of virtual slices. The methodology is based on waves which are able to penetrate the sample.<sup>1,2</sup> Although multiple types of waves can be employed (e.g. X-rays or sound waves), the focus in this work will be solely on X-ray based analysis by X-ray absorption and fluorescence, both of which will be elaborated on.

For micro-scale X-ray absorption based computed tomography<sup>3</sup>, referred to as  $\mu$ CT throughout this work, the entire sample is irradiated with an X-ray beam (in case of the HERAKLES 3D X-ray scanner a conical beam). A 2D detector is used to acquire the images formed by the transmitted X-ray photons. This transmission image is a 2D projection of the 3D information present in the sample. The X-ray intensity in each image pixel depends on the attenuation characteristics of the material encountered by the photon on its path from the source to the detector. By taking transmission images under a large number of rotational angles, a data set is constructed from which the 3D distribution of attenuation in the sample can be reconstructed using suitable reconstruction algorithms.

X-ray fluorescence tomography (XRF-CT) uses the same basic principle of obtaining a projected image at different rotational angles as  $\mu$ CT, however, instead of generating one intensity value per pixel (as in the transmission images of a  $\mu$ CT scan) in XRF-CT a complete XRF spectrum is acquired per point.<sup>4-8</sup> Although 2D energy dispersive detectors for XRF analysis exist, in most cases a single element ED detector is used to perform XRF-CT. Due to the single-point nature of this type of detectors, the 2D projection image will have to be constructed point by point by performing line scans through the sample under different rotational angles, which will yield a sinogram for each detectable element present in the investigated object slice. Stacking several such sinograms (by measuring at different heights) yields a data set for each of these elements which is comparable to the data set recorded with  $\mu$ CT. In case of negligible XRF self-absorption effects, similar reconstruction algorithms can be used in both cases.<sup>9-11</sup>

### 3.1.2. Reconstruction algorithms

There exists a multitude of different reconstruction algorithms for computed tomography,<sup>1,2</sup> however, only the (filtered) back projection method was used during this project.<sup>1</sup> Without going into mathematical details, the principle of this algorithm will first be explained in this paragraph. Afterwards, some other algorithms will be briefly discussed.

The principle of the back projection algorithm is best understood using a visual representation as given in Figure 3-1 for a simple parallel beam experiment. On the left, the measurement is visualized by a sample consisting of a blue matrix, with two red inclusions. When considering a single (2D) slice through a sample, as is the case in Figure 3-1, a CT measurement will project the 2D information to a 1D line of the detector output (i.e., in practice 3D info is projected to a 2D matrix). To reconstruct the original sample using the acquired experimental data, the detector output at each position is projected back along the original direction of X-rays, as is shown on the right in Figure 3-1. As can be seen, even with only four well-chosen detection angles, the shown reconstruction of the sample yields two locations with clearly elevated “red” intensity, roughly at the location of the two inclusions. Adding additional projections under different angles would of course enhance the quality of the data set and enable a better reconstruction, however, due to the point spread function introduced by this very simple back projection, only a blurred image would be obtained, even at a very high number of projections. To resolve this fundamental challenge associated with the back projection algorithm, the filtered back projection was developed. To demonstrate the problem, we will look at the imaging of a 2D object, being a rectangle. Straightforward back projection would reconstruct a rectangle as a Gaussian shape. The filtering introduced in the filtered back projection algorithm truncates the Gaussian (recreating the flat top of the rectangle) and cuts away the edges, reconstructing a shape much closer to the imaged object compared to simple back projection.

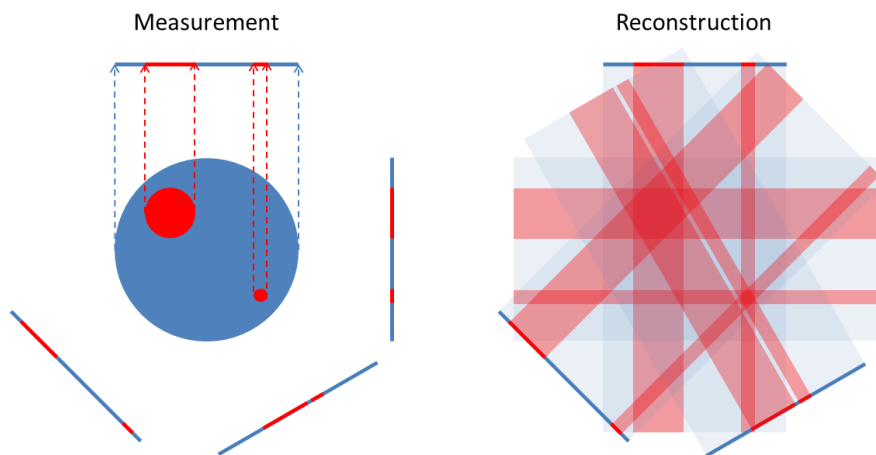


*Figure 3-1 The back projection algorithm: a visual example using 4 projections. On the left the experiment is represented, the dotted lines indicating the projection of the information onto the detector. On the right, the back-projection algorithm smears this data along the path of the X-rays, generating a rough reconstructed image.*

The mathematical background of the filtered back projection algorithm relies on the stabilized and discretized (inverse of the) Radon transformation.<sup>1</sup> The filtering is done in the Fourier domain, before the data is back projected. Additional filter functions are used to optimize the results.<sup>12</sup> Detailed analysis of these algorithms however exceeds the scope of this thesis. In practice, software provided by our industrial partner, X-ray Engineering (XRE), was used to reconstruct the  $\mu$ CT data throughout the thesis, while TOMX, an IDL program developed at the University of Antwerp and modified at the ESRF and Ghent University, was used for the XRF-CT analysis.

Back projection algorithms reconstruct the data in a single step. On the other hand there exist a number of reconstruction algorithms relying on iterative procedures. These have the advantages of enabling the introduction of physical properties of the samples (or estimations thereof) to be implemented and updated in the subsequent iteration steps. Certainly for XRF-CT reconstruction, where self-absorption effects play a major role, iterative procedures are better suited than the filtered back projection algorithm. Examples of these reconstruction algorithms are the algebraic reconstruction and statistical reconstruction strategies.<sup>13</sup> The algebraic reconstruction method considers the imaging process as a large



set of linear equations (corresponding to the intensity in the detector pixels). Solving this set of equations would yield the reconstructed image. However, due to the very large dimensions of the matrix which needs to be inverted and the fact in most practical cases this matrix is not square, iterative algorithms have been developed to solve this mathematical problem (e.g. the algebraic reconstruction technique). Statistical techniques such as the maximum likelihood algorithm maximize the probability of the object function in case of a given set of measured numbers (e.g. detector readouts). As with the algebraic techniques, this problem is solved through an iterative procedure, enabling the inclusion of physical parameters during the optimization steps.<sup>1,13</sup> Even though the fundamental ideas behind the algebraic and statistical reconstruction algorithms differ, they lead to similar procedures. The major differences are in the first forward project step and the normalization.<sup>13</sup> However, these mathematical implementations are beyond the scope of this thesis, which focusses on the hardware side of the HERAKLES scanner.

## 3.2. Quantification of XRF data

X-ray fluorescence not only yields qualitative information on the (detectable) elements present in a sample, it also offers the possibility to quantify the concentration of each of these elements. Several approaches can be applied to obtain quantitative information from an XRF spectrum, of which the most important will be discussed next.

### 3.2.1. Semi-quantitative analysis using elemental yields

The most straightforward and fastest way to estimate the concentration of the elements present in a sample is using the elemental yield method.<sup>14</sup> Due to the relatively large errors on the obtained concentration values, this is considered to be only a semi-quantitative method. However, it is a

fast and straightforward way to obtain the initial estimate for the more accurate methodologies. Nevertheless, in some instances the concentration estimates calculated through this method are sufficient for the application.

The semi-quantitative approach is based on the use of one or more reference materials with matrix and composition very similar to the investigated samples, in such way that the selected reference material(s) and the sample under investigation show a similar or identical response in the XRF experiments (i.e. absorption of the primary beam, self-absorption, geometry factor, etc.). Since the (certified) composition of the reference sample is well-known, it is possible to calculate the elemental yield of all detectable elements in the reference from an XRF experiment by dividing the measured intensity (in counts per second, cps) by the illuminated mass of the element in question. It is assumed the elemental yield for each element in the sample is the same as that of the reference. Hence from an XRF measurement, which yields a value for the intensity, the concentration can be calculated in case the illuminated masses are known for both sample and reference.

### 3.2.2. Fundamental parameter method

Since the semi-quantitative analysis only yields a rough estimation of the concentration values, for most scientific questions a more accurate methodology will be needed. One such methodology is the fundamental parameter method (FPM).<sup>15-18</sup> The FPM still uses a standard (or multiple standards) to calculate a conversion factor which links the intensities of the detectable elements in the sample with their concentration values, however, in the FPM extra parameters such as the absorption of X-rays by the sample and geometry factors are taken into account. A short overview of the methodology will be given in this paragraph, for a detailed derivation of these formulas, the reader is referred to literature.<sup>15,18</sup>

The FPM procedure first considers the interactions of the sample with the incoming X-rays produced by the X-ray source. Hence, the depth, X-ray energy and matrix dependent changes in intensity of the primary beam are taken into account. Next, the generation of fluorescent X-rays is determined by using known physical parameters of the considered elements (e.g. cross-sections, fluorescence yields) and the energy of the exciting X-rays. Finally, the attenuation of the fluorescent radiation escaping the sample and reaching the detector is calculated, which once more depends on the matrix of the sample, energy of the considered X-ray photon and pathway through the sample. Finally, some geometrical parameters are taken into account, such as the active area of the detector crystal, its position relative to the sample etc.

By calculating these parameters for both sample and reference sample, a correction factor can be determined, which takes into account the difference between the two materials. Hence, using FPM more reliable concentration values can be determined compared to the semi-quantitative elemental yield based method. The formulas of the FPM in the case of a monolayer sample and a monochromatic beam will be given based on the parameters introduced in Figure 3-2.

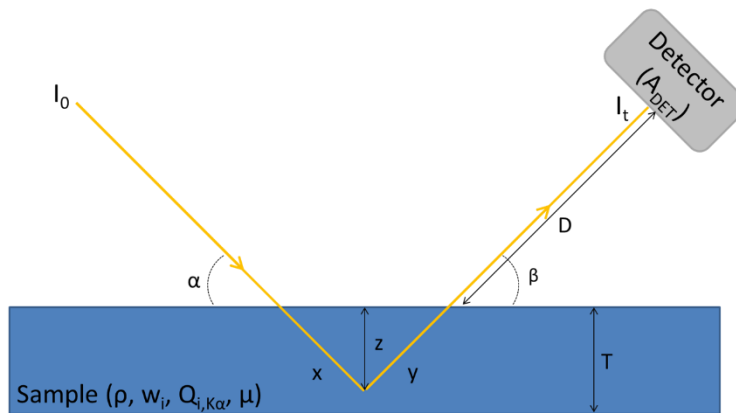


Figure 3-2 Schematic representation of an XRF experiment with the different parameters to construct the formulas of the FPM indicated.

The parameter that needs to be determined is  $w_i$ , the weight fraction of element  $i$  in the sample. This can be done by linking  $w_i$  to  $I_i$ , the intensity of the fluorescent radiation of element  $i$ , which is a known value through data analysis of the measured spectrum. All parameters but  $w_i$  should be known or measured.  $I_0$  is the intensity of the exciting beam. Upon entering the sample,  $I_0$  gets attenuated by the matrix of the sample (which is considered homogeneous). The attenuation length of the incident beam is  $x$ , while  $y$  is the attenuation length of the fluorescent radiation. The attenuation depends on the composition of the matrix and the mass attenuation coefficient for all elements at the energy of the exciting beam. In a similar way, the fluorescent radiation will be attenuated while leaving the sample. All attenuation effects corresponding to a given element  $i$  are grouped in a single parameter called the absorption correction factor  $A_{i,cor}$ .

$$A_{i,cor} = \left( \frac{1 - \exp(-\chi \rho T)}{\chi \rho T} \right) \quad (3.1)$$

Where  $\rho$  is the density of the sample,  $T$  the thickness and  $\chi$  is determined by Eq. 3.2, which can be derived using the depth of the interaction ( $z$  in Figure 3-2) an geometry of the experimental setup.

$$\chi = \frac{\sum_{i=1}^n w_i \mu_{i,0}}{\sin(\alpha)} + \frac{\sum_{i=1}^n w_i \mu_{i,1}}{\sin(\beta)} \quad (3.2)$$

In this equation  $\alpha$  and  $\beta$  are the angles in the experimental setup as shown in Figure 3-2,  $w_i$  is the weight percentage of element  $i$  in the sample and  $\mu_{i,0}$  and  $\mu_{i,1}$  are the mass attenuation coefficients of element  $i$  at the energy of  $I_0$  and the considered fluorescent line, respectively.

Further parameters influencing the fluorescent elemental line intensity  $I_i$  are the geometry factor  $G$ , which depends on the detector characteristics and its position relative to the sample and the XRF production cross-section for the considered XRF line in the spectrum  $Q_{i,K\alpha}$ . All combined, these parameters give the relation between  $I_i$  and  $I_0$ :

$$I_i = I_0 G w_i Q_{i,K\alpha} \rho T A_{i,cor} \quad (3.3)$$

Knowing this relationship for both sample ( $s$ ) and reference material ( $r$ ), we can write:

$$\frac{I_i^{(s)}}{I_i^{(r)}} = \frac{I_0^{(s)} G w_i^{(s)} Q_{i,K\alpha} \rho^{(s)} T^{(s)} A_{i,cor}^{(s)}}{I_0^{(r)} G w_i^{(r)} Q_{i,K\alpha} \rho^{(r)} T^{(r)} A_{i,cor}^{(r)}} \quad (3.4)$$

Measuring the sample and reference under the same experimental conditions simplifies this relation. The geometry factor is identical in both cases, as is the XRF production cross-section. Hence, the equation can be rewritten as follows:

$$\frac{I_i^{(s)}}{I_i^{(r)}} = \frac{I_0^{(s)} w_i^{(s)} \rho^{(s)} T^{(s)} A_{i,cor}^{(s)}}{I_0^{(r)} w_i^{(r)} \rho^{(r)} T^{(r)} A_{i,cor}^{(r)}} \quad (3.5)$$

From this equation it is easy to calculate the weight fraction  $w_i^{(s)}$  of the unknown element. Since the absorption correction factor depends on the composition, an iterative procedure will be needed to obtain the final results. The previously discussed semi-quantitative procedure is a good way to quickly determine a suitable initial guess for the composition of the sample to calculate  $A_{i,cor}$  in the first step of the iterative procedure.

### 3.2.3. Monte Carlo simulation aided quantification

Although the FPM is a very effective quantification technique, its applicability is highly dependent on the availability of a good reference material. An alternative is to use Monte Carlo (MC) aided quantification. MC is a stochastic methodology, simulating the physical process behind an experiment to predict its outcome based on random statistical sampling using an appropriate probability density function. MC methodologies are used to solve (physical) problems which are too complex to be solved relying on analytical methods. The Monte Carlo code used during this research was the in-house developed XMI-MSIM software, which is discussed in detail in scientific literature.<sup>19-24</sup>

The MC aided quantification has two distinct steps. During the first step all experimental parameters of the setup, such as distances and angles between components, the properties of source and detector and the composition of the sample, are determined. An experiment using a reference material is used to check if the predicted response of the system is in good accordance with reality by simulating the spectrum and comparing this with the obtained experimental spectrum. The input parameters of the model are optimized until both experiment and simulation yield the same result.

During the second step, the obtained simulation parameters are used to simulate the spectrum of a given sample. Since the system is well-defined by now, all differences between the two spectra (simulation and experiment) are due to the composition of the sample given as input to the simulation. Optimizing the sample composition iteratively until the MC simulated spectrum coincides with the experimental spectrum gives the requested set of concentrations of all elements present in the sample.

Although the MC aided quantification method still uses a reference material in its first step, it has several advantages compared to the FPM. First of all, the reference material is mainly used to determine the response factor of the system and as such it can deviate from the samples to some extent, in contrast to FPM where the reference sample should resemble the samples. Furthermore, once a good simulation of an instrument is established, it can be used for the quantification of multiple experiments as long as no changes are made to the setup. Finally, it is an excellent way to fundamentally understand the XRF experiments, since the effects of all possible experimental parameters can easily be investigated by simply changing their value in the simulation code. In that respect the MC aided quantification method could also be used to optimize a given instrument or predict the effect of future changes to certain components.

### 3.3. Recent trends in XRF techniques

Although X-ray fluorescence spectroscopy is a well-established analytical technique which has been used by scientists for decades to analyse a huge amount of samples from a wide variety of scientific fields, it is also a field which is still well-alive and evolving. This section gives an overview of the main literature concerning laboratory and synchrotron XRF technologies published over the period of this PhD project (i.e. 2014-2017). This should give the reader a sound idea of the current state-of-the-art in the XRF community.

#### 3.3.1. Latest trends in laboratory XRF imaging

In the past years several groups have published on their development of novel laboratory XRF instruments, incorporating new optics or detector technologies to provide high spatial resolution, fast 2D mapping or advanced energy resolution. These instruments have widely different characteristics, optimized for the envisaged methodology and application.

Kayser et al.<sup>25</sup> reported on a new XRF setup coupling a wavelength dispersive detector (based on the von Hamos geometry) with a 50 W tungsten target tube. Polycapillary optics were used to focus the X-rays in a 56  $\mu\text{m}$  spot. Compared to the previous configuration of the instrument (with a high power X-ray tube) the new setup yields a lower count rate, but a slightly better energy resolution. The low count rate results in very long measurement times per image. Romano et al.<sup>26</sup> used a CCD detector (1024x1024 pixels) combined with a tungsten anode tube (100 W). The beam generated by this source is not collimated and has a spot size of several centimeters at the sample position. A pinhole is positioned between the sample and the detector, varying the relative distance between sample, pinhole and detector allows the user to change the magnification. A minimal spatial resolution of 30  $\mu\text{m}$  can be reached. The setup allows to generate a 2D XRF image of the sample in one go with a good energy resolution (133 eV at 5.9 keV in optimal acquisition

conditions) in about 19 h, which is still significantly faster than taking the 1024 by 1024 point spectra separately. The detector operated remarkably well for low energy elements, when used under vacuum and without kapton or beryllium windows, however, at energies above 10 keV, the efficiency dropped drastically. A group of the TU Berlin worked on a novel method for quantification of 3D depth profiles using their pre-existing laboratory confocal XRF setup based on a 30 W Mo tube with a full polycapillary lens and a Si(Li) detector with a polycapillary half-lens to collect the fluorescent X-rays.<sup>27</sup> In a study mainly focusing on the development of microfluidic chips, McIntosh and her coworkers extended on the breadboard XRF setup employed for examination of these sample carriers.<sup>28</sup> The setup uses DCC optics at the X-ray source, providing focused monochromatic excitation (@ 20.214 keV) and a 50 mm<sup>2</sup> SDD with second set of DCC optics as detector, specifically selecting the Pu-L<sub>α</sub> line for analysis. Although this setup makes a very sensitive instrument for Pu detection, it will not yield information on other elements without alteration of the detector optics. Hampai et al.<sup>29</sup> reported on the development of a laboratory XRF spectrometer specifically designed for analysis of large and heavy samples dubbed ‘Rainbow X-ray’ (RXR). The setup works in confocal mode with a Mo anode tube equipped with a polycapillary full lens focusing the beam to 50 μm and two 30 mm<sup>2</sup> SDD detectors with a polycapillary half lens, one optimized for energies below 5 keV and the other for energies from 4 to 25 keV. Loads up to 100 kg can be mounted in the RXR spectrometer, which can optionally be equipped with a vacuum chamber. The possibility to put heavy objects in the scanner sets it apart from most XRF setups, which can only take small and light objects. A team from Stanford University described their lab-based XRF-CT setup in a study on gold nano-particle phantoms.<sup>30</sup> A Varian G-1593bi X-ray tube was used as excitation source while the fluorescent photons are detected with a 9 mm<sup>2</sup> CdTe detector having 8192 energy bins of 19.5 eV bin width. Slits were used to create a 2.6 x 6.4 mm<sup>2</sup> (h x v) pencil beam, the scans were performed by making line scans at several rotation angles. Using the Au-K lines makes this methodology feasible for large, quite attenuating samples, but at relatively low resolution. Garrevoet et al.<sup>31</sup>



described the development of a monochromatic laboratory XRF setup, aiming at relatively easily quantifiable XRF analysis. This setup uses a Mo anode tube equipped with DCC optics, both monochromatizing the beam around the Mo- $K_{\alpha}$  line and focusing it to a spot size of  $120 \times 50 \mu\text{m}^2$  (h x v). A  $50 \text{ mm}^2$  SDD detector is used to collect the fluorescent radiation. The XYZ $\theta$  motor system allows for several types of measurement, including XRF-CT. In 2016, Romano and colleagues published on an upgraded version of their CCD based 2D XRF setup previously described in 2014.<sup>26,32</sup> A fast shutter synchronized with the detector read-out was installed on the X-ray source, minimizing multiple event and signal smearing. The pinhole from the early design had been replaced by a polycapillary optic, resulting in a much faster acquisition time, although this went at the cost of a slightly poorer spatial resolution ( $55 \mu\text{m}$  compared to  $30 \mu\text{m}$ ) and energy resolution ( $155 \text{ eV}$  instead of  $133 \text{ eV}$  at  $5.9 \text{ keV}$ ). Alternatively, the detector setup was also applicable for PIXE analysis. Our group published about a laboratory XRF-CT setup based on a Mo anode tube with a monocapillary optic, creating a focused pencil beam ( $20 \times 20 \mu\text{m}^2$  spot size).<sup>33</sup> The setup was based on a previous instrument described by Garrevoet and coworkers, using the same motor system and detector.<sup>31</sup> XRF-CT scans were performed in a point-by-point fashion, performing line scans at different rotational angles. Unlike other benchtop XRF-CT instruments, which mostly have biomedical applications, this setup was aimed at characterization of small samples in among others earth sciences, toxicology and material sciences. One last benchtop XRF instrument reported on during the period covered by this review paragraph was developed by Ricketts et al.<sup>34</sup> and was once more an XRF instrument aiming at biomedical applications through the imaging of gold nano-particles using the Au K-lines. The detector was a collimated,  $7 \text{ mm}$  thick Ge detector with a crystal diameter of  $36 \text{ mm}$ . The Ge detector replaced a SDD detector previously used in the setup due to the inability of the latter to detect Au K-lines efficiently. Incident X-rays were generated with a tungsten source; a polycapillary optic was employed to create a parallel beam of  $3.4 \text{ mm}$  wide by  $1.5 \text{ mm}$  high. According to the authors detection limits

of this instrument are an order of magnitude better than for comparable instruments previously discussed in literature.

### 3.3.2. Developments at synchrotron radiation facilities

To detail all new developments at synchrotron radiation facilities over the past three years would be an immense task and take us way off the topic of this thesis, even more so if all publications using existing experimental setups for new applications would be taken into account. However, since nanoscopic XRF imaging using synchrotron setups formed a considerable part of this PhD project, the latest additions to synchrotron instrumentation in this specific field is highlighted here.

A series of new beamlines at the Advanced Photon Source (APS) in Argonne (IL, USA) have been commissioned. One of these, the in situ nanoprobe,<sup>35</sup> aims at analysis of advanced materials and devices under working conditions (i.e. in situ and operando). The nanoscopic X-ray beam generated using a KB mirror system yields a 50 nm pink beam ( $\Delta E/E = 10^{-2}$ ) with a photon flux around  $10^{12}$  photons/s. Using diffracting optical focusing devices such as zone plates an even better resolution of 20 nm proved achievable with a monochromatic beam ( $\Delta E/E = 10^{-4}$ ) at the cost of a lower photon flux ( $10^{10}$  photons/s). X-ray energies can be varied between 4 and 30 keV. The combination of the high photon flux with fast hardware (e.g. detectors) and large working distances makes this beamline very suited for experiments with a relatively high throughput. At the ESRF, the brand-new ID16 extended beamline was developed, comprising two independent end-stations being present in two separate experimental hutches: ID16A-NI (nano-imaging) and ID16B-NA (nano-analysis). Although they use the same SR source, the beam is split well before the experimental end-station, feeding separate X-ray beams to both ID16 beamlines. These beamlines are part of the ESRF upgrade Phase I and aim at nanoscopic analysis with a versatile set of applications. The ID16A beamline specializes in ultra-high resolution imaging techniques, including computed tomography, X-ray fluorescence

imaging and phytography. The instrument can provide beamsizes down to 10 nm in specialized sample environments such as a cryochamber.<sup>36</sup> Multiple samples can be introduced at once, enabling relatively high-throughput experiments. Martinez-Criado et al.<sup>37</sup> described the new ESRF ID16B beamline in their 2015 publication. ID16B focuses on nanoscopic analysis using XRF, XRD, XAS and X-ray imaging techniques (e.g. holotomography). By use of a tungsten multilayer KB mirror system a beamsize of 50 nm can be achieved with a high photon flux ( $10^{12}$  photons/s) pink beam or monochromatic beam with energy tunable between 5 and 70 keV. The Nanoscopium beamline at the SOLEIL synchrotron (France) was discussed by Somogyi and coworkers<sup>38</sup>. This X-ray nanoprobe aims at a resolution below 100 nm in the 5 – 20 keV photon energy range by using slits which can be positioned very precisely and additional guard slits to reduce the effects of parasitic scattering. The setup allows multitechnique analysis by X-ray fluorescence, absorption and phase contrast. Beginning 2016, Cerenius et al.<sup>39</sup> published a paper on the new MAX IV synchrotron facility in Lund (Sweden) which was inaugurated on June 21 later that year. Max IV has two storage rings, a smaller ring at 1.5 GeV (96 m circumference) and a larger ring at 3 GeV (528 m). In the context of nano-analysis, the NanoMAX beamline will be of most interest with a predicted beamsize down to 10 nm at 5 – 30 keV. Several other beamlines were disrobed which will be specialized in a wide arsenal of X-ray based methodologies, such as the BALDER beamline for XRF and XAS. At the Australian Synchrotron a combined CT – XRF setup was introduced<sup>40</sup> at the Imaging and Medical beamline. This combination of techniques aimed at biomedical applications, with an XRF point detector capturing the fluorescence signal during the CT scans. No detailed information in terms of resolution was given, although it was said to be lower than the resolution in normal operating mode.

### 3.4. References

- (1) Kak, A. C.; Slaney, M. *Principles of computerized tomographic imaging*; Society for Industrial and Applied Mathematics: Philadelphia, 2001.
- (2) Bleuet, P.; Gergaud, P.; Lemelle, L.; Bleuet, P.; Tucoulou, R.; Cloetens, P.; Susini, J.; Delette, G.; Simionovici, A. *TrAC Trends in Analytical Chemistry* **2010**, *29*, 518-527.
- (3) Cnudde, V.; Boone, M. N. *Earth-Science Reviews* **2013**, *123*, 1-17.
- (4) de Jonge, M. D.; Vogt, S. *Current opinion in structural biology* **2010**, *20*, 606-614.
- (5) De Samber, B.; Vanblaere, S.; Evens, R.; De Schamphelaere, K.; Wellenreuther, G.; Ridoutt, F.; Silversmit, G.; Schoonjans, T.; Vekemans, B.; Masschaele, B.; Van Hoorebeke, L.; Rickers, K.; Falkenberg, G.; Szaloki, I.; Janssen, C.; Vincze, L. *Powder Diffraction* **2010**, *25*, 169-174.
- (6) Silversmit, G.; Vekemans, B.; Brenker, F. E.; Schmitz, S.; Burghammer, M.; Riekkel, C.; Vincze, L. *Analytical Chemistry* **2009**, *81*, 6107-6112.
- (7) Golosio, B.; Simionovici, A.; Somogyi, A.; Lemelle, L.; Chukalina, M.; Brunetti, A. *Journal of Applied Physics* **2003**, *94*, 145-156.
- (8) Golosio, B.; Somogyi, A.; Simionovici, A.; Bleuet, P.; Susini, J.; Lemelle, L. *Applied Physics Letters* **2004**, *84*, 2199-2201.
- (9) Simionovici, A.; Chukalina, M.; Schroer, C.; Drakopoulos, M.; Snigirev, A.; Snigireva, I.; Lengeler, B.; Janssens, K.; Adams, F. *IEEE Transactions on Nuclear Science* **2000**, *47*, 2736-2740.
- (10) Rust, G. F.; Weigelt, J. *IEEE Transactions on Nuclear Science* **1998**, *45*, 75-88.
- (11) Brunetti, A.; Golosio, B. *Computer Physics Communications* **2001**, *141*, 412-425.
- (12) Vlassenbroeck, J.; Ghent University faculty of Sciences: Ghent, 2009.
- (13) De Witte, Y. *Improved and practically feasible reconstruction methods for high resolution X-ray tomography*. Ghent University, Ghent, 2010.
- (14) Brouwer, P. N. In *Handbook of Practical X-ray Fluorescence Analysis*, Beckhoff, B.; Kanngießner, B.; Langhoff, N.; Wedell, R.; Wolff, H., Eds.; Springer: Berlin, Germany, 2006.
- (15) Schoonjans, T.; Silversmit, G.; Vekemans, B.; Schmitz, S.; Burghammer, M.; Riekkel, C.; Brenker, F. E.; Vincze, L. *Spectrochimica Acta Part B: Atomic Spectroscopy* **2012**, *67*, 32-42.
- (16) De Boer, D. K. G.; Borstrok, J. J. M.; Leenaers, A. J. G.; Van Sprang, H. A.; Brouwer, P. N. *X-Ray Spectrometry* **1993**, *22*, 33-38.
- (17) Mantler, M. In *Handbook of Practical X-ray Fluorescence Analysis*, Beckhoff, B.; Kanngießner, B.; Langhoff, N.; Wedell, R.; Wolff, H., Eds.; Springer: Berlin, Germany, 2006.

- (18) Rousseau, R. M.; Boivin, J. A. *Rigaku* **1998**, *15*, 13-28.
- (19) Schoonjans, T.; Solé, V. A.; Vincze, L.; Sanchez del Rio, M.; Appel, K.; Ferrero, C. *Spectrochimica Acta Part B: Atomic Spectroscopy* **2013**, *82*, 36-41.
- (20) Schoonjans, T.; Vincze, L.; Solé, V. A.; Sanchez del Rio, M.; Brondeel, P.; Silversmit, G.; Appel, K.; Ferrero, C. *Spectrochimica Acta Part B: Atomic Spectroscopy* **2012**, *70*, 10-23.
- (21) Vincze, L.; Janssen, K.; Adams, F. *Spectrochimica Acta Part B: Atomic Spectroscopy* **1993**, *48*, 553-573.
- (22) Vincze, L.; Janssens, K.; Adams, F.; Jones, K. W. *Spectrochimica Acta Part B: Atomic Spectroscopy* **1995**, *50*, 1481-1500.
- (23) Vincze, L.; Janssens, K.; Adams, F.; Rivers, M. L.; Jones, K. W. *Spectrochimica Acta Part B: Atomic Spectroscopy* **1995**, *50*, 127-147.
- (24) Vincze, L.; Janssens, K.; Vekemans, B.; Adams, F. *Spectrochimica Acta Part B: Atomic Spectroscopy* **1999**, *54*, 1711-1722.
- (25) Kayser, Y.; Blachucki, W.; Dousse, J. C.; Hoszowska, J.; Neff, M.; Romano, V. *The Review of scientific instruments* **2014**, *85*, 043101.
- (26) Romano, F. P.; Caliri, C.; Cosentino, L.; Gammino, S.; Giuntini, L.; Mascali, D.; Neri, L.; Pappalardo, L.; Rizzo, F.; Taccetti, F. *Anal Chem* **2014**, *86*, 10892-10899.
- (27) Mantouvalou, I.; Wolff, T.; Seim, C.; Stoytschew, V.; Malzer, W.; Kanngießer, B. *Analytical Chemistry* **2014**, *86*, 9774-9780.
- (28) McIntosh, K. G.; Neal, J. A.; Nath, P.; Havrilla, G. J. *X-Ray Spectrometry* **2014**, *43*, 332-337.
- (29) Hampai, D.; Liedl, A.; Polese, C.; Cappuccio, G.; Dabagov, S. B. *X-Ray Spectrometry* **2015**, *44*, 243-247.
- (30) Ahmad, M.; Bazalova-Carter, M.; Fahrig, R.; Xing, L. *IEEE Transactions on Medical Imaging* **2015**, *34*, 1140-1147.
- (31) Garrevoet, J.; Vekemans, B.; Bauters, S.; Demey, A.; Vincze, L. *Analytical Chemistry* **2015**, *87*, 6544-6552.
- (32) Romano, F. P.; Caliri, C.; Cosentino, L.; Gammino, S.; Mascali, D.; Pappalardo, L.; Rizzo, F.; Scharf, O.; Santos, H. C. *Analytical Chemistry* **2016**, *88*, 9873-9880.
- (33) Laforce, B.; Vermeulen, B.; Garrevoet, J.; Vekemans, B.; Hoorebeke, L. V.; Janssen, C.; Vincze, L. *Analytical Chemistry* **2016**, *88*, 3386-3391.
- (34) Ricketts, K.; Guazzoni, C.; Castoldi, A.; Royle, G. *Nuclear Instruments and Methods in Physics Research Section A: Accelerators, Spectrometers, Detectors and Associated Equipment* **2016**, *816*, 25-32.
- (35) Maser, J.; Lai, B.; Buonassisi, T.; Cai, Z.; Chen, S.; Finney, L.; Gleber, S.-C.; Jacobsen, C.; Preissner, C.; Roehrig, C.; Rose, V.; Shu, D.; Vine, D.; Vogt, S. *Metallurgical and Materials Transactions A* **2014**, *45*, 85-97.
- (36) Cesar da Silva, J.; Pacureanu, A.; Yang, Y.; Bohic, S.; Morawe, C.; Barrett, R.; Cloetens, P. *Optica* **2017**, *4*, 492-495.

- (37) Martinez-Criado, G.; Villanova, J.; Tucoulou, R.; Salomon, D.; Suuronen, J.-P.; Laboure, S.; Guilloud, C.; Valls, V.; Barrett, R.; Gagliardini, E.; Dabin, Y.; Baker, R.; Bohic, S.; Cohen, C.; Morse, J. *Journal of Synchrotron Radiation* **2016**, *23*, 344-352.
- (38) Somogyi, A.; Medjoubi, K.; Baranton, G.; Le Roux, V.; Ribbens, M.; Polack, F.; Philippot, P.; Samama, J. P. *J Synchrotron Radiat* **2015**, *22*, 1118-1129.
- (39) Cerenius, Y.; Hennies, F.; Fernandes Tavares, P. *Synchrotron Radiation News* **2016**, *29*, 34-38.
- (40) Hall, C.; Acres, R. G.; Winnett, A.; Wang, F. *Journal of Instrumentation* **2016**, *11*, C03048.

# Chapter 4

## HERAKLES: a combined 3D-XRF and X-ray computed tomography scanner

Any scientific question is a jigsaw puzzle, which requires the use of several analytical techniques and collaborations between different scientific fields to formulate a satisfying answer. Several studies have already shown the opportunities of combining the morphological information obtained with  $\mu$ CT with the elemental distribution as revealed through 3D XRF techniques, both at synchrotron radiation facilities<sup>1-3</sup> and in the laboratory<sup>4-8</sup>. However, most often the use of different methodologies implies using separate instruments, which are often not even found at the same location. Performing different experiments on the same sample using separate instruments not only requires time-consuming and error-prone alignment procedures during the experiments but also extra attention during data analysis regarding fusion of the experimental data. A good example from literature demonstrating the added value of multi-technique analysis of a microscopic sample, but as well of the added workload, is the work by De Samber et al. on *D. magna* model organisms.<sup>1</sup> The authors combined lab-based  $\mu$ CT with 2D SR-XRF mappings and SR based XRF-CT. The combination of spatially resolved elemental information with detailed morphological analysis of the sample undoubtedly aided in unambiguously identifying the organs or tissues where increased element intensity was detected. However, moving the sample from one experimental setup to another poses several challenges such as integrity of the sample over possibly a long time, and challenging alignment of the different measurements.<sup>9</sup>

Few instruments combining multiple, complementary analysis techniques in a single laboratory setup are currently available. One example is the commercial instrument SkyScan2140 (Brüker Corporation, Billerica, MA, USA) which combines XRF-CT and  $\mu$ CT.<sup>5,6</sup> However, this instrument is being phased out by the company. The development of the HERAKLES 3D X-ray scanner<sup>10</sup> aimed at creating a novel, multi-methodological 3D analysis instrument by incorporating X-ray  $\mu$ CT and two different 3D XRF methodologies in a single instrument: namely confocal XRF (cXRF) and XRF computed tomography (XRF-CT). The integration of the three different imaging end-stations is realized through a very high precision motor stage in order to actively couple the data from the different techniques, allowing for optimal use of the measured data.

## 4.1. Concept of the scanner

Previous attempts at integrating multiple X-ray based analysis techniques in a single instrumental setup had a fixed sample stage with all components arranged around it (e.g. Skyscan2140 of Brüker)<sup>5,6</sup>. This allows for a compact setup, but unavoidably forces some compromises to the design. As a result, the setup is not optimized for either of its experimental techniques. Therefore, the HERAKLES 3D X-ray scanner uses a fundamentally different approach, where the sample stage is no longer a fixed point in the setup. On the contrary, the high precision XYZ $\theta$  air bearing motor stages used in HERAKLES allow movement of the sample stage from one instrumental module (representing a given analysis technique) to the other as is shown in the schematic overview of Figure 4-1. The sample is aligned with the rotational axis using piezoelectric motors mounted on top of the main motor stages, which allows the sample coordinate system to be retained during translation movements between the various instrumental modules of HERAKLES.

Since the three instrumental modules ( $\mu$ CT, XRF-CT and cXRF) are completely independent entities in this instrument, their components and



settings can be fully optimized for the envisaged methodology without compromising the performances of the other techniques. Hence, each single one of the incorporated techniques represents the state-of-the-art of current lab-scale XRF and  $\mu$ CT technology. Furthermore, the fact the end stations are independent makes upgrading components of one setup possible without interfering with the other end stations, minimizing the workload when e.g. changing from one type of X-ray tube to a new, better performing version in the future.

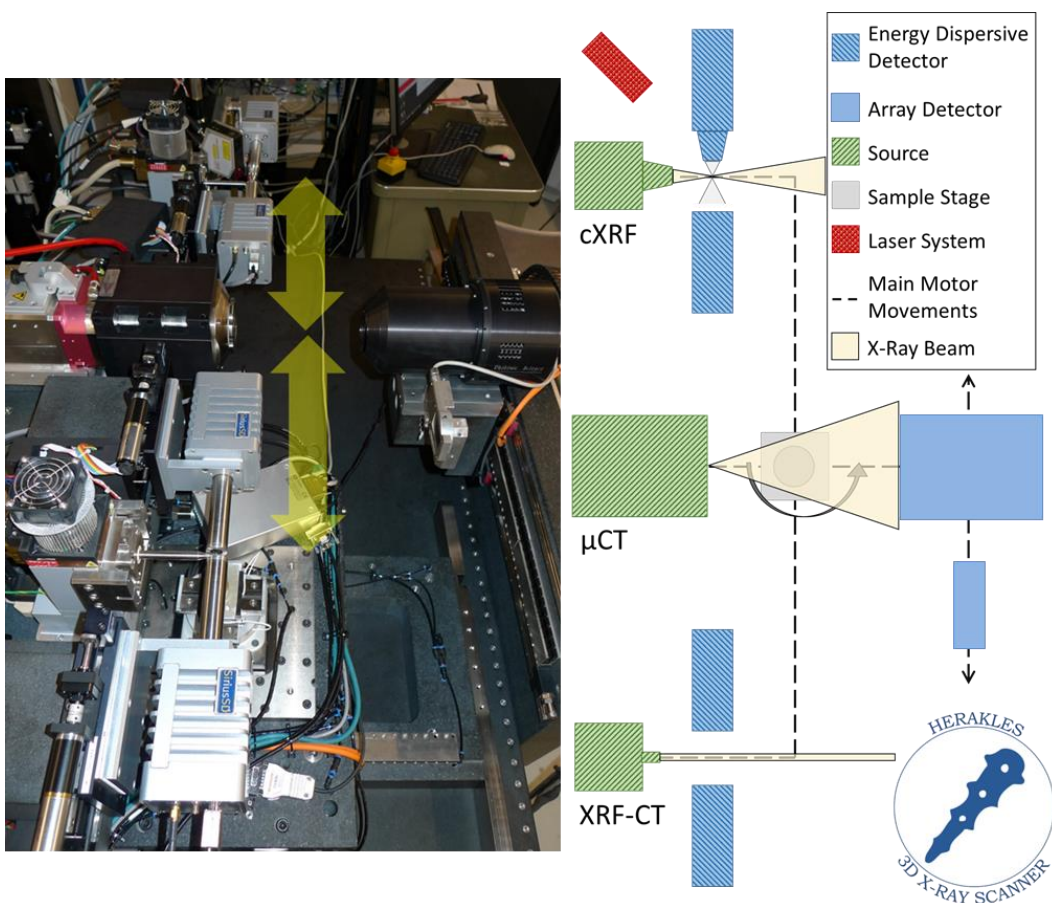


Figure 4-1 Design of the HERAKLES 3D X-ray scanner, on the left a picture of the setup, with a schematic representation on the right. From top to bottom you see the confocal XRF (cXRF), micro-tomography ( $\mu$ CT) and XRF tomography (XRF-CT) stations.

A typical experiment on the HERAKLES 3D X-ray scanner starts at the centrally positioned  $\mu$ CT station, where a high resolution, three-dimensional data-set (image-stack) of the scanned object is acquired. Based on this 3D data-set and the specific research question, the implemented software allows the user to select certain points, lines, areas, slices, sub-volumes or even the complete sample to be investigated for their elemental composition using one (or both) of the XRF end-stations. The control software will autonomously move the sample to the right position, even taking into account the optimal sample orientation when the experiment is to be performed at the confocal XRF imaging station. Since the coordinate system is retained between the two scans, coupling the data sets has become relatively easy and straightforward.

Further advantages of integrating these three techniques is the complementarity of their respective output in terms of data analysis. Information on the X-ray attenuation properties of the sample matrix is crucial for quantitative XRF microanalysis, allowing to correct for self-absorption effects. Since the  $\mu$ CT experiments yield the average attenuation coefficient in a spatially resolved manner, coupling data sets will lead to faster and better quantification of the XRF data. On the other hand, XRF can help in interpreting  $\mu$ CT data and the retrieved elemental information is very useful when modelling the experiment. Although the integration of data analysis will have an important impact on the user-friendliness of HERAKLES in order to maximize the information extracted from a sample, the software itself is still under development.

## 4.2. Components of the HERAKLES scanner

### 4.2.1. High-resolution X-ray computed tomography module

The  $\mu$ CT setup is equipped with an open microfocus X-ray tube with a high resolution transmission target (X-RAY WorX GmbH, Garbsen, Germany). High voltage values between 20 and 100 kV can be applied,

with a maximum target power of 3 W when using a microfocus spot. The smallest achievable spot size is approximately 700 nm, as stated by the manufacturer. The tube head is water cooled to reduce spot drift during a  $\mu$ CT scan. The setup is equipped with two different X-ray detectors (Figure 4-2). One of the two X-ray detectors can be selected by moving the chosen detector performing a simple linear motor movement (see Figures 4-1 and 4-2). For the imaging of low-attenuating samples, a Photonic Science Very High Resolution (VHR) CCD sensor (Photonic Science, Millham, UK) is used. This cooled CCD detector has 4008 x 2672 pixels of 9 by 9  $\mu\text{m}^2$  (36 x 24  $\text{mm}^2$  active area) with a clock speed of 20 MHz. It is equipped with a very thin  $\text{Gd}_2\text{OS:Tb}$  scintillator, making it inefficient for high-energy X-ray photons. Alternatively, a Radeye CMOS detector can be employed (Teledyne DALSA Inc., Ontario, Canada) which has a thicker scintillator, making it better suited for the analysis of highly attenuating samples such as geomaterials. Due to the conical shaped beam, the magnification of the object can be optimized by changing the sample-to-source distance.

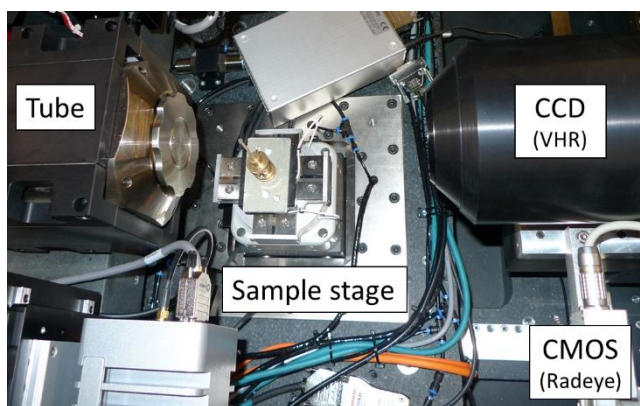


*Figure 4-2 Picture of the centrally positioned  $\mu$ CT station. The tube, sample stage and two array detectors can be seen.*

#### 4.2.2. Confocal XRF module

The confocal XRF setup (Figure 4-4) can be used for conventional 2D XRF experiments, 3D confocal XRF analysis and experiments using both

techniques simultaneously. It uses a 50 W (and 50 kV) Mo anode microfocus X-ray tube equipped with polycapillary optics (Xbeam, X-ray Optical Systems Inc., East Greenbush, NY, USA) to generate a focussed X-ray beam with a working distance of 3.6 mm and a spot size of 10  $\mu\text{m}$  x 13  $\mu\text{m}$  (H x V) at the Mo  $K_{\alpha}$  – line energy (17.48 keV), which is the current state-of-the-art for lab instruments and ideally suited for a lot of XRF imaging applications. A Mo tube is fit for XRF imaging of most elements of the periodic table due to the relatively high K-line energy of Mo (at 17.48 and 19.61 keV). The divergence of the conical beam generated by the polycapillary optics is 240 mrad. Two large area SDD detectors (SiriusSD, SGX Sortech Ltd, Chelmsford, UK) with 100 mm<sup>2</sup> crystal area (collimated on chip to 80 mm<sup>2</sup> active area) and a thickness of 450  $\mu\text{m}$  are used to collect the fluorescent photons. These detectors have an energy resolution of 136 eV at the Mn- $K_{\alpha}$  energy (5.9 keV) as stated by the manufacturer<sup>11</sup>. SDD detector technology was the preferred option due to their ability to cope with high count rates, which are important in some envisaged applications of HERAKLES (e.g. analysis of geological materials). Furthermore, the detectors can be quite compact in comparison to the alternative of Si(Li) detectors (which need liquid nitrogen cooling). This was an important advantage in designing the instrument, incorporating as many components as needed in a quite confined space. The big advantage of the SiriusSD detectors is the option offered by the manufacturer to optimize the layout of the SDD (e.g. change the nose length). On special request to the manufacturer, the detectors on the HERAKLES scanner have a 100 mm nose length with the detector crystal put as close to the tip as possible (2.8 mm). An additional collimator is used in default configuration, minimizing unwanted effects from radiation hitting the housing of the detector or the edges of the crystal. A secondary function of these collimators is to protect the crystal when an object would hit the detector nose, e.g. due to an incorrect motor movement during operation of the scanner. One of these SDD detectors is employed in conventional 2D XRF-mode, while the other is equipped with polycapillary optics (XOS) which were designed specifically for this instrument (Figure 4-3). The main design characteristic was the large output aperture, which is adapted to the

80 mm<sup>2</sup> active area of the SDD. The XOS company reported it proved a real challenge to make a polycapillary lens this large, putting a practical limit on the active area of the SDD crystal selected for this application. The optics are mounted to the detector with an in-house developed connector piece. The small black dot which can be seen on the top view of the optics in Figure 4-3 is an entrance for venting gases which allows flushing the polycapillary lens with helium if desired. Measuring under helium atmosphere would increase the sensitivity towards low Z elements. However, only the optics can be be flushed with helium gas instead of the optimal situation where the whole experiment is performed under helium atmosphere, hence the effect in case of the HERAKLES instrument would be sub-optimal.

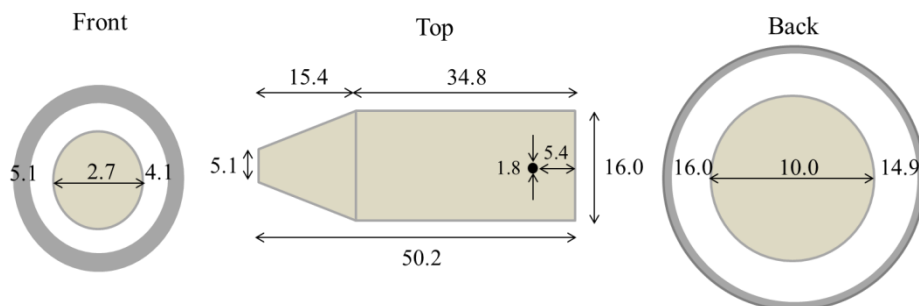
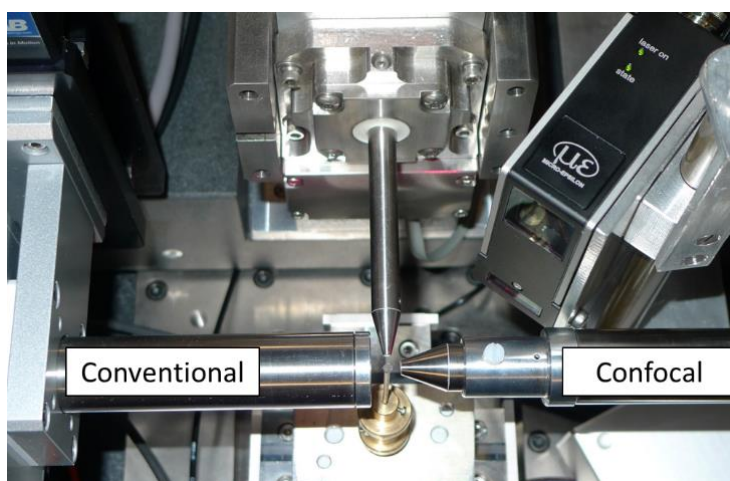


Figure 4-3 Design of the polycapillary optic mounted on the confocal detector (see Figure 4-4), the main dimensions of the optics are given (in mm).

By aligning the focal points of the X-ray source and the confocal detector equipped with these optics, a single and well-defined micro-volume can be analysed. The polycapillary source produces a fixed point in space, its focal point is one of the reference positions of the setup, so alignment happens by movement of the motorized detector. The size of the created microvoxel was determined to be 30 x 30 x 10  $\mu\text{m}^3$  (length-width-height, FWHM) using line scans over a 10  $\mu\text{m}$  thick stainless steel wire (Goodfellow Cambridge Ltd., Huntingdon, UK). These experiments are described in more detail further on in this chapter. By moving a sample

on a line or following a grid of such voxels, it is possible to extract direct 3D information. Using the setup in confocal configuration yields a signal with very low intensity compared to the conventional mode ( $\approx 150$  times smaller when using a  $10\text{ }\mu\text{m}$  stainless steel wire) since only a fraction of the generated X-rays are detected, hence long measurement times are necessary to extract statistically significant information. On the other hand, the amount of scatter detected is very low, leading to a good signal to background ratio, which partially remedies the lower count rate. A 1D laser triangulation system for distance measurements (Micro-Epsilon Messtechnik, Ortenburg, Germany) is also installed, both as a safety system and to aid the alignment of the setup.



*Figure 4-4 The confocal XRF setup, incorporating a Mo anode tube with polycapillary optics, two detectors (the confocal detector has polycapillary optics installed) and the Micro-Epsilon laser triangulation positioning system.*

Several confocal XRF laboratory setups are described in scientific literature.<sup>12-17</sup> The instrument described by Kanngießer and co-workers<sup>15</sup> was developed with the specific application of cultural heritage in mind. In this research field multi-layered samples (e.g. paintings) often occur, making 3D analysis crucial for a detailed investigation of these artefacts. The described instrument uses a Mo X-ray tube equipped with a polycapillary lens (spot size  $80\text{ }\mu\text{m}$ ) as excitation source and  $30\text{ mm}^2$

Si(Li) detector with a conical collimator to detect the fluorescent radiation. The detector collimator creates a fixed point in space, so alignment of the focal points is performed using the excitation source. This is a fundamental difference compared to the confocal XRF setup at HERAKLES, where the detector is moved during the alignment procedure and the focal point of the tube optics is the reference. Hence, the reference point at HERAKLES is active: it generates signal when a sample is aligned in the focal point, which significantly simplifies the alignment procedure. The authors demonstrated the good performance of their setup by analysing paint layers for their composition and thickness with convincingly good results. When comparing this instrument with the HERAKLES confocal XRF setup, it should be noted it is more than 10 years older, meaning the incorporated technology is in some cases outdated by today's standards. The spot size achieved with the polycapillary lens of the tube described by Kanngießer et al. (around 80  $\mu\text{m}$  FWHM) is considerably larger than the spotsize at HERAKLES, while the SDD technology of HERAKLES is superior compared to the more old-fashioned Si(Li) detectors on the older setup (developed in 2005) although the energy resolution of the two setups is comparable. The instrument of Kanngießer is positioned in a vacuum chamber, increasing the sensitivity towards low Z elements, an advantage over HERAKLES. Overall, the ten years of developments in the field of X-ray tubes, detectors and optics make HERAKLES a better performing instrument.

Patterson and Havrilla describe a laboratory based confocal XRF setup in their 2006 publication.<sup>13</sup> The instrument used a 25 W Ag X-ray tube and Si pin diode detector, both equipped with capillary optics by XOS (the same manufacturer as the optics of HERAKLES). The source and detector angle deviate from the ideal 90° configuration. To get a larger penetration capability, they are positioned under a 60° angle instead. The working distance is 10 mm. The confocal volume was determined to be 40 x 40 x 60  $\mu\text{m}^3$  (length-width-height, FWHM). These authors used a sample with different paint layers as well to demonstrate the performance of their setup. Compared to the confocal XRF end-station of HERAKLES, this instrument has a slightly larger confocal volume. The

non-ideal tube-detector angle will increase the impact of scattering on the recorded spectra, although no details hereon were given in the paper.

The third laboratory based confocal XRF setup, as described by Smolek et al.<sup>17</sup>, was based on a pre-existing micro-XRF instrument which was optimized for the detection of low Z elements.<sup>18</sup> Therefore, this micro-probe operates under vacuum conditions. The spot size of the Mo tube with capillary optics is 44  $\mu\text{m}$  FWHM for the Cu-K $\alpha$ -line. In order to modify their original instrument to a confocal setup, the authors added polycapillary optics to the detector. Alignment is performed by moving the optics themselves, with both the source and detector optics being placed on a XYZ motor stage. The detector optics can be easily removed to return the instrument to conventional scanning mode. A second tube (20 W Rh anode tube) was incorporated in the instrument to increase its versatility, offering a broader range of excitation energies. For Fe, the depth resolution of the setup is 50  $\mu\text{m}$  (compared to 30  $\mu\text{m}$  at HERAKLES). Detection limits for Fe lie around 20 ppm (1000 s LT) using either of the available sources, which is approximately 10 times higher than the values obtained at HERAKLES (see paragraph 4.6.2. on limits of detection). Measurements using test samples and artefacts provided by the Vienna Museum of Fine Arts were used to demonstrate to capabilities of the confocal instrument with satisfying results. In terms of spatial resolution the HERAKLES confocal XRF setup performs better than this instrument, however, the main advantage of the scanner from Smolek et al. is the ability to detect low Z elements.

#### 4.2.3. XRF tomography module

In XRF tomography, line-scans are systematically performed through the sample at multiple rotational angles. Analysis of the XRF spectra thus generates sinograms for all detectable elements present in the investigated object. Through the use of a suitable reconstruction algorithm, the elemental distributions in a virtual slice of scanned object can be retrieved. A 50 W/50 kV Mo anode microfocus source with



monocapillary optics (X-Ray Optical Systems Inc.) is used to generate the pencil beam which is needed for the XRF tomography procedure. The spot size of the beam is  $20\text{ }\mu\text{m}$  in both vertical and horizontal direction (@ Mo-K $\alpha$ , 17.48 keV) at 4 mm from the tip of the optics. The beam has a small divergence of 8 mrad. Once more a Mo tube is employed for its excellent characteristics in XRF elemental imaging. Furthermore, employing comparable instrumentation on the different end-stations (i.e. confocal XRF and XRF-CT end station) of the HERAKLES instrument makes comparison of data more straightforward. Two large area SDD detectors (SGX) are installed on this end-station. They have a crystal area of  $170\text{ mm}^2$ , collimated to  $150\text{ mm}^2$  active area. The detectors are employed in dual detection mode, maximizing the detector solid angle as can be seen in Figure 4-5.

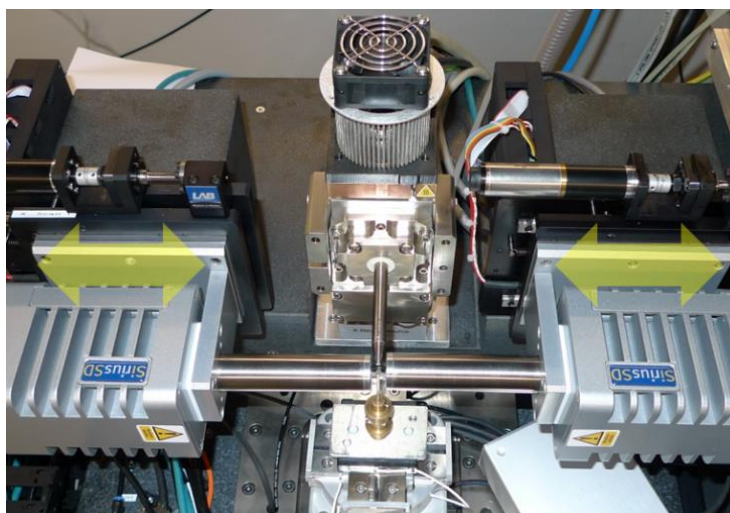


*Figure 4-5 The XRF-CT setup has a tube with monocapillary optics and two identical large area SDD detectors. The yellow arrows indicate the possible motor movement to maximize detector solid angle.*

Since the SDDs are motorized and can be moved as close to the sample as possible, the detector solid angle can be maximized to nearly the full  $4\pi$  in case of small objects. As illustration of the performance of this dual detector setup, a function can be formulated to determine the fraction of the fluorescent radiation which is detected as a function of the distance

between the detector and the trajectory of the X-ray beam. For the derivation it is assumed the sample is positioned exactly in front of the midpoint of the SDDs of the setup. The dual detector setup is assumed perfectly symmetrical and the fluorescence radiation is assumed to propagate from the intersection of the X-ray beam and the sample as a perfect sphere. Under these assumptions, the fraction of the fluorescent radiation capture by the active area of the detectors can be calculated by dividing the surface area of the spherical cap defined by the intersection of the detectors with the sphere of the propagating X-rays as can be seen in Figure 4-6. The formulas for the surface area of a sphere and a spherical cap are:

$$S_s = 4\pi r^2 \quad S_{sc} = 2\pi r h \quad (4.1)$$

With  $r$  the radius of the sphere and  $h$  the height of the spherical cap.

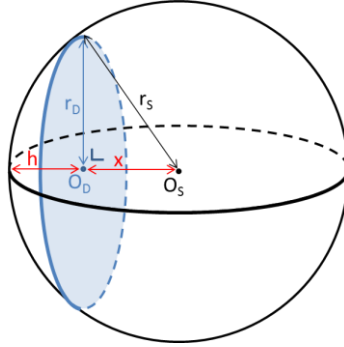


Figure 4-6 Scheme introducing the notations for the derivation of Equation (4.1).

When the detector is positioned  $x$  mm from the trajectory of the X-ray beam, the radius of the sphere can be calculated using Pythagoras theorem:  $r_s^2 = r_D^2 + x^2$  where  $r_D$  is the radius of the detector crystal active area.

The surface areas of the sphere and the spherical caps are:

$$S_s = 4\pi(r_D^2 + x^2) \quad (4.2a)$$

$$\begin{aligned}
S_{sc} &= 2\pi\sqrt{r_D^2 + x^2} \cdot \left( \sqrt{r_D^2 + x^2} - x \right) \\
&= 2\pi[(r_D^2 + x^2) - x\sqrt{r_D^2 + x^2}]
\end{aligned} \tag{4.2b}$$

Using these equations, the fraction of the fluorescent radiation which is detected using dual detector mode can be determined as a function of  $x$ :

$$\text{detected fraction} = 1 - \frac{x}{\sqrt{150 \text{ mm}^2/\pi + x^2}} \tag{4.3}$$

When the detectors are positioned 2 mm from the trajectory of the X-ray beam, 72 % of the emitted fluorescent radiation will be captured. With the detectors 2 mm further away, this value drops to 50 %. These calculations show the importance of the motorized detectors to optimize the detector-sample distance.

Several authors have reported on laboratory based XRF-CT setups.<sup>5,6,19</sup> In order to assess the performance of the XRF-CT end-station, it will be compared to these instruments. Wegrzynek describes an XRF-CT instrument which is part of a multi-tube laboratory setup for X-ray based analysis. This instrument has a Mo and a Cr tube and a Si(Li) detector. A collimator is used to create a microscopic X-ray beam. No definite value for the beamsize of the setup is given, but it is stated it amounts to a few tens of micrometers, which is slightly larger than the beamsize at the HERAKLES scanner. The results of the study by Wegrzynek (published in 2001) were meant to prove the feasibility of a laboratory XRF-CT instrument, which it does by providing nice results on four test objects (a glass capillary, the tip of a match, a burned wooden stick and the head of a fly). However, the specifications of the XRF-CT setup of HERAKLES outperform those of this much older instrument.

A second instrument incorporating XRF-CT was introduced by Sasov et al. and Bruyndonck et al..<sup>5,6</sup> The described instrument was later on commercialized by Brüker. This instrument, the Skyscan2140, had two tomographic techniques:  $\mu$ CT and XRF-CT yielding morphological and elemental information respectively. The sample is illuminated with a conical X-ray beam, while an energy-dispersive X-ray camera is used for

detection of the fluorescent radiation. This instrument yielded a spatial resolution of 70  $\mu\text{m}$ , with 180 eV energy resolution (@ Fe- $K_{\alpha}$ , i.e. 6.4 keV). Compared to this instrument, the XRF-CT setup incorporated in the HERAKLES scanner performs slightly better both in terms of spatial resolution (70  $\mu\text{m}$  vs. 20  $\mu\text{m}$ ) and energy resolution (180 vs. 136 eV). Due to the working principle of the Skyscan instrument (using a 2D detector) it is considerably faster than HERAKLES.

#### 4.2.4. Complementarity of the XRF techniques

Two of the three methodologies incorporated in the HERAKLES scanner are 3D XRF techniques. Although these yield very similar experimental results, they use a fundamentally different approach to acquire these data. Due to the difference in methodology, confocal XRF and XRF-CT analysis are highly complementary.

The virtual slicing performed with XRF-CT is ideally suited for samples of which cross-sections need to be investigated. The sample size could be a limiting factor, both in terms of spatial restriction of the instrument and due to self-absorption effects playing an important role. Low-attenuating (e.g. biological) samples should be no larger than 5 mm, while highly attenuating samples should not exceed 0.5 mm or even smaller, depending on the elements of interest. Furthermore, samples deviating strongly from a spherical cross-section such as large, flat, multi-layered samples are hard to investigate with this technique.

The confocal XRF setup is ideally suited for this last type of samples. Multi-layered samples can be easily assessed through depth scans. Furthermore, when only local information is needed, confocal point scans will yield the desired information much faster than XRF-CT scanning. The lower count-rate of this setup in confocal mode does increase the measurement time significantly, hence, for large cross-section is it less well-suited than XRF-CT. Feasible sample sizes are comparable to the XRF-CT end-station, with the focal distance of the capillary optics on the X-ray tube (3.6 mm) adding a hard limit for the possible 3D experiments.

Since both XRF end stations are operated in ambient conditions, they are only sensitive to elements starting from atomic number 14 (i.e. Si). In both cases sample size remains a critical parameter, both due to the confined arrangement of tube and detectors and self-absorption effects, limiting the feasible applications to rather small objects.

### 4.2.5. Overview of the HERAKLES X-ray equipment

*To have a clear overview of the different X-ray equipment installed on the HERAKLES 3D X-ray the HERAKLES 3D X-ray scanner, the main features of the X-ray sources (*

*sources (*

Table 4-1) and detectors (

Table 4-2) are listed in the tables below. Please note the minimal beam size reported for the XRF tubes is energy dependent due to the use of capillary optics. The minimum reported here is an extrapolation to the beamsizes at the Mo-K $\alpha$  line energy and is very close to the value reported by the manufacturer.

*Table 4-1 Properties of the X-ray tubes of HERAKLES*

Setup	Manufacturer	Beam shape	Power (W)	Max. Volt. (kV)	Min. beam size (µm)	Working distance
µCT	X-RAY WorX, Garbsen, Germany	Fan beam	200 (software limited to 100)	100	0.7	As close as possible
XRF-CT (monocap)	XOS, East Greenbush, NY, USA	Parallel beam 8 mrad div.	50	50	20	≈ 5 mm

<b>Confocal XRF (polycap)</b>	XOS, East Greenbush, NY, USA	Conical beam 180 mrad div.	50	50	10	3.6 mm
-------------------------------	------------------------------	----------------------------	----	----	----	--------

*Table 4-2 Properties of the detectors of HERAKLES*

<b>Detector</b>	<b>Type</b>	<b>Manufacturer</b>	<b>Size</b>	<b>Scintillator</b>	<b>Additional info</b>
<b>VHR detector</b>	CCD	Photonic Science, Millham, UK	4008 x 2672 pixels of 9 by 9 $\mu\text{m}^2$	Gd <sub>2</sub> OS:Tb	Best suited for low-attenuating samples (e.g. bio-materials)
<b>RadEye</b>	CMOS	Teledyne DALSA, Ontario, Canada	1020 x 512 pixels of 127 by 127 $\mu\text{m}^2$	Gd <sub>2</sub> OS:Tb	Better suited for high-attenuating samples
<b>XRF-CT</b>	SDD	SGX Sensortech, Chelmsford, UK	170 mm <sup>2</sup> coll. to 150 mm <sup>2</sup> , 450 $\mu\text{m}$ thick	/	Dual detector mode
<b>Confocal XRF</b>	SDD	SGX Sensortech, Chelmsford, UK	100 mm <sup>2</sup> coll. to 80 mm <sup>2</sup> , 450 $\mu\text{m}$ thick	/	1 det. has polycap. optics (XOS): conf. vol. 30 x 30 x 10 $\mu\text{m}^3$

### 4.3. Instrument stability and safety measures

Integrating the different end-stations requires exact knowledge of their relative positions. At the micron-scale thermal expansion of materials could become a problem. To illustrate the importance of stringent temperature control, a simple example of linear thermal expansion can be calculated. The linear thermal expansion coefficient of aluminium is  $24 \cdot 10^{-6} \text{ }^\circ\text{C}^{-1}$ , if an aluminium object of 20 cm undergoes a temperature increase of 2°C, its length increases with 10  $\mu\text{m}$ . Clearly thermal stability of the setup had to be considered when developing the HERAKLES scanner. The instrument is placed in a concrete bunker, isolated from its

surroundings (Figure 4-7). Next from shielding these surroundings from the X-rays produced by the scanner, this bunker also helps to establish a constant temperature at the level of the instrument.

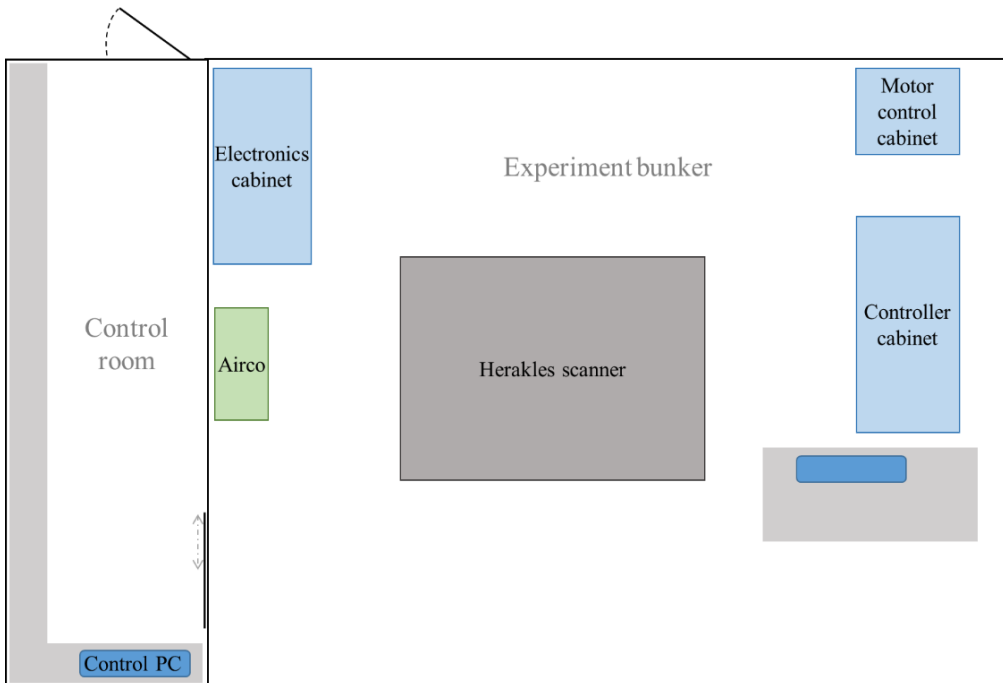


*Figure 4-7 Overview of the HERAKLES bunker and control room*

A stringent temperature control by an air-conditioning system keeps the bunker within  $0.5^{\circ}\text{C}$  from the set point temperature of  $24^{\circ}\text{C}$ . Regular visual inspection throughout this project confirmed the air-conditioning performed its task well. The heated or cooled air from this system is brought into the bunker through a stocking placed at the ceiling in order to create the least atmospheric disturbance as possible. When blowing directly on the sample it could cause microscopic vibrations interfering with experiments. A second cloth was hung above the instrument table to prevent dusts from falling on its polished granite surface, with as a secondary function extra shielding the sample stage against air currents.

To enter the experimental bunker, one needs to pass through the control room, which is also air-conditioned and serves as a thermal buffer. A plastic curtain is mounted in the door opening to prevent dust from entering the bunker and providing some thermal insulation when the door of the bunker is open.

The bunker also houses the controller cabinets where all motor, source and detector controllers are positioned, as well as the electronics cabinet of the HERAKLES 3D X-ray scanner. A secondary control module for the control pc is also present inside the bunker, which can be used when visual monitoring of risky motor movements requires the operator to be present inside the experiment bunker. Obviously no one is to enter the bunker while one of the X-ray tubes is on. A buzzer is installed in the bunker, signalling the presence of radiation, while an interlock system at the door of the bunker will immediately shut down all X-ray tubes as soon as the door is opened.

## 4.4. Integration of the end-stations

Although the separate end-stations of HERAKLES are already a valuable addition to the experimental capabilities of the combined XMI and UGCT groups, the integration of the different techniques makes the instrument unique in the world.

### 4.4.1. Motor system

The heart of the experimental setup is the high-precision motor system, consisting of thirteen independent motors (see

Table 4-3 for a summary), installed on a granite table (LAB Motion Systems, Leuven, Belgium) which measures 1.48 m x 0.77 m x 0.81 m



(length x width x height) and is highly polished (to within  $< 1 \mu\text{m}$ ) in order for the air-bearing motors to function properly. Additionally, the table has air-bearing controlled damping (Thorlabs Inc., USA) in its legs to minimize external vibrations.

*Table 4-3 Overview of the motors of the HERAKLES system*

<b>Name</b>	<b>Type</b>	<b>Manufacturer</b>	<b>function</b>	<b>Travel range (mm)</b>
<b>tra_obj</b>	Air bearing motor	Leuven Air Bearing (LAB), Leuven, Belgium	movement of sample stage perpendicular to X-ray beam + XRF mapping	0 to 811
<b>mag_obj</b>	Air bearing motor	LAB	movement of sample stage parallel with X-ray beam (magnification) + XRF mapping	0 to 179
<b>ver_obj</b>	Air bearing motor	LAB	Vertical movement of sample stage + XRF mapping	0 to 30
<b>rot_obj</b>	Air bearing motor	LAB	rotational movement of sample stage + CT exp.	No limits
<b>PIEZOX</b>	Piezo motor	SmarAct, Oldenburg, Germany	Aligning sample + mappings	-100 to 100
<b>PIEZOY</b>	Piezo motor	SmarAct, Oldenburg, Germany	Aligning sample + mappings	-24 to 24
<b>tra_det</b>	Air bearing motor	LAB	Selection and alignment of $\mu\text{CT}$ detector	-25 to 830
<b>XRFTLEFT</b>	Linear motor	LAB	Solid angle optimization	0 to 22
<b>XRFTRIGHT</b>	Linear motor	LAB	Solid angle optimization	0 to 24
<b>XRFCNFLEFT</b>	Linear motor	LAB	Solid angle optimization	0 to 20
<b>XRFCNRIGHTX</b>	Linear motor	LAB	Alignment of the confocal setup	0 to 11
<b>XRFCNRIGHTY</b>	Linear motor	LAB	Alignment of the confocal setup	0 to 13
<b>XRFCNRIGHTZ</b>	Linear motor	LAB	Alignment of the confocal setup	0 to 6.4

The motors can be subdivided into three categories with respect to their function, including 1) sample positioning and measurement 2) sample alignment and 3) movement of detectors.

First, an ultra-high precision air-bearing XYZ motor system (LAB) is used for the movement of the sample stage between the three different stations of the instrument ( $\mu$ CT, XRF-CT and cXRF). This stage has an excellent positional reproducibility of  $\pm 100$  nm over a travel range of nearly 1 m to allow for very precise movement of the sample between all three measurement stations. By defining a reference point for each setup which is calibrated on a regular basis, the sample can be moved while retaining the coordinate system, which is the key to integrated multi-technique measurements.

The rotational motor (LAB), crucial to the tomography techniques, is integrated in the main XYZ motor system. On top of the rotation stage are two piezo electric motors (SmarAct GmbH, Oldenburg, Germany) which are connected to their controllers using a slip-ring connection. The piezo-motors are employed to position the samples relative to the rotation axis of the system. These piezo motors are also used to define the coordinate system of the scans, since they are moved together with the sample from one station to the other. Depending on the envisaged measurement, both the air-bearing and piezo motors can be used to scan an object with the microbeam X-ray modules, although most often the main air-bearing system is used for scanning.

Finally, all detectors are motorized to some degree. A long range translational motor (LAB) allows the selection of the most favourable detector for a  $\mu$ CT application (the Photonic Science for light matrices or the Radeye for heavy matrices), while shorter range translational motors (LAB) are used to optimize the detector-sample position of the conventional XRF detectors (XRF-CT and part of the cXRF setup) to achieve the largest possible detector solid angle. The XRF detector equipped with polycapillary optics of the confocal XRF end-station is installed on an XYZ motor stage which is crucial in for the alignment procedure of the cXRF setup. Originally, a different set of motors was

used for the movement of the XRF detectors (Thorlabs Inc, Newton, New Jersey, USA) but these proved insufficiently strong to carry the weight of the detectors.

#### 4.4.2. Control software

It is clear creating a userfriendly control software controlling the various components of HERAKLES (motors, X-ray tubes and detectors) is no trivial task, not in the least because all these components communicate through different protocols and use various dll's provided by the manufacturers. In order to control the scanner and integrate all components, a dedicated control software has been developed using the LabVIEW programming language (National Instruments, Austin, Texas, USA) which was based on an existing platform of the UGCT group.<sup>20</sup> LabVIEW is a visual programming language, where pictograms represent parameters, functions, logical values, etc. and lines are used to connect these pictograms, performing e.g. a mathematical operation as demonstrated in Figure 4-8.

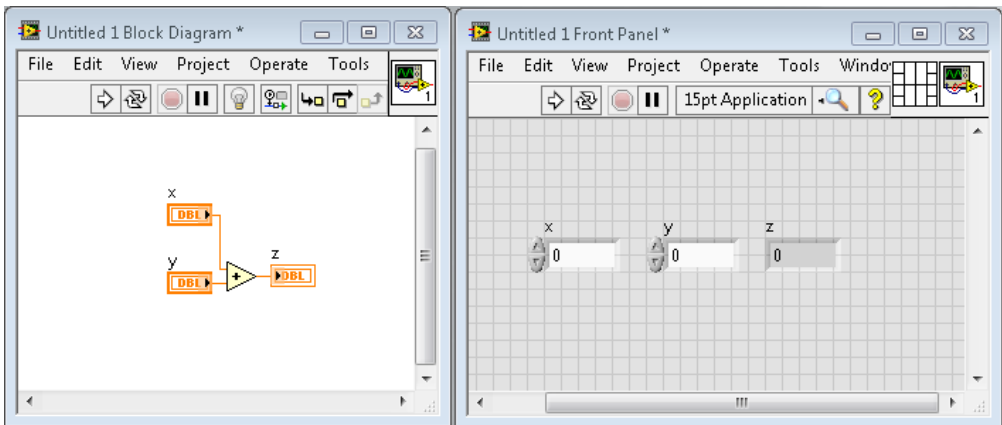


Figure 4-8 Working principle of the Labview programming language. Example: code to define the function  $x + y = z$ .

A LabVIEW program is called a *virtual instrument* (VI) because it mimics a physical instrument in both appearances and operation. The LabVIEW environment has a wide range of predefined functions for data treatment and acquisition, making it well-suited for the development of control software. It is very easy to create sub VI's (i.e. small programs performing a specific section of your code) in LabVIEW, keeping the code neat. The use of these sub VI's at other points in the software is straightforward, making them a useful tool.

The control software separates the scanner operation from the code to address the hardware components. An overall, control software (called the scannerGUI) is used to generate abstract commands while running the scanner, which are then sent to the targeted hardware component. To achieve this, several so called "user events" were defined. These are clusters containing the name of the addressed component, the command, arguments and feedback. For each type of hardware component, a specific set of commands was predefined. To execute a certain action, the abstract command is generated in the control software, addressed to a specific hardware component. In the dedicated, stand-alone control software of the addressed component, this command is received and translated into the correct format to generate a command to the controller of this hardware. Furthermore, sub-programs, components and add-ons can also generate these type of commands, which can be addressed to multiple components at once, which will execute to order as soon as possible. The presented structure decouples the control of the instrument, which uses general commands such as "tube on" or "move motor", from the practical implementation which depends on the specific hardware.

The XRF sources are not included in the above described structure, due to issues with the dll-files provided by the manufacturer. These dll-files were only provided in a 32 bit version, not all commands present in the dll-files were documented (e.g. the reset function) and most importantly, the dll's are named identically so LabVIEW currently cannot distinguish between the two tubes when incorporating them in a single instrument. Work is in progress to overcome these challenges and integrate these sources as well in the central control software.

The procedure of starting all software and performing a measurement is given in a flowsheet in Figure 4-9. A detailed guide, including all functionalities can be found in appendix A3.

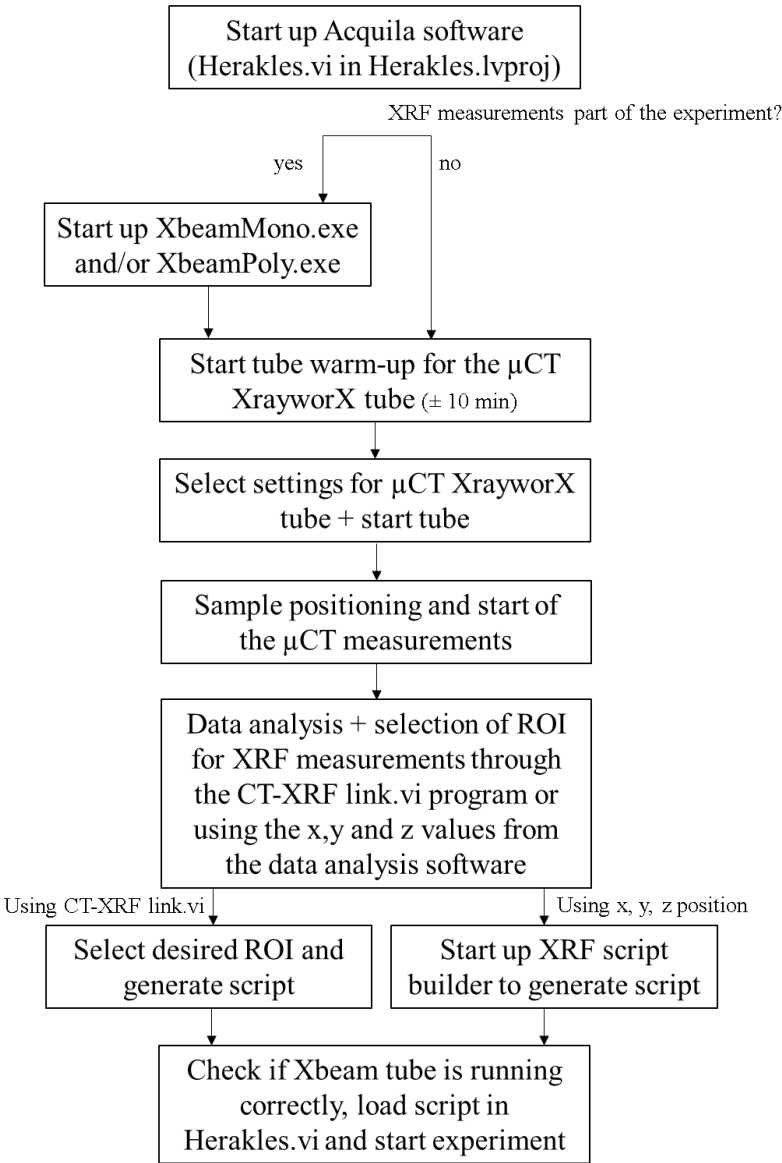


Figure 4-9 Flow sheet for starting up the software to perform a measurement.

#### 4.4.3. $\mu$ CT – XRF linking software

A second software package created specifically for HERAKLES is the  $\mu$ CT – XRF linking software, which uses reconstructed tomographic data of the scanner as a visual aid in generating a script for 3D experiments using the confocal XRF end-station. The procedure goes through following steps:

- Align the sample on the  $\mu$ CT end-station and perform a tomography
- Analyse the tomographic data (e.g. using the XRF software or Octopus Reconstruction)
- Open the linking software
- Read in the reconstructed  $\mu$ CT data
- Based on selected virtual slices,, select the desired points, lines, grids or contours to be analysed using 3D XRF and add them to the point matrix
- Generate the script
- Start the polycapillary source with desired settings (in Xsource-poly.exe)
- Read and run the script in Herakles.vi

A detailed manual on how to operate the software can be found in Appendix A3.

This  $\mu$ CT-XRF linking program could be considered the ultimate proof of the successful integration of the different components of the HERAKLES setup, even paving the way for possibilities of completely automated ROI retrieval an XRF analysis based on preliminary  $\mu$ CT imaging in the future.

## 4.5. Alignment and calibration of the instrument

Meticulously installing all components on the granite table is the very first step of realizing the scanner. However, at least as important for its well-functioning is determining all reference positions, aligning the sources and detectors and calibrating the overall system, linking the reference positions of the different end-stations.

### 4.5.1. $\mu$ CT alignment

It is of crucial importance that the source and detector of the  $\mu$ CT setup are aligned along the same optical axis, looking straight at each other. If this is not the case, the sample will move relative to the optical centre of the image when one changes its magnification. Furthermore, misalignment needs to be taken into account during the data processing, which becomes more difficult if the experiment was performed under non-ideal circumstances.

The first step in aligning the  $\mu$ CT setup is defining a reference position. This reference is optically defined using a transmission image of a test sample and indicated with a red cross on the monitoring window. This cross eases alignment of the sample later on. In practice, the cross is placed exactly in the middle of the image captured with the detector and the translational motor of the object is moved until the rotational axis of the rotation motor is well-aligned with this reference position. By observing the sample under different rotational angles, the position of its rotational axis can be assessed; the sample should stay centrally positioned in the captured image if the rotational axis and the center of the image (i.e. the reference position) are at the same position.

In the next step, the sample is moved along the magnification axis of the setup (i.e. closer to, or further away from the source) and the previous procedure is repeated. When the sample has moved relative to the reference position on the captured image, the detector position is altered accordingly until this shift is no longer observed. This alignment is not only necessary when building the instrument, but must also be performed

during intermediate calibration sessions which should be performed on a regular basis to keep the instrument in perfect condition. When the filament of the  $\mu$ CT tube is changed, a severe shift in the X-ray spot was noted ( $> 200 \mu\text{m}$ ) with a slight drift over the next few months, indicating a regular recalibration is necessary each time the filament is changed.

Other steps in the initial alignment are the optimization of the detector angle, which was performed during the construction of the scanner. Both tilt and skew need to be checked and optimized to obtain high quality  $\mu$ CT images. The procedure for these optimizations is very alike the optimization of the detector position and is based on visual inspection of imaging experiments. Only when the detector is replaced or has been removed from its holder these parameters need to be recalibrated, since they are mechanically fixed.

#### 4.5.2. Calibration of the coordinate system

The position where the rotational axis of the rotation motor is centered in front of the  $\mu$ CT setup is chosen as main reference point for the overall instrument. This is a practical choice, since most experiments will start at this position with a  $\mu$ CT measurement. To calibrate the coordinate system of the instrument, two further reference positions must be defined, one for each XRF end-station.

As reference position of the confocal XRF setup, the logical option is the focal point of the polycapillary optics of the X-ray tube mounted on this setup, located approximately 4 mm in front of the tip of these optics. A cross made of stainless steel wires (Goodfellow, UK) with a diameter of  $10 \mu\text{m}$  was used to locate this focal point through two subsequent mappings. The first mapping was a horizontal xy map over the vertical wire of the cross, in order to determine the position of the focal point along the X-ray beam, which is very similar to the scan to determine the beamsize as given in Figure 4-11. This position was determined to be at 4.6 mm from the zero position of the magnification motor and at 5.06 mm for the translational motor. Next, a vertical yz map over the



horizontal wire was used to determine the vertical position of the focal spot, which was determined to be 0.89 mm higher relative to the vertical center of the  $\mu$ CT setup. It should be noted that these positions are determined after the sample was aligned with the rotational axis of the rotation stage. Movement of this axis can alter the exact values linked to this reference point, since the sample will not be at the same position as it was when aligned previously. In fact, this has happened after the refurbishment of the piezoelectric motors with a new slip ring. To prevent alignment errors, the reference position should be recalibrated on a regular basis through wire scans as described above.

The reference position for the XRF-CT setup was determined using an analogue procedure. The main difference with determining the reference point of the confocal XRF setup lies with the pencil beam produced by the monocapillary optics which does not have a focal point. Hence, there is not one specific position along the X-ray beam which is the one and only optimal position for XRF experiments. The beamsize is minimal upon leaving the optics, so measuring very close to the tip of the capillary would be ideal in terms of spatial resolution. Of course this increases the potential of sample-source collision, so a safe working distance of at least 4 to 5 mm is advised. Mechanically, the detectors are positioned aiming at a point 7 mm in front of the tube optics, which is approximately the radius of the detector crystal of 150 mm<sup>2</sup>. Due to this mechanically fixed position, placing the sample very close to the source has relatively little advantage.

Table 4-4 gives an overview of typical scan settings for these calibration measurements. For a detailed (re)calibration, first a relatively big area will be scanned using larger steps, with relatively short scanning times at high tube power to approximately locate the reference position. This coarse map is followed by a smaller, more detailed scan, possibly at lower tube power. When quickly checking the reference point in between experiments, a sole rapid scan is sufficient. All reference positions are given in Table 4-5.

Table 4-4 Typical scan settings for the calibration experiments.

	Tube voltage (kV)	Tube current (mA)	step size ( $\mu\text{m}$ )			Mapping size		
			x	y	z	x	y	z
<b>XRF-CT</b>	40	0.6-0.7	5-20	-	2-15	100-300	-	100-300
<b>Confocal XRF</b>	40	0.5-0.6	2-15	50	2-15	100-300	100-1000	100-300

Table 4-5 Overview of the reference positions for the different end-stations of HERAKLES. These positions are subject to change and have proven to show a small drift over time. Periodical recalibration is of vital importance.

	tra_obj (mm)	mag_obj (mm)	ver_obj offset (mm)
<b><math>\mu\text{CT}</math></b>	415.78	100	0
<b>XRF-CT</b>	805.5	5	+ 2.27
<b>Confocal XRF</b>	5.05	4.6	+ 0.89

### 4.5.3. Alignment of the confocal setup

The final alignment in order to get the HERAKLES 3D X-ray scanner fully operational, is also the most demanding, namely the alignment of the confocal setup. The focal points of the optics on both source and detector need to coincide before a confocal measurement is possible, which is no trivial task given their size of only a few tens of micrometers. Once again, the 10  $\mu\text{m}$  diameter stainless steel wire cross (or its 15  $\mu\text{m}$  brass equivalent) is employed. Only the vertically oriented wire is used during this procedure. First, the wire is brought into the focal spot of the X-ray source, which was determined during the previous calibration of the coordinate system. To be sure that the wire is exactly on the desired position, a short local mapping may be performed. Once the user is confident in the position of the wire relative to the source, a large, coarse 3D mapping using the detector motors is performed. During this scan, the incoming count rate of the confocal detector is observed, although it is also possible to acquire and evaluate the entire XRF spectrum in each point of the map. Next, a smaller map with reduced step size is acquired around the location of maximum intensity found with the first scan. This second 3D mapping should yield the exact location of the confocal point

of the optics on the X-ray source and the detector. Moving the detector to this position aligns the setup for confocal experiments. Fortunately, the focal spot of both source and detector has proven to be quite stable, so the time consuming first mapping (the large, coarse map) can in practice be rather fast for day-to-day recalibration of the setup.

## 4.6. Instrument characterization and test cases

### 4.6.1. Beamsize determination

The beamsize produced by the XBeam sources used for cXRF and XRF-CT is of crucial importance regarding the performance of the XRF methodologies, since it directly affects the spatial resolution which can be achieved. To determine the beamsize a line scan is performed over a metal wire, mounted as a cross on a polymer (PMMA) ring. Several types of metal wire were used, being a 10  $\mu\text{m}$  stainless steel (Cr, Fe, Ni), 5  $\mu\text{m}$  platinum-rhodium, 10  $\mu\text{m}$  palladium and 15  $\mu\text{m}$  brass wire (Cu, Mn, Ni) all purchased from Goodfellow Cambridge Ltd (UK). When the XRF intensity of a certain element from these line scans is plotted as a function of wire displacement relative to the incident beam, a Gaussian-like curve is obtained. This curve is then fitted with a Gaussian function. The full width at half maximum (FWHM) of this fitted curve is used as a first estimation of the beamsize. In a subsequent step, a deconvolution is used to take into account the non-negligible diameter of the wire. Since the beamsize of the Xbeam source is given by the manufacturer at the energy of the Mo- $K_\alpha$  line of the tubes, an extrapolation to this line energy is performed in order to check their claimed spot size. Next to the beamsize, the divergence of the beam is determined.

### **Polycapillary source**

Figure 4-10 gives Cr, Fe and Ni  $K_\alpha$  intensity distributions derived from a yz mapping over the horizontal wire of the stainless steel cross

corresponding to the polycapillary based Xbeam source. The conical shape of the beam is very obvious from these images, as is the approximate location of the focal spot. A second, more detailed mapping can be used to determine the exact position of the focus and the minimal beamsize.

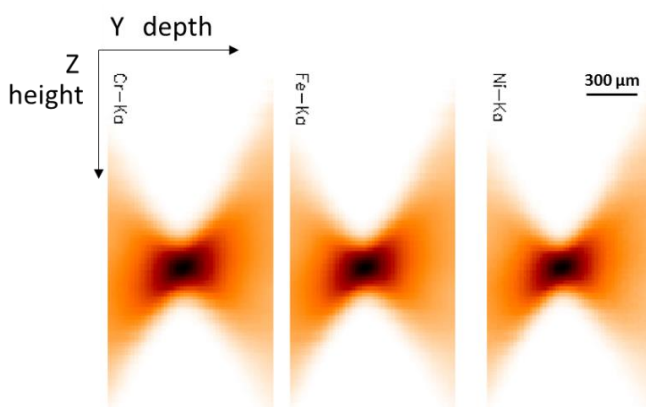


*Figure 4-10 Profile scan of polycapillary source. The divergence of the beam is clearly visible.*

The line scan for Fe at this minimal position is shown in (Figure 4-11). The Gaussian fit has a FWHM of  $20.8\text{ }\mu\text{m}$  at the Fe- $K_{\alpha}$  line. The convolution with the wire diameter yields an estimated beamsize of  $18.2\text{ }\mu\text{m}$  in the vertical direction. Via a similar procedure, the horizontal beamsize is determined to be  $17.1\text{ }\mu\text{m}$  (FWHM).

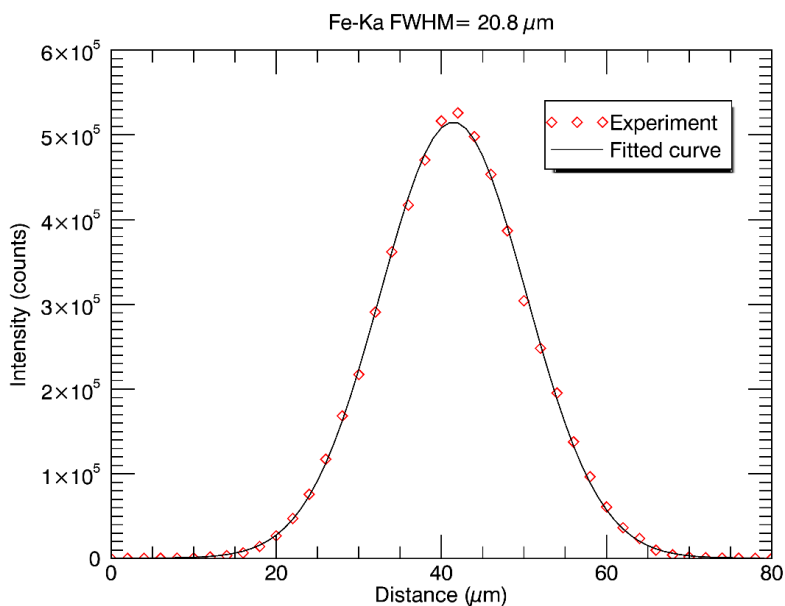


Figure 4-11 Line scan at the Fe-K $\alpha$  line over 10  $\mu$ m stainless steel wire (Goodfellow) used to determine the FWHM and beamsize.

Being a chromatic optic, a polycapillary lens focusses X-rays with different energies into a focal spot which has an energy dependent diameter due to the energy dependence of the critical angle for total reflection (as has been discussed in Chapter 2). In other words, the spatial and energy distribution of X-rays within the focal spot are coupled, with the center corresponding to X-rays with a harder energy distribution. Hence, it is important to determine the beamsize for several elements in order to obtain information about how the beamsize evolves as a function of atomic number of the excited elements.

In practice, a larger focal spot will be found for lower Z elements, as their absorption edges have lower energies and because they are mainly excited by incident photons having energies just above their edges. As a demonstration of this effect, the elements of the stainless steel wire can be compared (Figure 4-12). In the order of increasing atomic numbers these are Cr, Fe and Ni, exhibiting beamsizes of 20.9, 19.2 and 17.4  $\mu$ m (FWHM), respectively. Extrapolating to the Mo K $\alpha$  energy yields a

beamsize of approximately 10  $\mu\text{m}$ , which is close to the value given by XOS (11  $\mu\text{m}$ ).

From the profiles that are plotted in Figure 4-12 the divergence of the beam can also be calculated, by selecting several points in the linear parts of the full 0.8 mm scan interval, calculating the beamsize at these locations and fitting a linear function to these points. The angle derived from this linear fit is a good estimate of the angle of divergence. In the case of the polycapillary source, a divergence of 240 mrad was found. Moving away more than 50  $\mu\text{m}$  from the focal spot will increase the beamsize with 10% compared to the minimal value. This indicates the importance of careful sample alignment and positioning with respect to the focal point.

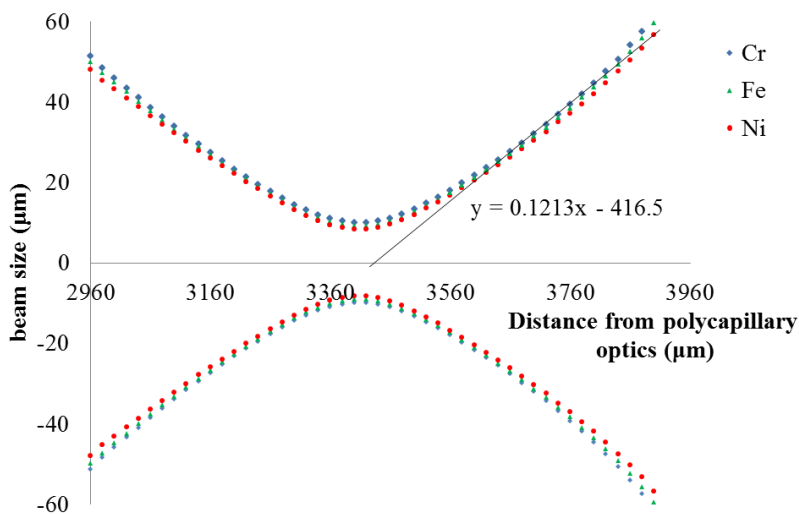


Figure 4-12 Beam size and divergence estimation using a stainless steel wire (Goodfellow). Points measurements on a line following the beam trajectory around the minimum beam size position. Note the curves for the three indicated elements (Cr, Fe, Ni) deviate due to the properties of capillary optics.

## Monocapillary source

The procedure to determine the beamsizes of the monocapillary X-ray tube is comparable to the procedure of the polycapillary tube described above. However, there is one major difference between the beam profiles of the two tubes, which translates in a slightly different experiment. The polycapillary optic of the first tube creates a truly focused beam which converges into a well-defined focal spot and diverges again once past this position of minimal beamsize. The monocapillary optic on the other hand was designed to create a quasi-parallel pencil beam, which diverges very slowly and has a minimal spot size at the tip of the capillary. Hence, the first step of the protocol, determining the focal spot, becomes obsolete when dealing with the monocapillary tube. Instead, a specific reference position is chosen where the beamsize is determined. Due to collision related safety considerations this position cannot be too close to the tip of the capillary. It was opted to work at 4 mm from the optics, a comparable distance to the working distance of the polycapillary tube (i.e. 3.6 mm). As before, horizontal and vertical line scans were performed to assess the beamsizes, yielding a 32.0 by 28.4 mm (H x V, FWHM) spot size. To image the shape of the beam, a large mapping (0.5 x 8 mm<sup>2</sup>) was performed over the stainless steel wire. The results of this mapping are shown in Figure 4-13. The divergence was determined based on the map shown in Figure 4-13, resulting in a value of 8 mrad (using the wire corrected beamsizes), which is clearly much smaller than the divergence obtained in case of the polycapillary source. In practice the beamsizes of the monocapillary source can be considered to be constant across the entire sample for typical sample thicknesses of objects analysed with the Herakles setup (~ 1 mm) (~1 mm) which makes this XRF-CT procedure truly applicable as a viable 3D XRF method.

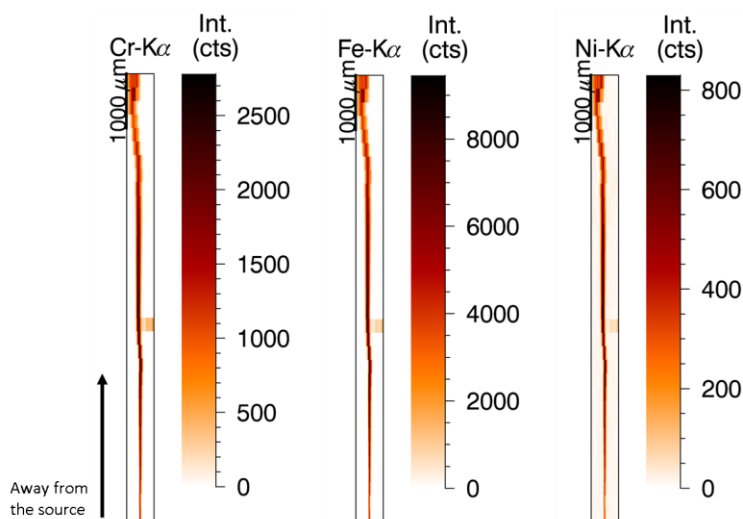


Figure 4-13 Profile scan of the monocapillary source, demonstrating the relatively low divergence. At the top the image gets blurred where the support PMMA ring starts, while near the middle the second, perpendicular wire of the wire cross can be seen.

#### 4.6.2. Limits of detection (LOD) determination

To determine the analytical capabilities of the two XRF methodologies incorporated in the HERAKLES scanner, several experiments on reference materials with widely different matrices have been performed. These measurements are square 10 by 10 point mappings with 10 s live time per point. Summing up the obtained spectra yields a sum spectrum corresponding to a total dwell time of 1000 s, averaging a relatively large area of the reference material, which is then analysed and used to determine the detection limits of the setup. These settings mimic an actual scan, to get information on the true detection limits. In case of 3D XRF experiments, this is not a trivial challenge. Figure 4-14 shows the limits of detection for both XRF end-stations used in conventional mode based on the measurement of a 100  $\mu\text{m}$  thick NIST SRM 1577c bovine liver reference material using exactly the same settings.



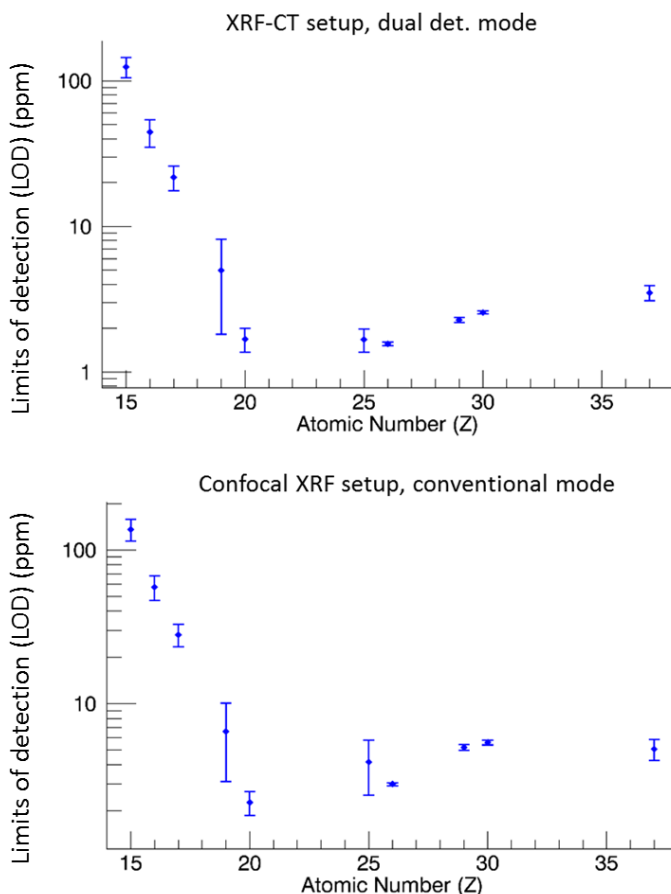


Figure 4-14 Detection limits for the XRF-CT setup and the conventional mode of the confocal XRF setup determined using a 1000 s scan on a 100  $\mu\text{m}$  thick pressed pellet of the NIST SRM 1577c bovine liver. (40 kV, 0.5 mA)

The limits of detection for both the XRF-CT setup and the confocal setup in conventional mode prove to be very similar, although the setups themselves are quite different. The confocal XRF station is equipped with detectors having a much smaller crystal area than the detectors of the XRF-CT (80 mm<sup>2</sup> active area compared to 150 mm<sup>2</sup>). Furthermore, the XRF-CT uses two detectors in dual detection mode, where the confocal XRF setup in conventional operation uses only one SDD detector. However, the polycapillary tube is approximately 30 times more intense than the monicapillary tube ( $7.40 \cdot 10^7$  photons/s vs.  $2.54 \cdot 10^6$

photons/s @ 50 kV and 1 mA), which cancels out the lower detection efficiency.

Focusing on the values for the limits of detection, both end-stations are capable of detecting a few ppm's of all elements with atomic number larger than 19 (i.e. K), while for P around 150-200 ppm can be detected significantly in this biological sample.

To demonstrate the importance of the sample matrix when assessing detection limits of XRF experiments, the measured results for another reference material having a much denser matrix than the biological NIST SRM (bovine liver) are shown, namely the MPI DING ATHO-G<sup>21</sup>, a geological reference material. This scan is plotted in Figure 4-15. The LOD values for the higher Z elements do not differ much compared to those attainable from the biological standard sample, however, for lighter elements (e.g. K) the detection limit lies considerably higher in this heavier matrix (27 ppm compared to 7 ppm). This effect can be explained by the higher level of self-absorption when X-rays (especially low energy X-rays) pass through a sample with a higher mean atomic number and density (X-ray attenuation is directly correlated with both of these properties, as described in chapter 2).

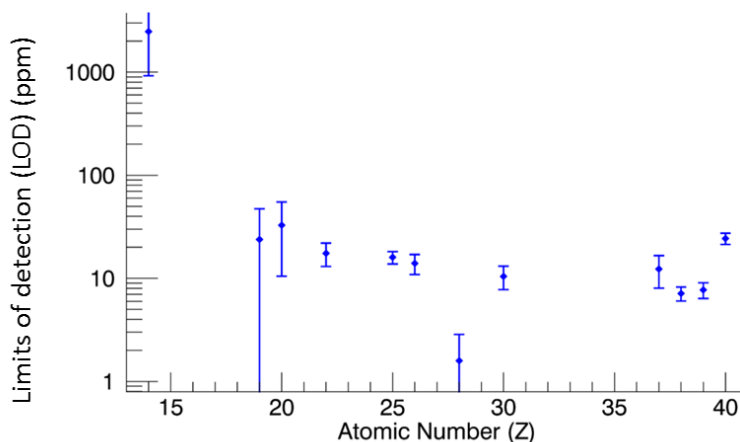


Figure 4-15 Detection limits for the XRF-CT setup determined using a 1000 s scan on a 100  $\mu\text{m}$  thick MPI DING ATHO-G reference sample. (40 kV, 0.5 mA)

#### 4.6.3. Test-case: $\mu\text{CT}$ – confocal XRF linking

One of the key aspects of the HERAKLES scanner is the ability to link the different end-stations, using a scan performed with one of the methodologies to define a measurement at one of the others. Most often, the  $\mu\text{CT}$  setup will be used as first technique, because it is by far the fastest technique to analyse a complete sample and its output (3D image of the sample) is ideally suited to select ROIs for further analysis.

Using the dedicated  $\mu\text{CT}$ -XRF linking software it is straightforward to select points, lines, areas or volumes for analysis with the confocal XRF setup, as was discussed in paragraph 4.4.2. and appendix A3 which describe the control software of HERAKLES.

Figure 4-16 shows the results of one of the very first test runs performed using this software. It clearly demonstrates the successful linking of the two techniques. On the left a render can be seen of a  $\mu\text{CT}$  scan on the test sample: a 100  $\mu\text{m}$  thick copper wire which was wound around a tooth pick and fixed using regular hobby tape. The render only shows the windings of the copper wire. Using this  $\mu\text{CT}$  scan, a set of points for confocal XRF analysis were determined, closely following the wire. In

the right part of Figure 4-16 the Cu-K $\alpha$  signal of these points is plotted in a 3D coordinated frame. Clearly, the scan was able to follow the shape of the wire nicely. A few points on the left side of the scan are darker in colour (brown to black) indicating a lower Cu intensity. The drop in intensity in these points could be caused by (near) misses of the XRF scan. Another explanation could be the uneven placement of the tape used to fix the wire, with the low intensity points caused by a thicker layer of tape and hence increased attenuation of the fluorescent X-rays. Since the relatively high energy Cu-K lines will only be little attenuated by a few layers of polymer tape, the near-miss hypothesis is the most likely. Performing local mappings could have been a good approach to investigate this observation, but since this scan was only a proof of principle, no detailed analysis was performed.

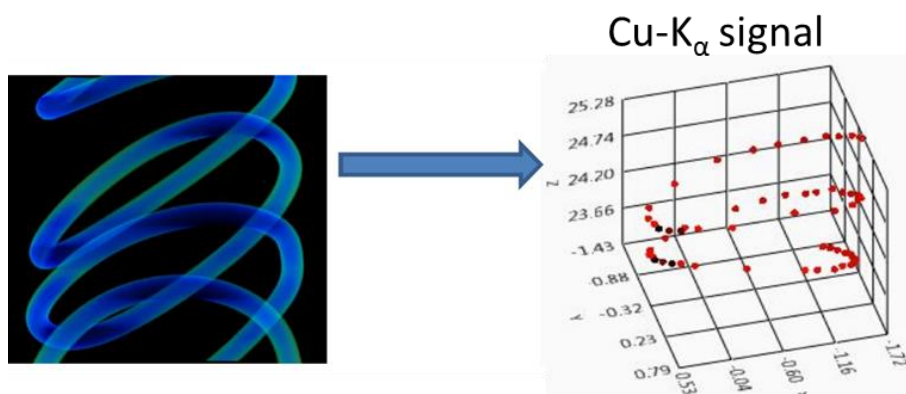


*Figure 4-16 Demonstrative experiment of the  $\mu$ CT – XRF linking: on the left a render from a  $\mu$ CT scan of a copper wire winding can be seen, which was used to construct the script for a set of confocal XRF point scans (right part of the image). The Cu-K $\alpha$  signal of these points scans plotted with their 3D coordinates follows the outline of the wire.*

## 4.7. References

- (1) De Samber, B.; Vanblaere, S.; Evens, R.; De Schamphelaere, K.; Wellenreuther, G.; Ridoutt, F.; Silversmit, G.; Schoonjans, T.; Vekemans, B.; Masschaele, B.; Van Hoorebeke, L.; Rickers, K.; Falkenberg, G.; Szaloki, I.; Janssen, C.; Vincze, L. *Powder Diffraction* **2010**, *25*, 169-174.
- (2) Golosio, B.; Simionovici, A.; Somogyi, A.; Lemelle, L.; Chukalina, M.; Brunetti, A. *Journal of Applied Physics* **2003**, *94*, 145-156.
- (3) Golosio, B.; Somogyi, A.; Simionovici, A.; Bleuet, P.; Susini, J.; Lemelle, L. *Applied Physics Letters* **2004**, *84*, 2199-2201.
- (4) Cordes, N. L.; Havrilla, G. J.; Usov, I. O.; Obrey, K. A.; Patterson, B. M. *Spectrochimica Acta Part B: Atomic Spectroscopy* **2014**, *101*, 320-329.
- (5) Bruyndonckx, P.; Sasov, A.; Liu, X. *AIP Conference Proceedings* **2011**, *1365*, 61-64.
- (6) Sasov, A.; Liu, X.; Rushmer, D. In *Developments in X-Ray Tomography VI*, 2008, pp 70780R-70780R-70789.
- (7) Cnudde, V.; De Boever, W.; Dewanckele, J.; De Kock, T.; Boone, M.; Boone, M. N.; Silversmit, G.; Vincze, L.; Van Ranst, E.; Derluyn, H.; Peetermans, S.; Hovind, J.; Modregger, P.; Stampanoni, M.; De Buysser, K.; De Schutter, G. *Quarterly Journal of Engineering Geology and Hydrogeology* **2013**, *46*, 95-106.
- (8) Cnudde, V.; Silversmit, G.; Boone, M.; Dewanckele, J.; De Samber, B. W. E.; Schoonjans, T.; Van Loo, D.; De Witte, Y.; Elburg, M.; Vincze, L.; Van Hoorebeke, L.; Jacobs, P. *Science of The Total Environment* **2009**, *407*, 5417-5427.
- (9) De Samber, B., Laforce, B., Ed.: Ghent, 2018.
- (10) Laforce, B.; Masschaele, B.; Boone, M. N.; Schaubroeck, D.; Dierick, M.; Vekemans, B.; Walgraeve, C.; Janssen, C.; Cnudde, V.; Van Hoorebeke, L.; Vincze, L. *Analytical Chemistry* **2017**.
- (11) RaySpec. 2017.
- (12) Patterson, B. M.; Campbell, J.; Havrilla, G. J. *X-Ray Spectrometry* **2010**, *39*, 184-190.
- (13) Patterson, B. M.; Havrilla, G. J. *American Laboratory* **2006**, *38*, 15-22.
- (14) Kanngießer, B.; Malzer, W.; Reiche, I. *Nuclear Instruments and Methods in Physics Research Section B: Beam Interactions with Materials and Atoms* **2003**, *211*, 259-264.
- (15) Kanngießer, B.; Malzer, W.; Rodriguez, A. F.; Reiche, I. *Spectrochimica Acta Part B: Atomic Spectroscopy* **2005**, *60*, 41-47.
- (16) Mantouvalou, I.; Wolff, T.; Seim, C.; Stoytschew, V.; Malzer, W.; Kanngießer, B. *Analytical Chemistry* **2014**, *86*, 9774-9780.
- (17) Smolek, S.; Pemmer, B.; Fölser, M.; Streli, C.; Wobrauschek, P. *Review of Scientific Instruments* **2012**, *83*, 083703.

- (18) Smolek, S.; Streli, C.; Zoeger, N.; Wobrauschek, P. *Review of Scientific Instruments* **2010**, *81*, 053707.
- (19) Węgrzynek, D. *X-Ray Spectrometry* **2001**, *30*, 413-418.
- (20) Dierick, M.; Van Loo, D.; Masschaele, B.; Boone, M.; Van Hoorebeke, L. *Journal of X-ray science and technology* **2010**, *18*, 451-461.
- (21) Jochum, K. P.; Pfänder, J.; Woodhead, J. D.; Willbold, M.; Stoll, B.; Herwig, K.; Amini, M.; Abouchami, W.; Hofmann, A. W. *Geochemistry, Geophysics, Geosystems* **2005**, *6*, n/a-n/a.

## Chapter 5

# Applications of HERAKLES

The scientific relevance of a new instrument is best demonstrated by the amount and versatility of the performed experiments. Not only some long term collaborators, but also several new research groups have made use of the HERAKLES 3D X-ray scanner. Next to the busy experimental schedule on HERAKLES, the number of different scientific fields these experiments originate from is a second indication this type of instrument has without doubt its place in the instrument park of a research group focusing on X-ray based imaging techniques. HERAKLES has been used during these collaborations to scan samples from geology, biology, ecotoxicology, biomedical sciences, cosmology, archeology, material sciences, etc.

This chapter illustrates representative case studies selected from the various experiments performed throughout this PhD project. Using these examples, the usability of the HERAKLES 3D X-ray scanner for microscopic analysis of a wide variety of samples is demonstrated. The analysis of micro-krystites and micro-meteorites, an additional example, will be given in Chapter 7 which discusses the complementarity of different analytical methodologies and the added value of multi-method research, with a focus on the combination of laboratory with synchrotron radiation based measurements.

## 5.1. Ecotoxicology: *Daphnia magna* model organism

*Daphnia magna*, a small freshwater crustacean, has been studied earlier by the XMI group in collaboration with the Ghent University Laboratory of Environmental Toxicology and Aquatic Ecology, resulting in a substantial knowledge regarding the sample preparation and trace-level elemental microanalysis of this model organism. The dimensions of the *D. magna* organism are perfectly compatible with the resolution of the HERAKLES scanner and the elements of interest (among others Ca, Fe, Cu, Zn) are ideally suited for XRF analysis. Furthermore, biological samples pose less limitations and challenges for 3D XRF analysis (e.g. due to limited self-absorption) compared to other sample/matrix types (e.g. some highly attenuating geological samples). The *Daphnia magna* was selected as the first “real life” sample to be measured once the scanner was being commissioned. This test case was used to demonstrate the capabilities of the new HERAKLES 3D X-ray scanner when analyzing the internal morphology and elemental distributions within biological samples. The samples have been chemically fixated according to the procedure described by De Samber et al., which was first used for their synchrotron radiation based experiments combining micro-CT with three dimensional XRF.<sup>1,2</sup>

In our test experiments, the usual procedure for a combined XRF- $\mu$ CT measurement on HERAKLES was employed. First the three dimensional morphology of the sample has been visualized using  $\mu$ CT. Figure 5-1 represents a rendering of the *D. magna* sample, clearly showing some of the reproductive eggs and internal organs. Since the sample was relatively large ( $\approx 4$ mm high) a three dimensional scan of the complete organism using the 3D XRF techniques would have been very time consuming (timescale  $\geq 1$  week). Hence, it was opted to investigate one virtual slice of the sample with respect to its elemental distribution. In Figure 5-1 the location of this slice is indicated by a red dotted line.



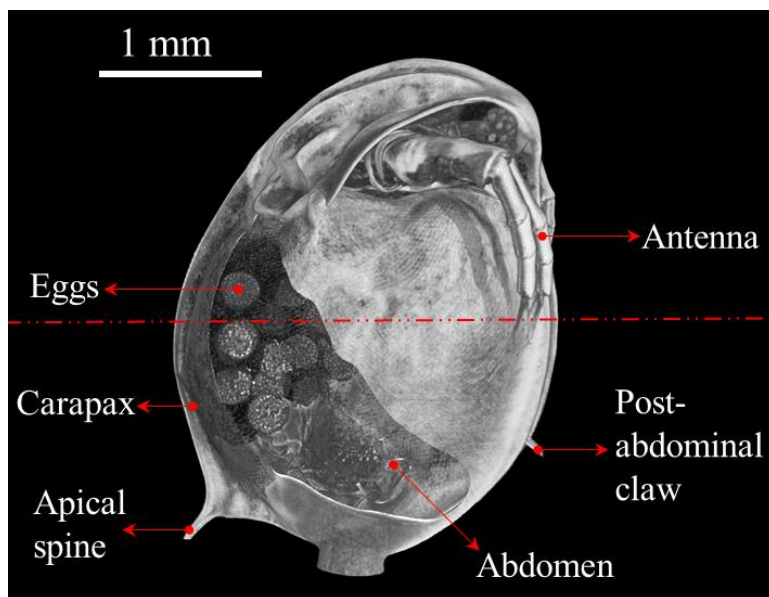


Figure 5-1 Rendered image of 360°  $\mu$ CT scan on a *Daphnia magna* (1501 projections, 500 ms exposure time, 70 kV, 3W); the dotted red line indicates the position of the XRF-CT scan.

Using the automated sample transfer to move the *D. magna* from the  $\mu$ CT stage to the confocal XRF end-station, a confocal mapping of one virtual slice was performed with 30  $\mu$ m scanning step size. Next, the sample was moved towards the XRF-CT setup for a second XRF analysis of the same virtual slice with comparable resolution. The scan settings were optimized to obtain good resolution within a feasible measurement time (each scan took more than 24 h to complete). Figure 5-2 shows the red-green-blue (RGB, Fe-Ca-K) images of the confocal XRF measurement (a) and the XRF-CT analysis (b), overlaid with their corresponding virtual slice from the  $\mu$ CT experiment. For the confocal XRF measurement, this is exactly the slice selected using the rendered  $\mu$ CT scan, however, a misalignment of 70  $\mu$ m was observed for the XRF-CT setup, causing a virtual slice slightly lower in the organism to be analyzed. This mismatch shows the importance of regular recalibration of the setup, to keep the reference positions of the different experimental end-stations up to date.

In the XRF virtual slices, the Ca signal outlines the organism, due to the calcium-rich structure of its carapax. Internally, some organs (e.g. the

gills) also show an elevated Ca content. K is mainly present in the internal organs of the daphnia, with an elevated presence in the eggs, which is most clearly visible in the XRF-CT virtual slice. Furthermore, iron is also predominantly present in the eggs and some internal structures of the model organism. In their study, De Samber et al. found similar elemental distributions for calcium and iron, but they did not report on potassium.<sup>1-3</sup> Another study of Kawasaki et al did investigate the elemental composition of daphnia eggs and reported an elevated K concentration, especially in or around the embryo.<sup>4</sup>

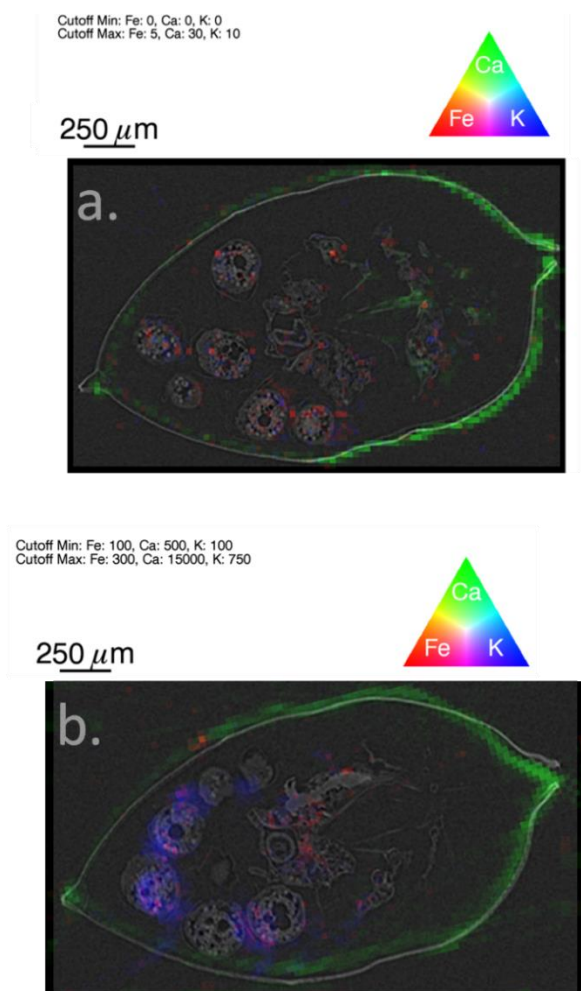


Figure 5-2 RGB (Fe/Ca/K) XRF image overlaid with  $\mu$ CT virtual slice for a. Confocal XRF (40 kV, 0.8 mA, 30  $\mu$ m step size, 10 s LT) and b. XRF-CT (360° rotation, 40 kV, 0.8 mA, 30  $\mu$ m step size, 10 s LT, 90 projections); due to misalignment of the setup, the images are not identical.

When comparing the two XRF techniques, it is apparent the XRF-CT measurement yields a more intense signal than the confocal XRF measurement; however, due to the very low background signal and the absence of reconstruction artifacts in the latter technique, the amount of information that can be extracted is quasi equivalent, as was the total experiment time. In this specific application (virtual slicing of a biological sample with comparable dimensions along x and y axis) XRF-CT would be the preferred analysis technique, however, there are many other possible scenarios where confocal XRF would perform best (e.g. large, thin multi-layered samples).

It should be noted that the lower eggs of the XRF-CT slice do not perfectly align with the  $\mu$ CT slice. During earlier experiments using these freeze-dried samples, it was noted that the eggs are prone to shifting when the sample is moved suddenly. A slow acceleration for the motor movements has to be employed to avoid this kind of damage to vulnerable samples in the future. However, the high risk of damaging vulnerable samples while moving them is yet another incentive for the development of multi-modal instrumentation, which limits the number of sample-transfers.

As discussed in section 3.1.2. on the different types of tomographic reconstruction algorithms, iterative reconstruction procedures are better suited for XRF-CT reconstruction than the filtered back-projection as was used to generate the image shown in Figure 5-2. When comparing FPB to the maximum likelihood algorithm as an example of an iterative technique (Figure 5-3) it is clear the second algorithm yields a better result, with reduced streak artefacts. Currently, an associated project is working on the development of dedicated reconstruction software for the HERAKLES scanner, incorporating several algorithms, which should allow the selection of the optimal reconstruction methodology when analysis integrated  $\mu$ CT – XRF-CT data sets in the future.

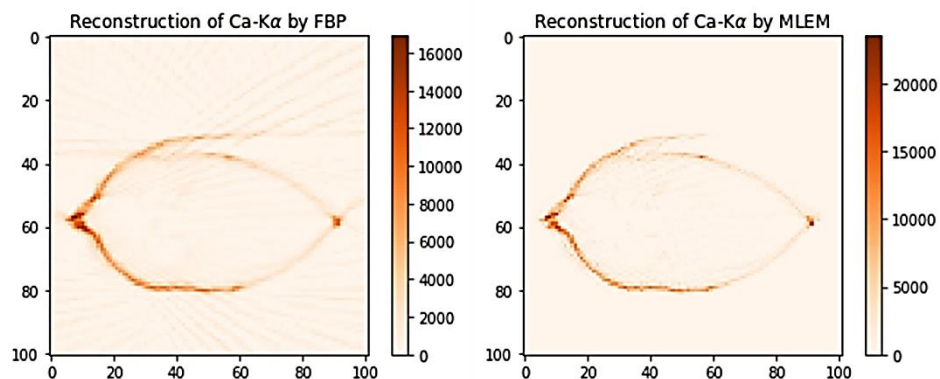


Figure 5-3 Comparison of FBP reconstruction (left) and maximum likelihood algorithm with 2000 iterations (right) for the  $\text{Ca-K}\alpha$  signal of the described *Daphnia* experiment ( $360^\circ$  rotation, 40 kV, 0.8 mA,  $30\ \mu\text{m}$  step size, 10 s LT, 90 projections).

## 5.2. Catalysis: Expanded perlite support material

Treatment of waste gas flows, both small scale such as in car exhaust systems as on an industrial scale, is a pressing issue due to environmental and climate concerns. For an industrial installation, bio catalysis poses an interesting possibility since it has several advantages over classical solutions.<sup>5</sup> A biocatalyst (bacterial or fungal) can be operated without the need for high pressure or temperature, making them energy efficient.<sup>5</sup> Furthermore, no dangerous chemicals are needed to run the process. A biocatalyst removes the pollutants by using them as nutrients, altering their chemical composition and thus effectively destroying them, while the classical waste flow treatments merely transfer the pollutants from one medium to another.

In order for these bacteria or fungi to grow, a support material is needed. Next to structural support and the necessary strength to keep the catalyst mechanically stable, these materials also provide a catalyst bed, regulating amongst others the transport phenomena governing the performance of the catalysts.

Perlite is a naturally occurring siliceous volcanic glass. When quickly heated to high temperatures, it drastically increases in volume.<sup>6,7</sup> Expanded perlite has multiple applications in sectors such as

construction, agriculture and the chemical industry.<sup>6-9</sup> It has already been implemented as support material for heterogeneous catalysis<sup>7</sup> and during the study discussed during this section its possible use as support for a fungal bio catalyst for hexane treatment was examined.

The goal of the X-ray based analysis of the expanded perlite support material was to determine the presence of the biofilm inside the particles. Both  $\mu$ CT and XRF were used to this extend, the  $\mu$ CT using the difference in X-ray attenuation to image the biofilm and estimate its relative volume, while several XRF methodologies were employed to analyze the elemental composition. The first step in practically any analysis using the HERAKLES scanner is performing a  $\mu$ CT scan. Although the expanded perlite is very porous and has a low density, the relatively high atomic number of the constituting elements of its geological raw material still make it quite attenuating. Hence, a high voltage (70 kV) was used, combined with the Radeye detector due to the thicker scintillator on this detector. The X-ray tube was used at a power level of 3 W for the scans. Each scan had 1530 projections with 500 ms acquisition time. Figure 5-4 shows a slide through the center of two perlite particles. The one on the left is a “blank” sample, which is an unused support particle, while on the right a used particle is shown. The highly porous, candy floss-like structure of the expanded perlite can clearly be seen. It is due to this porosity that this material makes an excellent support for the biofilm, which can reside inside the perlite structure as can be seen on the right. There a large portion of the pores are filled with a second phase (i.e. the biofilm) which attenuates less than the perlite structure.

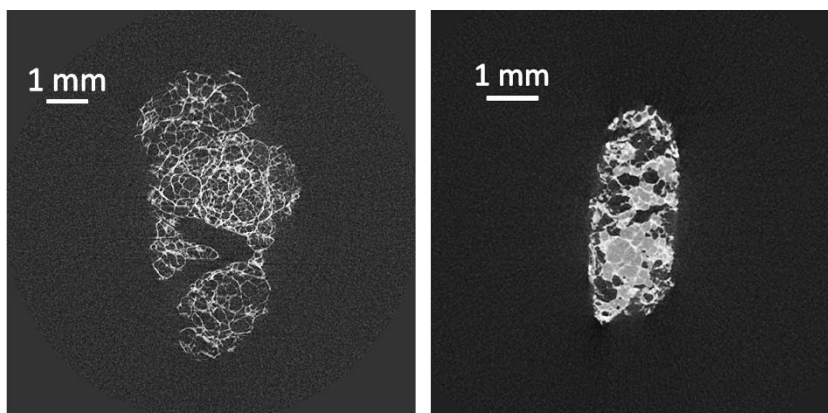


*Figure 5-4  $\mu$ CT slice through the middle of a perlite particle (Radeye, 70 kV, 3 W, 1530 projections, 500 ms). On the left is a blanc (unused) perlite particle, while on the right a used particle is shown. The fibrous structure of expanded perlite is nicely demonstrated in the blanc sample, while the biofilm filling the pores can clearly be discerned on the right.*

To estimate the amount of biofilm present in the pores of the used perlite, several sets of samples were analyzed using  $\mu$ CT, each set containing between 8 and 11 samples. The selected sets were: blanc (non-used perlite), perlite sampled at the “gate2” catalyst extraction position of the experimental reactor and perlite sampled at the “gate3” position. The used perlite was extracted at two different time points, being 20 days and 277 days after start-up of the reactor. Using the Octopus Analysis software package, the porosity (as a percentage of the total volume) of each scanned sample was calculated and an average for each category was determined. In fact, what was calculated was the portion of the sample which was not pore, but “matter”, being either perlite or biofilm. Using the measurements on the blank group, the expected value of the percentage perlite in a particle was estimated. By subtracting this value from the used samples, the percentage of the total volume which is biofilm could be determined.

For the blank sample, on average 25.2 % of its volume consisted of solid perlite, hence the porosity can be calculated to be about 74.8 %. In literature, the porosity of expanded perlite is given as 79 % which is quite close to the value found through the current procedure.<sup>10</sup> When

comparing the results shown in Figure 5-5 it is evident the blank sample has the lowest amount of material, as was expected, followed by the gate2 position and the pores at the gate3 position are smallest. The difference between two data sets of the same position at a different time point is too small to be significant, although in both cases a small increase in the biofilm can be seen at the later time. It can be concluded  $\mu$ CT is a feasible technique to assess the presence and the amount of biofilm in this type of support materials.

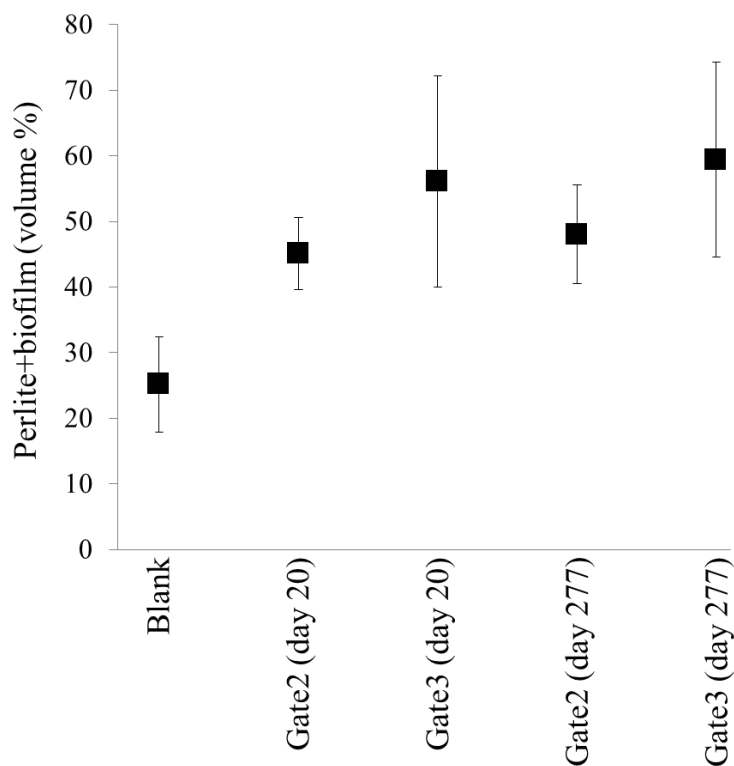


*Figure 5-5 Volume percentage of the perlite structure+biofilm determined using  $\mu$ CT for unused (blank) and used perlite. The used perlite was extracted at two positions (gate2 and 3) and two different time points. Each point is the mean of ten individual measurements, with  $2\sigma$  error bars.*

Next to  $\mu$ CT, XRF analysis was used to extract elemental information from the expanded perlite particles. Several methodologies were employed, being conventional XRF using the HERAKLES scanner, conventional XRF under vacuum conditions using the EDAX Eagle-III and XRF-CT at HERAKLES.

The first conventional scans using HERAKLES had three main aims. Namely, 1) identifying the elements present in the samples 2) assessing the heterogeneity of the elemental distribution throughout the particles using a 2D overview and 3) locating a representative position to perform an XRF-CT scan. Figure 5-6 gives the result of such an overview scan on a gate2 (day 20) sample, on the left a transmission image is given, while on the right an RGB (Fe/Si/Ca) image of the sample is shown. Clearly, Si forms a major component of the glass matrix of the perlite sample, while Fe and Ca rich regions are dispersed in the form of small inclusions throughout the sample.

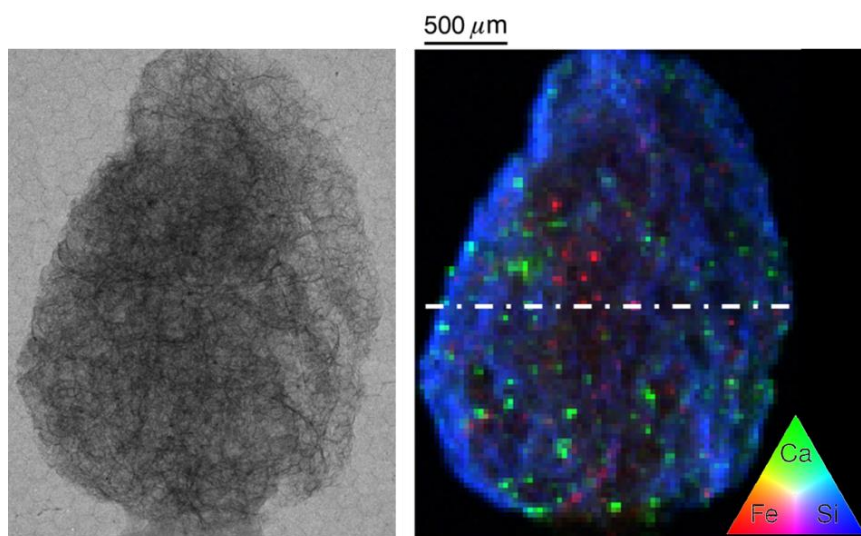


*Figure 5-6 Transmission image and conventional XRF based RGB image (Fe/Ca/Si) of a gate2 (day 20) particle. XRF settings: XRF-CT setup in dual detector mode, 40 kV, 0.6 mA, 4 s LT, 30  $\mu$ m step size*



The sum spectrum of the given scan is represented in Figure 5-7 and can be used to examine the composition of the sample in more detail. A lot of elements can be discerned, the major elements being Si, K, Ca, Ti and Fe. A central slice was selected for XRF-CT analysis to investigate the depth distribution of the different detected elements, mainly focusing on elements linked to the biofilm (e.g. K and S). The position of this slice is indicated by the line in Figure 5-6.

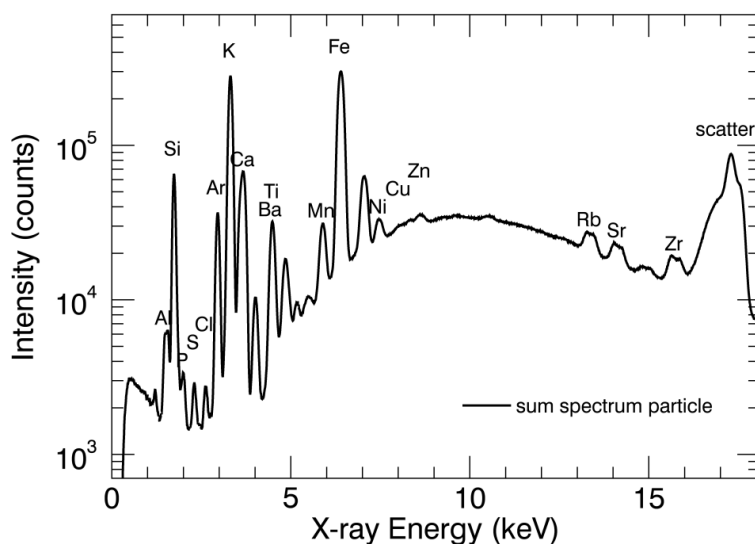


*Figure 5-7 Sum spectrum of the XRF mapping shown in Figure 5-6. XRF settings: XRF-CT setup in dual detector mode, 40 kV, 0.6 mA, 4 s LT, 30  $\mu$ m step size*

The result of the XRF-CT scan at the position indicated in Figure 5-6 can be seen in Figure 5-8. This figure also incorporates a virtual slice of the  $\mu$ CT at the same height in the sample. To image the perlite structure in the XRF mapping, the Compton scatter signal (green) was selected, giving a very good agreement with the  $\mu$ CT slice. Additional elements included in the RGB image are K (blue) and Fe (red). Potassium (K) is a main nutrient component for the biofilm and hence a possible indicator element, while Fe was present in a lot of small hotspots on the overview scan. The  $\mu$ CT image shows a small bright spot in one of the major cavities of the perlite structure. This proves to be an Fe-rich inclusion. K

is only found on the outer surface of the perlite particle, however, this might be due to self-absorption effects. Indeed, the absorption length of K in expanded perlite is only about 100  $\mu\text{m}$ .

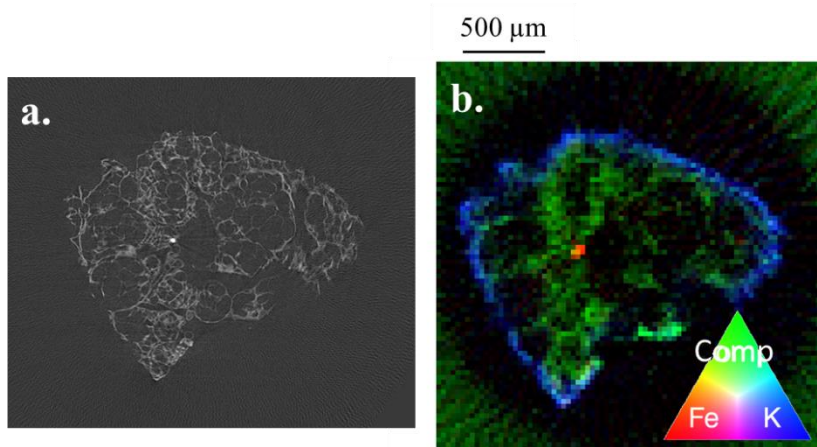


*Figure 5-8 Reconstructed virtual slice of a)  $\mu\text{CT}$  (Radeye, 70 kV, 3 W, 500 ms, 1530 projections) and b) RGB (Fe/Compton/K) image of virtual slice by XRF-CT at corresponding position (40 kV, 0.6 mA, 4 s LT, 30  $\mu\text{m}$  step size, 90 projections)*

The negative effects of self-absorption will be even more pronounced for Si and S, two other major elements of interest, since these have an even lower atomic number than K. To resolve this issue, several perlite particles were embedded in two component epoxy resin (EpoFix Resin + Epofix Hardener, Struers GmbH, Maassluis, the Netherlands) and grinded until their interior was positioned on the surface of the resin block using the Struers LaboPol-5. A conventional 2D XRF scan could then give direct information on the interior of the expanded perlite particles. However, this solution comes at a price: the technique is no longer strictly non-destructive and due to the relatively thick layer of epoxy surrounding the sample, no  $\mu\text{CT}$  could be performed on the embedded samples. The presence of surrounding epoxy makes it impossible to differentiate between resin and biofilm, with epoxy resin now filling large parts the pores in the perlite structure. Furthermore, there is the risk of the resin having an effect on the biofilm. It could change its shape and composition, dissolve the biofilm or interfere with

the XRF signal. Two observation justify the use of resin to fixate the particle. First of all, it was noticed the resin did not penetrate into the pores of the perlite particles, which minimizes its possible effects on the interior structure of the expanded perlite or the biofilm. Secondly, no detectable elements were found leaching out of the perlite particle, which could be expected when some elements are being dissolved in the resin.

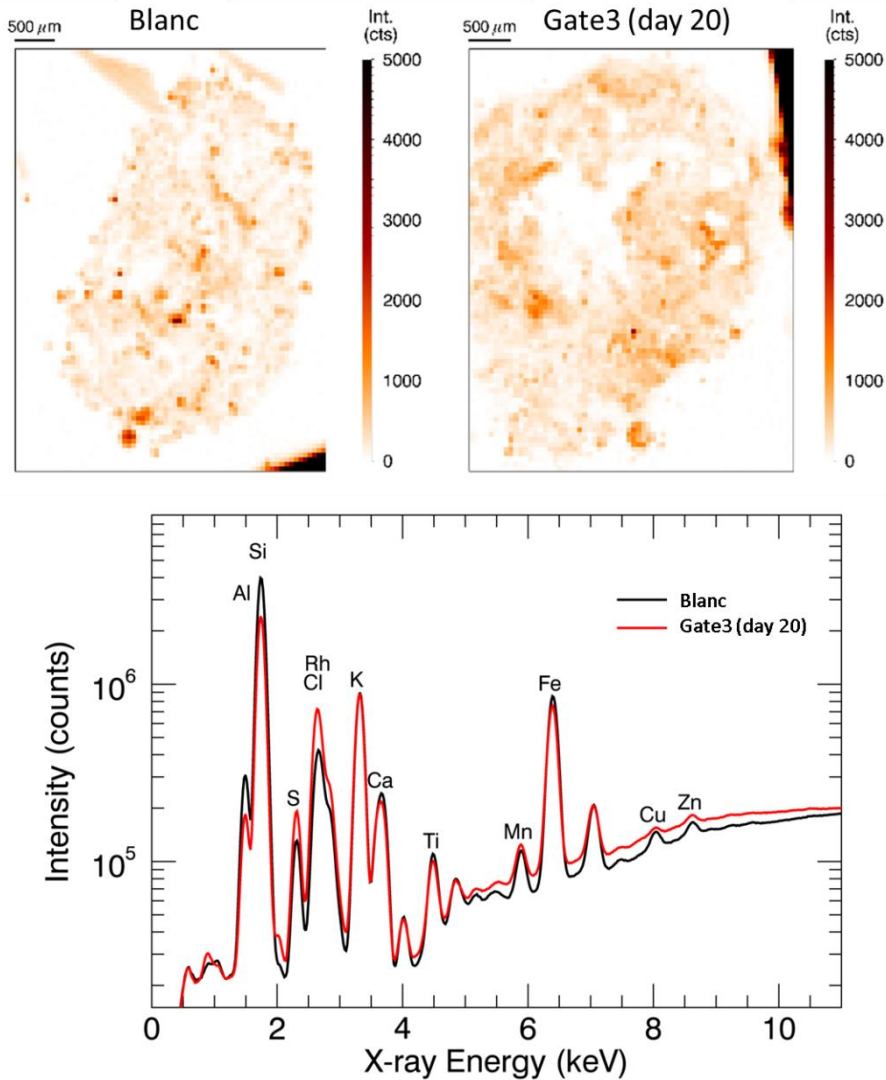


Figure 5-9 S-K $\alpha$  map for blanc (left) and used (right) perlite particle (40 kV, 80  $\mu$ A, 10 s LT, 60  $\mu$ m step size). Although both samples contain S, the used particle has a little more as can be seen in the comparison of the Compton scatter normalized sum spectra.

These 2D XRF scans (Figure 5-9) were not performed at the Herakles 3D X-ray scanner but using two other lab scale setups: an in-house developed monochromatic micro-XRF instrument for preliminary scans and an EDAX Eagle III scanning micro-XRF spectrometer for scans under vacuum conditions. The latter was much more sensitive towards the light elements compared to the two other XRF instruments working in air. Although these scans were not performed at HERAKLES, their results are presented for completeness.

Figure 5-9 shows the S- $K_{\alpha}$  maps of a scan on a blank expanded perlite particle and a used perlite spherule (taken from gate3 on day 20 of the experiment). Sulphur being an indicator element for bio-material, it was expected to be detected in higher concentrations in the used sample. However, this is not really obvious in the mappings themselves, but it can be seen in the Compton scatter corrected sum spectra of the scans which are also pictured in the figure. Based on their sum spectrum it could be calculated that the S- $K_{\alpha}$  signal in the used perlite particle was 1.7 times as intense (in  $\text{cts.pixel}^{-1}.\text{s}^{-1}$ ) as the intensity in the blank sample, indicating the presence of biofilm.

### 5.3. Layered samples in cultural heritage

In a lot of applications, layered samples play an important role. A classic example is the analysis of cultural heritage objects such as paintings, where the presence of multiple coats of paint poses a challenge when trying to characterize the bottom layers.<sup>11</sup>

During a study in collaboration with Claudia Conti from the Institute for the Conservation and Valorization of Cultural Heritage in Milan (Italy) we compared the performance of two relatively new, non-destructive chemical analysis techniques with the capability of depth-characterization, being confocal XRF<sup>12,13</sup> analysis and Micro-Spatially Offset Raman Spectroscopy (micro-SORS).<sup>14</sup>

The micro-SORS technique allows the detection of deep Raman photons and has two variants: defocusing and full micro-SORS. The most basic type is the defocussing technique. In fact this methodology can be performed on a conventional Raman spectrograph. By enlargement of the laser illumination and Raman collection area, photons coming from the deeper layers can be detected. The full micro-SORS methodology needs minor modifications to the conventional hardware and/or software to achieve a separation between illumination and collection zones. Full micro-SORS is less widely applicable, but provides a higher penetration depth and discrimination power between layers. For more details on these techniques we refer the reader to the scientific literature.<sup>15-17</sup>

### 5.3.1. Methods

The confocal XRF setup of the HERAKLES instrument was used to perform the XRF analysis. This setup is suited with a Mo anode tube and a large area SDD which are both equipped with polycapillary optics, creating a confocal volume of  $30 \times 30 \times 10$  (XYZ)  $\mu\text{m}^3$ . The reader is referred to Chapter 4 for detailed information on this instrument.

The micro-SORS measurements were performed on a Senterra dispersive micro-Raman spectrometer (Bruker Optik GmbH, Ettlingen, Germany) using both types of micro-SORS. The spectra were recorded with a 785 nm (red) laser in the spectral range between 80 and  $2600 \text{ cm}^{-1}$ . For the defocusing measurements the microscope objective was moved away from the sample surface, while full Micro-SORS spectra were measured using an external Raman probe (UniLabII, Bruker Optik GmbH). This probe was equipped with a  $4\times$  lens (18 mm working distance), delivering the laser beam to the sample (30  $\mu\text{m}$  spot size). The Raman signal was recorded with a Peltier cooled CCD detector of  $1024 \times 256$  pixels. Standard microscope optics were used (Olympus BX51): for the defocussing measurements a  $20\times$  objective and a  $4\times$  objective for full micro-SORS. The laser power ranged from 10 to 100 mW and the acquisition times from 10 to 100 s.

### 5.3.2. Materials

For the comparison of micro-SORS with confocal XRF, several test samples were prepared, their characteristics can be found in Table 5-1.

S1 is composed of a paper support with three layers of acrylic paint made resp. of red ochre (which is rich in ferric oxide), titanium dioxide and bismuth yellow applied. S2 also has a sequence of acrylic paint layers on a carbonatic stone support, the pigments being cadmium red, zinc white and cobalt blue. S3 is a thin metal foil (brass: Cu, Zn) placed on a paint layer of lead white paint on top of a gypsum substrate. S4 is made by two acrylic spray paint layers on a carbonatic stone support. The paints of S4 do not contain metallic components.

*Table 5-1 Overview of the layerd test samples for confocal XRF and micro-SORS analysis*

	Colour	Pigment(s) Metallic Alloy	or Medium	Fillers and extenders	Layer thickness ( $\mu\text{m}$ )
S1	Layer 1	Red ochre	Acrylic	Calcite, zinc white	36
	Layer 2	Titanium white	Acrylic	Calcite, zinc white, silicates	33
	Layer 3	Bismuth yellow	Acrylic	Calcite, zinc white	167
S2	Layer 1	Cadmium red	Acrylic	Barite	43
	Layer 2	Zinc white	Acrylic	-	158
	Layer 3	Cobalt blue	Acrylic	-	77
S3	Layer 1	Brass			~ 1
	Layer 2	Lead white	Oil		75
S4	Layer 1	Mixture of a monoazo red pigment (PR 170) and a isoindoline pigment (PY 139)	Acrylic	Titanium white	40
	Layer 2	A monoazo yellow pigment (PY 151)	Acrylic		34

The layer thickness of the different parts of these samples was determined prior to the experiments at Ghent University using optical microscopy. The configuration of these samples was specifically designed to create a versatile set of objects, with different support materials, varying types of layers (including paints and thin metal foils) and a wide range of elemental compositions. The main goal of the experiment was determining the performance of confocal XRF and micro-SORS analysis for these various types of samples in order to be able to select to optimal methodology during future experiments and to assess the complementarity of the acquired information. Two parameters were monitored to assess to performance of the techniques, being the depth-resolving power (i.e. how well are the different layers being separated) and the elemental composition found for each layer.

### 5.3.3. Results

The results will focus predominantly on the confocal XRF analysis performed with the HERAKLES scanner. A quick overview of the conclusions that could be drawn from the micro-SORS analysis will be given at the end of this paragraph.

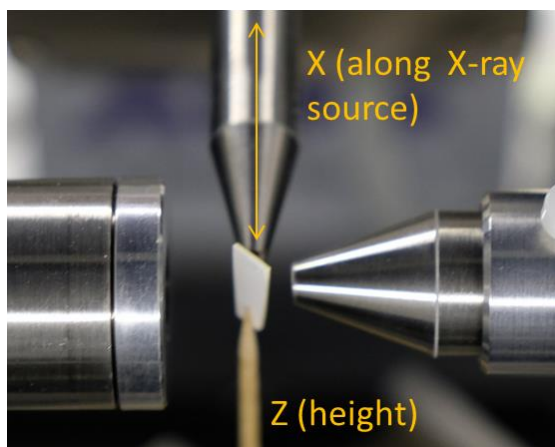


*Figure 5-10 Picture of S1 mounted in the confocal setup of HERAKLES with indication of the used nomenclature for the axis system*

The first sample (S1) has three layers with a mixture of pigments, fillers and an organic binder (Table 5-1). The pigments are red ochre ( $\text{Fe}_2\text{O}_3$ ), titanium white ( $\text{TiO}_2$ ) and bismuth vanadate yellow ( $\text{BiVO}_4$ ). Calcite ( $\text{CaCO}_3$ ), zinc white ( $\text{ZnO}$ ), talc ( $\text{Mg}_3\text{Si}_4\text{O}_{10}(\text{OH})_2$ ) and muscovite ( $\text{KAl}_2(\text{Si}_3\text{Al})\text{O}_{10}(\text{OH})_2$ ) were used as fillers. Figure 5-10 shows the sample mounted in the instrument.

Both line scans (Figure 5-11A) and mappings (Figure 5-11B) were performed using the confocal XRF setup. The layered structure can clearly be discerned. Zn is measured with a slightly elevated intensity throughout the entire sample, which is consistent with zinc white being used in the three paint layers.

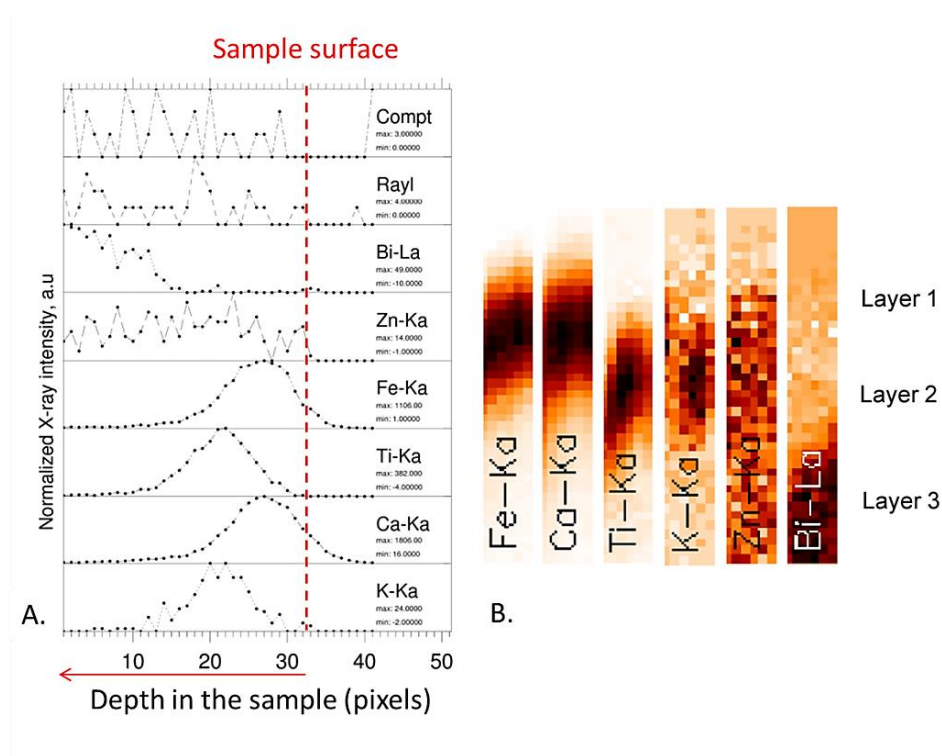


Figure 5-11 (A.) Confocal XRF line scan profiles (40 kV, 0.8 mA, 5  $\mu\text{m}$  step size, 10 s LT) and (B.) mappings (40 kV, 0.8 mA, 5  $\mu\text{m}$  step size in x, 20  $\mu\text{m}$  steps in z, 10 s LT) of the elements detected from the surface to the inner parts of sample S1.



The top layer is rich in Fe and Ca, which is according to its composition, i.e. red ochre combined with calcite. The middle layer has an elevated Ti and K content, being resp. linked to the pigment and the silicate fillers. The third layer has Bi as characterizing element, stemming from the bismuth yellow. Ca is only measured in the topmost layer, but was present throughout the sample. However, due to self-absorption effects, no signal from the deeper layers could reach the detector. This is also the reason why no Si is detected from the second layer or V from the bottom one.

Using the profile of the first layer, an estimation for the layer thickness is made based on the XRF signal. The beginning of the layer is defined using the scatter signal. Outside of the sample, no scatter is detected, making the Compton and Rayleigh intensity ideal markers for the edge of the sample. The internal edge of the top layer is defined by the intersection of the regions with higher Fe and Ti intensity. Between these two borders, there is 50  $\mu\text{m}$ . However, as can be seen in Figure 5-10, the sample is positioned under a  $45^\circ$  angle to the source, necessitating a correction. The estimated layer thickness then becomes 35.4  $\mu\text{m}$ , which is in excellent agreement with the value of 36  $\mu\text{m}$  determined preliminary to these experiments by Dr. Conti.

The second sample (S2) was made of three layers spread on top of a marble block used as substrate. The top layer was cadmium red pigment ( $\text{CdSe}$ ) mixed with barite ( $\text{BaSO}_4$ ) used as filler, zinc white was used for the second position ( $\text{ZnO}$ ) and cobalt blue ( $\text{CoAl}_2\text{O}_4$ ) for the bottom internal layer.

Confocal XRF was again able to detect characteristic elements for each of the three paint layers (Figure 5-12). Barium, cadmium, selenium and a low intensity S signal are the main detected elements at the top position. Zinc dominates the second layer, while cobalt could be detected in the third layer, albeit with a very low intensity. The Compton and Rayleigh scatter intensity can again be used to determine the interface between the sample and the surrounding air.

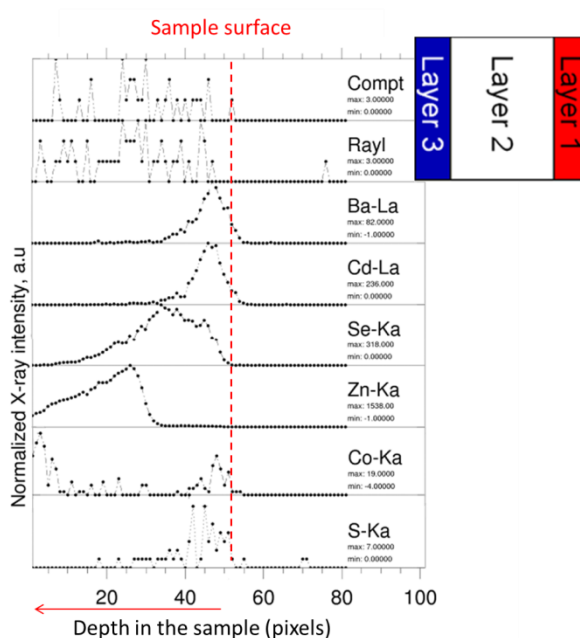


Figure 5-12 Confocal XRF line scan profiles of the elements detected from the surface to the inner parts of sample S2 (40 kV, 0.8 mA, 5  $\mu$ m step size, 10 s LT)

S3 is very different compared to the previous samples, since the top layer is not a paint, but a metal foil (i.e. brass: copper and zinc alloy), put over a lead white paint layer. The substrate is gypsum.

Confocal XRF is able to distinguish the foil from the bulk of the sample, detecting copper and zinc at the very surface (Figure 5-13). The lead scan does not provide a homogeneous view. The presence of a minimum could indicate holes within the lead white layer, which were also detected by SEM imaging as can be seen on the right part of Figure 5-13. Lead is a heavy element, shielding the inner gypsum layer from the incident radiation and attenuating the little fluorescent X-rays that might be produced deep in the sample.

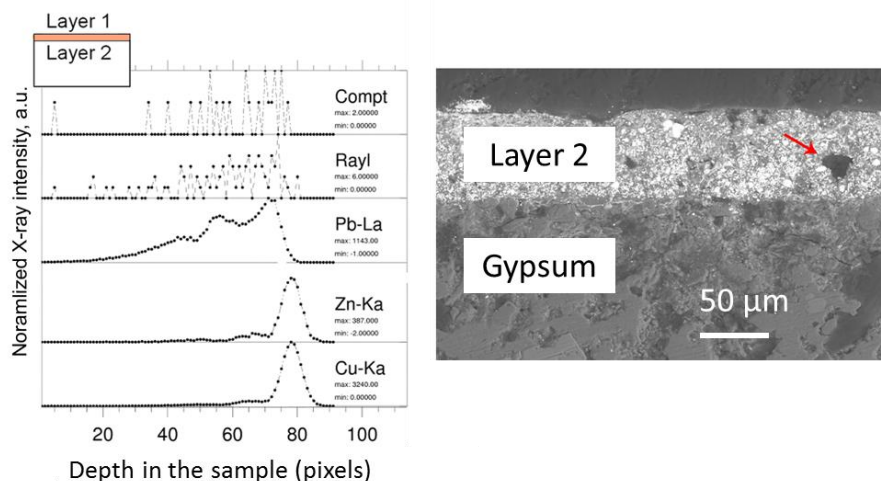


Figure 5-13 Left: Confocal XRF line scan on S3 (40 kV, 0.8 mA, 5 μm step size, 10 s LT) and Right: SEM image of a cross-section from the same sample revealing the presence of holes in the lead white layer

The XRF analysis of S4 can be discussed very briefly. Due to the mainly organic composition of the different layers, with only the fillers containing elements detectable with the confocal XRF setup at HERAKLES, little information could be retrieved. It is a well-known fact that one of the limitations of XRF lies in the detection of low Z elements.

For S1 the micro-SORS maps allowed to closely reconstruct and easily visualize the pigment stratigraphy. The red ochre signal was more intense at image position, and successively rutile, bismuth vanadate and calcite were detected following the correct sequence of the stratigraphy. However, the micro-SORS measurements could not provide information on the zinc white due to its weak Raman scattering cross-section, neither on the silicates used in the middle layer, for the same reason.

Micro-SORS was not able to provide results on S2 due to the high fluorescence generated by the top layer pigment, nor could S3 be characterized. Raman spectroscopy cannot detect the molecular composition of metals, while the thin brass prevented any information to be gathered from the underlying layers.

S4 could be nicely analysed using micro-SORS, revealing the different paint layers and the marble substrate.

It can be concluded confocal XRF analysis and micro-SORS are highly complementary, the one technique being able to analyse samples which yield no information with the other and vice versa. Depending on the used pigments, either XRF or micro-SORS might be the preferred technique, while the presence of (thin) metal foils forces the use of confocal XRF for micro-SORS fails to provide any info in these instances. Finally, organic pigments can only be assessed using micro-SORS, XRF being insensitive towards to main composing elements (C, H, O and N).

## 5.4. References

- (1) De Samber, B.; Vanblaere, S.; Evens, R.; De Schamphelaere, K.; Wellenreuther, G.; Ridoutt, F.; Silversmit, G.; Schoonjans, T.; Vekemans, B.; Masschaele, B.; Van Hoorebeke, L.; Rickers, K.; Falkenberg, G.; Szaloki, I.; Janssen, C.; Vincze, L. *Powder Diffraction* **2010**, *25*, 169-174.
- (2) De Samber, B.; Silversmit, G.; Evens, R.; De Schamphelaere, K.; Janssen, C.; Masschaele, B.; Van Hoorebeke, L.; Balcaen, L.; Vanhaecke, F.; Falkenberg, G.; Vincze, L. *Analytical and Bioanalytical Chemistry* **2008**, *390*, 267-271.
- (3) De Samber, B. W. E.; Evens, R. U.; De Schamphelaere, K.; Janssen, C. L. A.; Ridoutt, F.; Rickers, K.; Falkenberg, G.; Szaloki, I.; Vincze, L.; Wellenreuther, G. (2009) *Hasylab Annual Report 2008* **2009**.
- (4) Kawasaki, T.; Sakata, M.; Namiki, H. *Zoological Science* **2004**, *21*, 1019-1023.
- (5) Mudliar, S.; Giri, B.; Padoley, K.; Satpute, D.; Dixit, R.; Bhatt, P.; Pandey, R.; Juwarkar, A.; Vaidya, A. *Journal of environmental management* **2010**, *91*, 1039-1054.
- (6) Rashad, A. M. *Construction and Building Materials* **2016**, *121*, 338-353.
- (7) Radonjić, V.; Krstić, J.; Lončarević, D.; Jovanović, D.; Vukelić, N.; Stanković, M.; Nikolova, D.; Gabrovska, M. *Russian Journal of Physical Chemistry A* **2015**, *89*, 2359-2366.
- (8) Kotwica, Ł.; Pichór, W.; Kapeluszna, E.; Różycka, A. *Journal of Cleaner Production* **2017**, *140*, Part 3, 1344-1352.
- (9) Sun, D.; Wang, L. *Construction and Building Materials* **2015**, *101*, Part 1, 791-796.
- (10) Celik, A. G.; Kilic, A. M.; Cakal, G. O. *Physicochemical Problems of Mineral Processing* **2013**, *49*, 689-700.
- (11) Alfeld, M.; Broekaert, J. A. C. *Spectrochimica Acta Part B: Atomic Spectroscopy* **2013**, *88*, 211-230.
- (12) Kanngießer, B.; Malzer, W.; Reiche, I. *Nuclear Instruments and Methods in Physics Research Section B: Beam Interactions with Materials and Atoms* **2003**, *211*, 259-264.
- (13) Kanngießer, B.; Malzer, W.; Rodriguez, A. F.; Reiche, I. *Spectrochimica Acta Part B: Atomic Spectroscopy* **2005**, *60*, 41-47.
- (14) Matousek, P.; Conti, C.; Realini, M.; Colombo, C. *Analyst* **2016**, *141*, 731-739.
- (15) Conti, C.; Colombo, C.; Realini, M.; Zerbi, G.; Matousek, P. *Appl. Spectrosc.* **2014**, *68*, 686-691.
- (16) Conti, C.; Realini, M.; Colombo, C.; Matousek, P. *Analyst* **2015**, *140*, 8127-8133.
- (17) Vandenabeele, P.; Conti, C.; Rousaki, A.; Moens, L.; Realini, M.; Matousek, P. *Analytical Chemistry* **2017**, *89*, 9218-9223.

## Chapter 6

# Towards nanometer resolution at ESRF ID16B-NA

One of the main motivating factors in the development and realization of the HERAKLES 3D X-ray scanner was the need to perform preliminary/preparatory studies for (sub)micron spatial resolution synchrotron X-ray imaging experiments and to enhance academic collaborations with applications from diverse scientific fields using various X-ray spectroscopy/imaging based techniques. In case (sub)micron spatial resolution level was required for the application in question, exploratory non-destructive elemental/morphological pre-characterization was performed as a first step of the analysis using one or more of the laboratory instruments available in the XMI laboratories, most certainly once HERAKLES entered its commissioning phase.

Indeed, some scientific questions cannot be answered using laboratory instruments alone, mainly due to a discrepancy between the spatial resolution needed to image the region of interest with high enough detail and the resolution of the instruments available in the lab. In those cases, a synchrotron radiation based setup can resolve the problem. Nowadays multiple beamlines in Europe have a beamsizes below 100 nm (e.g. ID16A<sup>1</sup>, ID16B<sup>2,3</sup> and ID13<sup>4</sup> at the ESRF or P06 at Petra-III<sup>5</sup>), so very small regions of interest can be assessed in great detail.

In the framework of this project, a number of experimental sessions took place at the ESRF in order to perform nanoscale X-ray imaging

experiments in collaboration with our academic partners, most notably at the ESRF nanoanalysis beamline ID16B-NA. This chapter describes applications of nanobeam elemental imaging at ID16B-NA. This new beamline was being commissioned at the beginning of this PhD project and several of our SR based experiments were performed there.

## 6.1. Experimental Setup: ID16B-NA beamline

The ID16 beamline of the ESRF is a new extended beamline with two independent end-stations, ID16A-NI (nano-imaging) optimized for imaging applications with a spatial resolution down to 10 nm<sup>1</sup> and ID16B-NA (nano-analysis) specializing in a wide range of X-ray spectroscopic techniques such as X-ray fluorescence, X-ray diffraction and X-ray absorption spectroscopy with a resolution of 50 nm. The key to the very high spatial resolution of the two ID16 probes is the long distance between the source (i.e. the corresponding undulators in the storage ring of the synchrotron) and the experimental station (>160 m). This results in the potential of a high demagnification of the source which, achieved by a sophisticated KB mirror system, enables spot sizes of the X-ray beam below 50 nm. The experiments in April 2014 were performed with the then available pink beam mode ( $\Delta E/E \approx 10^{-2}$ )<sup>3</sup> having an energy of approximately 17.5 keV. Recent optimization enables a much wider range of X-ray energies to be selected, including monochromatic operation of the beam, which is crucial for certain application such as XAS.

The sample stage is positioned in such a way that the lateral scanning plane is perpendicular to the X-ray beam. A pierced-mirror video microscope with a view along the X-ray beam can be used to monitor the sample positioning and indicate the focal plane of the setup. The configuration of the sample mounting system makes it impossible to position the X-ray detectors under the ideal angle of 90° to the incoming X-ray beam as can be seen in Figure 6-1. Although this unavoidably results in an increased scatter signal (as explained in Chapter 2, Eq. 2.6), the effect is minimized by keeping the setup close to the optimal

geometry by placing the detectors under an angle close to  $90^\circ$  and in the plane of polarization.

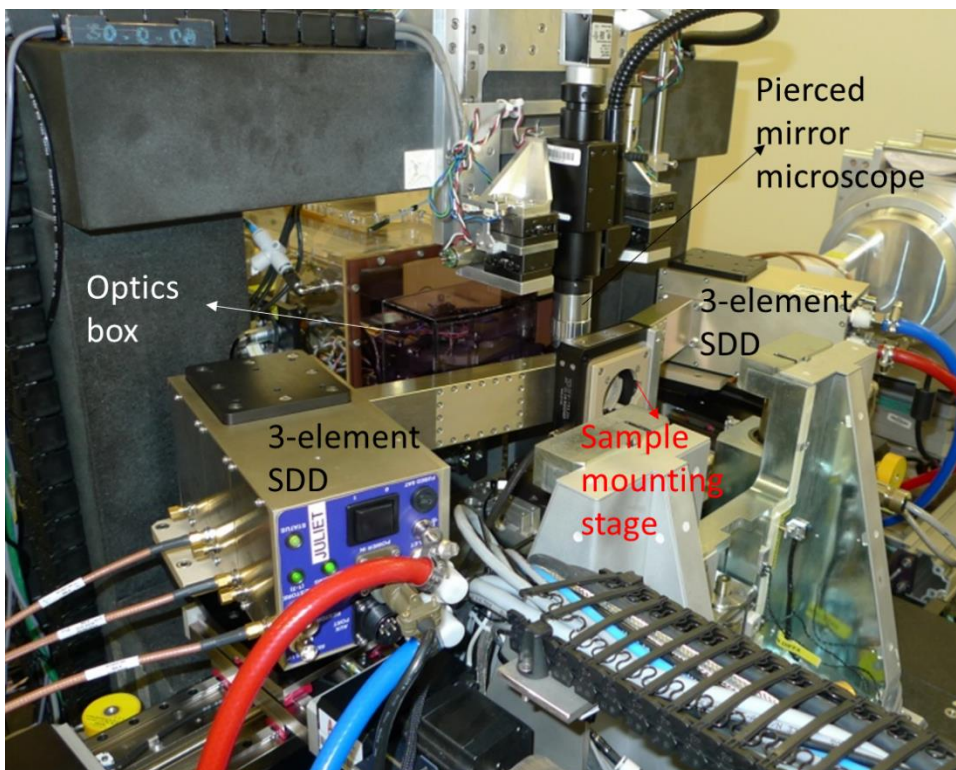


*Figure 6-1 Photo of the ID16B setup with the major components (sample mounting stage, SDD detectors, optics box and beamline microscope) indicated.*

## 6.2. Analytical characteristics during the experiments

At the time of the first experiments described in this section, the beamline was still in the commissioning phase, so further optimization has since improved its properties. Since these were some of the very first experiments on the new ID16B beamline, characterization of the setup was even more relevant than usual, so an important part of the experimental time was allocated to the measurement of reference materials and the determination of the beamsize, which at that stage of



operation of the beamline was not yet as stable and reliable as it is nowadays.

The X-ray beam was characterized using vertical and horizontal knife-edge scans to determine its dimensions. A gold test pattern composed of 20 x 20  $\mu\text{m}$  gold squares (200 nm thick) manufactured at PSI (Switzerland) by Christian David was used for these measurements.<sup>6</sup> The full width at half maximum (FWHM) of the first derivative of an error function fitted to the results of these knife-edge scans was used as beamsizes estimation, resulting in a 59 (horizontal) by 48 (vertical) nm beam. During the beamtime, temporary loss of temperature control led to a sharp increase in beamsizes which is indicative for the stringent temperature control needed when working on the nano-scale. A second beam optimization resulted in a focal spot of 50 by 46 nm (FWHM).

The analytical characteristics of the setup were assessed using three reference materials, being the NIST SRM 1832, NIST SRM 1577b (bovine liver) pressed into a pellet with an areal mass of 7.96 mg/cm<sup>2</sup> (both by the National Institute of Standards and Technology, Gaithersburg (MD), USA) and the AXO thin film XRF reference sample RF8-200-S2453 (AXO-Dresden GmbH, Dresden, Germany). Halfway through the experiment (and after the second beam optimization) the AXO standard was measured a second time to assess the stability and reproducibility of the setup; both scans were virtually identical.

For each reference material an 85 by 90  $\mu\text{m}^2$  area was sampled with steps of 0.85  $\mu\text{m}$  and 0.90  $\mu\text{m}$  respectively (0.1 s real time per point). It should be noted all dwell times mentioned in this chapter are real time values. The resulting point spectra were normalized using an ionization chamber monitoring the intensity of the incident beam right before the KB mirror system. Next all spectra were summed to form a sum spectrum with 1010 s measurement time, which was then rescaled to 1000 s for further analysis. Figure 6-2 gives the spectrum of 10 points summed (1 s real time) and the full 1000 s spectrum measured on the NIST SRM 1832 standard reference material. This spectrum was then analyzed using

AXIL, an iterative least squares fitting procedure to retrieve the XRF line intensities for each detected element.<sup>7,8</sup>

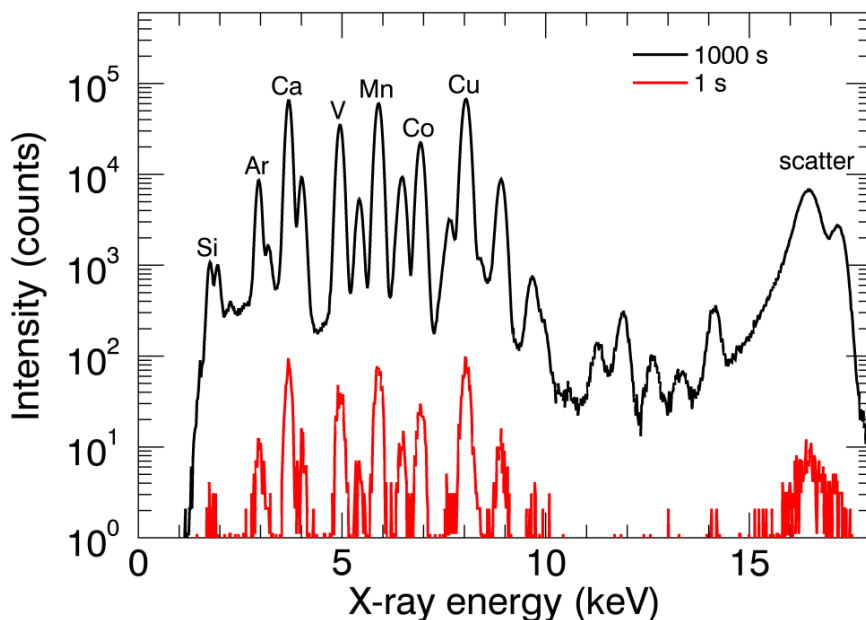


Figure 6-2 XRF spectra of the NIST SRM 1832 standard for 1000 s (black) and 1 s (red) measurement time.

Based on these measurements, the limits of detection (LODs) for all detectable elements present in the reference samples were calculated according to:

$$LOD_i = \frac{3\sqrt{I_b} \cdot C_i}{I_i} \quad (6.1)$$

In this equation,  $LOD_i$  is the limit of detection of element  $i$  in units of concentration  $C_i$ ,  $I_b$  is the background signal intensity determined via the data fitting procedure,  $C_i$  is the certified concentration of element  $i$  in the reference material and  $I_i$  is the measured peak intensity of element  $i$ .

Based on the analysis of NIST SRM 1832, the relative detection limit for Cu is 4 ppm at a measurement time of 1000 s RT. Using the areal density of this reference material and the dimensions of the beam, it can be calculated that this corresponds to an absolute detection limit of 13.6 zg

(i.e.  $^{132}\text{Cu}$  atoms). Next, the DLs were also extrapolated to the more realistic dwell time per pixel of 1 s real time (typically used during the experiments). This gives a value of 112 ppm for the relative DL of Cu. The detection limits for all detectable elements between Si and Cu are given in Figure 6-3.

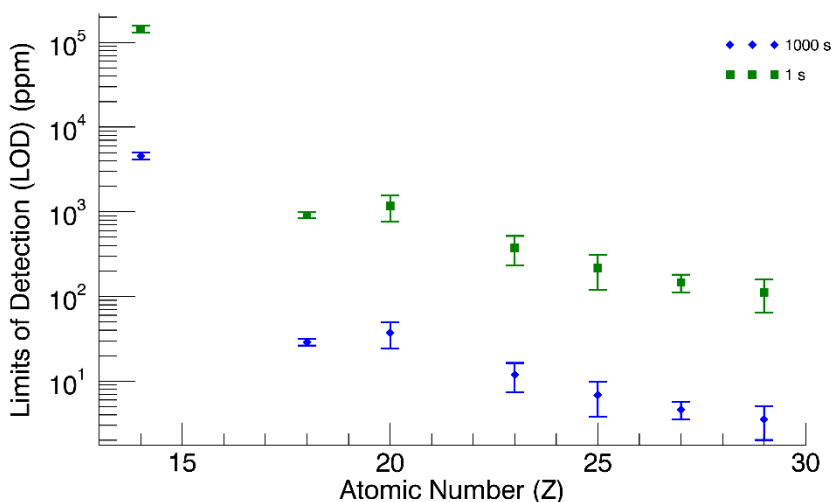


Figure 6-3 Rel. LODs of the ID16B-NA nano-probe for NIST SRM 1832 standard material (April 2014), 1000 s and 1 s measurement time. Please note these data correspond to one of the first experiments at the new ID16B-NA setup, which is still under development, using a single-element SDD detector and attenuated primary beam.

During the last beamtime performed in the context of this PhD research, the NIST SRM1832 was again analyzed. The limits of detection calculated from the latest scan were slightly better than those of the 2014 analysis. The relative limit of detection for Cu at 1000 s RT was now found to be 1 ppm, amounting to an absolute LOD of 3.4 zg, which are only 33 Cu atoms. Figure 6-4 gives the detection limits for 1000 s measurement time for all elements present in the reference material with atomic number between 20 and 29 (i.e. Ca to Cu) with an extrapolation of the results to a measurement time of 1 s. Since the beamline has been further optimized during these last three years of operation and the dual

detector setup could be used during the second experiment an amelioration of the detection limits was expected. The beamsize was also determined during the 2017 experiment. No major change was noted there, the beamsize again ranged around 50 nm.

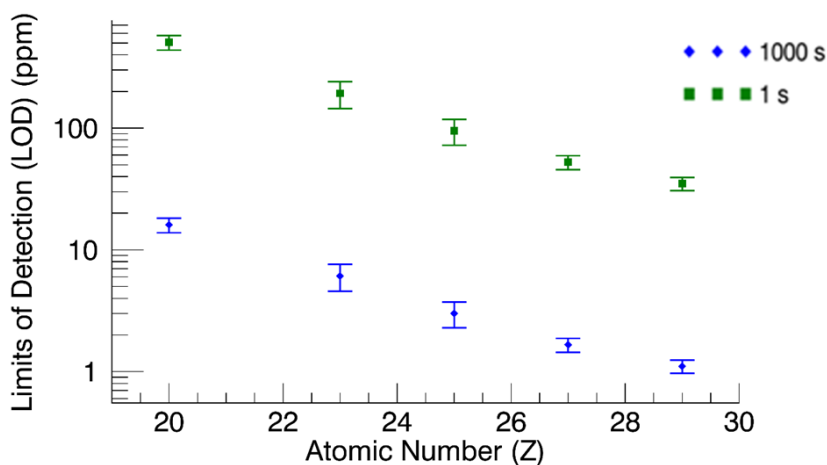


Figure 6-4 Rel. LODs of the ID16B-NA nano-probe for NIST SRM 1832 standard material (October 2017), 1000 s and 1 s measurement time.

### 6.3. First Earth and planetary science applications at ID16B - April 2014

As mentioned above, ID16B is among the most recently completed beamlines of the ESRF, being commissioned with limited user access in March 2014.<sup>2,3</sup> The XMI group had the privilege to perform one of the first experiments at this new beamline in April of the same year, within one month after the first measurements were being performed.

The samples for the initial test experiments included 1) meteorite particles stemming from achondrite Northwest Africa (NWA) 6693 with a series of so-far not characterized inclusions and 2) a deep-Earth diamond with several inclusions, one of which was thought to be a ringwoodite phase. Ringwoodite has only recently been discovered in a

naturally occurring terrestrial material<sup>9</sup>: previously, it was only found in meteoritic materials<sup>10</sup> or had been synthesized in the lab.<sup>9</sup> The size of these samples and, more importantly, the size of the inclusions of interest made nanometer scale resolution of primordial importance for a successful experiment.

Achondrite NWA 6693 has a characteristic composition and a typical igneous texture. The meteorite was found near Amazraou (Morocco) in May 2010 by E. Thompson as a single mass of about 5.1 kg. Based on interrelated features, it is proposed that NWA 6693 is paired with NWA 6704 and NWA 6926. Most often achondrites can be grouped according to their common origin (e.g., originating from the same asteroid), but NWA 6693 appears to be new when compared to other achondrites.

The composition of this sample had previously been determined using reflectance microscopic studies. It is 70% pyroxene, 15% olivine, 13% feldspar, and smaller amounts of accessory phases. Olivine and orthopyroxene are Fe-rich phases. The bubble-like tracks present in the meteorite deserve special interest since some individual “bubbles” are composed of multiple mineral phases, possibly indicating fluids or melts as precursor material. The main phases trapped within the meteorite are Cr-spinel, FeNi metal (awaruite), and FeNi sulfide. During the beamtime, nano-XRF imaging has been used to gain additional information on the elemental composition and distribution of these “bubble” tracks throughout two fragments of the achondrite.

Diamond “Sao Luiz” 05 (SL05) originates from the Juina region in the northwest of the Brazilian Mato Grosso state. There are several river valleys in this region with diamondiferous alluvial deposits, one of these rivers being the Sao Luiz River.<sup>11-13</sup> The XRF imaging experiments on diamond SL05 were focused on the region where preliminary Raman spectroscopy scans yielded results which might indicate the presence of ringwoodite. In order to confirm these findings, additional scans were needed, the first of which was chosen to be an XRF measurement due to the non-destructive nature of this methodology.

### 6.3.1. Sample preparation and mounting

It was a serious challenge to handle the microscopic meteorite particles. To be able to mount them on the beamline setup, they were attached to the tip of a quartz capillary as shown in Figure 6-5, a picture taken with the video microscope of the beamline. The green area in the magnified view indicates the overview map, this area was taken relatively far away from the quartz capillary in order to minimize possible interferences.

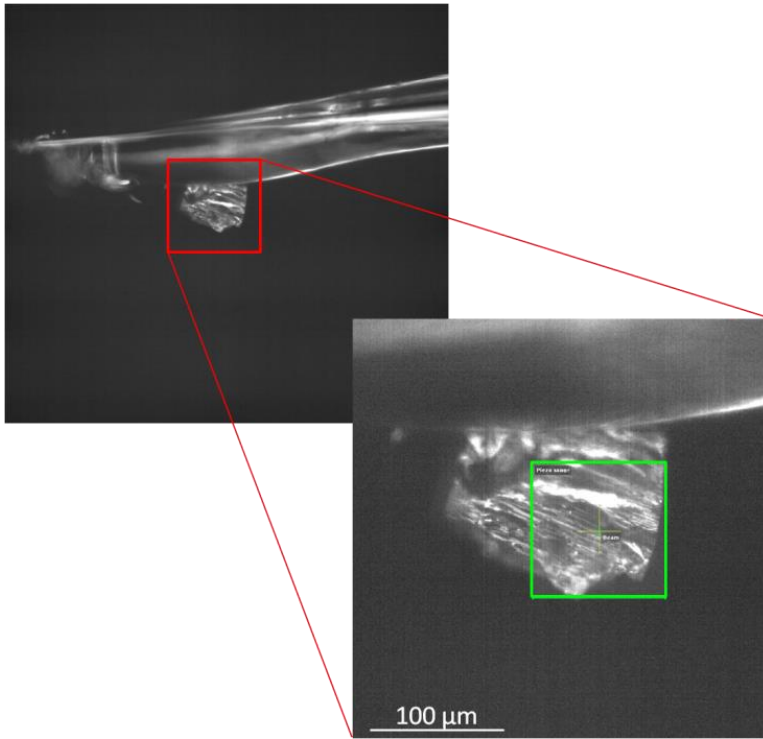


*Figure 6-5 Fragment of NWA 6693 mounted on a quartz capillary, the zoomed in view shows the measured area indicated in green*

The diamond was first cleaned using pure ethanol and an ultrasonic bath and then fixed to a plastic sample holder using wax. Prior to the beamtime experiment, two inclusions were polished with an  $\text{Ar}^+$  ion beam in the laboratory (at Frankfurt University) to bring them closer to the surface of the diamond and minimize the scatter caused by the matrix material. After this  $\text{Ar}^+$  ion beam treatment the two targeted inclusions

were partly on the surface and partly still below the surface of the diamond.

The ID16B beamline setup has a specifically designed sample changing system which enables to switch samples fast and easy while quasi retaining the optimal sample position relative to the focal plane of the nanoscopic X-ray beam. To mount the samples this system uses poly-ether-ether-ketone (PEEK) slides (see Figure 6-6) with a central opening through which the X-rays pass.



*Figure 6-6 Poly-ether-ether-ketone (PEEK) slides for sample mounting at ID16B*

Since the meteorite samples were attached to quartz capillary tips prior to the beamtime, this sample mounting system was not suitable for our experiments. A custom designed system as can be seen in Figure 6-7A was constructed on-site, since no regular solution for mounting this type of sample was present at ID16B at the time; by the time of writing an extra type of mounting head suitable for samples mounted on a pin has been developed by the ID16B staff and is available at the beamline. Due to the bulkiness of the custom designed sample holder system, only one of the two vortex detectors could be used (Figure 6-7B), lowering the detected signal with about a factor of two. However, due to the very high photon flux at this beamline ( $\sim 10^{11}$  ph/s)<sup>3</sup> this was still sufficient to achieve good counting statistics.

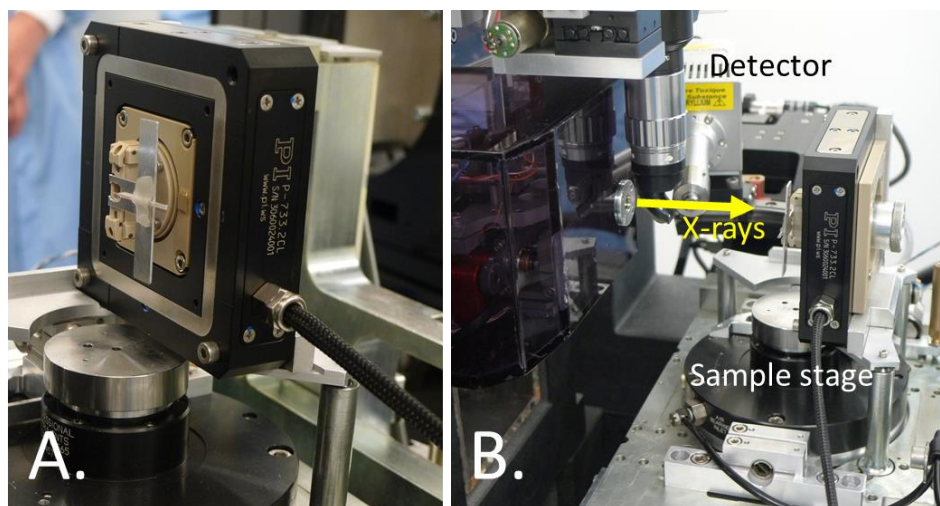


Figure 6-7 (A.) The on-site designed sample mounting system can be seen mounted on the sample stage of ID16B. (B.) The experimental setup of the beamline is shown with the remaining detector (at the far back), the path of the X-rays and the sample stage indicated. The polymer container on the left of image (B.) contains the focussing optics.

## 6.3.2. Results and Discussion

### 6.3.2.1. NWA6693 fragments

Since the feature of interest of the meteorite particles (the so-called “bubble-stream”) could not be discerned on the microscope image from the pierced-mirror beamline microscope, an overview mapping (100 by 100  $\mu\text{m}$ , 100 nm steps, 50 ms real time) was performed to localize regions with an elemental composition deviating from the bulk material. The result of such an overview scan is given in Figure 6-8 for both Ca and Cr, two elements which give a clearly heterogeneous view of the sample. Using the results of this overview scan, several smaller regions of interest were selected for detailed analysis with smaller step sizes (25 – 40 nm) and longer measurements times per point (1 s).



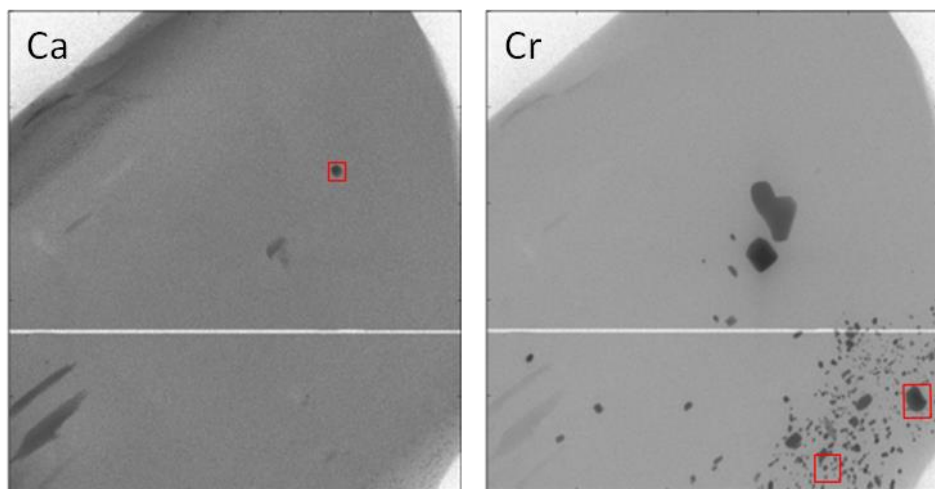


Figure 6-8 XRF Overview map (Ca and Cr signal) of NWA 6693, the 7 by 6 and 5 by 5  $\mu\text{m}^2$  ROIs are indicated on the Cr-image, the 3 x 3  $\mu\text{m}^2$  ROI on the Ca image. Scanned area: 100 x 100  $\mu\text{m}^2$ , beam dimensions: 46 nm (V) x 50 nm (H), step size: 100 nm, measurement time: 50 ms per point.

The main elements detected in the samples of NWA6693 were Ca, Ti, Cr, Mn, Fe, Ni and As in order of rising atomic number. Most inclusions are rich in Cr compared to the bulk of the material, with trace amounts of both Ti and Mn. A few differing inclusions could be detected which had Ni as signature element, with traces of As and Ca.

Previous studies also found Cr and Ni containing materials to be amongst the most common heterogeneities in achondrite NWA 6693.<sup>14,15</sup> The XRF mappings shown in Figure 6-9 are a perfect example of the huge value of this new XRF nano-probe for the analysis of this type of samples (containing sub-micron features). This figure represents a detail mapping of a 5 by 5  $\mu\text{m}$  section of the meteorite which has a wide range of predominantly Cr-rich inclusions of various sizes and one small Ni-rich inclusion. From the mere number of small, partially overlapping features it is apparent the 50 nm resolution was crucial to be able to differentiate the individual inclusions.

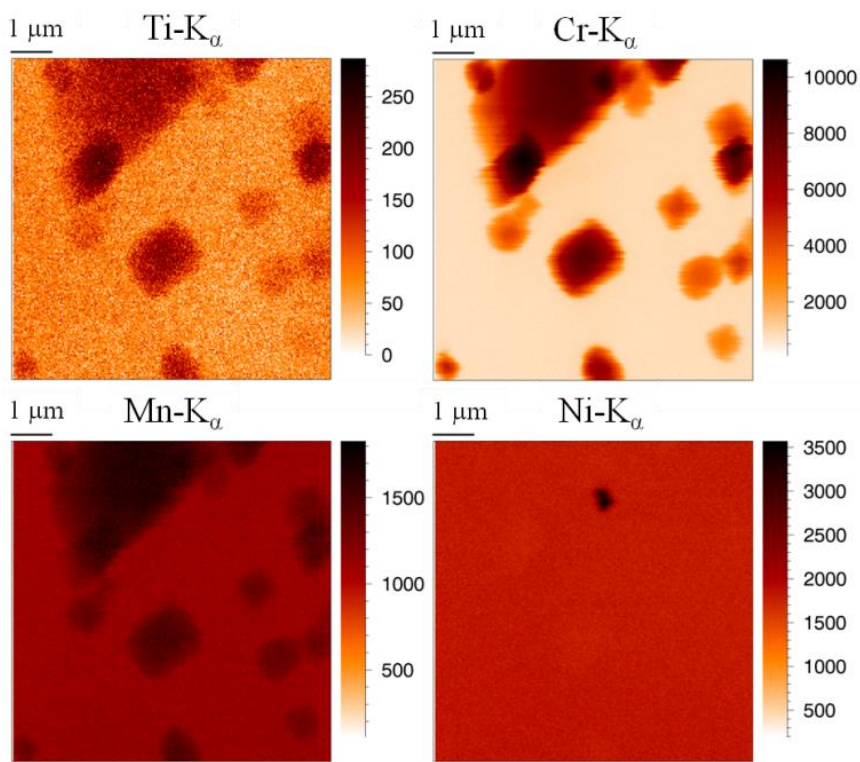
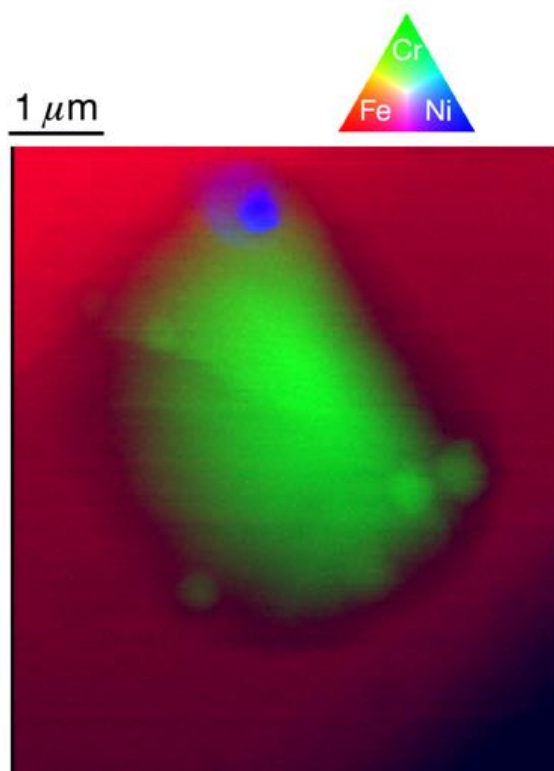


Figure 6-9 XRF mapping of fluid inclusions in NWA 6693, showing the image for Ti, Cr, Mn and Ni. Scanned area:  $5 \times 5 \mu\text{m}^2$ , beam dimensions:  $46 \text{ nm (V)} \times 50 \text{ nm (H)}$ , step size:  $25 \text{ nm}$ , measurement time:  $1 \text{ s per point}$ .

A further demonstration of the capabilities of the new nanoprobe can be given using the red/green/blue (RGB) image showing Fe, Cr and Ni resp. as given in Figure 6-10. According to Warren et al.<sup>14</sup> the main phases forming the meteorite matrix are rich in iron, which is confirmed by the RGB image, where Fe is the main detectable element of the surrounding material. The dimensions of the inclusions in this scan once more aptly demonstrate the huge importance of a nanoscopic beam when investigating this type of samples; larger beams would not be able to differentiate between these particles.



*Figure 6-10 Fe/Cr/Ni RGB image of inclusions in NWA 6693. Scanned area:  $7 \times 6 \mu\text{m}^2$ , beam dimensions:  $46 \text{ nm}$  (v)  $\times$   $50 \text{ nm}$  (h), step size:  $40 \text{ nm}$ , measurement time:  $1 \text{ s}$  per point.*

### **6.3.2.2. Diamond SL05**

Diamond SL05 was examined using the same procedure as the meteorite fragments. Once again an overview scan of  $100 \times 100 \mu\text{m}^2$  was made which was then used to determine a small region of interest for detailed analysis (as indicated in Figure 6-11).

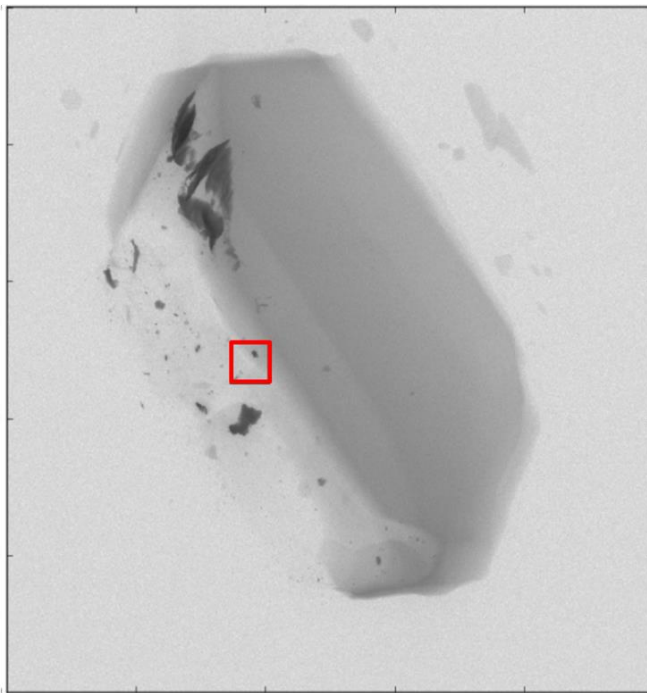


*Figure 6-11 XRF Overview mapping (Fe signal) of diamond SL05, the 7 by 7  $\mu\text{m}$  ROI is indicated. Scanned area: 100 x 100  $\mu\text{m}^2$ , beam dimensions: 46 nm (V) x 50 nm (H), step size: 100 nm, measurement time: 50 ms per point.*

Eight elements were detected in the diamond inclusions, being Ca, Ti, Cr, Fe, Ni, Cu, Zn and As. PCA analysis and k-means clustering<sup>16</sup> showed Cu and Zn to be present as one major inclusion, which also has a Ni-rich region (Figure 6-12). Since Cu and Zn are not typically linked to the deep-earth, it is hypothesized this is a secondary phase which adhered to the diamond somewhere on its journey from the deep-earth to the surface and even contamination cannot be excluded. 3D XRF analysis (i.e. confocal XRF) would yield additional information to confirm this hypothesis, but could not be performed during this experimental period.

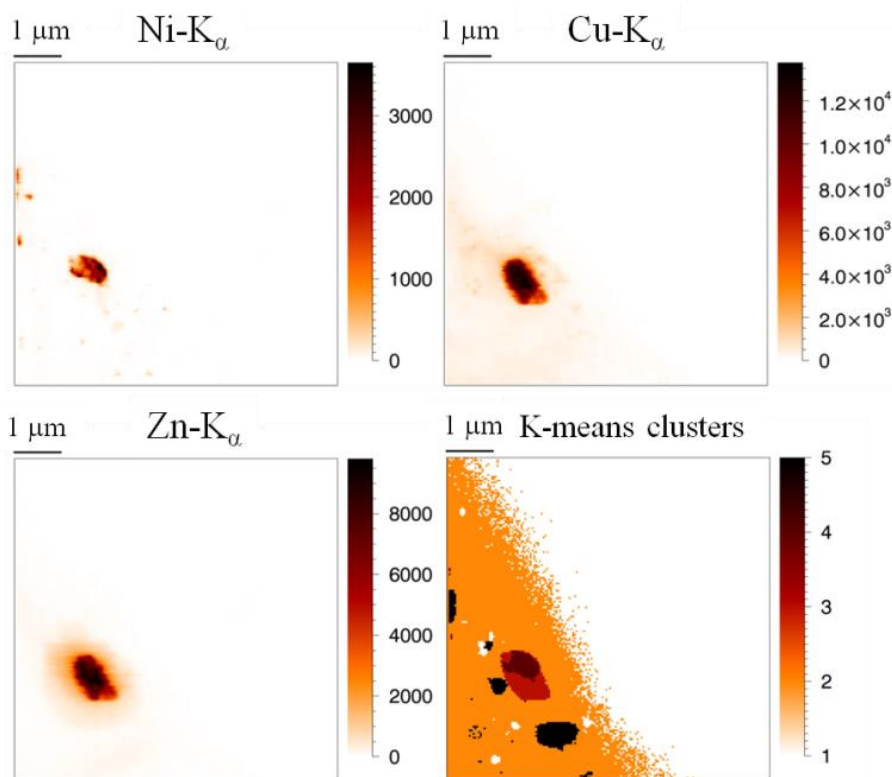


Figure 6-12 XRF mapping for Ni, Cu and Zn, the Cu-Zn-(Ni) particle can be clearly discerned. K-means clustering (bottom right) statistically confirms grouping these pixels as an entity. Scanned area:  $7\ \mu\text{m} \times 7\ \mu\text{m}$ , beam dimensions:  $46\ \text{nm}\ (\text{V}) \times 50\ \text{nm}\ (\text{H})$ , step size:  $40\ \text{nm}$ , measurement time:  $1\ \text{s}$  per point.

Figure 6-13 shows the XRF maps for Ca, Ti, Fe and As. None of these elements show the tendency to be present in the same inclusion. It can also be noted the density of inclusions is not the same throughout the sample, with the highest concentration in the lower-left corner of the mapping. Once again, the importance of a nano-beam for the analysis of this type of materials is evident by looking at the size of the inclusions.

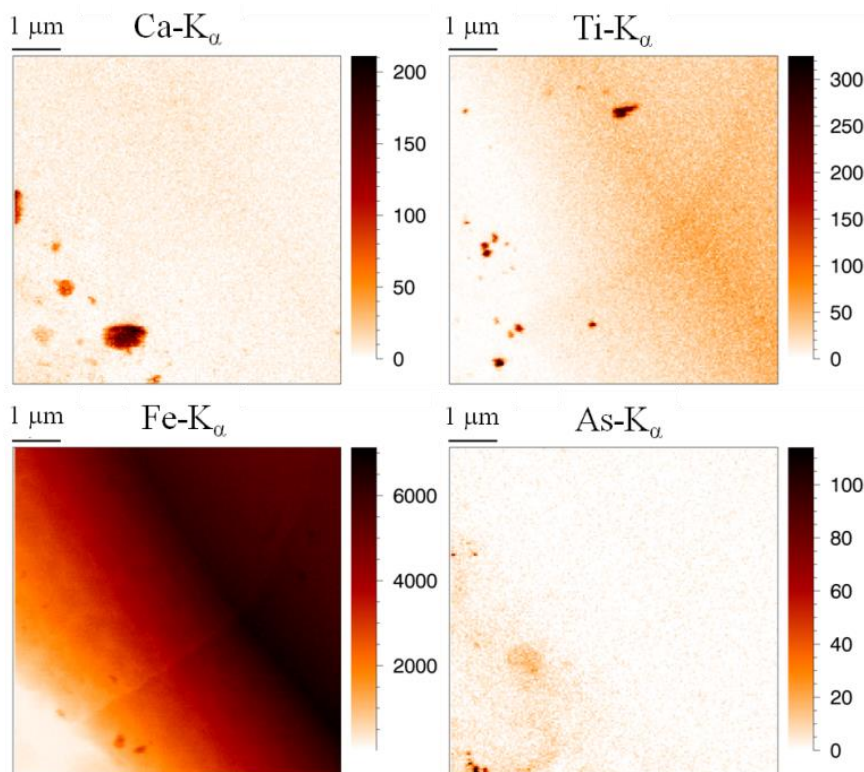


Figure 6-13 XRF map of Ca, Ti, Fe and As. The number of inclusions clearly varies throughout the diamond. Scanned area:  $7\ \mu\text{m} \times 7\ \mu\text{m}$ , beam dimensions:  $46\ \text{nm}\ (\text{V}) \times 50\ \text{nm}\ (\text{H})$ , step size:  $40\ \text{nm}$ , measurement time:  $1\ \text{s}$  per point.

### 6.3.3. Conclusions

This was one of the very first commissioning experiments at ID16B with external users and the first for the XMI group. It immediately proved the enormous progress made in the field of nano-XRF imaging represented by this new setup. With its excellent brilliance and small beamsize it really stands at the forefront of modern-day nano-XRF imaging. The geological samples of this experimental period aptly proved the added value and analytical possibilities of this beamline, with multiple submicron inclusions being perfectly separated and analyzed in detail in a matter of hours, a feat which most setups would not be able to accomplish.

## 6.4. Biomedical application: assessing the effect of cisplatin on ovarian cancer tumors

Ovarian cancer is one of the most common types of cancer in women, according to a study published by the International Agency for Research on Cancer in 2008<sup>17</sup>. The current overall cure rate for women diagnosed with ovarian cancer is only 30%<sup>18</sup>. Intraperitoneal (IP) chemotherapy with cisplatin drugs has been proven to be an active treatment for stage III disease<sup>19-21</sup>. At the time of writing, no standardized protocol for cisplatin IP treatment of ovarian cancer exists<sup>22</sup>. Furthermore, it has been shown the tumor cells develop resistance towards the drug relatively fast<sup>23-28</sup>. By studying the sub-cellular distribution of platinum (Pt) in tumor tissue and determining its chemical state after IP cisplatin chemotherapy, we try to unravel on the elemental correlations in the treated tumor tissue. Previous experimental work based on elemental imaging techniques investigating the cisplatin distribution in ovarian cancer tumors revealed the overall dispersion of Pt in the tissue and yielded crucial information on the penetration behavior of the cisplatin drug<sup>29-33</sup>. These experiments did not achieve the needed spatial resolution to visualize the platinum distribution in the tumor cells. Currently most experimental work is performed in vitro and very little data based on in vivo models are available.

Within the framework of this research project, three separate experiments at beamline ID16B of the ESRF were scheduled. The study aimed at obtaining information on the cisplatin-tissue interaction on the sub-cellular level, based on in vivo models using quantitative XRF experiments and nano-XANES analysis. By studying the Pt distribution, crucial information of the penetration behavior of the cisplatin drug, both macroscopically (throughout the tumor tissue) and sub-cellular, can be obtained. This information is crucial when studying the efficiency of the drug, since only Pt interacting with the DNA of the tumor cells, present in the nucleus, is able induce apoptotic cell death<sup>28,34</sup>. When these data are coupled to the XANES spectra of the found Pt-rich compounds, more

information on the drug-tumor interactions could be extracted, possibly finally revealing the resistance mechanism of these tumors.

Athymic nude mice were injected bilaterally with SKOV3-LUC IP1 ovarian cancer cells. Two weeks after the injection, tumors of approximately 3–5 mm in diameter had grown. Subsequently, the mice were treated with IP cisplatin (0.7 mg/mouse) at 2 different temperatures. The mice were euthanized directly after (H)IPEC by cervical dislocation. The tumor nodules were prepared in two distinct ways, depending on their intended use.

The nodules for XRF analysis were fixed in paraffin. These were excised, fixed in 4% formaldehyde (Klinipath, Olen, Belgium) during 24 h, and embedded in a paraffin block (Klinipath, Olen, Belgium) under orientation. Three consecutive sections of 2  $\mu\text{m}$  thickness were cut from the tumor using an HM355S microtome (Thermo Fisher scientific, Ghent, Belgium). The first and last slice were placed onto normal microscope glass slides. These were then air-dried and kept at room temperature before haematoxylin-eosin (H&E) staining. The middle slice was placed on Ultralene<sup>®</sup>foil (SPEX<sup>®</sup>SamplePrep, New Jersey, United States) which was subsequently placed onto a Polyether ether ketone (PEEK) slide with a central opening, specifically made for analysis using the ESRF ID16B SR beam. Paraffin fixation washes away all free cisplatin, hence only the active cisplatin, which is interacting with the tissue, remains in the sample.

Due to the risk of altering the chemical state of the cisplatin during chemical fixation using formaldehyde and paraffin embedding, the samples to be used for XANES experiments were made following a different routine. The tumor nodules were plunge-frozen in liquid nitrogen after excision and cut using a cryotome in 5  $\mu\text{m}$  thick slices which were again put on Ultralene<sup>®</sup>foil placed on a PEEK slide. Next, they were transferred in a dewar with liquid nitrogen to a freeze-dry installation, where they were put for 24h at -95°C and under light vacuum conditions to remove any residual water present in the samples.



During the first beamtime, the main goal was to investigate the feasibility of subcellular elemental imaging of tumor cells. The secondary aims were to determine the effect of the temperature protocol of the IP treatment on the penetration depth of the cytotoxic drug and to find out where the cisplatin predominantly resides inside the tumor tissue.

The first goal was met early on during this beamtime. Very nicely detailed elemental maps were made even on the first day, so the focus was changed to the scientific value of the results.

Figure 6-14 gives the results of the penetration depth experiments. Long, thin XRF mappings were made, going from the peritoneal membrane into the tumor. The pixels of the maps were summed parallel to the membrane to enhance the statistics. The penetration depth was then analyzed by determining at which point the Pt content had dropped down to only 1% of its signal at the border of the tumor. The IP protocol at elevated temperatures (41°C) caused a longer penetration depth compared to the protocol at body temperature, so higher temperatures will maximize the amount of tumor tissue affected by the drug.

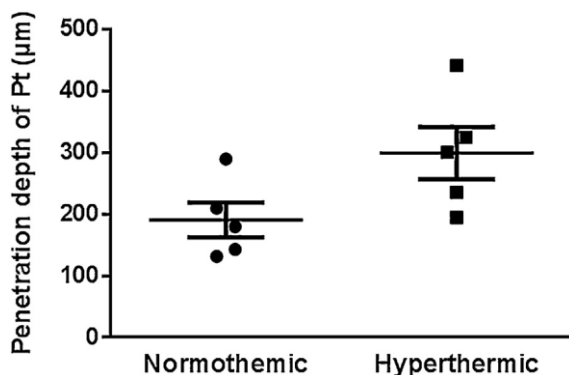


Figure 6-14 Penetration depth of Pt in the tumor tissue for normothermic (37-38°C) and hyperthermic (40-41°C) treated ovarian tumors

The final question to be answered during this first beamtime was the Pt distribution inside the tumor tissue. In order to be effective, the cisplatin

should bind to the DNA in the nucleus of the tumor cells, so by locating Pt on elemental maps and comparing this location to the other detected elements, some insights into the effects of the therapy can be gained. Figure 6-15 shows the elemental maps for P (A), S (B), Ca (C), Zn (D), Pt (E) and Cu (F). The first four elements give a detailed image on the structures in the tumor tissue. The cells are enriched in P, Ca and Zn compared to the surrounding extracellular matrix (ECM), while S is mainly present in structures of the ECM and to a smaller degree in the nucleus. Furthermore, Zn is mainly present in the nucleus, while P and Ca are also present in the cell membrane and other cell structures. Based on these observations, we could use the correlation of Pt with these elements to determine its predominant location. Visually Pt appears to reside mostly outside of the cell, in string-like structures which are also found in the S map.

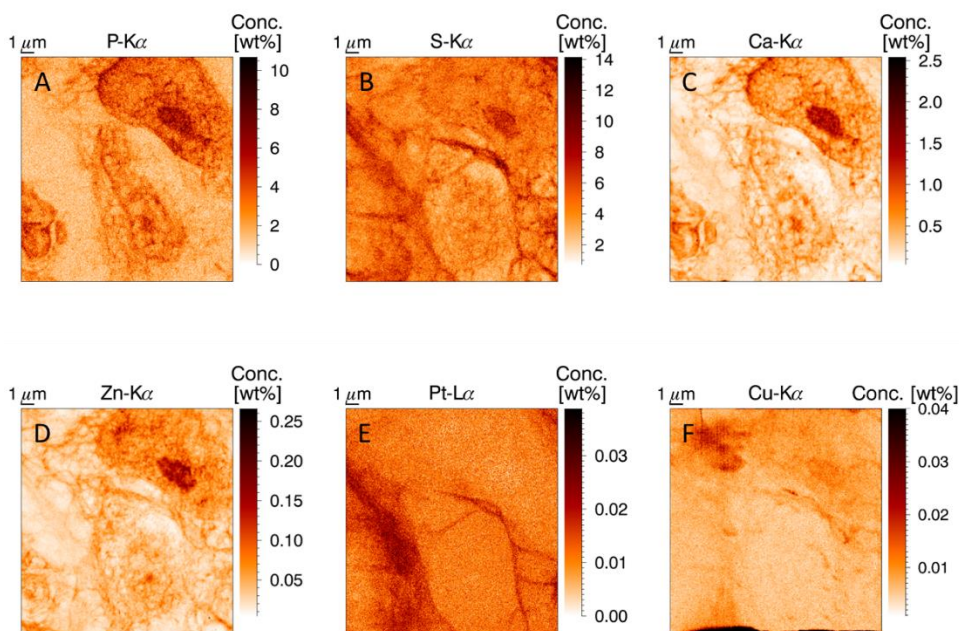


Figure 6-15 XRF elemental maps of P, S and Zn. Scanned area  $18 \times 18 \mu\text{m}$ , beam dimensions  $50 \times 50 \text{ nm}^2$ , 50 nm step size, measurement time 0.1 s per point, primary beam energy 17.5 keV. A tumor cell (nucleus and part of the cell membrane) can be discerned in the upper right part of the image, while two smaller cells are found in the middle and the lower left corner.

To confirm the observations of the XRF mappings statistically a PCA analysis is performed, the results of which can be found in Figure 6-16. As expected based on visual analysis of the elemental maps, P, Ca, Zn form a cluster which also includes Mn. This group of elements can be assigned to the tumor cells. Pt is correlated with S, but even more so with Br, although no direct explanation for the Pt-Br correlation can be given. Bromine could be an impurity in the cisplatin drugs, but a posteriori XRF analysis of the drug with a lab instrument did not reveal any Br, however, this could be due to the lower sensitivity towards this element compared to the ID16B probe.

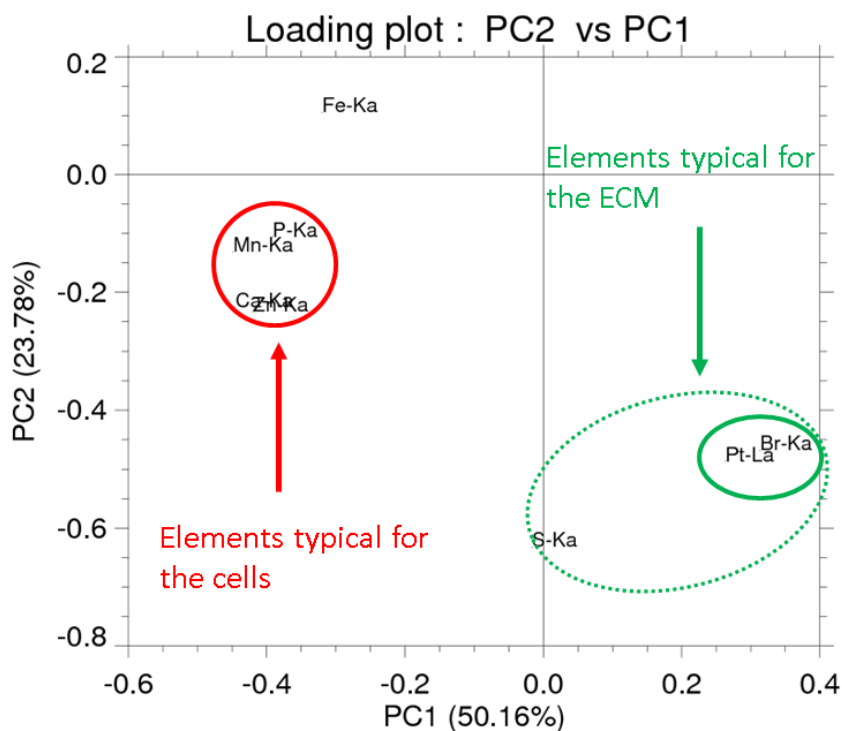


Figure 6-16 PCA clustering on the XRF mapping of Figure 6-15: links between P, Mn, Ca and Zn and between Pt, Br and to a lesser extent S

The discovery of the string-like structures with an elevated S and Pt content triggered a new question: under what form is Pt present. Is it unreacted cisplatin which accumulates in lower-density tumor regions, or has the cisplatin drug bound to some protein, the latter possibility would effectively capture the cisplatin and prevent the drug from diffusion into the cells. If cisplatin is bound to some structure outside the nucleus, this phenomenon might be part of the explanation of the resistance mechanism of ovarian cancer tumors towards cisplatin.

Since XRF measurements cannot give information about the chemical state of an element (e.g. the oxidation number), another technique is needed to yield this crucial information. This technique was readily found in X-ray absorption spectroscopy (XAS) and more specifically, X-ray absorption near-edge structure (XANES) analysis. Due to the rich experience of XMI group member Pieter Tack, it was possible to analyse tumor sections using nano-XANES during a second beamtime on ID16B.

Since nano-XANES on biological samples hadn't been tried before, this experiment proved much more challenging than the previous beamtime.

## 6.5. Nano-XANES experiments on cisplatin treated ovarian cancer tumors

The second beamtime dedicated to the research on intraperitoneal cisplatin treated ovarian cancer tumors also took place at ESRF beamline ID16B, which next to being an excellent nano-XRF beamline also houses a wide range of other X-ray based analysis techniques such as XRD, XANES and EXAFS. During this beamtime, the goal was to use XANES to determine in which chemical form Pt was present in the investigated tumor sections, as this added information would significantly increase our knowledge on how tumor cells react to the cisplatin drug and it might explain (part of) the resistance mechanisms at work.

For this beamtime, several changes were made to the experimental protocol, starting with the sample preparation. To avoid the possibility of changes to the chemical state of the Pt present in the tumor section due to sample preparation, part of the tumor section were no longer paraffin-embedded, but freeze-dried as discussed in the previous paragraph. A set of paraffin embedded tumor sections was also prepared as back-up samples, since these had proven to yield good XRF imaging results in the past.

The experimental setup at the beamline would also undergo several changes in order to be able to perform XANES experiments. The main modification was using a tunable monochromatic X-ray beam with energies around 11.6 keV ( $\sim$ Pt-L3 edge). Although monochromatizing the beam would cause a drop in intensity compared to the pink beam mode of the previous beamtime, ID16B produces such a brilliant beam this was not expected to provide any real issues and in any case it was unavoidable when performing XANES experiments. Unfortunately, the KB mirrors which were used at ID16B at the time of this beamtime were made of a tungsten multilayer. The W-L2 edge (11.544 keV) lies very close to the Pt-L3 edge (11.564 keV) which was selected for the XANES measurements, hence the mirrors interfered with the scans in two ways: a large drop in intensity due to absorption on the primary beam by the mirrors and a superimposed W-profile in the Pt XANES scans. Although normalization could correct for the latter interference, the added drop in intensity seriously hampered the measurements by lowering the signal to an intensity barely above the noise level.

The experiments were performed in two steps. First a quick overview scan was used to image the elemental composition of the sample in order to find regions with augmented Pt concentrations. Care was taken to minimize exposure time during these scans, in order to avoid beam damage. Figure 6-17 shows the result of such an overview scan as a red/green/blue (rgb) image of sulfur, platinum and zinc. Based on the data of our previous beamtime at ID16B, Zn was selected as the signature element of tumor cells and more specifically their nucleus. As before, Pt was found to reside predominantly outside the Zn-rich regions (i.e. the

nucleus of the cells). To a smaller extent, S and Pt are once more found in augmented concentrations in the same parts of the scans. These zones were selected for further analysis using XANES in order to unravel the way Pt is present in these regions of the tumor.

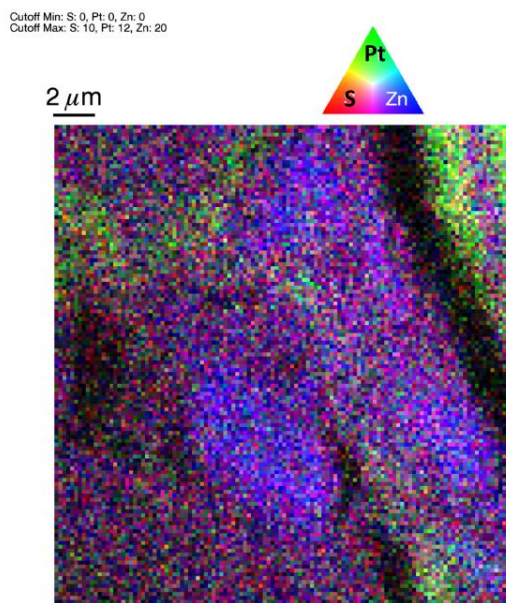


Figure 6-17 RGB image of S, Pt and Zn. Scanned area  $22 \times 22 \mu\text{m}$ , beam dimensions  $50 \times 50 \text{ nm}^2$ , 100 nm step size, measurement time 0.1 s per point, primary beam energy 11.6 keV.

Once a region of interest was determined, long XANES scans were performed on a single nanoscopic point (30 s measurement time). Instead of illuminating the sample for this long time span in one go, a series of short XANES measurements (500 ms real time/point) were performed which were then summed. This procedure allowed us to monitor possible beam damage, which was noted in some cases after several seconds of measurement time by a sudden change in the XANES pattern, most notably the lowering of the white line (i.e. the intense peak right after the edge in a XANES spectrum) which indicates a change in the oxidation state of Pt.

Measurements on several Pt containing reference materials allowed us to draw some conclusions on the state of the detected Pt, mainly based on the edge position and the white line. However, due to the instrumental issues discussed above the XANES-spectra were insufficiently detailed for accurate identification of the Pt compounds. Linear combination fitting indicated 60% of the detected Pt in the tumor sections is bound to phospho-organic compounds (similar but not necessarily identical to Pt-EBTPP, could be bound to S as well for instance) and 40% is original (unchanged) cisplatin.

A planned refurbishment of the ID16B beamline with new KB mirrors made from palladium promised to resolve the interference issue, so we applied for a third beamtime within this project, which was allocated to us at the end of January 2018. Additional challenges in the constructions of the mirrors has caused a postponement of this beamtime to June 2018.

## 6.6. References

- (1) Cesar da Silva, J.; Pacureanu, A.; Yang, Y.; Bohic, S.; Morawe, C.; Barrett, R.; Cloetens, P. *Optica* **2017**, *4*, 492-495.
- (2) Laforce, B.; Schmitz, S.; Vekemans, B.; Rudloff, J.; Garrevoet, J.; Tucoulou, R.; Brenker, F. E.; Martinez-Criado, G.; Vincze, L. *Analytical Chemistry* **2014**, *86*, 12369-12374.
- (3) Martínez-Criado, G.; Villanova, J.; Tucoulou, R.; Salomon, D.; Suuronen, J.-P.; Labouré, S.; Guilloud, C.; Valls, V.; Barrett, R.; Gagliardini, E.; Dabin, Y.; Baker, R.; Bohic, S.; Cohen, C.; Morse, J. *Journal of Synchrotron Radiation* **2016**, *23*, 344-352.
- (4) Riekkel, C.; Burghammer, M.; Davies, R. *IOP Conference Series: Materials Science and Engineering* **2010**, *14*, 012013.
- (5) Schroer, C. G.; Baumbach, C.; Döhrmann, R.; Klare, S.; Hoppe, R.; Kahnt, M.; Patommel, J.; Reinhardt, J.; Ritter, S.; Samberg, D.; Scholz, M.; Schropp, A.; Seiboth, F.; Seyrich, M.; Wittwer, F.; Falkenberg, G. *AIP Conference Proceedings* **2016**, *1741*, 030007.
- (6) Tucoulou, R., Laforce, B., Ed., 2014.
- (7) Vekemans, B.; Janssens, K.; Vincze, L.; Adams, F.; Vanespen, P. *Spectrochimica Acta Part B-Atomic Spectroscopy* **1995**, *50*, 149-169.
- (8) Vekemans, B.; Janssens, K.; Vincze, L.; Adams, F.; Vanespen, P. *X-Ray Spectrometry* **1994**, *23*, 278-285.
- (9) Pearson, D. G.; Brenker, F. E.; Nestola, F.; McNeill, J.; Nasdala, L.; Hutchison, M. T.; Matveev, S.; Mather, K.; Silversmit, G.; Schmitz, S.; Vekemans, B.; Vincze, L. *Nature* **2014**, *507*, 221-224.
- (10) Chen, M.; Goresy, A. E.; Gillet, P. *Proceedings of the National Academy of Sciences of the United States of America* **2004**, *101*, 15033-15037.
- (11) Hutchison, M. T. In *VIIIth international Kimberlite conference*, Gurney JJ, G. J., Pascoe MD, Richardson SH, Ed.; Red Roof Design: Cape Town, 1999, pp 372-382.
- (12) Hayman, P. C.; Kopylova, M. G.; Kaminsky, F. V. *Contributions to Mineralogy and Petrology* **2005**, *149*, 430-445.
- (13) Kaminsky, F. V.; Khachatryan, G. K.; Andreazza, P.; Araujo, D.; Griffin, W. L. *Lithos* **2009**, *112*, 833-842.
- (14) Warren, P. H.; Rubin, A. E.; Isa, J.; Brittenham, S.; Ahn, I.; Choi, B.-G. *Geochimica Et Cosmochimica Acta* **2013**, *107*, 135-154.
- (15) Lander, M. P.; Brenker, F. E. *NWA-6693: an ungrouped achondrite*. Goethe University, Frankfurt (Germany), Frankfurt, 2013.
- (16) Vekemans, B.; Janssens, K.; Vincze, L.; Aerts, A.; Adams, F.; Hertogen, J. *X-Ray Spectrometry* **1997**, *26*, 333-346.



- (17) Ferlay, J.; Shin, H.-R.; Bray, F.; Forman, D.; Mathers, C.; Parkin, D. M. *International Journal of Cancer* **2010**, *127*, 2893-2917.
- (18) Bast, R. C.; Hennessy, B.; Mills, G. B. *Nat Rev Cancer* **2009**, *9*, 415-428.
- (19) Zivanovic, O.; Abramian, A.; Kullmann, M.; Fuhrmann, C.; Coch, C.; Hoeller, T.; Ruehs, H.; Keyver-Paik, M. D.; Rudlowski, C.; Weber, S.; Kiefer, N.; Poelcher, M. L.; Thiesler, T.; Rostamzadeh, B.; Mallmann, M.; Schaefer, N.; Permantier, M.; Latten, S.; Kalff, J.; Thomale, J.; Jaehde, U.; Kuhn, W. C. *International journal of cancer. Journal international du cancer* **2015**, *136*, 699-708.
- (20) Bijelic, L.; Sugarbaker, P. H.; Stuart, O. A. *Gastroenterology Research and Practice* **2012**, *2012*, 5.
- (21) van der Vange, N.; van Goethem, A. R.; Zoetmulder, F. A.; Kaag, M. M.; van de Vaart, P. J.; ten Bokkel Huinink, W. W.; Beijnen, J. H. *European journal of surgical oncology : the journal of the European Society of Surgical Oncology and the British Association of Surgical Oncology* **2000**, *26*, 663-668.
- (22) Grosso, G.; Rossetti, D.; Coccolini, F.; Bogani, G.; Ansaloni, L.; Frigerio, L. *Archives of gynecology and obstetrics* **2014**, *290*, 425-434.
- (23) Tannock, I. F.; Lee, C. M.; Tunggal, J. K.; Cowan, D. S.; Egorin, M. J. *Clinical cancer research : an official journal of the American Association for Cancer Research* **2002**, *8*, 878-884.
- (24) Siddik, Z. H. *Oncogene* **2003**, *22*, 7265-7279.
- (25) Flessner, M. F.; Choi, J.; Credit, K.; Deverkadra, R.; Henderson, K. *Clinical cancer research : an official journal of the American Association for Cancer Research* **2005**, *11*, 3117-3125.
- (26) Tredan, O.; Galmarini, C. M.; Patel, K.; Tannock, I. F. *Journal of the National Cancer Institute* **2007**, *99*, 1441-1454.
- (27) Sun, Y.; Campisi, J.; Higano, C.; Beer, T. M.; Porter, P.; Coleman, I.; True, L.; Nelson, P. S. *Nature medicine* **2012**, *18*, 1359-1368.
- (28) Kartalou, M.; Essigmann, J. M. *Mutation Research/Fundamental and Molecular Mechanisms of Mutagenesis* **2001**, *478*, 23-43.
- (29) Davis, K. J.; Carrall, J. A.; Lai, B.; Aldrich-Wright, J. R.; Ralph, S. F.; Dillon, C. T. *Dalton transactions (Cambridge, England : 2003)* **2012**, *41*, 9417-9426.
- (30) Gil, S.; Carmona, A.; Martinez-Criado, G.; Leon, A.; Prezado, Y.; Sabes, M. *Biological trace element research* **2015**, *163*, 177-183.
- (31) Zhang, J. Z.; Bryce, N. S.; Lanzirrotti, A.; Chen, C. K.; Paterson, D.; de Jonge, M. D.; Howard, D. L.; Hambley, T. W. *Metallomics : integrated biometal science* **2012**, *4*, 1209-1217.
- (32) Ortega, R.; Moretto, P.; Fajac, A.; Benard, J.; Llabador, Y.; Simonoff, M. *Cellular and molecular biology (Noisy-le-Grand, France)* **1996**, *42*, 77-88.
- (33) Ilinski, P.; Lai, B.; Cai, Z.; Yun, W.; Legnini, D.; Talarico, T.; Cholewa, M.; Webster, L. K.; Deacon, G. B.; Rainone, S.; Phillips, D. R.; Stampfl, A. P. *Cancer research* **2003**, *63*, 1776-1779.
- (34) Florea, A.-M.; Büsselberg, D. *Cancers* **2011**, *3*, 1351.

## Chapter 7

# The symbiosis between laboratory and synchrotron

In this PhD thesis, both experiments at lab-scale setups and state-of-the-art synchrotron radiation based instruments have been discussed. Due to their superior characteristics in terms of (among others) beamsizes, intensity, polarization and coherence synchrotron radiation sources enable a wide range of applications which are unfeasible in the lab. However, lab-scale experiments still play an important role, even in the context of synchrotron experiments. Not only can they provide vital preliminary information, which can be used to select the optimal samples for analysis during a synchrotron beamtime, state-of-the-art lab instruments such as the HERAKLES scanner can also be used for training purposes in preparation of a beamtime or even to develop methodologies and experimental strategies later to be employed at the synchrotron. On the other hand, techniques and concepts developed at synchrotron radiation sources often find their way into the laboratory as well.

This chapter is devoted to the “symbiosis” between the lab and the synchrotron. Experiments performed with lab instruments used to simplify e.g. region of interest (ROI) retrieval during synchrotron measurements will be discussed. Furthermore, the methodological principles developed at the HERAKLES scanner used to improve our data output during beamtimes and vice versa will be highlighted. A case

study concerning microkrystite samples, condensation products of an impact vapor cloud, will be given as an example. From this chapter it should be clear that the lab and the synchrotron based X-ray spectroscopic/imaging techniques are not competitors fishing in the same pond, but rather teammates helping each other to perform their best in their respective specialties.

## 7.1. How a synchrotron experiment benefits from lab-based analysis

The main limitation of every synchrotron radiation based experiment is the limited time which is available to perform the measurements (for XRF imaging applications typically about 12 shifts of 8h each). Usually the number of samples a user would like to analyze considerably exceeds that permitted by the available beamtime. Hence, it is of crucial importance to minimize the time spend on samples potentially containing no useful information or scanning less interesting parts of the selected samples. Although lab instruments will normally fail to give all of the desired information at the preferred resolution, they can still be used to select the most promising samples, or visualize the ROI which should be scanned in greater detail at the synchrotron source.

### 7.1.1. Lab-based microscopy to locate the ROI

As a first example, the methodology developed to locate the region of interest during the biomedical beamtimes at ID16B concerning the effect of cisplatin drugs on tumor tissue will be discussed (more detail on these experiments can be found in Chapter 6).

During these experiments the elemental distribution of Pt in the tumor cells was to be investigated to gain knowledge on the processes taking place. In order to kill the malignant cells, the cisplatin drug should

interact with their DNA (present in the nucleus), while cytotoxic drug which is present and/or bound to structures outside of the nucleus, or even outside the tumor cells, will do little harm to the ovarian cancer tumor. Hence, it was crucial during this beamtime to be able to map the tumor sections with high resolution (about 50 nm or less) in order to derive the Pt distribution within individual cells. The characteristics of ID16B, with its small and intense spot of 50 nm combined with excellent detection using the two three-element SDD detectors in dual detector mode made this beamline perfectly suited for these measurements. Since these tumor cells have a diameter around 20  $\mu\text{m}$ , even a single scan with nanoscopic resolution took quite some time ( $\sim 4.5$  h for a 20 x 20  $\mu\text{m}$  scan).

To have a successful beamtime, scanning a large number of tumor cells, it was crucial to quickly locate interesting cells with high precision in order to avoid long maps without any relevant information. However, the resolution of the beamline microscope was insufficient to clearly visualize the cells in the tumor sections. Furthermore, it yielded a very low contrast. Using a suitable staining of the sections could partially resolve this problem, however, the staining compounds might interfere with the XRF analysis, adding elements to the spectrum, or might even cause a redistribution of certain elements. In order to retain the original composition and elemental distributions of the sample, and to avoid spectral interference, the use of a staining protocol therefore was not allowed on the samples analysed by nanobeam SR-XRF. A solution to the resulting challenge regarding high-resolution visualization was found using lab-based optical image analysis on a high resolution optical microscope (light microscope ColorView I, BX43F, Olympus, Tokyo, Japan) and the ImageJ software package available on the control pc of the beamline.

When preparing the samples with tumor sections, three adjacent sections of 2  $\mu\text{m}$  thickness were made using a Microm HM355S microtome (Thermo Scientific, Rockford, IL, USA). The first and the last were placed on a classical microscope slide, while the middle section was placed on Ultralene<sup>®</sup> foil. This latter sample was then mounted on a

specially designed poly-ether-ether-ketone (PEEK) slide as shown in the previous chapter.

The other two sections were hematoxylin and eosin (H&E) stained<sup>1</sup> by the Pathology Department of the Ghent University Hospital and imaged using an optical microscope in the lab at the Ghent University Hospital Department of Surgery.

These microscope images were scaled to exactly the same size as the online images generated by the beamline microscope, both in terms of the number of pixels and the pixel size. Before the synchrotron experiment started, all samples were investigated at Ghent University using the microscope images and regions of interest of the samples were indicated on these pictures.

Once at the synchrotron radiation facility (i.e. ESRF beamline ID16B) the lab-based images were uploaded to the ImageJ software package present on the beamline control pc and used as overlay for the output of the online beamline microscope. Rotating and translating the overlay image until a perfect fit with the live view was reached enabled a quick and precise determination of the microscopic scan areas based on the pre-determined regions of interest as is demonstrated in Figure 7-1. In this figure, the green dot within the red rectangle represents the pre-determined scanning area, while on the right the S-K $\alpha$  image of the resulting scan is shown. Further optimization of this protocol would include the possibility to load the overlay-images directly in the control software, however, the current procedure proved already sufficient for the envisaged application. It was employed with great success during two ID16B beamtimes dedicated to these ovarian cancer tumor samples, improving the efficiency of nanoscopic data acquisition from micron-sized ROIs.

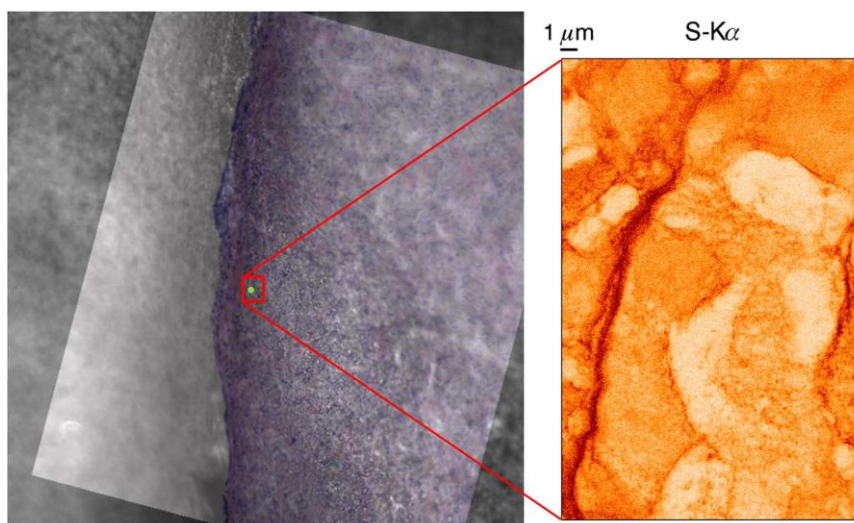


*Figure 7-1 H&E stained lab-based image aligned with online microscope view to select the ROI (left) yielding direct correlation with XRF mappings (e.g. S-K $\alpha$  on the right). Scanned area 18 (H)  $\times$  28 (V)  $\mu$ m, 50 nm spot size, 17.5 keV beam.*

### 7.1.2. Lab-based micro-XRF as a tool for sample selection

An even more straightforward way to maximize the amount of useful data acquired during a beamtime is applicable when the users are mainly interested in only a few target elements in their samples above a certain concentration level, expected to be detectable by lab-setups. In this case, preliminary micro-XRF scans using lab instruments can screen the sample set to identify relevant samples containing the elements of interest having sufficient concentration levels, either discarding the rest or giving those a lower priority. This methodology of beamtime preparation has been employed for several beamtimes (see the test case using microkrystites samples in section 7.4. for an extended example). Next to being preliminary scans for a synchrotron radiation based experiment, these measurements also have an added value of their own, since very often the investigated (entire) sample will be too large to scan completely using the nano-probe of the beamline. In such cases, laboratory scans can yield an overall average composition or low-resolution XRF image of the sample which, coupled with the detailed scans of the SR based

experiment, can give a broader and more complete view on the sample. This complementarity between laboratory and SR based analysis will be showcased in paragraph 7.4. with the study of microkrystite samples.

### 7.1.3. $\mu$ CT revealing the internal morphology of the samples

Finally, as a close companion of the preliminary XRF scans, preliminary  $\mu$ CT scans performed at the HERAKLES 3D X-ray scanner can shed light on the internal morphology of the samples. In some cases, the structure of a sample is at least as interesting and important to solve the scientific question as is the elemental composition. The presence of voids or e.g. metallic inclusions in micrometeorites is a good example of features which can be easily imaged using  $\mu$ CT, which in turn can identify a certain sample to be at the top of the priority list, providing also the means to pre-select ROIs in 3D for nano-XRF. Combined with lab-based XRF scans,  $\mu$ CT has been employed a number of times throughout this work to prepare for a nano-beam synchrotron experiments on cosmological samples. Together with the preliminary XRF scans, the use of lab-based  $\mu$ CT scans during a beamtime is demonstrated in paragraph 7.4. on geological samples.

## 7.2. Methodologies developed in the lab

There are two sides to the story of methodologies which are developed in the lab and later on used during synchrotron radiation based experiments. Firstly, there are the techniques incorporated in a lab instrument which are later on also employed at synchrotron beamlines after they have proven their usefulness. Secondly, methodologies designed specifically for a certain beamtime can first be developed and tested using lab instruments to get acquainted with their peculiarities. An example of the latter has been given previously within the context of XRF imaging on

ovarian cancer tumor sections. The sample alignment procedure using offline microscope images of H&E stained sections as an overlay for the online microscope was first tested using the facilities at Ghent University before they were employed at the ESRF.

An example of the other category, methodologies which were first purely developed for use on medical and lab instruments which later on found their way to the synchrotron, are represented by e.g.  $\mu$ CT based techniques. The preliminary  $\mu$ CT scans as performed on the HERAKLES scanner fall into this category. Being part of the very philosophy of this instrument, 3D imaging using  $\mu$ CT in order to select ROIs in 3D for XRF scans had been used for several years before it was first employed during a beamtime. While performing combined XRF/XRD scans at ID16B on micrometeorite samples, the presence of a 2D detector allowed for relatively fast tomography scans ( $\approx 15$  min) to be performed. The diffraction setup of this beamtime is shown in Figure 7-2.

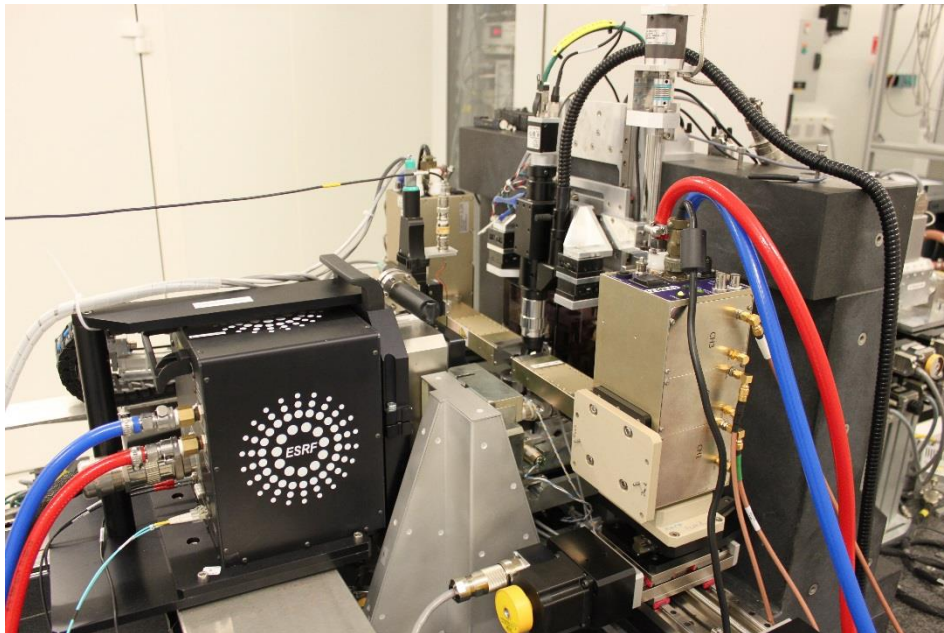


*Figure 7-2 Setup of ID16B with diffraction camera and dual detector SDD detectors installed.*



Taking this opportunity to use the well-known and familiar lab-based procedure, quick tomography scans were taken from each sample before moving it to the position for XRF/XRD analysis, thus gaining valuable information, enabling quick and secure sample positioning to find ROIs with specific morphological characteristics.

## 7.3. Synchrotron know-how transferred to the lab

At synchrotron radiation facilities there is an enormous concentration of know-how concerning X-ray based analysis techniques. The unique scientific environment, constant strive to optimize the beamlines, wide variety of applications and motivated scientists working in this thrilling setting really push the boundaries of knowledge and technology forward. Having the privilege to work in this setting allows the X-ray scientist to gather a lot of knowledge and inspiration which can be later on employed when designing new lab instruments and methodologies. Several procedures and even the basic concept of the HERAKLES 3D X-ray scanner are inspired by synchrotron technology as described below.

### 7.3.1. Basic principles and layout of the scanner

The Herakles 3D X-ray scanner follows the principles of a synchrotron beamline in terms of concept and construction. Most laboratory instruments are made as compact as possible to make them fit on a benchtop. As stated previously, this demands compromises, possibly hampering the ultimate performance of the instrument. HERAKLES on the other hand is constructed designed with the basic layout of a beamline in mind. The instrument itself is placed on a large granite table with dimensions 1.48 m x 0.77 m x 0.81 m (length x width x height) inside a bunker very similarly to the experimental hutch of a typical beamline. The setup is controlled by a PC located in a separate control room next to the experimental bunker, while a second pc inside the bunker can also be used for controlling motor movements during initial sample positioning. Such a system is also present at e.g. ID16B.

Incorporating several methodologies (3D XRF and  $\mu$ CT) in a single instrument is a concept which stems directly from synchrotron radiation facilities, where at most beamlines multiple techniques can be used, often even simultaneously. The added value of combining complementary techniques in a single instrument led to the conceptualization of HERAKLES. Next to extracting a great deal of extra information from a single experimental run, data treatment becomes much more easy due to the coordinate system staying the same for all measurements, an idea which has been directly transplanted to the HERAKLES scanner.

### 7.3.2. Sample visualization

The complexity of the sample environment at an SR nanoprobe makes visualization of the sample on different scales a pressing issue. The users should have a good overview of the complete instrument to assess the relative position of different components and monitor motor movements during sample change or while moving from one measurement mode to another. On the other hand, high resolution images of the sample must be available in order to select scan areas. All of this information should be available outside the experimental hutch while performing measurements. The solution at a lot of beamlines is placing several cameras in the hutch which have a large dynamic range in terms of zoom. A good example is the Axis camera (Axis Communications AB, Lund, Sweden) with its superb zoom used at ID13 and ID16B. Next to this camera a beamline microscope is used to image the sample. At HERAKLES the same issue had to be resolved, since just like at SR beamlines, large motor movements are sometimes necessary while the X-ray tubes are on and hence no direct monitoring of the setup is possible. The same type of camera (Axis) is employed as on ID13 and ID16B to monitor movements of the sample from one end-station to another. Furthermore, the concept of ID16B of imaging the sample along the direction of incident X-rays is employed. However, instead of using a pierced-mirror based optical microscope, at HERAKLES X-ray transmission images are taken and used to select the scan area.

### 7.3.3. User interface for ROI selection

At ESRF ID16B, the image taken by the beamline microscope is loaded in the software which generates the script for the scans. In a very straightforward way, a rectangular scanning region can be selected by drawing a box within this image. The graphically chosen area is then transformed to a set of coordinates by the scanning software and after defining the desired measurement time and step size the command script to start the scan is automatically generated. This user-friendly concept has been transferred to the scanning control software of the HERAKLES 3D X-ray scanner. Although in the basic software package no such function is available, a second script builder program has been developed which is strongly based on the above described concept. This program is the CT-XRF linking software by which, based on a reconstructed  $\mu$ CT scan, the scan settings for a subsequent confocal XRF mapping are generated. The procedure goes through the following steps.

1. The sample is aligned in front of the central  $\mu$ CT end-station of the HERAKLES scanner
2. A  $\mu$ CT scan is taken from the sample. The scan can be very fast and rough if the user is mainly interested in subsequent XRF, or very detailed if the  $\mu$ CT data are the primary focus.
3. While the sample is kept mounted on the instrument, the  $\mu$ CT scan is reconstructed.
4. The reconstruction is loaded in the CT-XRF linking software, where the virtual slices can be visualized.
5. The user selects the desired region of interest by browsing through the slices a picking points, lines, rectangles, random shapes or even volumes. For every type of ROI (except for the point scans) a step size should also be given. The users can add as many of these ROIs as needed to an array the software generates and select the measurement time.
6. When finished, the software will generate a script which moves the sample to the confocal XRF station and measures all selected ROIs.

For full details about the software the reader is referred to appendix A3 and the dedicated paragraphs in Chapter 4. This image based graphical selection of a scanning area can be traced back directly to the procedures used at the synchrotron radiation facility ESRF ID16B.

## 7.4. Experimental case: microkrystites and – meteorites

The experiments on the microkrystites and micro-meteorites are performed as preparation for two different beamtimes at ESRF beamline ID16B. One of the main applications of the HERAKLES scanner is performing lab-scale experiments to prepare for, or in addition to, synchrotron experiments. Due to the large difference in resolution level and typical scan-size achievable by these two types of experiments, they are highly complementary. During a beamtime, even though the high brilliance of a synchrotron source enables fast scans (down to 50 ms realtime per point is feasible at ID16B), there seldom is enough time to scan the entire (e.g. mm sized) sample, so only the elemental distributions in microscopic sub-regions of the investigated object can be determined. The larger spot size (e.g. between 10 and 30  $\mu\text{m}$  for the XRF techniques at HERAKLES) and virtually infinite measurement time available on a lab setup makes scanning the entire sample much more feasible. Furthermore, the possibility to obtain 3D morphological information using the HERAKLES 3D X-ray scanner is valuable added information to the nano-XRF scans performed at the synchrotron, since the tomographic data can reveal the presence of inclusions or different phases which, coupled with the elemental distribution, may yield additional insights in the structural and textural characteristics of the sample. As setup used for preliminary scans, HERAKLES is mainly used to select those samples from a larger set which show the most relevant morphological structures or which contain the elements of interest in the sum spectra of their overview scans. This procedure has led to a considerable gain in relevant measurement time during a beamtime by

omitting the less interesting samples from the experimental plan, allowing to concentrate entirely on the most relevant samples.

The illustrative case study focuses on geological materials with an extraterrestrial component, being microkrystites (spherulitic impact vapor condensates) and unmelted Antarctic micro-meteorites, both types of samples provided by Steven Goderis. The microkrystites were analyzed during a beam time in April 2016, while the micro-meteorites were characterized at the ESRF in October 2017.

#### 7.4.1. Microkrystite samples

Approximately 66 million years ago, a major event led to a key extinction event, which included the demise of the dinosaurs. It has been hypothesized that this mass extinction was triggered by the impact of an asteroid with a diameter of about 10 km. Unusual high concentrations of siderophile Ir and other platinum group elements (PGEs, i.e. Re, Os, Ir, Ru, Pt, Rh, Pd) were found in the Cretaceous-Paleogene boundary clay in Italy (at Gubbio) and Spain (Caravaca), and later confirmed at various locations worldwide. These geochemical anomalies could stem from the ejection of large volumes of Ir-rich projectile material upon the impact of this asteroid with Earth's crust.<sup>2</sup>

The clay layer of the Cretaceous-Paleogene boundary is about 2 to 3 cm thick and has concentrations of PGEs elevated several orders of magnitude above their normal value. An important part of the clay layer consists of so-called microkrystites which could potentially host a fraction of this extraterrestrial component. Microkrystites are small glassy spherules (> 1  $\mu$ m) with primary microlites (crystals) stemming from solidified droplets from melt or condensed from vapour. Microkrystites are part of the distal impact ejecta which are found well away from the crater of large impacts (more than 10 times the crater diameter).<sup>3</sup> In most of the Cretaceous-Paleogene boundary clays three types of microkrystites can be found with difference in both their mineralogy, morphology and elemental composition. There are the black

Goethite [ $\alpha$ -FeO(OH)] spherules, the K-feldspar [ $\text{K(AlSi}_3\text{O}_8)$ ] spherules which have a white to yellow color and the glauconite [ $(\text{K,Na})(\text{Fe}^{3+},\text{Al,Mg})_2(\text{Si,Al})_4\text{O}_{10}(\text{OH})_2$ ] spherules which are green. Their current day composition is largely defined by replacement products of their (unknown) original composition.

It has been suggested that the remnant textural characteristics of the spherules and the type of alteration product are indicative of the spherules' original compositions, which are important to constrain the physicochemical conditions prevailing in the impact vapor plume. Microkrystites can also have interesting elemental signatures due to high contamination by the meteorite responsible for their formation<sup>4,5</sup> and some contain unusual primary Ni-rich spinels. Spinel is the sole pristine phase surviving the diagenetic alterations. The spinel phases may represent one of the main PGE containing constituents of the Cretaceous-Paleogene boundary layer.<sup>6</sup> Until today the main composing phases of the spherules, consisting of replaced material, received little attention. The aim during this beamtime was to better understand the distribution of PGEs in the matrix and crystals of a set of Cretaceous-Paleogene boundary microkrystite spherules to close this gap in our knowledge.

#### 7.4.2. Preliminary scans at the HERAKLES scanner

A total of 14 microkrystite spherules were mounted on a polymer tip (made of nylon wire) which was then glued to a brass pin sample holder for easy handling. There were 8 goethite, 1 glauconite and 5 sanidine spherules from two localities in Italy (Petriccio and Furlo Pietralata) and from Deep Sea Drilling Project (DSDP) site 596, leg 91. Two of the goethite spherules were not mounted ideally and omitted from the sample set. Next to these microkrystite spherules, a single Antarctic micro-meteorite (MM06) was mounted. The complete set of samples would take several weeks of synchrotron experiments to analyze in detail, much longer than the allocated beamtime, so choices had to be made and priorities settled in the experimental roadmap.

To aid in this process, the HERAKLES 3D X-ray scanner was used to determine both the morphology and elemental composition of each spherule. First a  $\mu$ CT scan was made on each sample, which revealed very interesting internal structures in some of the spherules (e.g. Figure 7-3). This scan was also used to measure the spherules which proved to be quasi spherical. In the case of the sample shown in Figure 7-3 a height of 405  $\mu$ m was found, while the diameter varied a little according to the rotational angle ranging from 460 to 480  $\mu$ m. The values are in the typical range found for all measured spherules. Next, the microkrystites were subjected to micro-XRF analysis. Although XRF mappings with 20  $\mu$ m resolution were made of each sample, these were fairly homogeneous on this resolution level, so they were mainly used to construct a sum spectrum in order to analyze the presence of some elements of interest (Ir, Pt and their proxies).

Figure 7-3 Shows one of the goethite spherules (Lg 91 DSDP 596). The particle can be seen mounted to the polymer tip in the microscope image (upper left corner of the figure) next to that microscope image, a virtual slice from the  $\mu$ CT scan is shown. A shell-and-core morphology can clearly be discerned, with a few inclusions in the shell with lower attenuation than the matrix. The presence of a shell-core morphology is valuable input for further geological analysis of the sample.

The lower half of Figure 7-3 shows the sum spectrum of an XRF overview scan. A wide array of elements could be detected, although no PGEs. In fact, none of the overview scans using lab-based XRF revealed PGEs to be present in the samples at detectable concentration levels, so the decision on which microkrystites to analyze during the beamtime had to be made using other criteria such as the presence of other elements serving as proxy for PGEs, the shape, size and morphology of the spherule or the presence of other interesting elements (thus focusing on an additional research question).

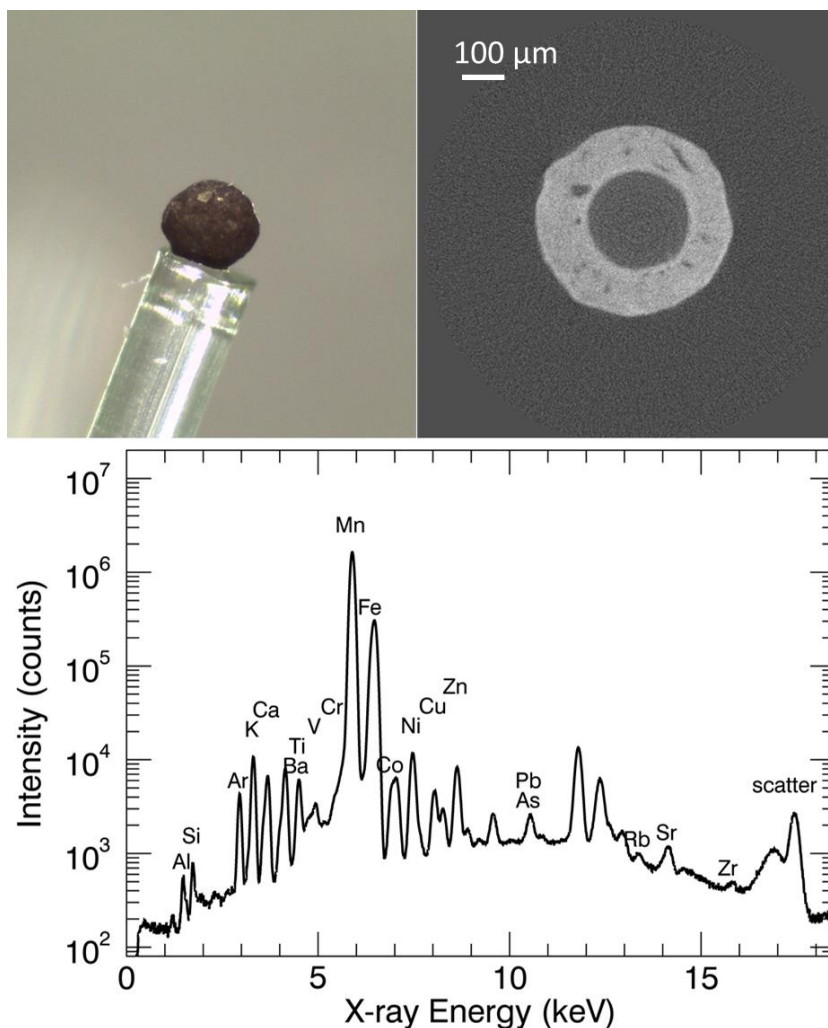


Figure 7-3 Analysis of goethite spherule Lg 91 DSDP 596. Top left: microscope image; top right: virtual slice of  $\mu$ CT scan (Radeye, 70 kV, 3 W, 500 ms, 1001 projections); bottom: sum spectrum of XRF scan (cXRF, 40 kV, 0.6 mA, 5 s LT, 20  $\mu$ m step size)

### 7.4.3. Synchrotron nano-XRF experiment: experimental setup ESRF ID16B

The microscopic size of the microkrystites calls for nanoscopic XRF techniques in order to visualize the elemental distributions in sufficient detail in terms of spatial resolution. Furthermore, monochromatic (or at



least pink beam) excitation with an energy around 14 keV is necessary to excite the Pt and Ir L-lines. State-of-the art detectors (preferably multi-element SDD detectors) are crucial to detect the ultralow concentrations of Pt and Ir expected to be present in the spherules. Finally, a fast scanning procedure is necessary in order to scan relatively large microscopic areas in a comparatively short time frame. All these requirements are met by the ESRF ID16B beamline and the first experiments on these samples took place in April 2016.

#### **7.4.3.1. Experimental results at ID16B**

Although no PGEs were unequivocally detected in the meteorites using the lab-scale setup, the much better detection limits at ESRF ID16B ( $\approx 0.2$  ppm for Pt with 1000 s RT) might still make the detection of some Pt or Ir feasible. Furthermore, the 50 nm beamsize could enable the detection of nanoscopic Pt- or Ir-rich inclusions which are invisible with X-ray probes with a micron-sized beam, because their composition (and XRF signal) get averaged out with that of the surrounding matrix.

Figure 7-4 shows the results of an overview scan with a relatively large step size (200 nm) and short dwell time (0.1 s) on one of the goethite spherules from Italy (PTC/12). This is the only scan where Ir was detected, albeit with a very low XRF intensity. Iridium is present exactly at the same position as that of the origin of an equally low Pt signal. The detail scans did not show much structure for both elements at the positions selected in the upper-left corner of Figure 7-4, which suggests these Pt and Ir signals might be artefacts, or these elements are present in concentrations below the detection limits of the setup. Importantly, the regions in Figure 7-4 with increased Pt and Ir signal are distinct from the Ni-rich spinel crystals that can clearly be recognized in the Fe- $K_{\alpha}$ , and Ni- $K_{\alpha}$  intensity maps of this sample.

Complementary measurements using laser ablation inductively coupled mass spectrometry (LA-ICP-MS) indicated that spinel-rich zones do not show Ir and Pt concentrations distinct from spherule matrix without

spinel crystals.<sup>7</sup> The probability of hitting exactly one of these higher concentration regions using the nanoscopic beam at ID16B did prove challenging.

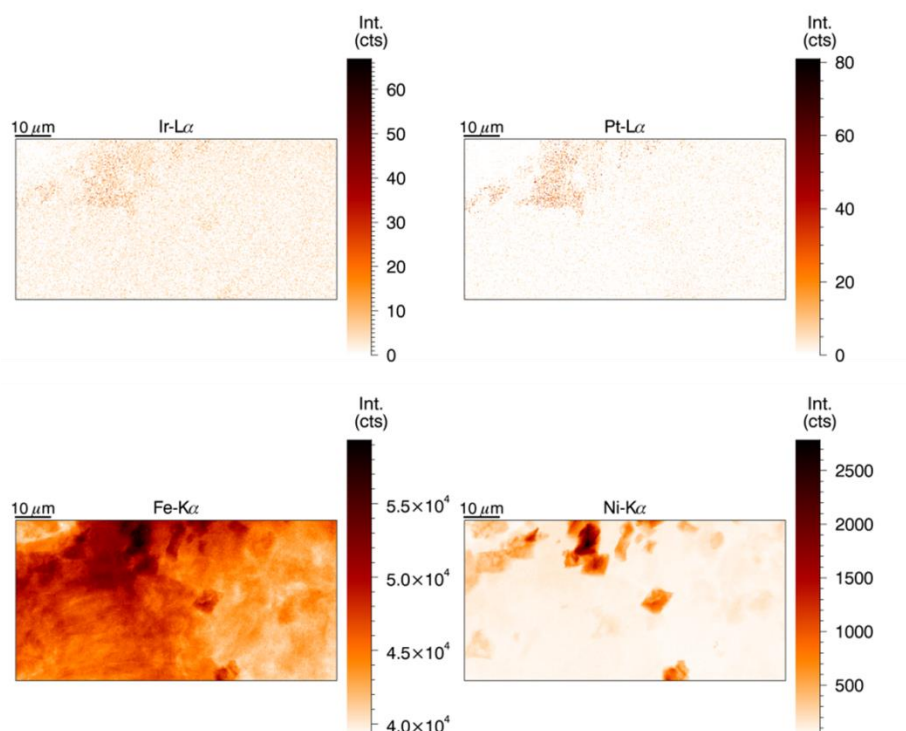


Figure 7-4 XRF image for Ir, Pt, Fe and Ni of the overview scan ( $93 \times 46 \mu\text{m}$ ) on goethite particle PTC/12 (200 nm step size, 0.1 s dwell time, 17.5 keV) a faint Pt and Ir signal is found in the upper-left corner, while clear Ni-rich spinel crystal can be seen throughout the map.

Figure 7-5 shows the laboratory based analysis of goethite spherule (PTC/12). The  $\mu\text{CT}$  virtual slice on the right of this image reveals some small bright spots dispersed throughout the spherule. These bright specks are the Ni-rich spinel crystals which also show up in the synchrotron measurements.

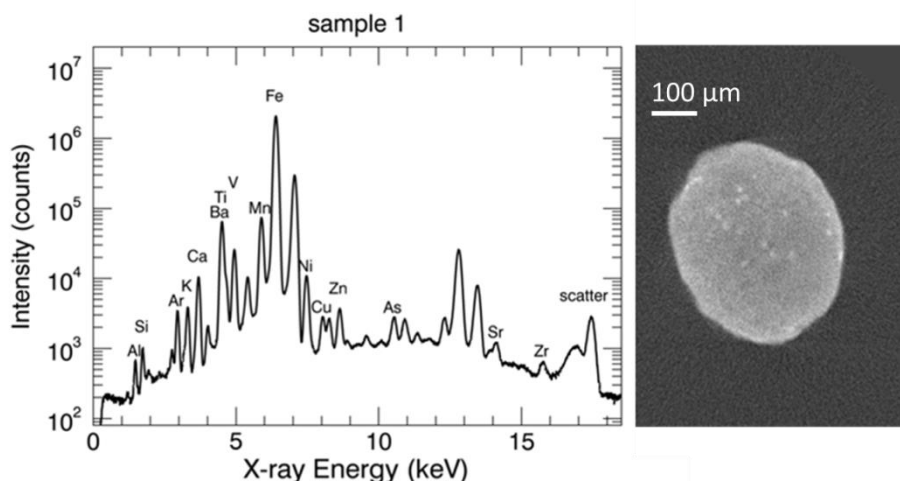


Figure 7-5 Lab-based analysis of goethite spherule PTC/12. Left: sum spectrum of XRF scan (cXRF, 40 kV, 0.6 mA, 5 s LT, 20  $\mu$ m step size); right: virtual slice of  $\mu$ CT scan (Radeye, 70 kV, 3 W, 500 ms, 1001 projections)

A second sample yielding a definite Pt signal was the sanidine spherule FPL/12. The lab-based analysis had revealed quite some internal structure in the sample, as can be seen in Figure 7-6. The arrow on this figure indicates the approximate region analysed during the SR experiment at ID16B.

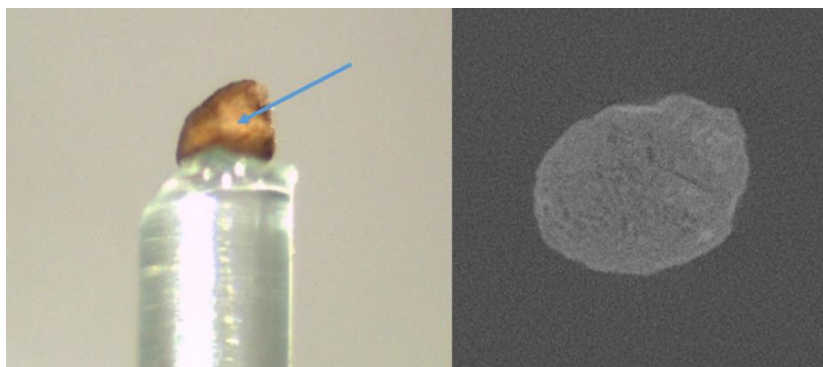
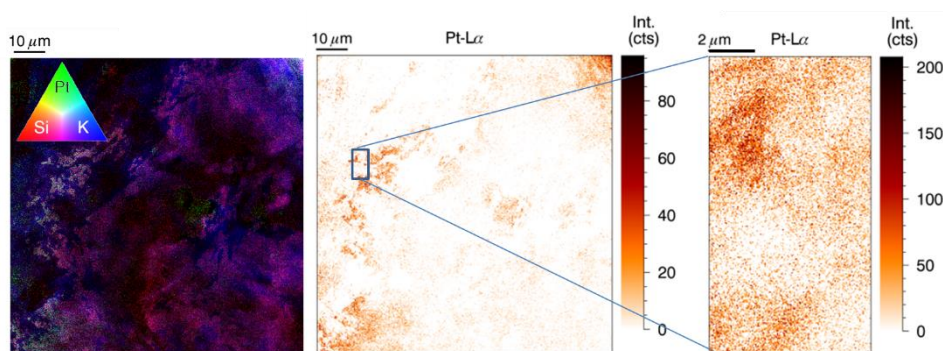


Figure 7-6 Lab-based analysis of sanidine spherule FPL/12. Left: microscope image with approx.. area of SR based analysis indicated; right: virtual slice of  $\mu$ CT scan (Radeye, 70 kV, 3 W, 500 ms, 1001 projections)

Some XRF maps on this particle are given in Figure 7-7. The RGB image on the left of this figure shows the beautiful structured matrix of this sample, which is predominantly visible in the Si and K signal. Pt is also included in this image and it can be seen it is dispersed all over the 99 by 99  $\mu\text{m}$  scanning area. This is more clearly visible in the central image, which solely depicts the Pt- $L_{\alpha}$  distribution. In the image in the middle, a small rectangle indicates the location of a 7 by 13  $\mu\text{m}$  detail scan (represented by the image on the right of Figure 7-7). In this detail scan, Pt is clearly visible and has a structure which resembles the one found in the overview scan.



*Figure 7-7 XRF imaging on a sanidine particle (FPL/12). On the left an RGB (Si/Pt/K) image of the overview scan (99 x 99  $\mu\text{m}$ ), showing the finely structured matrix with Pt present in several locations (200 nm step size, 0.1 s dwell time, 17.5 keV). In the middle is the Pt- $L_{\alpha}$  image of the same scan to get a clear view on the Pt structures. On the right, a detail scan on one of the Pt-rich areas is shown (50 nm step size, 0.3 s dwell time, 17.5 keV).*

Except for an association with Ti, Cr, and Y, no clear host phase for the Pt is apparent. The slight deformation noticeable when comparing the overview with the detail scan is due to the way the fast scan for the overview was performed. In the horizontal scanning direction, a continuous scan was employed, which means the motor is moving at a specific speed while the detectors periodically sample the XRF-signal with specific time intervals defined by the scanning speed and the requested pixel size. In this case, the speed of the motors was 2  $\mu\text{m/s}$  while the detectors saved their accumulated spectrum every 0.1 s. This creates an integrated spectrum of an area 200 nm wide and 50 nm (i.e. the

beam dimension) high. Hence, a minimal loss of information on the horizontal line is achieved. However, the vertical movement is performed in one single 200 nm step, causing a gap of 150 nm between 2 adjacent horizontal lines. To create an image with the correct aspect ratio, the pixels are made 200 x 200 nm in the overview map, which can cause a deviating image when compared to detail scans which can be further enhanced due to rescaling of the color bar.

Although Pt was found in some of the microkrystite spherules, the beamtime merely proved the fact that PGE rich regions are sparse, contain very low concentrations of these elements and are not restricted to particular mineral host phases (e.g., Ni-rich spinels). However, the analysis of these sample at given resolution and detection limits for a large part of the periodic table did give a considerable amount of additional information, which might help solving some additional scientific questions, next to the original problem statement.

#### **7.4.3.2. Additional scientific questions**

Coupled with other analytical techniques, the results of this beam time can aid in solving several scientific questions concerning the processes leading to the formation and subsequent alteration of distal impact spherules. These include:

1. Alteration of the original phases into the current composition of the spherules. Goethite may indicate pseudomorphic replacement after olivine, K-feldspar exhibit pseudomorphic textures after Ca-rich pyroxene or plagioclase, and glauconite represents former glass spherules without crystallites.
2. The behavior of refractory elements in the microkrystites to trace the potential occurrence and distribution among condensates. The original phases composing the spherules (likely olivine, pyroxene, plagioclase, and glass) may reflect a continuous series condensed at different temperatures within the vapor plume consisting of both vaporized target and projectile matter. Refractory high-T

condensation phases, such as olivine, may be enriched in moderately to highly refractory lithophile (Sc, V, Y, Zr, Nb, REE, Hf, Ta, Th) and siderophile (Cr, Co, Ni, W, Ir, Pt) elements, relative to lower temperature condensates.

3. Identification of the projectile. As the vapor plume consists of both vaporized target and projectile matter, chemical elements such as Cr, Ni, Ir, and Pt may be used to trace and identify the meteoritic signature inherited from a CM or CO carbonaceous asteroid.
4. What is the role and origin of zinc? Zinc concentrations and isotope ratios have been used in impact products to trace the potential occurrence of impact volatilization. Inversely, condensation effects should induce opposite isotopic effects, provided that the Zn present in the spherules is primary.

Elemental information and in specific the (nanoscopic) elemental distribution can thus be important to solve this scientific jigsaw.

In order to resolve the first question, concerning the alteration of the pristine phases to their current form, several well-documented replacement paths are known and may be confirmed by tracing the distribution of major elements such as Ca and K. Refractory elements (Ti, Ca, Y and V) appear to be present in small nuggets and may in some cases be linked to siderophile element enrichments. Their behavior and distribution can thus help us understand the history of these spherules.

With regard to determining the origin of the projectile and the distribution of the meteoritic matter, the PGE signature would be an important step forward, however, information on the Ni content or the role of Zn can also provide insights.

Finally, Zn shows a strange signature in these samples, with possible correlation to e.g. Ni, a correlation which is tricky to explain, since it concerns a moderately refractory and a moderately volatile element. Understanding the primary nature or subsequent redistribution of one of

these elements can thus aid in refining the origin and distribution of the other. Further investigations to determine amongst other the isotopic signature of these elements (mainly Zn) will be needed, but the elemental information already available from this beam time has been crucial in identify these four scientific questions and will be valuable when trying to answer them.

## 7.5. References

- (1) Fischer, A. H.; Jacobson, K. A.; Rose, J.; Zeller, R. *Cold Spring Harbor Protocols* **2008**, 2008, pdb.prot4986.
- (2) Alvarez, L. W.; Alvarez, W.; Asaro, F.; Michel, H. V. *Extraterrestrial cause for the Cretaceous-Tertiary extinction*. **1980**, 1095-1108.
- (3) Belza, J.; Goderis, S.; Smit, J.; Vanhaecke, F.; Baert, K.; Terryn, H.; Claeys, P. *Geochimica Et Cosmochimica Acta* **2015**, 152, 1-38.
- (4) Goderis, S.; Simonson, B. M.; McDonald, I.; Hassler, S. W.; Izmer, A.; Belza, J.; Terryn, H.; Vanhaecke, F.; Claeys, P. *Earth and Planetary Science Letters* **2013**, 376, 87-98.
- (5) Goderis, S.; Tagle, R.; Belza, J.; Smit, J.; Montanari, A.; Vanhaecke, F.; Erzinger, J.; Claeys, P. *Geochimica et Cosmochimica Acta* **2013**, 120, 417-446.
- (6) Montanari, A.; Hay, R. L.; Alvarez, W.; Asaro, F.; Michel, H. V.; Alvarez, L. W.; Smit, J. *Geology* **1983**, 11, 668-671.
- (7) Belza, J.; Goderis, S.; Montanari, A.; Vanhaecke, F.; Claeys, P. *Geochimica et Cosmochimica Acta* **2017**, 202, 231-263.



# Chapter 8

## Summary, conclusions and outlook

This doctoral dissertation focussed on X-ray based imaging techniques through the development of the laboratory based HERAKLES 3D X-ray scanner and by optimizing procedures for nanoXRF imaging experiments at synchrotron radiation facilities. The main applications were found in biomedical research (i.e. ovarian cancer treatment) and in Earth and planetary sciences (e.g. meteorite particles and deep-Earth diamonds), where the elemental information with trace level sensitivity retrieved by XRF spectroscopy yields valuable insights into the origin and history of these unique samples.

### 8.1. Summary and conclusions

#### 8.1.1. The HERAKLES 3D X-ray scanner

The primary task during this PhD project was the development, characterization and application of the novel HERAKLES laboratory based X-ray imaging setup. It contains three complementary 3D analysis methodologies, being  $\mu$ CT, XRF-CT and confocal XRF analysis. Depending on the envisaged application, morphological and/or elemental information can be obtained in a single experimental run. Chapter 4 of this work introduced the reader to this instrument and its characteristics.

The  $\mu$ CT setup has the capability of sub-micron imaging (minimal spot size 700 nm) and offers a choice between two detectors, each optimized for a different type of sample, i.e. samples with a heavy (e.g. geological materials) or light matrix (e.g. biological samples).

Three dimensional elemental information can be obtained by using either the XRF-CT or confocal XRF setup. Both are based on a Mo anode tube equipped with capillary optics.

The tube with monocapillary optics at the XRF-CT end-station creates a quasi-parallel X-ray beam (divergence 8 mrad) with a 20  $\mu\text{m}$  spot size (@ the Mo- $K_\alpha$  line). Two large area (150  $\text{mm}^2$  active area) SDDs in dual detector mode are used to create a large detector solid angle. This end-station is the optimal technique when 3D elemental information of relatively large regions of a sample is desired. Best results are obtained for samples with low self-absorption.

The confocal XRF setup uses polycapillary optics to create a conical X-ray beam with a focal point (10 x 13  $\mu\text{m}^2$  [H x V] @ Mo- $K_\alpha$ ) positioned 3.6 mm from the tip of the optics. Two SDD detectors (80  $\text{mm}^2$  active area) are positioned in dual detector layout. One detector is used in conventional mode, while the other is fitted with a specially designed polycapillary optics for confocal measurements. When the focal points of the optics of source and detector coincide, a 30 x 30 x 10  $\mu\text{m}^3$  (length-width-height, FWHM) volume can be probed. Due to the relatively low count rate in confocal mode, long measurement times are required to obtain statistically significant results, hence this setup is best suited when only a few hot spots are to be investigated, or to scan depth profiles of a layered sample.

Integration of the different techniques is realized via the high-precision motor system, with 13 independent motors, and dedicated control software. The performance of the integration procedure could be illustrated using experimental examples.

The HERAKLES scanner has many scientific applications, ranging from geology, archaeology, ecotoxicology, material sciences and catalysis to

biomedical and pharmaceutical applications. Three showcase applications were presented in Chapter 5, being the *Daphnia magna* model organism, perlite support material for bio-catalysis and the investigation of layered test samples in an cultural heritage setting (comparing confocal XRF with Micro-SORS). The internal structure of the daphnia could be imaged, coupled to a 3D elemental map which could be clearly correlated to organs of the organism (e.g. Ca being predominantly present in the carapax). The perlite scan could be used to calculate the difference in porosity between blank and used particles, while additional XRF scans (complemented by using a second laboratory based instrument) revealed S to be an indicative element for the biofilm. The layered test samples yielded insight in the strengths and weak points of confocal XRF spectroscopy for resolving microscopic layers of pigments. As could be expected, XRF scored best for pigments based on high Z elements and was unable to detect layers based on organic compounds. The complementarity with Micro-SORS was indicated in the latter case.

### 8.1.2. Nanoscopic XRF imaging at SR facilities

Within the context of this PhD project, several experimental periods at state-of-the-art SR facilities were devoted to nanoXRF imaging, in some cases coupled to complementary X-ray based analysis techniques such as XANES. In this work the focus was put on the ID16B beamline where most of these experiments were performed.

Detailed characterization of the properties of the ID16B setup was performed during each beamtime. The properties of the first experimental session (April 2014), when the instrument was still in its commissioning phase, and the last (October 2017) were compared. In terms of beamsize, there was no significant difference ( $\approx 50$  nm in each case). When comparing the detection limits, an improvement was noted, (e.g. rel. LOD of Cu went from 4 to 1 ppm at 1000 s RT) although part of this

improvement was due to the dual detector mode which could be employed during the 2017 beamtime, but not in 2014.

The samples which were analysed during these beamtimes were meteorite fragments from achondrite NWA6693, diamond inclusions in diamond SL05, sections of cisplatin treated ovarian cancer tumors and microkrystites and Antarctic micro-meteorite spherules.

The NWA6693 fragments contained a “bubble-like” stream of inclusions which were shown to be enriched in Cr, Ti and Mn, while a few Ni-rich inclusions were found. A large fraction of these features was smaller than 1  $\mu\text{m}$ , indicating the vital role of nanoXRF imaging. Diamond SL05 revealed a lot of features with varying elemental compositions. Some of these inclusions were enriched in iron, and could hence add information to preliminary Raman scans possibly detecting ringwoodite inclusions. Other phases most likely did not stem from deep-Earth based on their elemental composition and hence were hypothesized to have stuck to the diamond on its way to the surface.

There were two separate beamtimes dedicated to the ovarian cancer tumor samples, the first of which was purely focussing on XRF imaging. It was discovered the cisplatin drug (detected by its indicative element Pt) resides mostly outside the tumor cells, while it should enter the nucleus of these cells to be effective. Pt appeared to be linked to string-like S rich structures in the ECM. This could be important information on the resistance mechanism of the tumors towards the drugs, hence during the second beamtime the nature of the Pt residing outside the cells was assessed with nanoXANES. Due to technical issues (interference of the W-L2 lines of the beamlines multi-layer mirror with the targeted Pt-L3 line) no optimal results were obtained, although the fact even these low-quality scans showed some info was encouraging the retry the experiment once a new multi-layer made of Pd was installed at ID16B (planned in June 2018).

The microkrystites beamtime aimed at determining the distribution of PGEs in these samples, however, only in a few scan traces of Pt and possibly Ir were found. The nanoscopic elemental distribution of

elements such as Ca, Zn and Ni provided new research questions which will certainly increase our knowledge on the major impact event responsible for these distal impact ejecta samples.

### 8.1.3. Symbiosis of the laboratory and synchrotron

When comparing the characteristics of SR and laboratory based instruments, it is obvious the latter is by far outperformed by the first. However, in Chapter 7 it was shown these two settings can be highly complementary when optimizing the procedure of preliminary beamtime preparation. Examples were given where synchrotron technology and know-how was used to optimize lab procedures, while some experimental procedures developed and tested in the lab proved advantageous during a beamtime. Preliminary characterization of samples taken to a SR experiment proved its worth in constructing an experimental roadmap, optimizing the output of the beamtime. An illustration on microkrystites samples was given.

## 8.2. Future outlook

Although the HERAKLES scanner is fully operational, some work still remains in further improving its control software and to optimize the experimental protocols. Certainly in terms of integrated data analysis there is still room for additional developments, e.g. the use of the 3D map of mean attenuation coefficients obtained with  $\mu$ CT could be employed in the reconstruction algorithms for XRF-CT or the quantification of confocal XRF analysis to correct (partially) for the self-absorption effects. Naturally, further optimization of the setup will make it even more suitable for a wide field of applications and hopefully in the next few years a lot of academic collaborators will perform high-impact experiments using HERAKLES.

In terms of synchrotron based nanoXRF imaging the developed experimental procedures, with a large focus on lab-based preliminary characterization of the samples, will be used in the future to further maximize the information gather during beamtimes. Furthermore, the design of the HERAKLES scanner might prove interesting for implementation at a synchrotron beamline, with some adaptations dictated by the layout of the beamlines in question. Certainly with the oncoming upgrade program of the ESRF (starting in 2019) it is an excellent timing to perhaps rethink how we perform experiments and to design novel, multi-methodological approaches for X-ray based analysis.

Hopefully the fruitful collaborations with our current academic partners and new partnerships will keep on providing exciting scientific results in the future.

### 8.3. Summary of the authors input to HERAKLES

Building the HERAKLES scanner was of course a team effort, With several scientists working to complete the setup. Hence this section to elucidate the contribution of the author to this state-of-the-art instrument.

- ✓ Testing and characterization of all XRF equipment
- ✓ Incorporation of the XRF setups in the overall instrument
- ✓ Installation of the  $\mu$ CT setup (in collaboration with Bert Masschaele)
- ✓ Calibration of motor system (in collaboration with Bert Masschaele)
- ✓ Identification of the reference positions for the instrument
- ✓ Design of mounting system for capillary optics on confocal detector (in collaboration with Bart Vekemans and Davy Depauw)
- ✓ Development of control software for the XRF tubes and detectors
- ✓ Development of software for XRF experiments and preliminary (online) data analysis

- ✓ Co-development of software linking the different setups (in collaboration with Bert Masschaele)
- ✓ Design of experimental protocols incorporating multiple analysis techniques
- ✓ Characterization of the completed HERAKLES instrument
- ✓ Application of the HERAKLES instrument to investigate multiple samples in scientific collaborations

# A1: English summary

In many scientific fields there is a need to three-dimensionally analyse unique and precious samples in a non-destructive way. X-ray based 3D analysis techniques are well-suited to resolve this challenge.<sup>1-5</sup>

The development of the HERAKLES 3D X-ray scanner at Ghent University created a unique scientific instrument incorporating three complementary methodologies being microscopic X-ray computed tomography ( $\mu$ CT), X-ray fluorescence tomography (XRF-CT) and confocal XRF.<sup>4</sup> The  $\mu$ CT setup yields morphological information on the interior of an object, while the two XRF techniques provide a 3D elemental distribution. Certain applications require high spatial resolution (i.e. submicron) chemical information for solving the scientific question. Not even the current state-of-the-art in laboratory based XRF imaging instruments can achieve scans with this kind of resolution. Synchrotron radiation (SR) based experiments at high-end setups such as beamlines ID16 or ID13 of the European Synchrotron Radiation Facility (ESRF, Grenoble, France) offer the possibility to use a diverse set of X-ray based analysis techniques with a spatial resolution of 100 nm or smaller.<sup>6,7</sup> A drawback of SR based experiments however that there is typically restricted experiment time available.

Since high-end SR based and laboratory based setups are working at very different levels of spatial resolution, their techniques are highly complementary. Making use of this complementarity, a lab-based procedure can optimize the output of SR experiments by preliminary characterization of the samples, providing a detailed roadmap for the beamtime and aiding in region of interest (ROI) selection.



## Methods

### HERAKLES 3D X-ray scanner

The HERAKLES 3D X-ray scanner was developed during this project in a collaboration between the Ghent University XMI and UGCT groups with financial support from the Hercules foundation. It incorporates three 3D X-ray based analysis techniques. Unlike most multi-methodological instruments, HERAKLES uses its high precision air-bearing motor system coupled with dedicated control software to integrate three separate end stations by moving the sample stage from one to another as can be seen in Figure A1-0-1, instead of arranging all the hardware around a central, fixed sample stage. This approach allows each technique to be optimized without compromises being necessary.

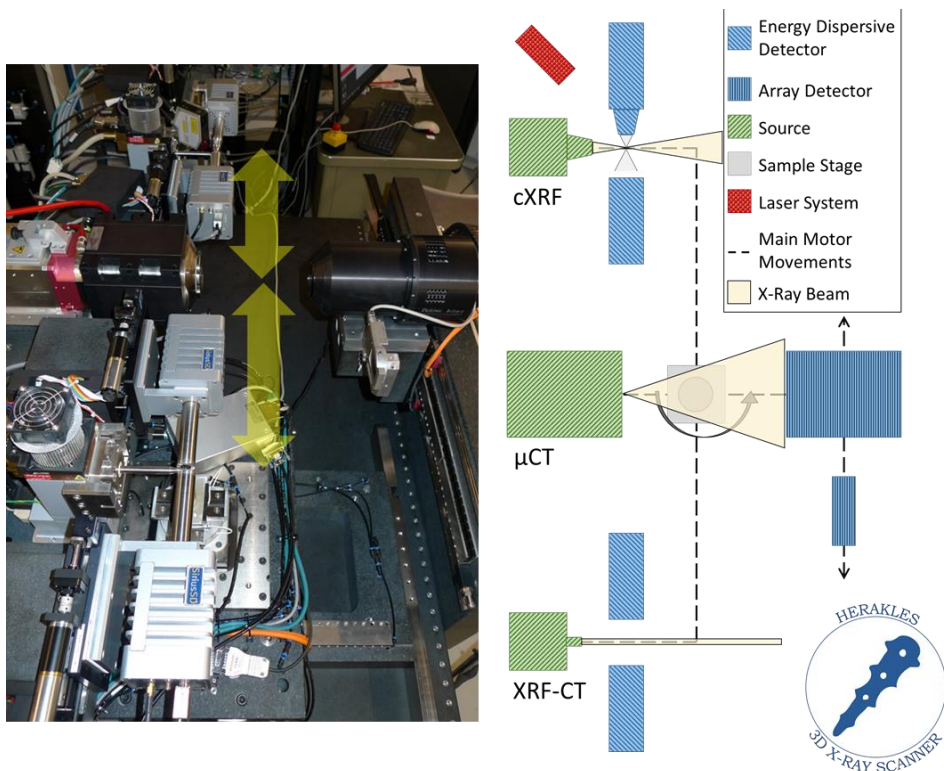


Figure A1-0-1 Design of the HERAKLES 3D X-ray scanner, on the left a picture of the setup, with a schematic representation on the right. From top to bottom you see the confocal XRF (cXRF), micro-tomography ( $\mu$ CT) and XRF tomography (XRF-CT) stations.

## **X-ray Computed Tomography**

The  $\mu$ CT setup uses a high resolution transmission target open microfocus X-ray tube (X-RAY WorX GmbH, Garbsen, Germany). Voltage values between 20 and 100 kV can be applied, with a maximum target power of 3 W using a microfocus spot. The smallest achievable spot size is 700 nm, as stated by the manufacturer. The tube head is water cooled. Two different X-ray detectors are available: a Photonic Science Very High Resolution (VHR) CCD sensor (Photonic Science, Millham, UK) equipped with a very thin Gd<sub>2</sub>OS:Tb scintillator and a RadEye CMOS detector (Teledyne DALSA Inc., Ontario, Canada) which has a thicker scintillator, making it better suited for the analysis of highly attenuating samples. The fan shaped beam allows changing the magnification of the object by altering the sample-to-source distance.

## **X-ray Fluorescence Tomography**

A 50 W/50 kV Mo anode microfocus source with monocapillary optics (Xbeam, X-ray Optical Systems Inc., East Greenbush, NY, USA) with a spot size of 20  $\mu$ m (@ Mo-K $\alpha$ , 17.48 keV) is used to generate the pencil beam needed for XRF tomography. The beam has a small divergence of 8 mrad. Two large area SDD detectors (SGX) are installed in dual detector mode. They have a crystal area of 170 mm<sup>2</sup>, collimated on chip to 150 mm<sup>2</sup> active area. When positioned at 2 mm from the sample, the dual detector setup is able to detect 72% of the total emitted photons assuming a point source at the position of the sample.

## **Confocal X-ray Fluorescence Spectroscopy**

The confocal XRF setup uses a 50 W and 50 kV Mo anode microfocus X-ray tube equipped with polycapillary optics (Xbeam, X-ray Optical Systems Inc., East Greenbush, NY, USA). It has a working distance of 3.6 mm and a spot size of 10  $\mu$ m x 13  $\mu$ m (H x V @ Mo K $\alpha$ ). Two SDD

detectors (SiriusSD, SGX Sensortech Ltd, Chelmsford, UK) with 80 mm<sup>2</sup> active crystal area and a crystal thickness of 450 µm collect the fluorescent photons. One detector is equipped with polycapillary optics (XOS) to allow confocal measurements. The size of the microvoxel is 30 x 30 x 10 µm<sup>3</sup> (length-width-height, FWHM). A 1D laser triangulation system for distance measurements (Micro-Epsilon Messtechnik, Ortenburg, Germany) is installed as a safety system and to aid during alignment.

### **ESRF beamline ID16B**

The ESRF ID16 beamline is an extended beamline with two independent end-stations, ID16A-NI (nano-imaging) for imaging applications with a spatial resolution<sup>8</sup> down to 10 nm and ID16B-NA (nano-analysis) specializing in a wide range of X-ray spectroscopic techniques with a resolution of 50 nm by making use of a KB mirror system. Both pink beam mode ( $\Delta E/E \approx 10^{-2}$ )<sup>6</sup> having an energy of approximately 17.5 keV and tunable monochromatic radiation ( $\Delta E/E \approx 10^{-4}$ )<sup>6</sup> can be requested. Relative limits of detection for elements such as Cu and Zn are approximately 1 ppm (determined using long point scans on NIST SRM1832).

## **Results**

The performance of the developed HERAKLES scanner was demonstrated using several real-life applications including the ecological model organism *D. magna*, perlite support material for bio-catalysis and the analysis of multi-layered samples in a cultural heritage setting. In all cases the scanner performed well, giving detailed information on the interior morphology of the daphnia which could be coupled to the elemental distribution (Figure A1-0-2).

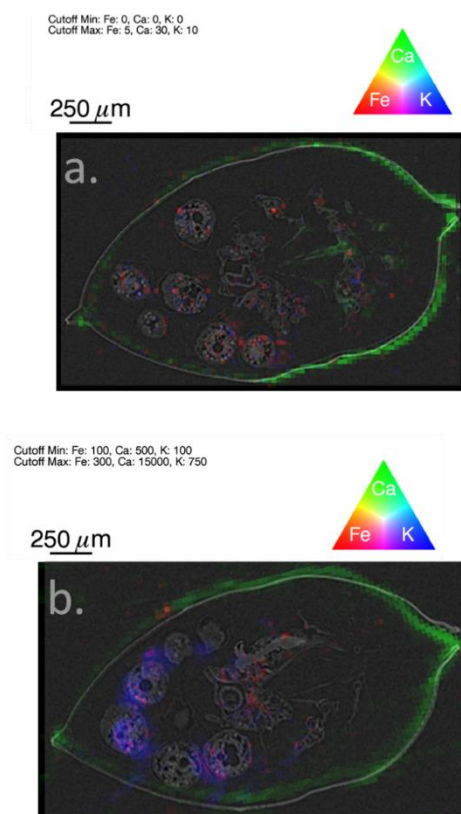
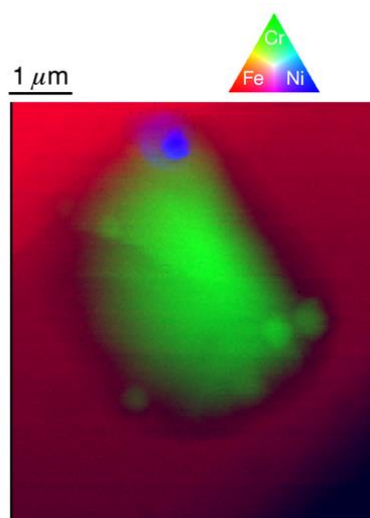


Figure A1-0-2 RGB (Fe/Ca/K) XRF image overlaid with  $\mu$ CT virtual slice for a. Confocal XRF (40 kV, 0.8 mA, 30  $\mu$ m step size, 10 s LT) and b. XRF-CT (40 kV, 0.8 mA, 30  $\mu$ m step size, 10 s LT, 90 projections); due to a slight misalignment of the XRF-CT setup, the images are not identical.

The feasibility of assessing the formation of biofilm in perlite particles using  $\mu$ CT was proven, while additional 2D XRF mappings revealed S to be a good indicative element for the presence of this biofilm. In a comparison with micro-SORS (a Raman spectroscopy based, depth sensitive methodology), confocal XRF proved to perform well for samples with paints containing high Z elements (e.g. Ti, Fe, Cd, Bi) or thin metal foils. It failed to yield good results when organic paints were used. These results proved highly compatible with the micro-SORS technique.

During the high resolution SR experiments, the elemental signature of the bubble-like inclusions in fragments of achondrite NWA6693 was determined to be mainly Ti, Cr and Mn with a few Ni-rich inclusions also detected. A large part of these inclusions were considerably smaller than 1  $\mu\text{m}$ , highlighting the importance and value of submicron elemental analysis techniques (Figure A1-0-3). This could also be concluded from the analysis of diamond SL05, where a lot of submicron inclusions were found, with varying elemental compositions.



*Figure A1-0-3 Fe/Cr/Ni RGB image of inclusions in NWA 6693. Scanned area:  $7 \times 6 \mu\text{m}^2$ , beam dimensions: 46 nm (v)  $\times$  50 nm (h), step size: 40 nm, measurement time: 1 s per point.*

In a biomedical application at ID16B, ovarian cancer tumors treated intraperitoneally with cisplatin drugs were analyzed. Both the penetration depth into the tumor tissue of the drug at different temperatures of administering the cisplatin and the sub-cellular Pt distribution were analyzed. Temperatures above body temperature were found to give a significantly deeper penetration of the drug, yielding important experimental proof for optimization of the treatment of ovarian cancer. Pt was found to reside predominantly around string-like S structures outside the tumor cells (Figure A1-0-4), although it should penetrate into the nucleus of the cells before it is able to kill the cancer. This observation could yield new insights in the resistance mechanism of tumor cells to cisplatin treatment.

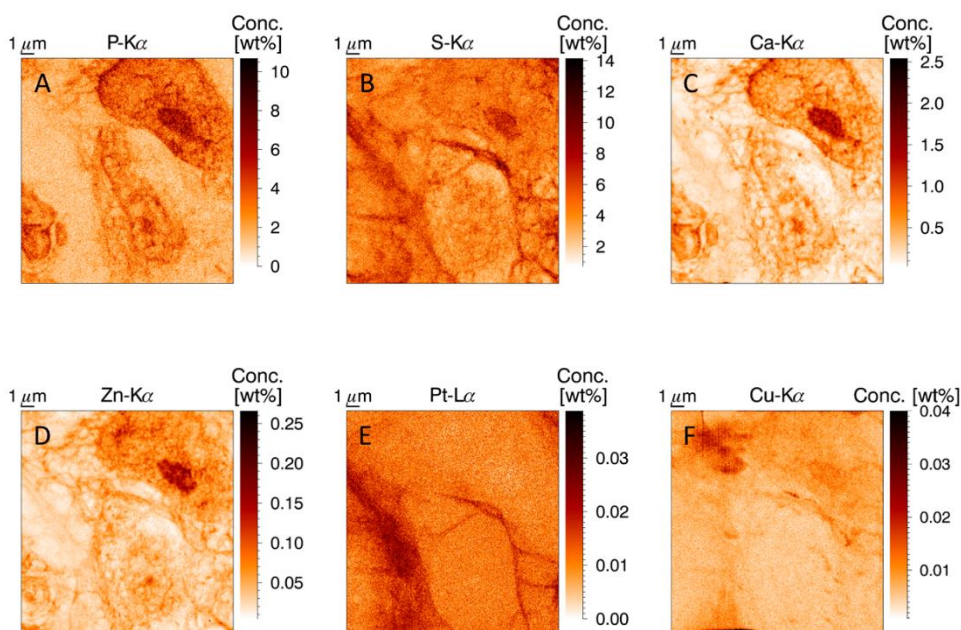


*Figure A1-0-4 XRF elemental maps of P, S and Zn. Scanned area 18 × 18 μm, beam dimensions 50 × 50 nm<sup>2</sup>, 50 nm step size, measurement time 0.1 s per point, primary beam energy 17.5 keV. A tumor cell (nucleus and part of the cell membrane) can be discerned in the upper right part of the image, while two smaller cells are found in the middle and the lower left corner.*

Further analysis using nano-XANES was performed, however due to technical issues these experiments did only reveal most cisplatin in the tumor sections was present unaltered or in a chemical state very similar to the unbound drug.

## Conclusions

The developments of several X-ray based imaging methodologies were discussed. The laboratory based HERAKLES 3D X-ray scanner was elaborated on and its characteristics were determined. The performance of this instrument relative to comparable instruments was discussed.

Nano-XRF imaging using high-end SR setups was proven to be an invaluable technique for submicron sample analysis. The specifications

of the ID16B setup were mentioned, as was the complementarity of high spatial resolution experiments with laboratory based techniques.

The applications on both the HERAKLES scanner and ID16B yielded new insights in a wide range of scientific fields, adding information to the existing knowledge and proving X-ray based imaging methodologies to be powerful techniques for 2D and 3D analysis.

The complementarity of the different techniques indicated a well-designed experimental protocol can hugely optimize the output of scientific research, by selecting the best-suited methodology for each specific research question and using information gathered with one technique to maximize the efficiency during the subsequent experiments on the same sample.

## References

- (1) De Samber, B.; Vanblaere, S.; Evens, R.; De Schamphelaere, K.; Wellenreuther, G.; Ridoutt, F.; Silversmit, G.; Schoonjans, T.; Vekemans, B.; Masschaele, B.; Van Hoorebeke, L.; Rickers, K.; Falkenberg, G.; Szaloki, I.; Janssen, C.; Vincze, L. *Powder Diffraction* **2010**, *25*, 169-174.
- (2) Golosio, B.; Simionovici, A.; Somogyi, A.; Lemelle, L.; Chukalina, M.; Brunetti, A. *Journal of Applied Physics* **2003**, *94*, 145-156.
- (3) Golosio, B.; Somogyi, A.; Simionovici, A.; Bleuet, P.; Susini, J.; Lemelle, L. *Applied Physics Letters* **2004**, *84*, 2199-2201.
- (4) Laforce, B.; Masschaele, B.; Boone, M. N.; Schaubroeck, D.; Dierick, M.; Vekemans, B.; Walgraeve, C.; Janssen, C.; Cnudde, V.; Van Hoorebeke, L.; Vincze, L. *Analytical Chemistry* **2017**.
- (5) Sasov, A.; Liu, X.; Rushmer, D. In *Developments in X-Ray Tomography VI*, 2008, pp 70780R-70780R-70789.
- (6) Martínez-Criado, G.; Villanova, J.; Tucoulou, R.; Salomon, D.; Suuronen, J.-P.; Labouré, S.; Guilloud, C.; Valls, V.; Barrett, R.; Gagliardini, E.; Dabin, Y.; Baker, R.; Bohic, S.; Cohen, C.; Morse, J. *Journal of Synchrotron Radiation* **2016**, *23*, 344-352.
- (7) Riekkel, C.; Burghammer, M.; Davies, R. *IOP Conference Series: Materials Science and Engineering* **2010**, *14*, 012013.
- (8) Cesar da Silva, J.; Pacureanu, A.; Yang, Y.; Bohic, S.; Morawe, C.; Barrett, R.; Cloetens, P. *Optica* **2017**, *4*, 492-495.

## A2: Nederlandse samenvatting

In veel wetenschapsdomeinen is er grote vraag naar niet-destructieve, drie-dimensionale analyse van unieke en waardevolle stalen. X-straal gebaseerde 3D analyse technieken zijn uitstekend geschikt om deze uitdaging aan te pakken.<sup>1-5</sup>

De ontwikkeling van de HERAKLES 3D X-straal scanner aan de Gentse universiteit creëerde een uniek wetenschappelijk instrument dat drie complementaire methodologiën omvat, zijnde microscopische X-straal tomografie ( $\mu$ CT), X-straal fluorescentie tomografie (XRF-CT) en confocale XRF analyse.<sup>4</sup> De  $\mu$ CT opstelling levert morfologische informatie betreffende het inwendige van een object, terwijl de twee XRF technieken een 3D elementendistributie geven.

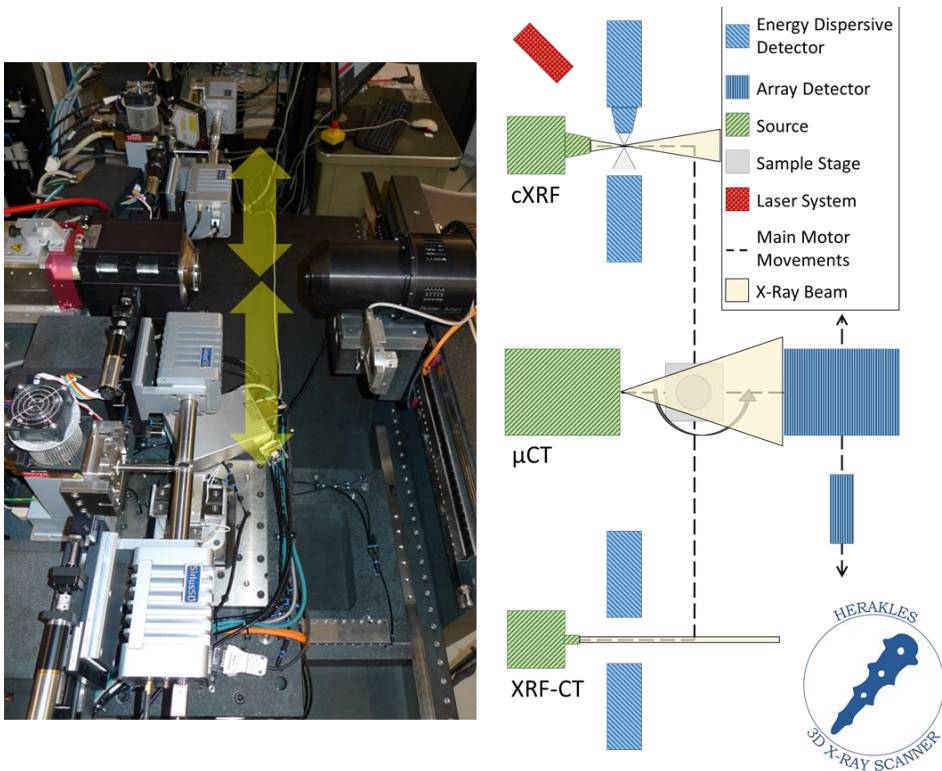
Bepaalde toepassingen vereisen chemische informatie met hoge spatiale resolutie (sub-micrometer) om het wetenschappelijk vraagstuk op te lossen. De huidige state-of-the-art in laboratorium gebaseerde XRF beeldvormingstoestellen zijn niet in staat tot scans met deze resolutie. Synchrotron straling (SR) gebaseerde experimenten aan top-opstellingen zoals beamlines ID16 of ID13 van het European Synchrotron Radiation Facility (ESRF, Grenoble, Frankrijk) bieden een diverse set aan X-straal gebaseerde analyse technieken met spatiale resoluties van 100 nm of kleiner.<sup>6,7</sup> Een nadeel van synchrotronexperimenten is de beperkte meettijd die beschikbaar is per beamtime. Daar SR en laboratorium setups op een heel verschillende schaal meten, zijn hun technieken zeer complementair. Hiervan gebruik makende kon een procedure ontwikkeld worden die gebaseerd op laboratorium technieken de output van SR experimenten optimaliseert door preliminaire analyses van de stalen.



## Methodes

### HERAKLES 3D X-straal scanner

De HERAKLES 3D X-straal scanner is ontwikkeld in samenwerking tussen de UGent XMI en UGCT groepen met financiële steun van de Hercules stichting. Het omvat drie 3D X-straal analysetechnieken. In contrast met veel multi-methodologische instrumenten gebruikt HERAKLES precieze luchtlagermotoren en toegewijde controlesoftware om de drie onafhankelijke technieken met elkaar te verbinden door het staal te bewegen van de ene opstelling naar de andere (Figure A1-0-1) in plaats van alle hardware rond een vaste montagepositie voor de stalen te plaatsten. Deze werkwijze voorkomt dat er compromissen gemaakt moeten worden, waardoor iedere techniek geoptimaliseerd is.



*Figuur A2-0-1 Design van de HERAKLES 3D X-straal scanner, links: foto van de the setup, rechts: schematische voorstelling van het toestel. Van boven naar onder ziet men de confocale XRF (cXRF), micro-tomografie ( $\mu$ CT) and XRF tomografie (XRF-CT) stations.*

## **X-straal Micro-Tomografie**

De  $\mu$ CT setup gebruikt een hoge resolutie transmissietarget open micro-focus X-straal buis (X-RAY WorX GmbH, Garbsen, Duitsland). Spanningen tussen 20 en 100 kV kunnen aangelegd worden, met 3 W maximaal vermogen bij een micro-focus spot. De kleinst mogelijke spot grootte vermeld door de fabrikant is 700 nm. De kop van de buis is watergekoeld. Twee verschillende X-stralendetectors zijn beschikbaar: een *Photonic Science Very High Resolution* (VHR) CCD sensor met een dunne  $\text{Gd}_2\text{O}_3\text{:Tb}$  scintillator en een RadEye CMOS detector (Teledyne DALSA Inc., Ontario, Canada) die een dikkere scintillator heeft, waardoor deze beter geschikt is voor hoog-attenuerende stalen. De waaier-vorm van de straling zorgt dat de vergroting kan aangepast worden door de afstand tussen het staal en de bron te wijzigen.

## **X-straal Fluorescentie Tomografie**

Een 50 W Mo anode microfocus buis met monocapillaire optica (Xbeam, X-ray Optical Systems Inc., East Greenbush, NY, USA) en een spot grootte van 20  $\mu\text{m}$  (@ Mo- $K_\alpha$ , 17.48 keV) genereert de parallelle bundel die nodig is voor XRF-CT. De divergentie van de bundel is 8 mrad. Twee SDD detectoren (SiriusSD, SGX Sensortech Ltd, Chelmsford, UK) staan in duale detector modus. Deze hebben een kristaloppervlakte van 170  $\text{mm}^2$ , die on-chip tot 150  $\text{mm}^2$  gecollimeerd wordt. De detector setup kapteerd 72 % van de fluorescente straling wanneer de detectoren op 2 mm van het staal geplaatst worden.

## **Confocale X-straal Fluorescentie Spectroscopie**

De confocale XRF setup heeft een 50 W Mo anode X-straal buis met polycapillaire optica (Xbeam, X-ray Optical Systems Inc., East Greenbush, NY, USA). Deze heeft een werkingsafstand van 3.6 mm en een 10 x 13  $\mu\text{m}$  bundel (H x V @ Mo  $K_\alpha$ ). Twee SDD detectoren (SiriusSD, SGX Sensortech Ltd, Chelmsford, UK) met 80  $\text{mm}^2$  actieve

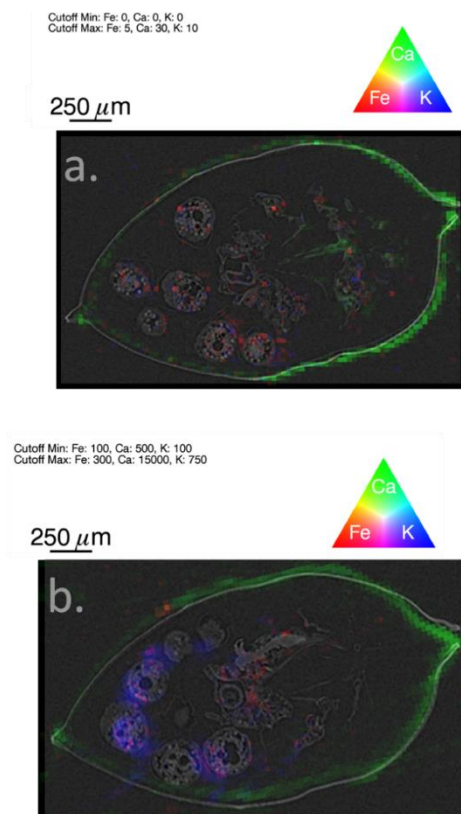
kristaloppervlakte en een kristaldikte van 450  $\mu\text{m}$  meten de fotonen op. Één detector is uitgerust met polycapillaire optica (XOS) om confocale metingen mogelijk te maken. De afmetingen van de micro-voxel zijn 30 x 30 x 10  $\mu\text{m}^3$  (lengte-breedte-hoogte, FWHM). Een 1D laser triangulatie systeem (Micro-Epsilon Messtechnik, Ortenburg, Duitsland) wordt gebruikt als veiligheidssysteem en als hulp bij het uitlijnen.

### **ESRF beamline ID16B**

Beamline ID16 aan het ESRF is een verlengde beamline met twee onafhankelijke eind-stations, ID16A-NI (nano-imaging) voor beeldvormingstoepassingen met spatiale resolutie<sup>8</sup> tot 10 nm en ID16B-NA (nano-analyse) gespecialiseerd in een breed spectrum aan X-straal spectroscopische technieken met 50 nm resolutie gebruikmakende van een KB spiegel systeem. Zowel *pink beam* ( $\Delta E/E \approx 10^{-2}$ )<sup>6</sup> als monochromatische modus ( $\Delta E/E \approx 10^{-4}$ )<sup>6</sup> kan gebruikt worden.

## **Resultaten**

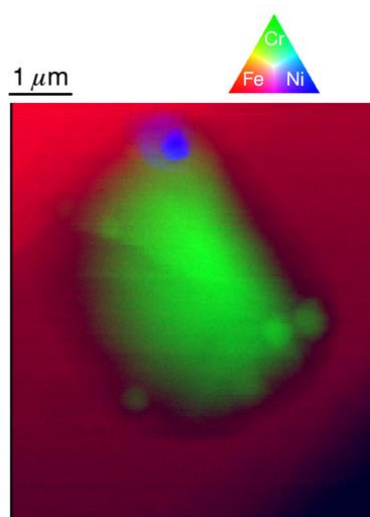
De performantie van de ontwikkelde HERAKLES scanner werd gedemonstreerd gebruikmakende van meerdere toepassingen uit de praktijk, onder andere het ecologisch model organisme *D. magna*, perliet dragersmateriaal voor bio-katalyse en de analyse van meerlagige samples in een cultuur-historische context. Bij alle toepassingen presteerde de scanner goed. Zo werd ondermeer gedetailleerde informatie verkregen over de inwendige structuren van de daphnia, gekoppeld aan de 3D elementen distributie (Figure A1-0-2).



*Figuur A2-0-2 RGB (Fe/Ca/K) XRF beeld bovenop  $\mu$ CT virtuele doorsnede van a. Confocale XRF (40 kV, 0.8 mA, 30  $\mu$ m stap grootte, 10 s LT) en b. XRF-CT (40 kV, 0.8 mA, 30  $\mu$ m stap grootte, 10 s LT, 90 projecties); door lichte misalignering van de XRF-CT zijn de beelden niet identiek.*

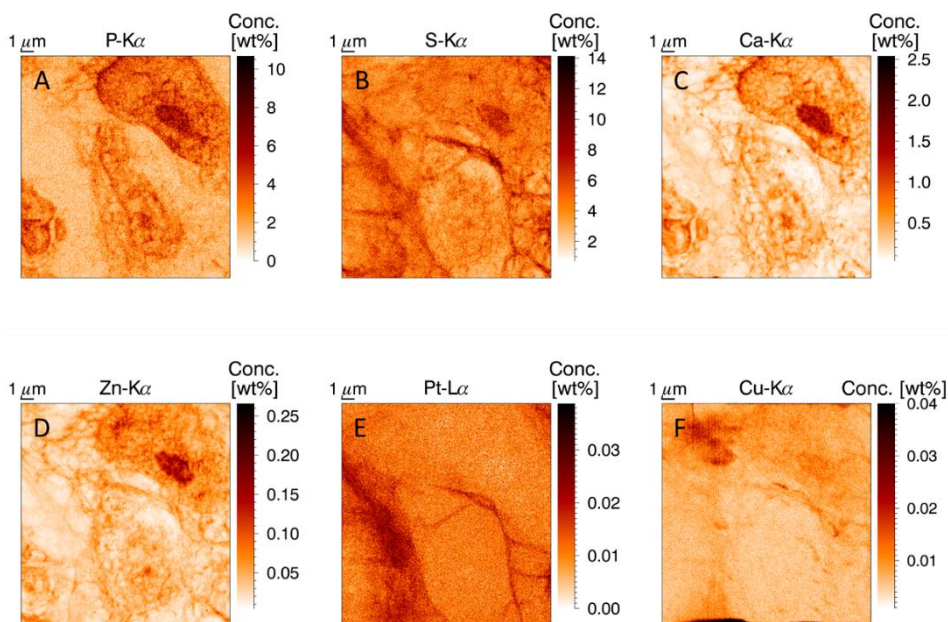
De haalbaarheid van het analyseren van de vorming van biofilm in de perliet deeltjes met behulp van  $\mu$ CT werd aangetoond, terwijl bijkomende 2D XRF beelden onthulden dat S een goed indicator element is voor deze biofilm. In een vergelijking met micro-SORS (Raman spectroscopie gebaseerde, dieptegevoelige methodologie) bewees confocale XRF goed te presteren voor stalen waarin verf met hoge Z elementen (zoals Fe en Bi) gebruikt werd of bij dunne metaallagen. Bij organische verf werden geen goede resultaten bekomen. Deze waarnemingen waren in hoge mate complementair met de micro-SORS techniek.

Tijdens hoge resolutie SR experimenten werd de elementensignatuur van inclusies in fragmenten van achondriet NWA6693 bepaald. Het betrof vooral Ti, Cr en Mn rijke inclusies, met enkele die rijk aan Ni waren. Een groot aantal inclusies waren heel wat kleiner dan 1  $\mu\text{m}$ , wat duidelijk het belang van nanoscopische analyse technieken illustreert (Figure A1-0-3). Ook bij diamant SL05 werden een groot aantal inclusies met heel diverse samenstelling en sub-microscopische afmetingen teruggevonden.



*Figuur A2-0-3 Fe/Cr/Ni RGB beeld van inclusies in NWA 6693. Scan:  $7 \times 6 \mu\text{m}^2$ , bundelgrootte: 46 nm (v)  $\times$  50 nm (h), stap grootte: 40 nm, meettijd: 1 s per punt.*

In een biomedische toepassing aan ID16B werden eierstokkankertumoren die intraperitoneaal behandeld waren met cisplatin geanalyseerd. De penetratiediepte voor verschillende temperatuursprofielen bij toediening van het geneesmiddel werd onderzocht, net zoals de verdeling van Pt in de tumoren en de kankercellen. Een temperatuur boven lichaamstemperatuur bleek voor betere penetratie te zorgen. Deze waarneming was direct inzetbaar om de behandeling van patiënten te optimaliseren. Verder werd vastgesteld dat Pt voornamelijk buiten de cellen zat, op dezelfde positie als S-rijke draadstructuren (Figure A1-0-4). Voor een goede werking moet de cisplatin de celkern binnendringen. Deze waarneming kan dus cruciaal zijn in het begrijpen van de resistentiemechanismen van tumoren.



*Figuur A2-0-4 XRF element kaarten van P, S en Zn. Scan:  $18 \times 18 \mu\text{m}$ , bundelgrootte  $50 \times 50 \text{ nm}^2$ , 50 nm stapgrootte, meettijd 0.1 s per punt, bundelenergie 17.5 keV. Een tumor cel bevindt zich in de rechter bovenhoek, met kleinere cellen zichtbaar in het midden en de linker onderhoek.*

Verdere analyse met XANES moest licht werpen op de aard van deze S-Pt link, maar door technische problemen werd enkel gevonden dat de meeste Pt aanwezig was in ongewijzigde vorm, of een vorm die heel dicht bij het originele geneesmiddel aanleunt.

## Conclusies

De ontwikkeling van verschillende X-straal gebaseerde beeldvormingstechnieken werd besproken. De HERAKLES 3D X-straal scanner werd uitgebreid belicht en de eigenschappen van dit labo-toestel werden gegeven. Het toestel werd vergeleken met soortgelijke instrumenten.

Nano-XRF beeldvorming aan hoog-performante SR setups bleek een onschatbare techniek voor sub-micrometer analyse. De specificaties van de ID16B setup werden besproken, evenals de complementariteit van hoge resolutie experimenten met laboratoriumtechnieken.

De toepassingen van zowel de HERAKLES scanner als ID16B gaven nieuwe inzichten in een breed veld van wetenschappelijke domeinen. De metingen voegden informatie toe aan de reeds aanwezige kennis en toonden aan dat X-straal gebaseerde beeldvormingsmethodes sterke technieken zijn voor 2D en 3D analyse.

De besproken complementariteit van de verschillende technieken toont aan dat een goed ontworpen experimenteel protocol de output van wetenschappelijk onderzoek drastisch kan optimaliseren door de meest geschikte technieken te selecteren voor iedere specifieke onderzoeksvraag gebruikmakende van eerder verzamelde informatie om de nieuwe experimenten zo efficiënt mogelijk uit te voeren.

## References

- (1) De Samber, B.; Vanblaere, S.; Evens, R.; De Schamphelaere, K.; Wellenreuther, G.; Ridoutt, F.; Silversmit, G.; Schoonjans, T.; Vekemans, B.; Masschaele, B.; Van Hoorebeke, L.; Rickers, K.; Falkenberg, G.; Szaloki, I.; Janssen, C.; Vincze, L. *Powder Diffraction* **2010**, *25*, 169-174.
- (2) Golosio, B.; Simionovici, A.; Somogyi, A.; Lemelle, L.; Chukalina, M.; Brunetti, A. *Journal of Applied Physics* **2003**, *94*, 145-156.
- (3) Golosio, B.; Somogyi, A.; Simionovici, A.; Bleuett, P.; Susini, J.; Lemelle, L. *Applied Physics Letters* **2004**, *84*, 2199-2201.
- (4) Laforce, B.; Masschaele, B.; Boone, M. N.; Schaubroeck, D.; Dierick, M.; Vekemans, B.; Walgraeve, C.; Janssen, C.; Cnudde, V.; Van Hoorebeke, L.; Vincze, L. *Analytical Chemistry* **2017**.
- (5) Sasov, A.; Liu, X.; Rushmer, D. In *Developments in X-Ray Tomography VI*, 2008, pp 70780R-70780R-70789.
- (6) Martínez-Criado, G.; Villanova, J.; Tucoulou, R.; Salomon, D.; Suuronen, J.-P.; Labouré, S.; Guilloud, C.; Valls, V.; Barrett, R.; Gagliardini, E.; Dabin, Y.; Baker, R.; Bohic, S.; Cohen, C.; Morse, J. *Journal of Synchrotron Radiation* **2016**, *23*, 344-352.
- (7) Riekkel, C.; Burghammer, M.; Davies, R. *IOP Conference Series: Materials Science and Engineering* **2010**, *14*, 012013.
- (8) Cesar da Silva, J.; Pacureanu, A.; Yang, Y.; Bohic, S.; Morawe, C.; Barrett, R.; Cloetens, P. *Optica* **2017**, *4*, 492-495.

# A3: Software Manual

## HERAKLES

The HERAKLES software is used to control the setup via a central user interface. This software sends out commands to all components, moving motors, changing tube settings and even running the scripts to perform  $\mu$ CT and XRF measurements.

The HERAKLES software is part of the `acquila.lvproj` LabVIEW project which can be found in `C:\Program Files\aquila_development\acquila`.

Double clicking on the `.lvproj` icon will open the window displayed in Figure A3- 1.

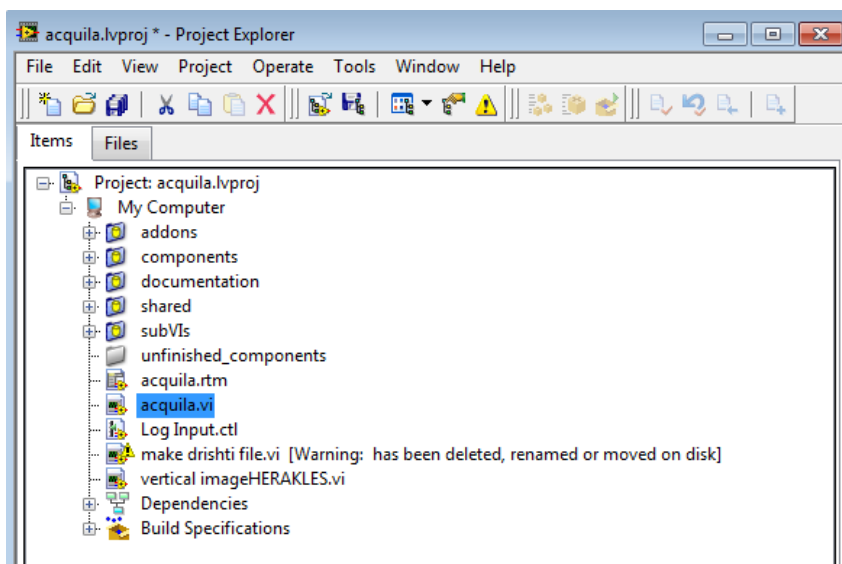


Figure A3- 1 Window of `acquila.lvproj`.



In this window all components of the project can be accessed, including all sub VI's, add-ons and control-files. However, for regular use of the HERAKLES scanner, only the *acquila.vi* virtual instrument has to be used. It can be opened by double clicking its name (indicated in blue on Figure A3- 1). The software opened by clicking *acquila.vi* is called HERAKLES. Figure A3- 2 shows the main window of this program.

The software is started by clicking the arrow in the top left corner (blue circle in Figure A3- 1). The front panel of the HERAKLES software has two main components. On the right is the image window, where the transmission images made at the  $\mu$ CT end-station are displayed. On the left the controls can be found, where commands are generated and sent to the different components of the scanner. At the bottom left corner the big red emergency stop button can be seen. In the upper right corner, the QUIT button stops the program.

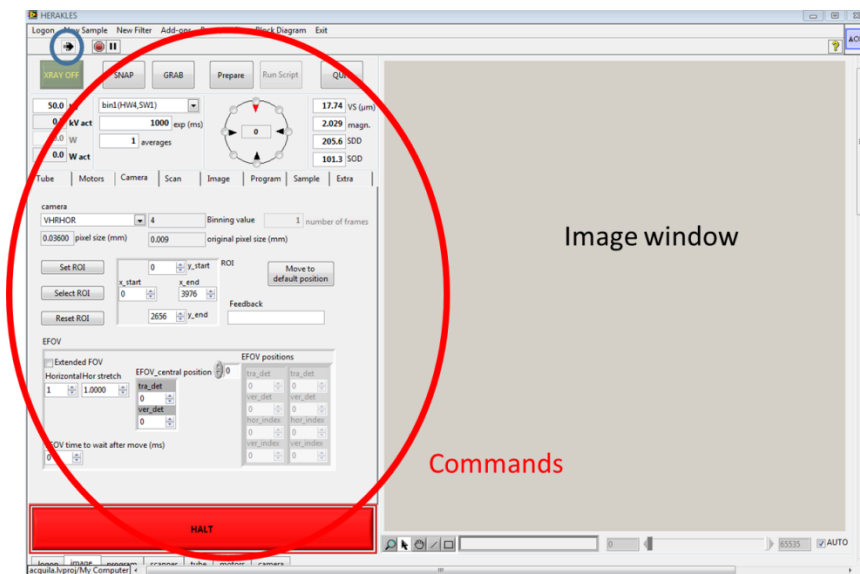


Figure A3- 2 HERAKLES software front panel.

The top section of the left panel is shown in more detail in Figure A3- 3, with the *tube* tab selected as active tab. After mounting the sample on the sample stage, the first step of an experiment is starting up the tube of the  $\mu$ CT end-station, since this equipment will be used to image and align the sample.

## Imaging the sample in transmission mode

The green button in the top left corner of Figure A3- 3 is used to start the X-ray tube on the  $\mu$ CT setup. When it is green with yellow lettering saying XRAY OFF, the tube is not active, otherwise the button flashes red and yellow, saying XRAY ON. When the XRAY button is faded (as in Figure A3- 3) it means the tube cannot be started right now.

There are two main reasons why the tube won't ramp: the door to the bunker is open (generating an interlock error) or the tube needs to go through the warm-up procedure. In the *tube* tab warmup, filament adjustment or auto-centre (bottom right corner of Figure A3- 3) can be started if needed. The interlock status is also shown there.

The settings for the tube can be selected on the top left hand side. In the *tube* tab the user can select which settings are user-controlled by selecting the desired parameter in the *output mode* drop down list. Most often the 'Target Power' is selected.

Returning to the top row of control buttons, the SNAP button is used to take a single transmission image, while the GRAB button starts a continuous data collection. The measurement time per projection is selected in *exp (ms)*, the number of averages for each image is given in *averages*, while the binning mode of the detector can also be selected (normally left on default value).

On the right hand side of Figure A3- 3, several parameters of the instrument are given: voxel size (*VS*), magnification (*magn.*) source-detector distance (*SDD*) and source-object distance (*SOD*). These data are useful when analysing the transmission image and setting up a  $\mu$ CT scan. In the future these parameters will enable definition of sample movements (e.g. by choosing a specific voxel size) but this has not been calibrated yet and is therefore not recommended! Moving the sample should always be performed with the dedicated motor commands.

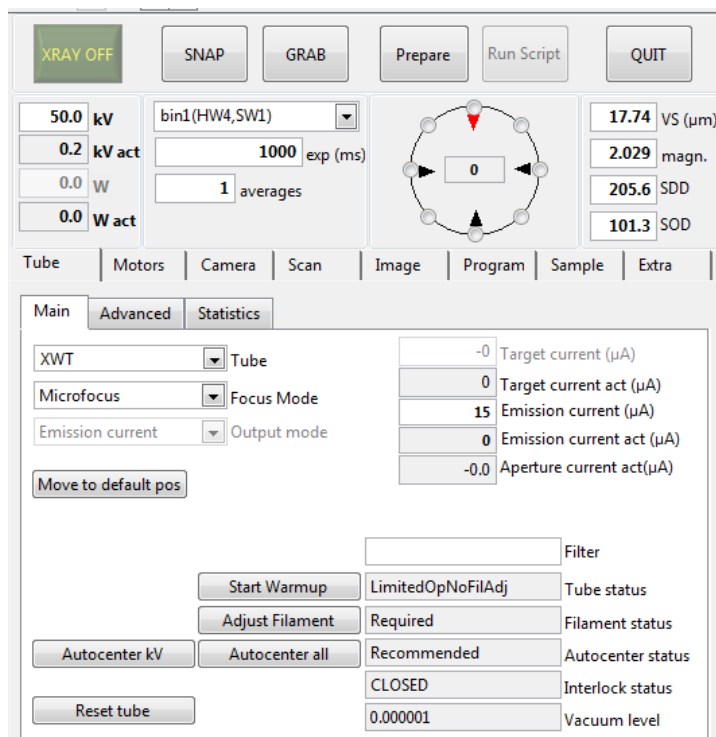


Figure A3- 3 Tube section of the command panel of the HERAKLES software.

## Movement and alignment of the sample

Figure A3- 4 gives the motor controls of the HERAKLES software, which can be accessed by selecting the *Motors* tab.

A motor is selected from the drop down list as indicated in the figure. Once a motor is chosen, the user can move it by either giving an absolute motor position or a relative movement. For absolute movement, the final destination is entered into the box and next *move abs* is clicked. For relative movement, the step size needs to be entered and then a movement in positive or negative direction can be performed.

The speed, acceleration and software limits of each motor can be changed via this tab, however, it is strongly recommended to keep the default values, since these are optimised for the individual motors.

In the bottom section, the motor can be disabled, enabled, referenced, moved to a pre-set position or reset. In practise, these functionalities are automated, the buttons only present for trouble shooting.

The circle in the top middle of the image can be used to move the rotational motor in an intuitive way. Clicking a location on the circle will rotate the sample to the corresponding angle. Central in the circle the current rotation angle is given, which is also indicated by the red triangle.

The piezo-motors can be commanded via the motor selection in the dropdown list, or with the relative movement buttons at the bottom.

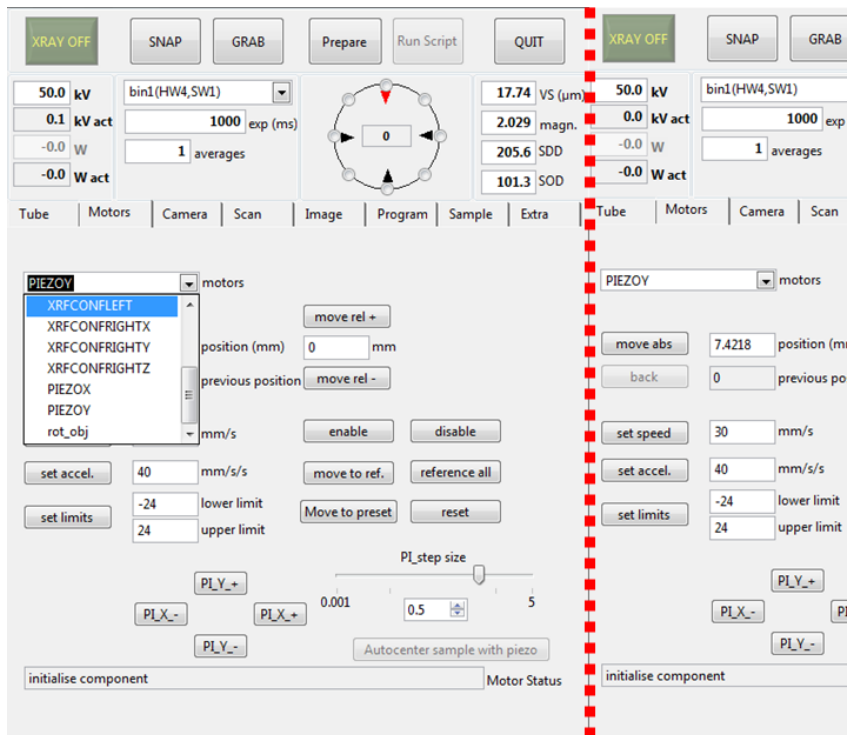


Figure A3- 4 Motor controls of the HERAKLES software, right of the red dotted line part of the interface is duplicated to reveal the functionalities hidden by the dropdown list in the left image.

Visualisation of the motor movement is performed by taking transmission images, either a SNAP after each movement or by the GRAB function. When working with the Radeye detector, using the GRAB is discouraged, since it can result in the program getting stuck.

# Camera settings

The *Camera* tab of the program (Figure A3- 5) can be used to select camera settings such as the ROI and extended FOV. In principle this tab can also be used to select the active camera. However, in practice the active camera and all these settings are predefined using the ‘settings.ini’ file and the component specific ‘\*.ini’ file before starting the program. If the user wishes to change cameras after the software has been started, this can be done via the settings.ini file (short-key: F3). A ‘\$’ is put in front of the inactive camera and then the software is reinitialised in the *Program* tab by clicking the OK button at *restore scanner default settings* as demonstrated in Figure A3- 6.

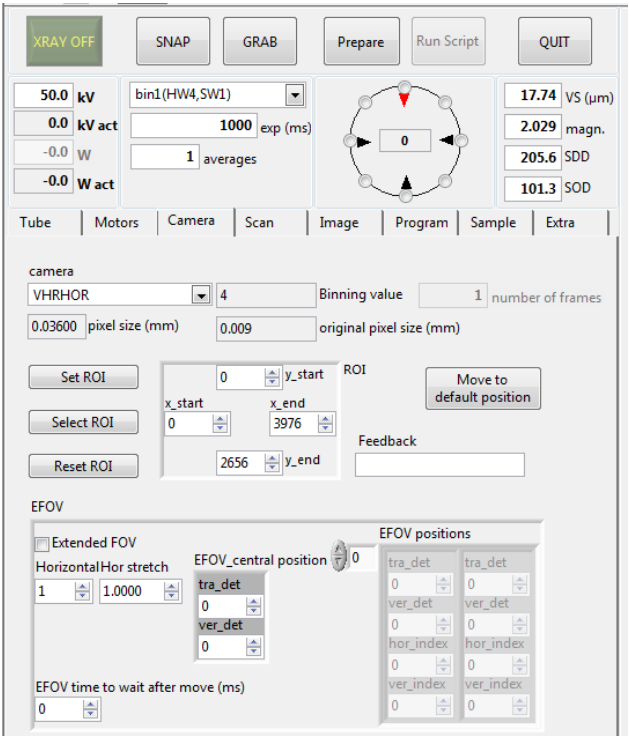


Figure A3- 5 Camera tab of the HERAKLES software.

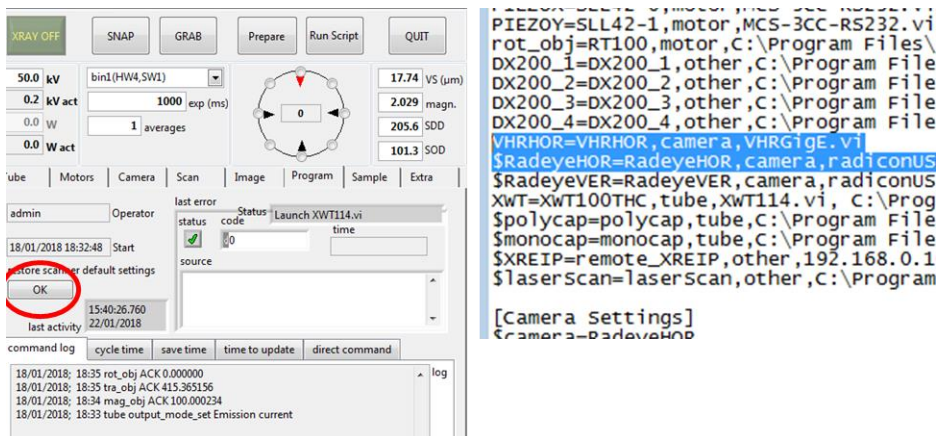


Figure A3- 6 Changing cameras during operation.

## Starting a $\mu$ CT scan

Above the rotation controller, the Prepare button can be seen. This opens the script builder for  $\mu$ CT scans. When clicking this button, the window shown in Figure A3- 7 opens, where all data on the sample needs to be completed (name, owner, size, etc.)

Figure A3- 7 Start screen of the  $\mu$ CT script builder.

Next, by clicking OK, the window as seen in Figure A3- 8 opens. The scan itself is defined in the *General* tab as shown in the figure. The scan type is smooth take and save by default (others scan types will be implemented in the future). The path to save the data should be chosen, the number of projections per 360° rotation has to be defined as should the number of each type of normalisation image (offset, pre flat field and post flat field). A prefix for the scan can be entered by the user. More detailed settings can be given using the tabs *Camera*, *Smooth*, *Motors*, *Other* and *Recon*. However, for a regular scan the *General* tab is sufficient. Once all parameters of the scan are defined, the script can be generated by clicking the *Generate script* button. Other options are also possible such as appending the script to a previous script, clearing the script(s) in the array, cancelling the script building, loading a previously saved script or saving the script. The *Accept* button saves the script and moves it to the scan section of the HERAKLES software, ready to be executed, as can be seen Figure A3- 9. At this point, it is still possible to manually change the script, adding or removing lines. The script can be started by clicking the *Run Script* button seen on the top right side.

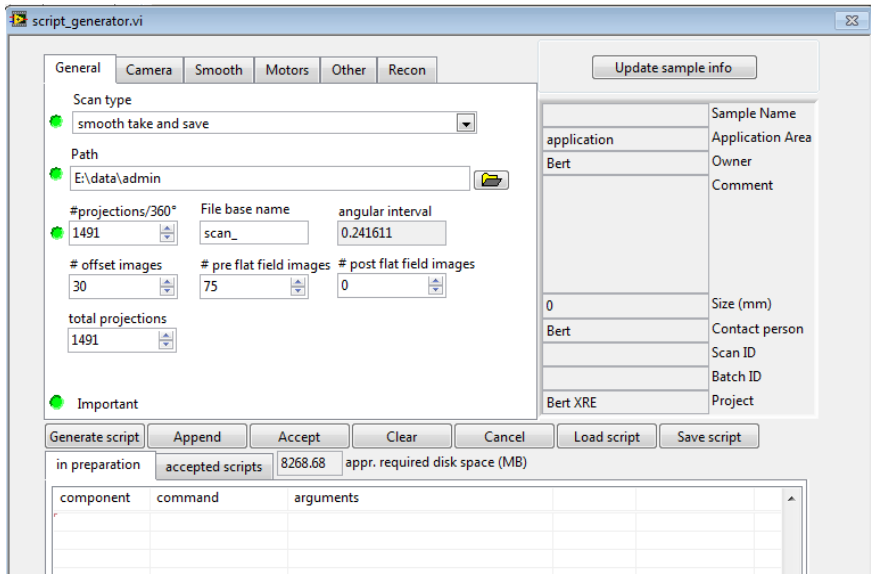


Figure A3- 8  $\mu$ CT script builder main window.

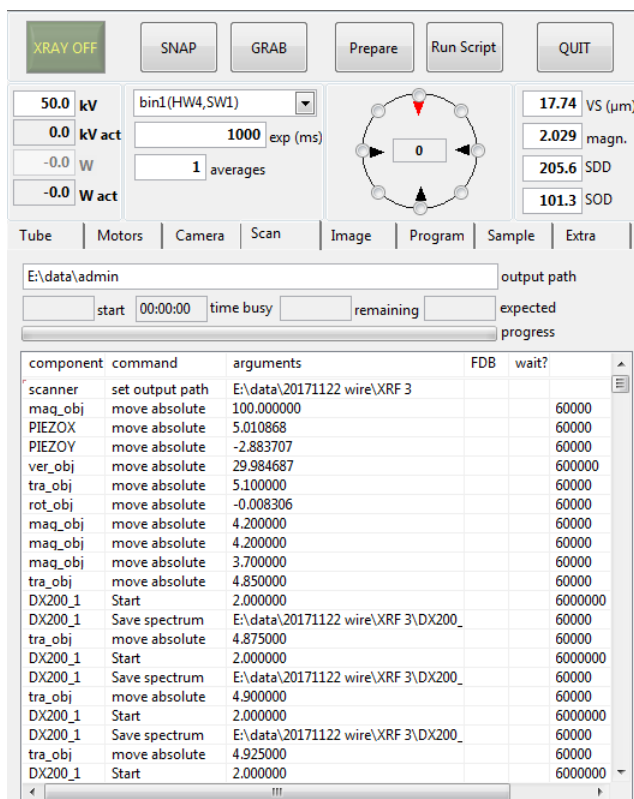


Figure A3- 9 Scan window of the HERAKLES software.

## Performing an XRF experiment

### Xsource software

To perform an XRF experiment, the first step is starting the tubes. Due to compatibility issues these are not include in the HERAKLES software. The dedicated Xsource program is started with the icons on the task bar as shown in Figure A3- 10. The moncapillary source (XRF-CT setup) is the icon on the left, the polycapillary (confocal XRF) on the right.



Figure A3- 10 The icons to start the Xsource software. The Monocap is found on the left and Polycap on the right.



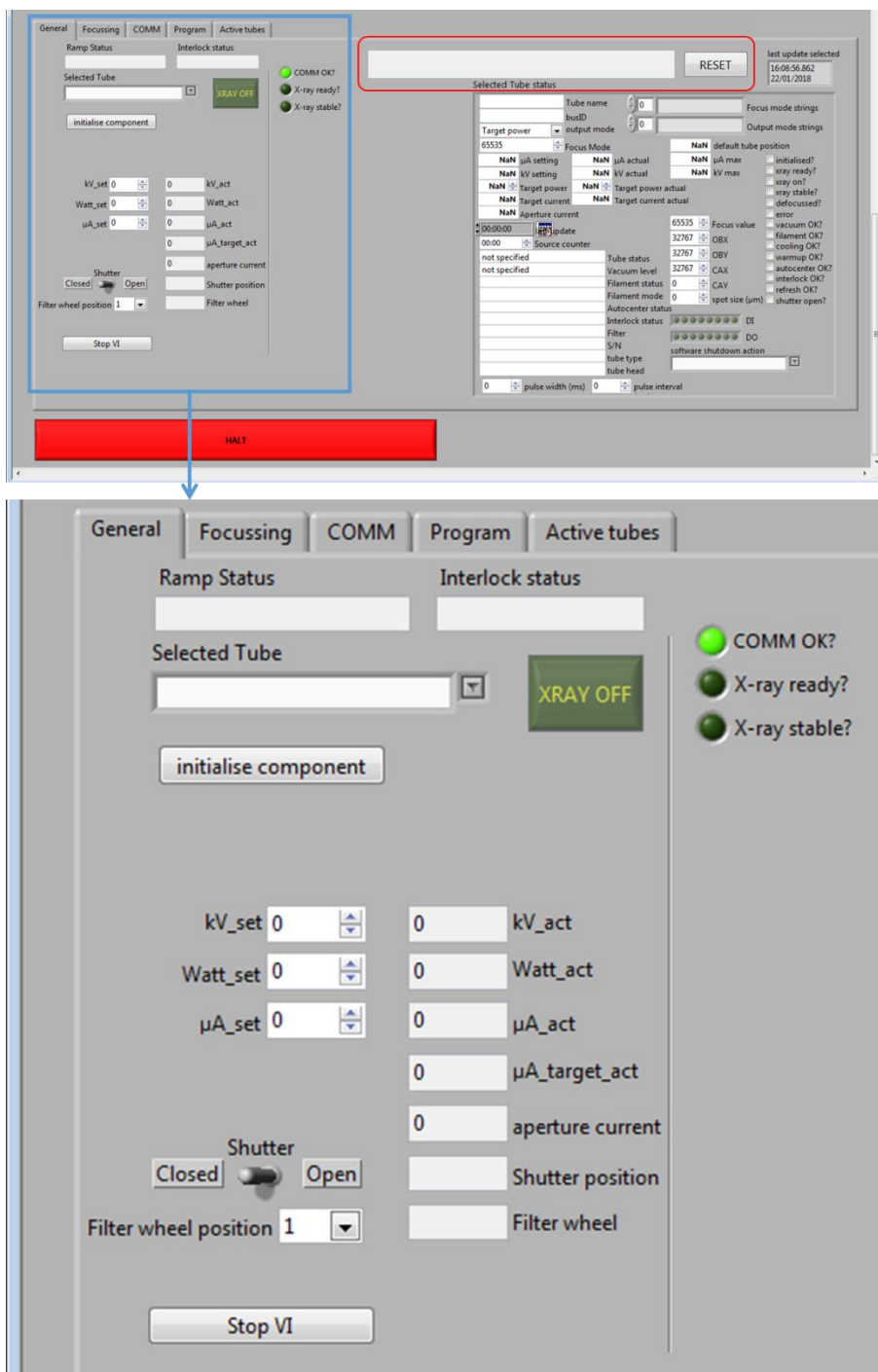


Figure A3- 11 Xsource software. Top: overview of the main window. Bottom: zoom on the tube control functions.

The main window of the Xsource software is shown in Figure A3- 11. The top part of the image gives an overview of the complete window. For day-to-day use of the tubes only the part indicated in blue is used.

The part on the top right indicated in red is also important. This field will show error messages (e.g. interlock error) and the reset button next to it can be used to restore the scanner. When an interlock error has occurred, resetting the software is obligatory before the tube can be started up again.

After starting the software, the tube must be selected in the *Selected Tube* dropdown list. Only one option will be available. Next, the tube is initialized with the *initialise component* button. After this action, the three indicators on the right should be bright green (as now only the top one is).

To generate X-rays, a voltage must be chosen, together with either the tube power or the current. Next the XRAY OFF button can be clicked to start the ramp. This button has the same functionality as the one in the HERAKLES software, serving both as controller and indicator for the tube status.

The XRF tubes are equipped with a shutter, which can be opened and closed with the switch at the bottom of the screen. The filter-wheel position can also be chosen there. Filter 1 (no filter) is the default position. No filters are present in the filter-wheel at the moment.

### **XRF script builder**

XRF measurements are based on a script with the same characteristics as the  $\mu$ CT scripts. They are executed in the same way using the *Scan* tab and the *Run Script* button of the HERAKLES software. However, they are made in a separate, dedicated XRF script builder, which can be found among the add-ons of the HERAKLES software (Figure A3- 12).

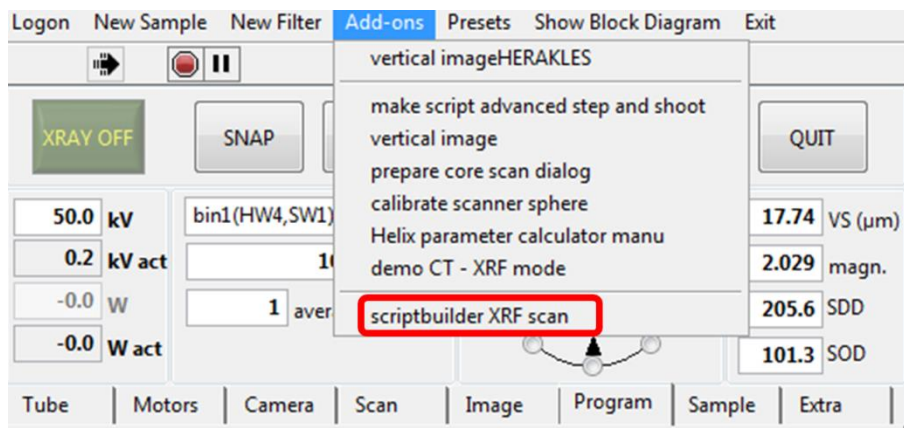


Figure A3- 12 Starting up the XRF scriptbuilder.

Generating an XRF script has three sequential steps. First, the scanning grid is defined (blue area in Figure A3- 13). It is possible to define a point scan, a line scan, a 2D mapping and a 3D mapping. Three motors can be selected for the main movements on the left hand side of the blue area. The bottom one (*Motor INNER*) will move the most while the top one (*Motor OUTER*) the least. The slowest motor should thus be put on top. Next to the motor selection, the range can be selected (in mm). Finally, the number of steps must be entered, defining the step size of the scan.

Once the grid is defined, the exact location of the scan must be chosen. This happens in the red area. In the top row of this area, four grey rectangles enclose (from left to right) the start position of the sample at the  $\mu$ CT station, the position of the feature (i.e. centre point of the scan) relative to the  $\mu$ CT station, the position of the XRF station and the default speeds of the motors.

When building the script based on a transmission image, the exact position of the four ‘\_obj’ motors used to capture this image must be entered (for ver\_obj an offset value is given instead of the absolute position). The position of the feature centred on the transmission stage can be loaded in the script builder by clicking the *Load from scanner*

button or the user can enter the desired values manually. The coordinates of the preferred XRF station should then be entered. These reference positions can be found in Chapter 4 of this work. If desired, the user can implement a different set of reference positions, performing the scan with an offset to the predefined focal point of the XRF-tube. The default speeds are typically left at their given values.

The option exists to scan with the confocal detector (for alignment purposes). In this case the check box *Confocal Movement* must be ticked off and the confocal detector positions entered.

It is important to note that a scan is always built around the centre point (i.e. if you select 4 points on a line scan, 2 will be on the left and 2 on the right of the selected feature).

Finally, in the black area the *measurement time*, *path to save spectra* and *detectors* are selected. Multiple detectors can measure simultaneously. Default scans are in real time. Switching to live time happens in the dedicated detector control software of the HERAKLES program.

Once all parameters are set, the *Generate* button can be used to write the script, which can then be loaded in the *Scan* tab of HERAKLES.

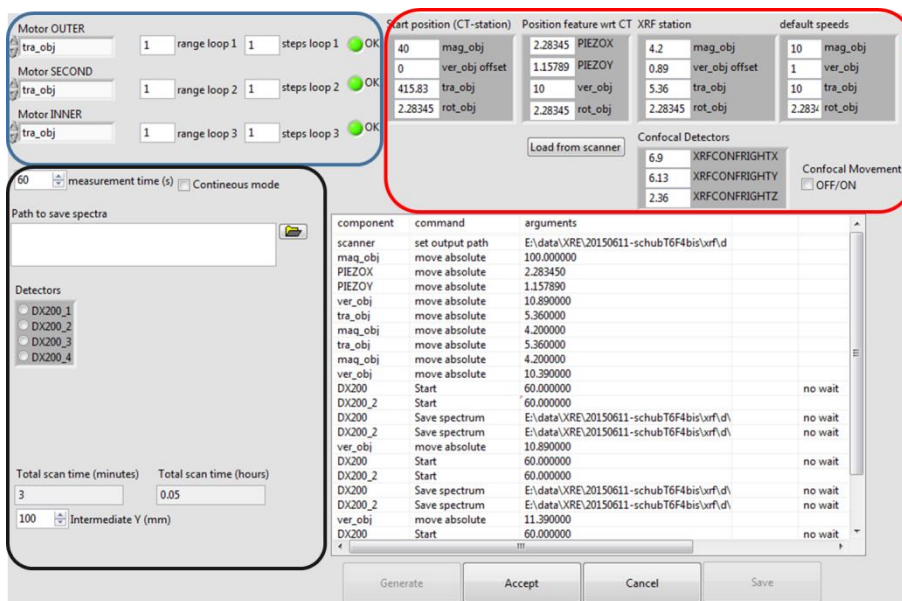


Figure A3- 13 Overview of XRF scriptbuilder window. Blue: scan grid definition; Red: scan position; Black: scan settings. The bottom right corner shows the generated script.

## μCT – XRF linking software

The μCT – XRF linking software is the ultimate tool to integrate different end-stations of the HERAKLES scanner. It is used to create the script for a confocal XRF measurement based on a reconstructed μCT scan, hence, preliminary to using this software a μCT scan should be made and reconstructed (using programs such as Octopus Reconstruction or the XRE reconstruction software present at the Herakles control pc).

Currently the CT-XRF Link software is still placed in the dropbox of XRE, but in the future it will be integrated in the HERAKLES software as an add-on, comparable to the conventional XRF scriptbuilder.

All components of this software are grouped in a LabVIEW project called *CT-XRF Link.lvproj* (Figure A3- 14). As can be deduced from the figure, this project also includes the conventional XRF scriptbuilder. By clicking on *CT-XRF Link.vi* the software will start.

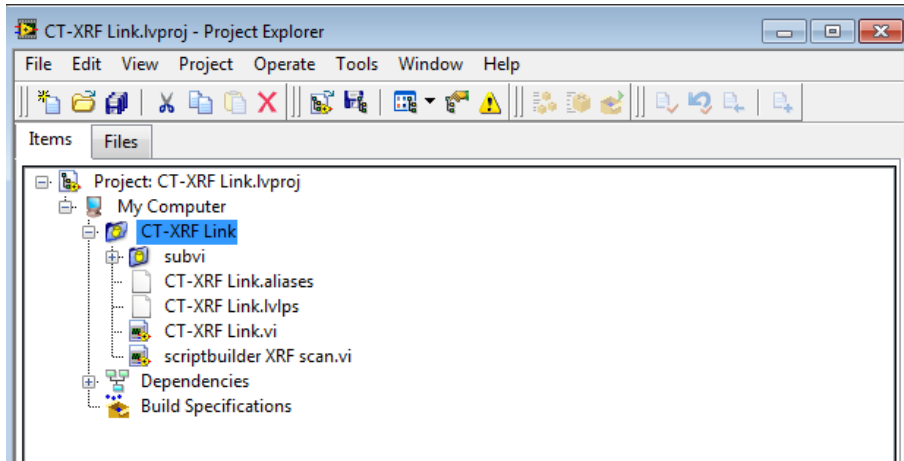


Figure A3- 14 CT-XRF Link.lvproj window.

When the software is started, a pop-up window will appear where the reconstructed  $\mu$ CT data are to be selected (Figure A3- 15). The software will then continue starting up and read the virtual slices of this reconstructed  $\mu$ CT scan.

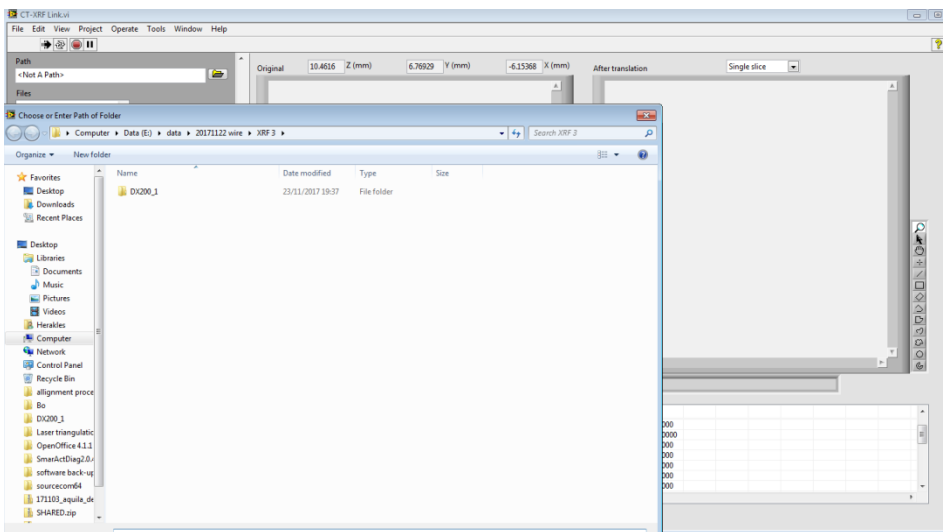


Figure A3- 15 Starting of the CT-XRF link software: pop-up window for data selection.

In the top left corner of the program a virtual slice can be selected, which then appears in the two image sections (Figure A3- 16). These two images are used to select the scan area. This can be a single point, a line, a rectangle or a random figure. Figure A3- 16 gives the example of a single point. By drawing an arrow to the desired measurement point in the left image, the location and angle of attack for the XRF scan are determined. The right image shows the feasibility of the designed scanning point by drawing the approximate position of the polycapillary optics of the X-ray tube and detector. For large samples, these positions might intersect with the sample under certain rotational angles, indicating a different angle of attack must be chosen. When the object on this image comes very close to the optics, it is good practice to check to 10 virtual slices above and below the selected slice to see if there are any possible problems with sample-optics collision there. When the selected point is feasible, its coordinates can be stored in the measurement matrix by clicking the *Add Point* button (Figure A3- 17).

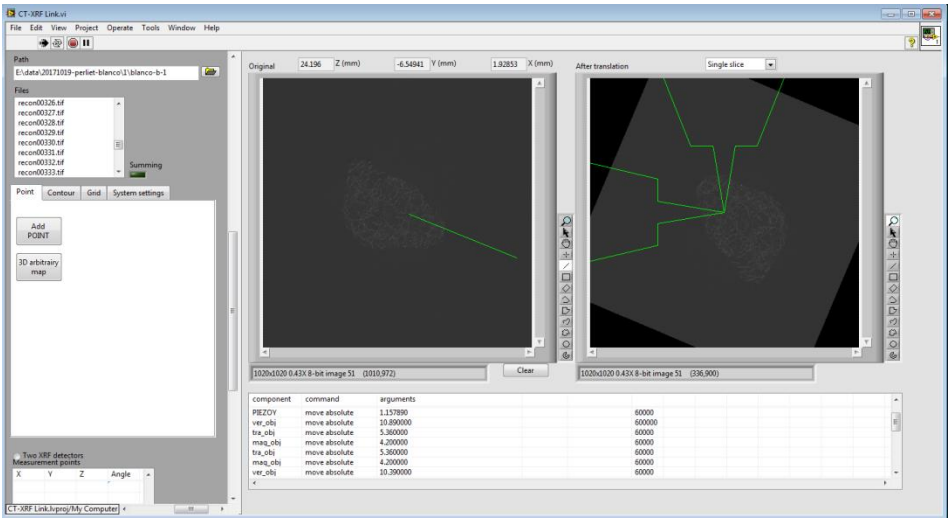


Figure A3- 16 CT-XRF Link: selection of a point.

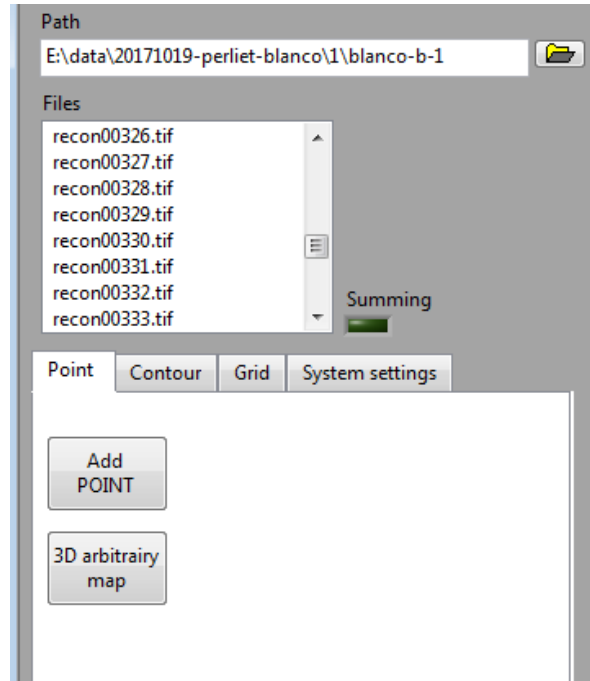


Figure A3- 17 Adding a point to the measurement matrix.

Further details of the scan can be given in the *System Settings* tab (Figure A3- 18). Here, the start position at the CT station is entered, as is the position of the XRF end-station (reference positions can be found in Chapter 4). An offset angle for the XRF scan is given. Default, the sample is rotated by  $-45^\circ$ , putting it at a  $45^\circ$  angle relative to both source and detector. The voxel size is read from the reconstruction data of the  $\mu$ CT scan and should typically not be changed, as are COR (X) and COR(Y).

To avoid sample-optics collision during rotation, it is safer to move the sample back automatically between two points. This is what is called the *safe operation*. The distance (of mag\_obj) where rotational movement is performed is chosen in the *Intermediate Y (mm)* field with 100 mm chosen as default value.



Tab	Start position (CT-station)	XRF station	Direction of rotation	XRF View offset angle	Voxel size	COR (X)	COR (Y)	back out distance	safe operation	Warning
Point										
Contour										
Grid										
System settings	40 0 415.8	4.2 0.89 5.36	0	-45	0.011	507	507	24.3719	<input checked="" type="checkbox"/>	If samples are large they can hit the optics. Use safe operation to prevent this.

Figure A3- 18 System settings tab: defining the details of the scan.

Scrolling down in the left hand box of the user interface will bring the scan matrix in view (Figure A3- 19). Each selected point is saved here with an X, Y, Z and Angle value. Since the coordinate system of the piezo motors is retained when moving the sample between end-stations, these are used to define the X and Y position. Vertical movement always happens with the ver\_obj motor, while rotation is performed with the rot\_obj motor.

Under the scan matrix, the detector can be selected. XRF detector DX200 is the conventional detector, while DX200\_2 is the confocal detector. It is also possible to use the detectors simultaneously. When all desired measurement locations are saved to the matrix and the scan time is selected, the script can be generated by clicking the *Generate script* button.

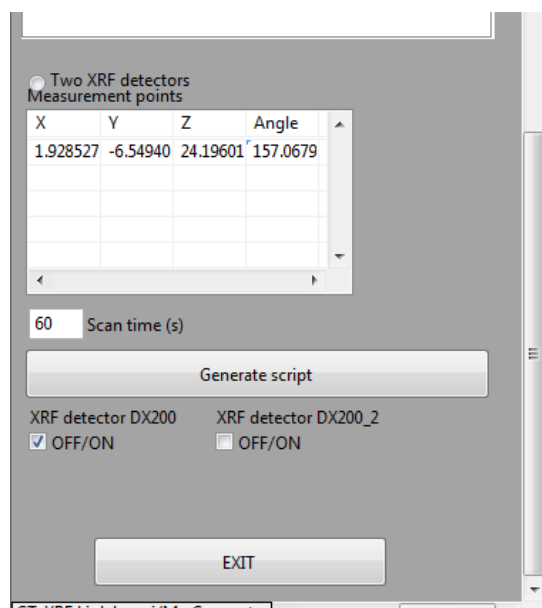
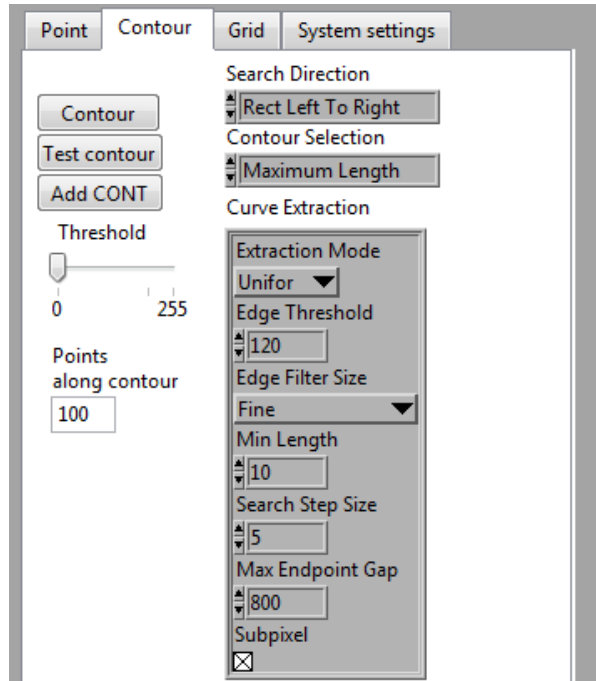


Figure A3- 19 Measurement matrix and scan setting selection.

Next to point scans, it is possible to define a contour and a grid scan. A contour scan is defined in the *Contour* tab (Figure A3- 20). This type of scan follows the external outline of a part of the sample (or the complete sample). The software automatically selects the contour based on a threshold defined by the greyscale of the image.

It takes some time and practice to fluently select a contour from a given scan. The settings giving the best result will be different in each case, depending on the greyscales, which part of the sample is to be selected and the immediate surroundings of this selection the *Contour* button will generate the contour based on these settings. The *Test contour* button plays a simulation of the image in the right image which will indicate possible collisions during the scan. If the automatically generated contour is deemed too dangerous, a manual scan should be constructed point by point using the previously described procedure for point measurements. When satisfied with the proposed contour, the *Add CONT* button adds it to the scan matrix.



*Figure A3- 20 Contour tab: define a contour scan following the outline of a (part of a) sample*

The final option, a grid scan, is used to define 1D or 2D mapping with any shape imaginable. Next to the predefined straight lines, rectangles and circles, free-hand drawn curves and shapes can be made, as seen in Figure A3- 21. 3D scans need to be constructed manually by adding the desired shape in subsequent virtual slices (or equidistantly spaced slices).

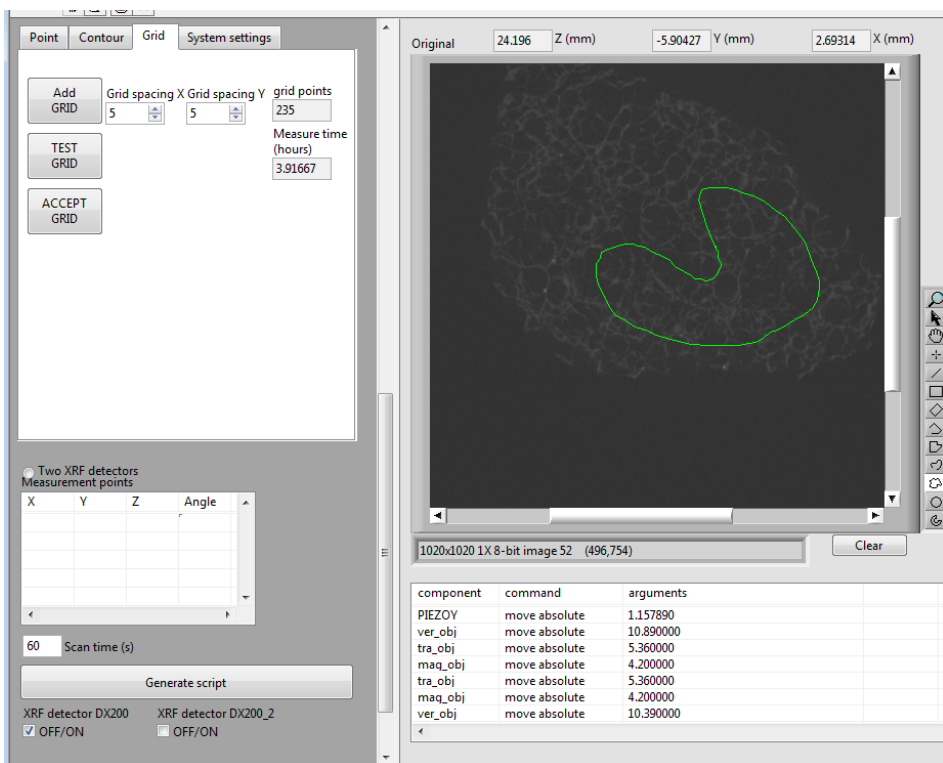
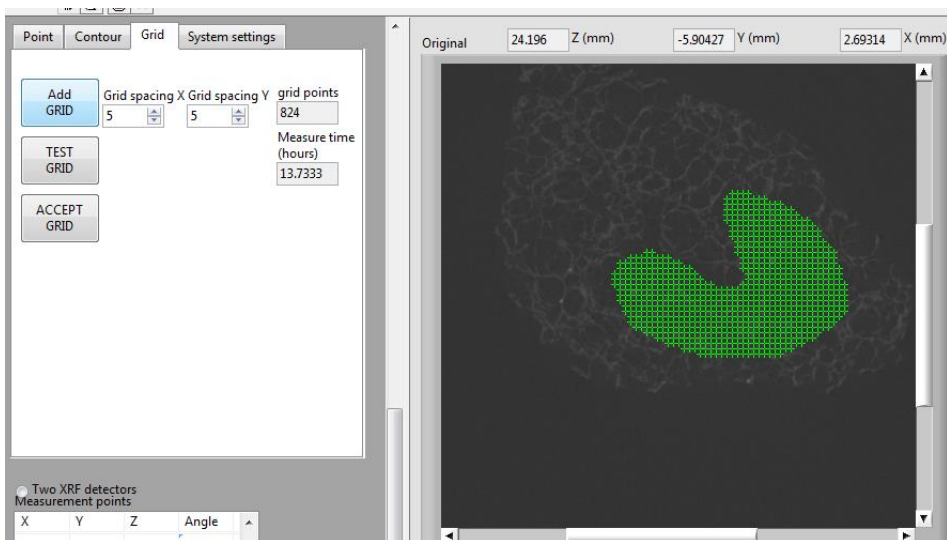


Figure A3- 21 Grid scan: free-hand drawn shape to define the grid outline

The grid itself is defined by an x-spacing and a y-spacing (in mm). By clicking *Add GRID* the measurement points are generated and displayed on the image (Figure A3- 22). This procedure allows the detailed elemental analysis of substructures of real-life samples even with the most irregular shapes (e.g. internal organs of organisms or diamond inclusions). The number of grid points is determined using the grid spacing values and based on the selected measurement time (*System Settings* tab) and the number of point scans the total scanning time is estimated.

As with the contour scan, The *TEST GRID* button simulates the scan in order to visually detect possible sample-optics collisions. When the scan is approved, it can be added to the scan matrix and the script is generated using the same procedure as for point scan measurements.



*Figure A3- 22 Grid points generated in a random free-hand drawn shape*

# A4: Start-up procedures for HERAKLES

## Normal procedure

Under normal circumstances, the components in the electronics and motor control cabinets are running at all times. In this case, it is sufficient to turn on the control pc and the controllers of the XRF sources and detectors (all located in the controller cabinet, see Figure A4- 1) to start the instrument.

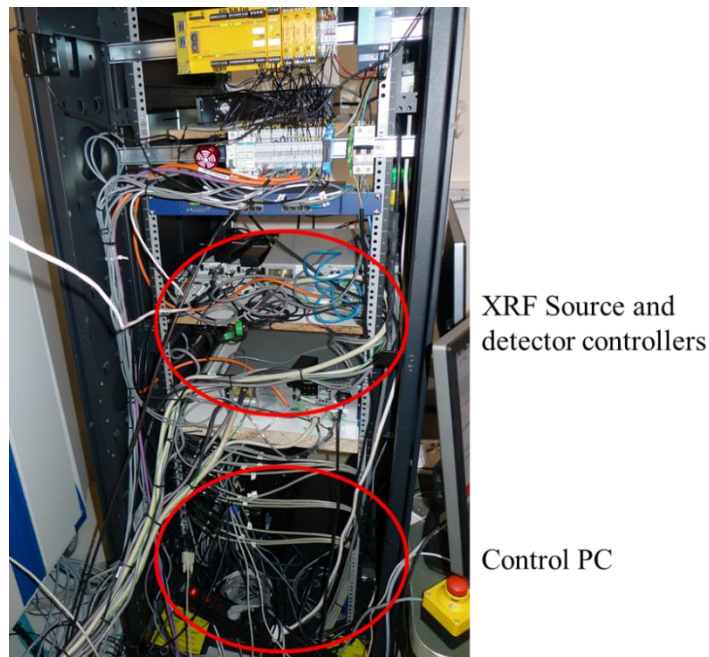


*Figure A4- 1 Picture of the controller cabinet, with the XRF controllers and control pc indicated*

## Procedure after complete shutdown of the instrument

When due to a power failure, a hard reboot of the entire system or any other cause the complete instrument needs to be restarted, the first task is to switch on the electronics in the electronics cabinet. To do so, turn the key, indicated with nr. 1 in Figure A4- 2 clockwise to the middle position (position 1 = off, 2 = on, 3 = standby) and then press the green button indicated with nr. 2.



*Figure A4- 2 Picture of the electronics cabinet, with the key and button needed to reboot the system indicated*

After restarting the electronics, the motor controllers must be switched on by turning the key indicated in Figure A4- 3 to the “on” position.

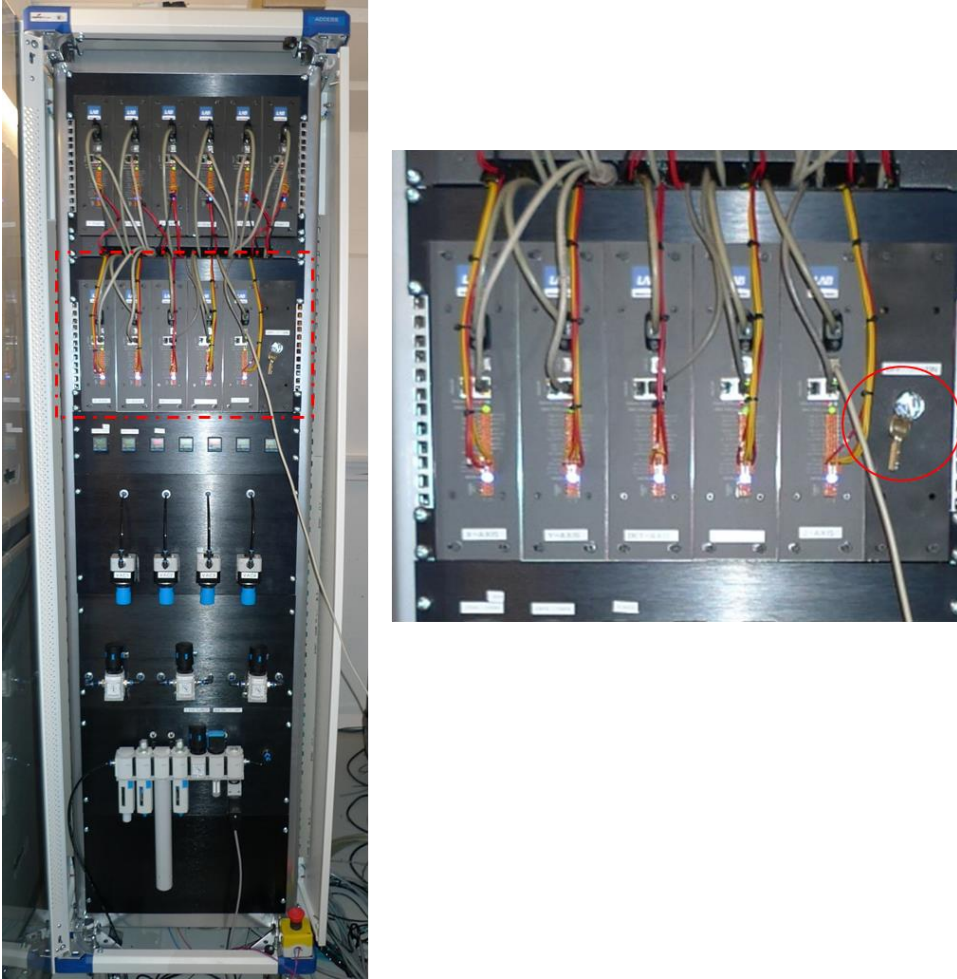


*Figure A4- 3 the motor controllers cabinet, with zoom in on the region with the on/off key*

Once the electronics and the motor controllers are running, proceed according to the “normal procedure”.



## A5: List of beamtimes

04/2014: ID16B

Non-destructive elemental and structural characterization of unique stellar condensate materials on the sub-micron scale

05/2015: ID13

In vivo X-ray fluorescence microimaging of biological model organisms manipulated by laser-based optical tweezers

10/2015: ID16A

Nano-XRF imaging of Fe distribution in mitochondria extracted from Fe-sufficient and Fe-deficient cucumber (*Cucumis sativus* L.) plants

11/2015: ID16B

Submicron XRF Imaging of the Cisplatin Distribution in Peritoneal Carcinomatosis Tumors Treated with Intraperitoneal Chemotherapy

04/2016: ID16B

XRF nano-analysis/nano-tomography of microkrystites from the Cretaceous-Paleogene (K-Pg) boundary

07/2106: ID16A

Nanosopic Imaging of Intracellular Fe within cryo-frozen fibroblasts isolated from patients with Friedreich's Ataxia

02/2017: ID16B

Assessment of drug-tissue interactions in cisplatin treated ovarian cancer tumors with nano-XRF and XANES

10/2017: ID16B

XRF and XRD nano-analysis of unmelted micrometeorites from the Sør Rondane Mountains, Antarctica

11/2017: ID13

Analysing the possible effects of deep sea mining on the nematodes of the abyssal plains using SR nano-XRF and ptychography

## A6: List of publications

### A1 publications:

2014

- Pieter Tack, Jan Garrevoet, Stephen Bauters, Bart Vekemans, **Brecht Laforce**, Eric Van Ranst, Dipanjan Banerjee, Alessandro Longo, Wim Bras, Laszlo Vincze; "Full-field fluorescence mode micro-XANES imaging using a unique energy dispersive CCD detector"; Anal. Chem.; vol.: 86 issue: 17 pag.: 8791 – 8797; IF 2014 : 5.636;
- **Brecht Laforce**, Sylvia Schmitz, Bart Vekemans, Jennifer Rudloff, Jan Garrevoet, Remi Tucoulou, Frank E Brenker, Gema Martinez-Criado, Laszlo Vincze; "Nanoscopic X-ray fluorescence imaging of meteoritic particles and diamond inclusions"; Anal. Chem.; vol.: 86 issue: 24 pag.: 12369 – 12374; IF 2014 : 5.636;

2016

- **Brecht Laforce**, Charlotte Carlier, Bart Vekemans, Julie Villanova, Rémi Tucoulou, Wim Ceelen, Laszlo Vincze; "Assessment of ovarian cancer tumors treated with intraperitoneal cisplatin therapy by nanoscopic X-ray fluorescence imaging"; Sci. Rep.; vol.: 6; IF 2016 : 4.259;
- **Brecht Laforce**, Bram Vermeulen, Jan Garrevoet, Bart Vekemans, Luc Van Hoorebeke, Colin Janssen, Laszlo Vincze; "Laboratory scale X-ray fluorescence tomography: instrument characterization and application in earth and environmental science"; Anal. Chem.; vol.: 88 issue: 6 pag.: 3386 – 3391; IF 2016 : 6.32;

- Charlotte Carlier, **Brecht Laforce**, Stijn Van Malderen, Félix Gremontprez, Remi Tucoulou, Julie Villanova, Olivier De Wever, Frank Vanhaecke, Wim Ceelen, Laszlo Vincze; "Nanoscopic tumor tissue distribution of platinum after intraperitoneal administration in a xenograft model of ovarian cancer"; J. Pharm. Biomed. Anal.; vol.: 131 pag.: 256 – 262; IF 2016 : 3.255;
- Björn De Samber, Maria J. Niemiec, **Brecht Laforce**, Jan Garrevoet, Eva Vergucht, Riet De Rycke, Peter Cloetens, Constantin F. Urban, Laszlo Vincze; "Probing intracellular element concentration changes during neutrophil extracellular trap formation using synchrotron radiation based X-ray fluorescence"; PLoS One; vol.: 11 issue: 11; IF 2016 : 2.806;

2017

- Anna M. Kaczmarek, Ying-Ya Liu, Chunhua Wang, **Brecht Laforce**, Laszlo Vincze, Pascal Van Der Voort, Kristof Van Hecke, and Rik Van Deun; "Lanthanide “Chameleon” Multistage Anti-Counterfeit Materials"; Adv. Funct. Mater.; vol.: 27 issue: 20; IF 2016 : 9.70;
- Stijn Van Malderen, **Brecht Laforce**, Charlotte Nys, Maarten De Rijcke, Riet De Rycke, Michiel De Bruyne, Matthieu Boone, Karel De Schamphelaere, Olga Borovinskaya, Björn De Samber, Laszlo Vincze, Frank Vanhaecke; "Three-dimensional reconstruction of the tissue-specific multielemental distribution within Ceriodaphnia dubia via multimodal registration using laser ablation ICP-mass spectrometry and X-ray spectroscopic techniques"; Anal. Chem.; vol.: 89 issue: 7 pag.: 4161 – 4168; IF 2016 : 6.32;
- Pieter Tack, Bart Vekemans, **Brecht Laforce**, Jennifer Rudloff-Grund, Willinton Y Hernandez, Jan Garrevoet, Gerald Falkenberg, Frank Brenker, Pascal Van Der Voort, Laszlo Vincze; "Application toward confocal full-field microscopic X-ray absorption near edge structure spectroscopy"; Anal. Chem.; vol.: 89 issue: 3 pag.: 2123 – 2130; IF 2016 : 6.32;

- Anna Kaczmarek, Jing Liu, **Brecht Laforce**, Laszlo Vincze, Kristof Van Hecke, Rik Van Deun; "Cryogenic luminescent thermometers based on multinuclear Eu<sup>3+</sup>/Tb<sup>3+</sup> mixed lanthanide polyoxometalates"; Dalton Trans.; vol.: 46 issue: 18 pag.: 5781 – 5785; IF 2016 : 4.029;
- Stijn Van Malderen, **Brecht Laforce**, Thibaut Van Acker, Laszlo Vincze, Frank Vanhaecke; "Imaging the 3D trace metal and metalloid distribution in mature wheat and rye grains via laser ablation-ICP-mass spectrometry and micro-X-ray fluorescence spectrometry"; J. Anal. At. Spectrom.; vol.: 32 issue: 2 pag.: 289 – 298; IF 2016 : 3.379;
- **Brecht Laforce**, Bert Masschaele, Matthieu Boone, David Schaubroeck, Manuel Dierick, Bart Vekemans, Christophe Walgraeve, Colin Janssen, Veerle Cnudde, Luc Van Hoorebeke, Laszlo Vincze; "Integrated three-dimensional microanalysis combining X-ray microtomography and X-ray fluorescence methodologies"; Anal. Chem.; vol.: 89 issue: 19 pag.: 10617 – 10624; IF 2016 : 6.32;
- Anna Kaczmarek, Ying-Ya Liu, Chunhua Wang, **Brecht Laforce**, Laszlo Vincze, Pascal Van Der Voort, Rik Van Deun; "Grafting of a Eu<sup>3+</sup>-tfac complex on to a Tb<sup>3+</sup>-metal organic framework for use as a ratiometric thermometer"; Dalton Trans.; vol.: 46 issue: 37 pag.: 12717 – 12723; IF 2016 : 4.029;

2018

- Björn De Samber, Eline Meul, **Brecht Laforce**, Boel De Paepe, Joel Smet, Michiel De Bruyne, Riet Derycke, Sylvain Bohic, Peter Cloetens, Rudy Van Coster, Peter Vandenabeele, Tom Vanden Berghe; "Nanoscopic X-ray Fluorescence Imaging and Quantification of Intracellular Key-Elements in Cryofrozen Friedreich's Ataxia Fibroblasts"; PLoS One; IF 2017: 3.54;

- Anna M. Kaczmarek, Dolores Esquivel, **Brecht Laforce**, Laszlo Vincze, Pascal Van Der Voort, Francisco J. Romero - Salguero, Rik Van Deun; "Luminescent thermometer based on Eu<sup>3+</sup>/Tb<sup>3+</sup>-organicfunctionalized mesoporous silica"; *Luminiscence*; 1-7; IF 2016 : 1.509
- Jing Liu, Hannes Rijckaert, Min Zeng, Katrien Hastraete, **Brecht Laforce**, Laszlo Vincze, Isabel Van Driessche, Anna Kaczmarek and Rik Van Deun; "Simultaneously excited downshifting/upconversion luminescence from lanthanide-doped core/shell fluoride nanoparticles for multimode anticounterfeiting"; *Adv. Funct. Mater.*; IF 2017: 12.124;

## A2 publications

2016

- **Brecht Laforce**, Sylvia Schmitz, Bart Vekemans, Jennifer Rudloff, Jan Garrevoet, Remi Tucoulou, Frank E. Brenker, Gemma Martinez-Criado, Laszlo Vincze; "Nanosopic X-ray Fluorescence imaging of meteoritic particles and diamond inclusions"; *ESRF Highlights* 2015; pag.: 13-14